



HAL
open science

Wetting of soluble polymers

Julien Dupas

► **To cite this version:**

Julien Dupas. Wetting of soluble polymers. Soft Condensed Matter [cond-mat.soft]. Université Pierre et Marie Curie - Paris VI, 2012. English. NNT: . pastel-00781130

HAL Id: pastel-00781130

<https://pastel.hal.science/pastel-00781130>

Submitted on 25 Jan 2013

HAL is a multi-disciplinary open access archive for the deposit and dissemination of scientific research documents, whether they are published or not. The documents may come from teaching and research institutions in France or abroad, or from public or private research centers.

L'archive ouverte pluridisciplinaire **HAL**, est destinée au dépôt et à la diffusion de documents scientifiques de niveau recherche, publiés ou non, émanant des établissements d'enseignement et de recherche français ou étrangers, des laboratoires publics ou privés.



**THÈSE DE DOCTORAT DE
L'UNIVERSITÉ PIERRE ET MARIE CURIE**

Spécialité
Physico-Chimie des Polymères

École doctorale de Physique et Chimie des Matériaux (Paris)

Présentée par

Julien DUPAS

Pour obtenir le grade de

DOCTEUR de l'UNIVERSITÉ PIERRE ET MARIE CURIE

Sujet de la thèse :

**Mouillage de polymères solubles
(Wetting of soluble polymers)**

soutenue le 6 décembre 2012
devant le jury composé de :

M. David QUÉRÉ	Président du Jury
M. Kari DALNOKI-VERESS	Rapporteur
M. Thierry ONDARÇUHU	Rapporteur
M. François LEQUEUX	Directeur de thèse
Mme. Emilie VERNEUIL	Invitée
M. Laurent FORNY	Invité

Abstract

Key words: wetting, evaporation, condensation, diffusion, dissolution, thin layers, glass transition, carbohydrates.

The wetting of a soluble substrate is a situation commonly encountered in day-to-day life. For instance, the practical motivation of this study concerns the preparation of beverages using dehydrated powders, consisting of water-soluble substances such as carbohydrates. Hydrodynamical theories describing wetting onto insoluble substrates cannot account for experimental observations in the case of a liquid spreading onto a soluble substrate. Tay *et al.*(1) made the hypothesis that the water content ϕ at the contact line controls the contact angle value θ and they showed the importance of the evaporation/condensation of the solvent during wetting. In this study, we demonstrate that other mass transfers have to be considered to improve the understanding on wetting dynamics on soluble surfaces; thus diffusion within the polymer of the condensed water or directly from the droplet are processes that contribute to the hydration of the substrate and the modification of the contact angle of the drop. Therefore, we use the following approach to carry out this study: (i) finite elements simulations are performed in order to take into account diffusion effects in the layer and validate our theoretical arguments, (ii) spreading experiments of water onto maltodextrin thin layers are performed in order to study the wetting and the hydration ahead the contact line. This work allows us to highlight the influence of the diffusion in the polymer that makes the hydration profiles ahead the contact line more complex with a diffusion region where evaporation occurs. A wetting diagram thickness-velocity ($e - U$) with different regimes is established. Those regimes are validated with the experimental data. In particular, we evidence a regime where the contact angle θ is a function of the quantity eU . Furthermore, we evidence the effect of glass transition in the polymer on the contact angle and the hydration of the substrate. Finally, a preliminary study is performed to understand the influence of another transfer at stake in the wetting process: the dissolution of the polymer in the solvent.

To my wife whose constant support and advices made
my research pleasant and efficient

Acknowledgements

I would like to thank to my PhD supervisor, Mr François Lequeux, for helping me during my researches these past three years. I express my gratitude to him since without his inspirational guidance, his enthusiasm and his encouragements, I could never produce such results. His will to let the students creative freedom but with constant good advices and relevant theoretical propositions allows to deliver our best at all times. I hope I could be as lively, enthusiastic, and energetic as François during my career. My special thanks go also to the other members of my supervising team. First, Emilie Verneuil who gave me many advices to build my experimental set-ups. She has this appreciable skill to quickly understand and identify the needs for a new experiment and to establish the link between the experimental results and the theory. Her detailed and constructive comments helped me a lot for the advancing of my work. Furthermore, her ability to write high-quality scientific articles allowed me to improve my writing skills on a number of points. Second, I thank Laurence Talini for her important support throughout this work. Arrived more lately on the project, she easily integrated into the team and demonstrated her passion for science. She provided invaluable feedback on my experimental results and their analysis. During the writing she responded rapidly to my propositions and modifications and her contribution made a significant difference to the overall shape of the dissertation.

As regards the industrial partner, I am grateful to Laurent Forny, without whom this PhD would have not be possible. After the promising results of the experiments performed during the internship at Nestlé Reserach Center in 2009, he convinced Nestlé executives to fund my work and went through many administrative difficulties, so that I could start my work in time. Then, over the three last years, he constantly followed the progress of the PhD work and proposed many ideas to improve the experiments or the analyses. I am thankful for his support especially when I had to prepare presentations for conferences or industrial meetings. His way of explaining science with clarity and impact have learnt me to select information depending on the attendance and to focus the attention on the key messages. I also would like to express my gratitude for Marco Ramaïoli, my other supervisor at Nestlé. Marco has been helpful in providing advice many times during my PhD. He is a wonderful and generous person and I admire his positive behaviour in all situations. Furthermore, he was very patient when we were trying to improve the FEM simulations by phone or email, despite the slow progress of the simulations. Finally, Marco has this remarkable faculty to point out the issues that nobody had suspected. Laurent and Marco left an indelible mark in my way of working that will undoubtedly help me in

my further industrial career.

I would also like to offer my thanks to both trainees I could work with. First, Leopold Mottet who had the difficult task to perform preliminary experiments on powder imbibition. Second, Clément Dupuy who helped me with wetting experiments and validated one of the observed effects. I also have to thank all the people from the laboratory who provide me indispensable help along PhD. In the PPMD laboratory, I think to Mohamed Hanafi for the experimental advices, Ludovic Olanier for helping me in the drawings of my experimental set-up, Antoine Chateauminois for the advices on the Labview software, Maxime Van Landeghem and Bruno Bresson for their enthusiasm in performing the NMR measurements, Cécile Monteux and Astrid Tay for the discussions about their previous results on my topic and Guylaine Ducouret for the formation on viscosity measurements. At Nestlé, I want to thank Jean-Christophe Andrieux who performed useful measurements for me, Gilles Vuataz and Adam Burbidge for the scientific discussions about my results and for sharing their experience in the field of food science, and finally Alejandro Marabi for his relevant comments on my monthly reports. Of course, I would like to thank all the students that I had the opportunity to meet during the PhD. I will miss the nice atmosphere of the laboratory.

Finally, I would like to thank the members of the Jury who accepted to evaluate my work during the PhD defense which took place on December, 6th, 2012 in the amphitheatre Langevin at ESPCI. I am grateful to David Quéré from PMMH laboratory at ESPCI in Paris, president of the Jury, and to both reviewers Kari Dalnoki-Veress from McMaster University, Canada and Thierry Ondarçuhu from CEMES in Toulouse.

Résumé en français

Mots Clés : mouillage, évaporation, condensation, diffusion, dissolution, couches minces, transition vitreuse, maltodextrine.

Dans cette étude, nous nous sommes intéressés au mouillage d'une surface soluble par l'un de ses solvants, le but étant de comprendre les mécanismes de transfert qui interviennent dans la dynamique de mouillage. Cette thématique s'inscrit dans la continuité de la thèse d'Astrid Tay qui avait mis en évidence le rôle clé de l'évaporation/condensation lors du mouillage d'une couche soluble. En ce qui nous concerne, le principal système utilisé pour cette étude a été l'eau mouillant des couches de maltodextrine. Cette étude a été initiée par Nestlé dans le but de comprendre comment les ingrédients des poudres alimentaires déshydratées interagissent avec l'eau lors de la reconstitution d'une boisson et de la phase de mouillage des grains.

Au cours de ce travail, nous avons développé un dispositif expérimental qui permet à la fois d'étudier le mouillage via la mesure de l'angle de contact θ de façon dynamique, mais aussi de quantifier les transferts de matière en avant de la ligne de contact. Pour cela, une couche mince de polymère est déposée sur un wafer de silicium. Lorsque l'épaisseur est de l'ordre des longueurs d'onde du visible, cette couche apparaît colorée. La couleur dépendant de l'épaisseur, nous sommes alors en mesure de suivre le gonflement de la couche résultant de l'hydratation dans le temps et l'espace. Ainsi, nous disposons d'une méthode précise pour étudier la relation entre l'angle de contact et l'hydratation de la couche. Grâce à différentes variantes du montage expérimental, 6 décades de vitesse de ligne de contact peuvent être observées. Par ailleurs, les principaux paramètres physico-chimiques des couches minces utilisées ont été mesurés : le coefficient de diffusion de l'eau dans la maltodextrine, la viscosité des solutions de maltodextrine, la vitesse de dissolution ou encore l'isotherme de sorption qui relie l'activité en eau à la fraction volumique d'eau dans la couche. Ces paramètres nous ont permis de valider nos mesures par des descriptions théoriques.

Classiquement, le mouillage est généralement décrit via des modèles hydrodynamiques qui font intervenir la circulation d'eau dans la goutte afin d'expliquer la relation entre l'angle de contact et la vitesse de la ligne de contact. Dans notre cas où le matériau est mouillé par l'un de ses solvants, l'hydratation de la couche contrôle principalement le mouillage.

Les mécanismes de transfert qui influencent l'hydratation de la couche mince sont bien identifiés. Nous pouvons en distinguer trois (voir la Figure 1):

- L'évaporation du solvant qui peut ensuite se condenser en avant de la ligne de contact : Tay *et al.*(1) ont démontré que ce transfert était le plus important

- La diffusion du solvant dans le polymère : directe (de la goutte vers le polymère) ou indirecte (l'eau condensée peut diffuser dans la couche)
- La dissolution du matériau soluble dans le solvant

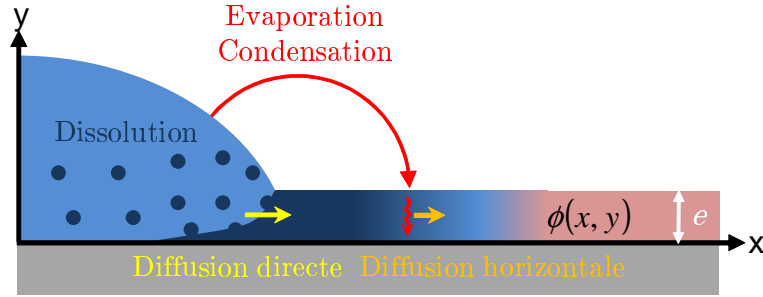


Figure 1: Transferts de matière intervenant lors du mouillage d'une surface soluble - Trois transferts ont été identifiés lors de l'étalement d'une goutte d'eau sur un polymère soluble : l'évaporation/condensation, la diffusion dans la couche (directe ou indirecte) et la dissolution.

A travers ce travail, nous avons confirmé que le principal transfert influençant le mouillage d'un composé soluble est bien l'évaporation/condensation comme prédit par Tay *et al.* Néanmoins, nous avons pu montrer que la diffusion d'eau dans la couche de polymère n'est pas négligeable. Nous avons commencé notre étude en utilisant des arguments théoriques basés sur l'évaporation/condensation et la diffusion dans le polymère, qui mettent en avant des longueurs caractéristiques de notre problème. Nous avons validé cette approche via des simulations en éléments finis qui sont en accord avec les prédictions théoriques. Ainsi, trois sortes de transferts interviennent dans la mise en place des longueurs caractéristiques : la condensation, la convection et la diffusion horizontale. Selon la valeur des nombres de Péclet dans la couche et dans l'air, l'un de ces transferts devient négligeable conduisant ainsi à différentes régions d'hydratation en avant de la ligne de contact. La principale longueur caractéristique correspond à la transition de la zone de diffusion/condensation proche de la ligne de contact vers la zone de condensation/convection à de plus grandes distances. Elle caractérise le passage d'un plateau de concentration vers un profil en loi de puissance. Si l'on introduit des non-linéarités dans le problème comme une isotherme de sorption $a_w = f(\phi)$ ou un coefficient de diffusion variable $D_p(\phi)$, cette longueur est alors plus de 100 fois supérieure à celle du cas linéaire.

La propriété principale de la région de condensation/convection est que la quantité d'eau ϕ est une fonction du produit eU , c'est à dire de l'épaisseur de la couche par la vitesse de ligne de contact. Cette propriété n'est pas valable dans les autres domaines. Néanmoins, si l'on ajoute la diffusion directe comme condition aux limites sous la goutte, le plateau de concentration est perturbé et cette propriété reste alors valable dans la zone de diffusion/condensation. Si le produit eU devient trop grand, un autre phénomène intervient. Des gradients verticaux de concentration se forment devant la ligne de contact jusqu'à une distance x_C . Dès que x_C devient plus grand que la zone de diffusion/condensation, la dépendance de la fraction d'eau ϕ en eU n'est alors plus valable devant la ligne de contact. Ainsi il ressort que pour des fortes valeurs de eU , ϕ

ne doit plus dépendre du produit eU . On complète donc le travail de Tay *et al.* en montrant que la prise en compte de la diffusion directe et de la diffusion horizontale dans la couche agrandit le domaine où ϕ ne dépend que de eU . En effet, la zone de diffusion/condensation correspond à une nouvelle longueur de coupure ξ de plusieurs micromètres là où une longueur nanométrique était auparavant considérée. Cela nous permet alors d'établir un diagramme de mouillage $e = f(U)$ avec différents domaines (voir la Figure 2) :

- Un régime mince à faible eU où ϕ dépend de eU .
- Un régime intermédiaire où l'on perd la propriété en eU mais où ϕ dépend encore de e et de U .
- Un régime épais où ϕ dépend seulement de U .
- Un régime sec où ϕ est attendu constant.

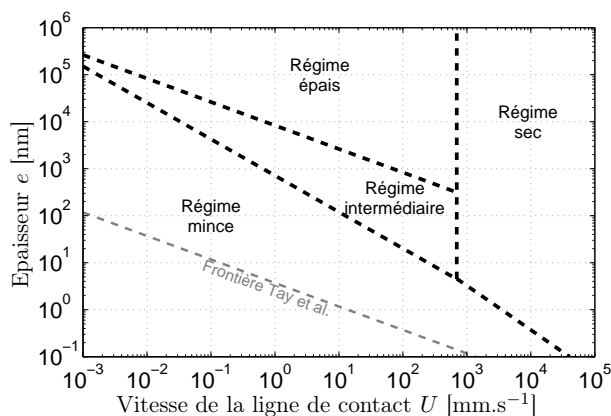


Figure 2: Diagramme de mouillage - Diagramme de mouillage construit avec les paramètres suivants : $D_p = 1.4 \cdot 10^{-11} \text{ m}^2 \cdot \text{s}^{-1}$, $D_v = 2.7 \cdot 10^{-5} \text{ m}^2 \cdot \text{s}^{-1}$, $\rho = 997.05 \cdot 10^3 \text{ g} \cdot \text{m}^{-3}$, $c_{sat} = 23 \text{ g} \cdot \text{m}^{-3}$, $\xi [\mu\text{m}] = 37 U [\text{mm} \cdot \text{s}^{-1}]^{-0.55}$, $\varepsilon = 1 \text{ nm}$, $L = 5 \text{ mm}$ et $K = 0.006$. L'ancienne frontière entre le régime mince et le régime épais correspondant aux prédictions de Tay *et al.* est représentée par un trait pointillés gris.

Nos expériences valident alors le diagramme de mouillage construit précédemment. Nos mesures d'angle de contact θ montrent un bon accord avec l'évolution attendue dans chaque régime. Par exemple, on confirme la dépendance en eU dans le régime mince ce qui indique que l'angle de contact est bien une fonction de ϕ à la ligne de contact. Ensuite, la position de la frontière entre le régime mince et le régime intermédiaire est confirmée expérimentalement. La position de cette frontière dépend de la taille de la région de diffusion/condensation devant la ligne de contact ξ . Cette région est bien observée dans nos profils expérimentaux de fraction en eau même si ceux ci affichent une complexité supérieure à nos prédictions.

Nous nous sommes également intéressés aux effets de la transition vitreuse qui a lieu dans le polymère durant le mouillage. En effet, quand l'humidité initiale est faible, la couche voit son

hydratation suffisamment augmenter pour croiser la transition vitreuse. Il en résulte une forte variation du coefficient de diffusion de l'eau dans le polymère. Nous avons alors montré que la transition vitreuse se manifeste à la fois dans la mesure de l'angle de contact $\theta(U)$ mais aussi dans la mesure de la concentration devant la ligne de contact via la couleur. Un coude prononcé apparaît dans la courbe de l'angle de contact à la vitesse U_g . De même, une forte variation de ϕ apparaît à une distance x_g de la ligne de contact dans la zone de transition vitreuse. Ainsi, à plus forte vitesse, x_g diminue et finit par être de l'ordre du nanomètre tout comme la taille de la zone de diffusion/condensation. Alors qu'à U élevé, la goutte progresse sur un substrat vitreux, l'hydratation de la ligne de contact engendre la transition vitreuse et l'augmentation rapide du coefficient de diffusion. A $U < U_g$, la goutte progresse sur un substrat fondu avec un angle de contact θ beaucoup plus faible. Cette variation de l'état d'hydratation a ensuite été mise en relation avec le diagramme de mouillage établi dans le chapitre précédent. La transition vitreuse modifie la position de la frontière entre le régime mince et le régime intermédiaire. La forte variation du coefficient de diffusion est à l'origine de la translation verticale de la frontière dans le diagramme.

Enfin, dans un dernier chapitre, nous avons discuté du rôle de la dissolution sur le mouillage des couches solubles. En effet, nous pouvons observer que la couche de polymère se dissout rapidement sous la goutte d'eau en déplacement. Dans un premier temps, nous avons tenté d'expliquer l'origine des rides observées derrière la ligne de contact durant le processus d'étalement de nos gouttes d'eau sur la maltodextrine. La compétition entre la dissolution du polymère sous la goutte et le mouvement de la ligne de contact laisse apparaître une bande de polymère non dissoute derrière la ligne de contact. En raison de l'hydratation, cette bande de matière est fortement gonflée ce qui engendre l'apparition de rides à cause des contraintes liées à la ligne de contact. Dans un second temps, nous avons commencé une étude préliminaire sur la vitesse de dissolution de la maltodextrine afin d'expliquer la taille de la bande de matière observée. Le processus de dissolution derrière la ligne de contact est suspecté de jouer un rôle sur le mouillage aux faibles vitesses. En effet, on s'attend à une augmentation de viscosité dans la goutte qui pourrait expliquer pourquoi l'on tend à observer un passage du régime mince vers un régime inconnu aux faibles valeurs du produit eU .

A travers cette étude, nous avons pu améliorer la compréhension des mécanismes de transfert qui influencent le mouillage d'un polymère par l'un de ses solvants. Nous avons ainsi montré que l'évaporation/condensation associée à la diffusion dans la couche déterminaient la valeur de l'angle de contact θ . On crée alors les conditions pour que θ soit une fonction de eU dans un régime mince plus grand que celui prédit par Tay *et al.* Nos expériences confirment cette propriété et les longueurs caractéristiques issues de nos arguments théoriques. Aussi, nous avons mis en évidence d'autres régimes à grand eU où des gradients verticaux de concentration apparaissent dans la couche. Ceci est synthétisé dans un diagramme de mouillage complet. Enfin, nous avons relié la transition vitreuse dans le polymère à nos observations expérimentales.

Table of Contents

List of Figures	xiii
List of Tables	xvii
Glossary	xix
1 Introduction	1
2 State of the art	5
2.1 Wetting	5
2.1.1 Young's relation	5
2.1.2 Spreading dynamics on a non-soluble surface	6
2.1.3 Wetting in presence of evaporation	7
2.1.4 Wetting of a soluble layer	8
2.2 Dissolution of polymers	12
2.3 Water imbibition in porous media	14
2.4 Open questions	14
3 Materials & Methods	17
3.1 Materials	17
3.1.1 From carbohydrates to lipids	17
3.1.1.1 Maltodextrins	17
3.1.1.2 Lactose	18
3.1.1.3 Lipids	19
3.1.2 Materials characterization	19
3.1.2.1 The structure of a powder grain	19
3.1.2.2 Water activity	19
3.1.2.3 Maltodextrin sorption isotherms	20
3.1.2.4 Glass transition	21
3.1.2.5 Diffusion coefficient	22
3.1.2.6 Dissolution speed	24
3.2 Preparation of carbohydrates samples	27
3.2.1 Thin layers	28
3.2.2 Thick layers	30

TABLE OF CONTENTS

3.3	Spreading experiments	31
3.3.1	Experimental set-up	31
3.3.2	Pulled substrate experiment or swollen droplet	33
3.3.3	Contact angle measurement	34
3.3.4	Color analysis	36
3.3.4.1	Interferences theory	36
3.3.4.2	Color analysis and thickness	38
3.3.4.3	Swelling and water content	41
3.4	Conclusions	42
4	Wetting regimes	43
4.1	Introduction	43
4.2	Preliminary observations	43
4.2.1	The failure of hydrodynamics theories	43
4.2.2	Discrepancy with the Tay <i>et al.</i> wetting diagram	45
4.3	The role of diffusion: FEM simulations	47
4.3.1	Characteristic lengths	49
4.3.1.1	Thin films	49
4.3.1.2	Effect of vertical gradient	51
4.3.2	Evaporation/water uptake (no direct diffusion)	52
4.3.2.1	Thin and thick layers: simulations vs. theory	52
4.3.2.2	Water content profiles in the thin film regime	54
4.3.2.3	The characteristic length κ	56
4.3.3	Direct diffusion without condensation	57
4.3.4	Condensation and direct diffusion	60
4.3.5	Scaling $\phi(eU)$	61
4.3.6	Non-linearities	64
4.3.6.1	Sorption isotherm $a_w = f(\phi)$	64
4.3.6.2	Concentration-dependent diffusion coefficient $D_p(\phi)$	67
4.3.7	Conclusions	67
4.4	New wetting diagram and confrontation with experimental data	68
4.4.1	Diffusion/Condensation region in hydration profiles	68
4.4.1.1	Experimental profiles $\phi(x)$	68
4.4.1.2	The broken wafer experiment	72
4.4.1.3	Measurement of the diffusion/condensation region size	74
4.4.2	Building the new wetting diagram	75
4.4.2.1	A new cut-off length	75
4.4.2.2	A larger thin film regime	78
4.4.2.3	Intermediary thick regime	78
4.4.2.4	Other frontiers	79
4.4.3	Experimental validation of wetting regimes	82
4.4.3.1	Validation of the scaling $\theta(eU)$ in the thin film regime	82
4.4.3.2	Observation of the thick film regime	84

4.4.3.3	Iso- θ in the wetting diagram	84
4.5	Conclusions	87
5	Glass transition effect in wetting dynamics	89
5.1	Introduction	89
5.2	Wetting dynamics	89
5.2.1	Contact angle measurements	90
5.2.2	Water content profiles	91
5.3	Consequences of glass transition on hydration mechanisms	93
5.4	Link with the wetting diagram	95
5.5	Confirmation with various polymers and solvents	97
5.6	Conclusions	99
6	Dissolution and wetting	101
6.1	Introduction	101
6.2	Wrinkles behind the contact line	101
6.2.1	Characterization	101
6.2.2	Origin of the wrinkles	104
6.3	Preliminary study on dissolution	106
6.3.1	Wrinkles: what is the link with the dissolution speed ?	106
6.3.2	Dissolution of a maltodextrin sphere	107
6.3.3	Dissolution at the contact line	109
6.4	Conclusions	109
7	Conclusions and open questions	111
A	Color scale	117
B	Water flux in spreading experiment	119
C	Direct diffusion: 1D-theory	123
D	Diffusion in a semi-infinite media	125
E	Dissolution of maltodextrins	127
E.0.1	Dissolution of a maltodextrin sphere	127
E.0.2	Dissolution of a soluble channel	128
F	Preliminary study of the imbibition in a soluble media	131
F.0.3	Water penetration in soluble capillary	131
F.0.4	Viscosity increase at the contact line	133
F.0.5	Effect of swelling behind the contact line	134
F.0.6	Dissolution and swelling	135
F.0.7	Towards powder imbibition	136

TABLE OF CONTENTS

References

137

List of Figures

1.1	Beverage reconstitution process	1
1.2	Mass transfers in carbohydrate aggregates	2
1.3	Wetting experiments	3
2.1	Energy parameters in Young's equation	5
2.2	Hydrodynamic wetting theories	6
2.3	Geometry of the evaporation problem	8
2.4	Mass transfers at stake during spreading onto a soluble surface	9
2.5	Geometry of the problem	9
2.6	Schematic representation of wetting regimes according to Tay et al.	12
2.7	Wetting diagram according to Tay <i>et al.</i>	12
2.8	Mechanistic events in the dissolution of polymeric particle according to Ranade and Mashelkar	13
3.1	Maltodextrin molecule	18
3.2	Lactose molecule	18
3.3	Sorptions isotherms	20
3.4	NMR measurement of maltodextrin DE29 diffusion coefficient	23
3.5	Maltodextrin spheres	24
3.6	Dissolution of maltodextrin spheres: experimental set-up	25
3.7	Dissolution of a maltodextrin DE29 sphere in water	26
3.8	Preparation methods of maltodextrin channels	27
3.9	Schematic representation of the spin-coating process	28
3.10	Spin-coating of carbohydrates	29
3.11	Preparation of maltodextrin thick blocks	30
3.12	Experimental set-up for spreading experiment	31
3.13	Dewetting of maltodextrin at high water activity	32
3.14	Experimental set-up for the pulled substrate experiment	33
3.15	Typical pictures obtained during pulled substrate experiment	34
3.16	Contact angle measurement on black and white pictures	34
3.17	Contact angle measurement on maltodextrin layers	35
3.18	Validation of the stationarity approximation	35
3.19	Color pictures obtained in spreading experiments	36

LIST OF FIGURES

3.20	Interferences formation in a thin layer of polymer	36
3.21	Camera sensors and hue	38
3.22	Ellipsometry versus Hue measurement	39
3.23	Color evolution with thickness and humidity	40
3.24	Validation of the color analysis	40
3.25	Color analysis on a hydrated maltodextrin thin layer	41
4.1	Contact angle measurement and hydrodynamics theory	44
4.2	Wetting of a soluble layer of maltodextrin	44
4.3	Contact angle measurement and water activity	45
4.4	Wetting diagram according to Tay et al.	46
4.5	Schematic representation of COMSOL geometry and boundary conditions	48
4.6	Mass transfers and Péclet numbers	50
4.7	Normalized characteristic lengths of the condensation/diffusion equation	51
4.8	Schematic representation of COMSOL geometry and boundary conditions in the case of condensation only	53
4.9	COMSOL simulation of evaporation/water uptake mass transfer	53
4.10	Schematic 2D view of water content calculated by simulation	54
4.11	Influence of speed and diffusion coefficient on evaporation/water uptake profiles obtained by simulation	55
4.12	Exponent k : comparison between theory and simulation	55
4.13	COMSOL simulations: validation of the characteristic lengths	56
4.14	Schematic representation of COMSOL geometry and boundary conditions in the case of direct diffusion only	57
4.15	COMSOL simulations: influence of Péclet number on direct diffusion	58
4.16	COMSOL simulations: direct diffusion profiles at different speeds	59
4.17	Schematic representation of COMSOL geometry and boundary conditions in the case where condensation and direct diffusion are considered	60
4.18	COMSOL simulations: influence of direct diffusion on evaporation/water uptake profiles	61
4.19	COMSOL simulations: scaling	62
4.20	COMSOL simulations: scaling of the water content profiles	63
4.21	Sorption isotherms used in FEM simulations	64
4.22	COMSOL simulations: influence of the sorption isotherm	65
4.23	COMSOL simulations: influence of direct diffusion on evaporation/water uptake profiles using Flory sorption isotherm	66
4.24	The diffusion/condensation region in water content profiles	69
4.25	Speed influence on water content profiles ahead the contact line	70
4.26	Water content profiles at small velocities	71
4.27	Direct diffusion validation with the broken wafer experiment	72
4.28	Simulation of coating hydration with or without direct diffusion	73
4.29	Measurement of the diffusion/condensation region size - power law fitting	74
4.30	Measurement of the diffusion/condensation region size - logarithmic fitting	75
4.31	Schematic 2D view of water content calculated by simulation	76

4.32 Schematic representation of the cut-off length	77
4.33 Flux calculation on an experimental water content profile	77
4.34 New schematic representation of the thin film regime	78
4.35 Schematic representation of the intermediary thick film regime	79
4.36 New wetting diagram	81
4.37 Thickness and speed effects on contact angle	82
4.38 Scaling $\theta(eU)$ for a given contact angle	83
4.39 Experimental frontier in the wetting diagram	83
4.40 Thick film regime evidence in contact angle measurements	84
4.41 Final wetting diagram and isotheta	85
4.42 Exponent of $e(U)$ function at various water activities	86
4.43 Diagram of existence of different mass transfers	87
5.1 Diffusion coefficient of water in maltodextrin DE29	90
5.2 Glass transition and contact angle	90
5.3 Kink coordinates in contact angle data	91
5.4 Glass transition and hydration profiles	92
5.5 Hydration profile at the critical glass transition speed	93
5.6 Schematic representation of hydration below and above glass transition	94
5.7 Assessment of the constant K	95
5.8 Glass transition in the wetting diagram	97
5.9 Kink on contact angle measurements for different systems	98
5.10 Kink coordinates for different solvents of maltodextrin	99
6.1 Wrinkles behind the contact line	102
6.2 Domains of observation of the wrinkles behind the contact line	102
6.3 Characterization of wrinkles dimensions	103
6.4 Measurement of wrinkles width	104
6.5 Hypotheses on the origin of wrinkles	104
6.6 The curtain effect in different systems	106
6.7 Dissolution at the contact line	107
6.8 Dissolution of maltodextrin spheres	108
7.1 Wetting diagram	112
7.2 Different kinds of hydration profiles	113
7.3 Contact angle and glass transition	114
7.4 Contact angle and viscosity increase	115
7.5 Possible effect of dissolution on the eU scaling	116
A.1 Color scale for thickness measurement	117
B.1 Schematic representation for water flux calculation	119
B.2 Flux calculation on an experimental water content profile	122
C.1 Theoretical diffusion close to the contact line	123

LIST OF FIGURES

D.1	Diffusion profiles in a semi-infinite media	126
E.1	Dissolution speed of maltodextrin spheres	127
E.2	Dissolution speed of maltodextrins channels	128
F.1	Schematic representation of capillary penetration	132
F.2	Effect of dissolution on capillary penetration	133
F.3	Effect of swelling on capillary penetration	134
F.4	Effect of dissolution and swelling on capillary penetration for small walls	135

List of Tables

3.1	Characteristics of maltodextrins by DE	21
4.1	Characteristic lengths at stake in the wetting problem	52
4.2	Péclet numbers in the free spreading experiments	71
5.1	Critical velocities U_g for different solvents	98
5.2	Calculation of the constant K	99

Glossary

$(Pe)_p$	Péclet number in polymer coating	ϕ	Volume fraction of solvent
$(Pe)_v$	Péclet number in air	ϕ^w	Water volume fraction in polymer channel walls
α_i	Light incident angle	ϕ_0	Initial volume fraction of solvent
α_r	Light refracted angle	ϕ_g	Volume fraction of solvent at glass transition
β	Power law exponent such $e \sim U^\beta$	ϕ_p	Volume fraction of polymer
χ	Flory interaction parameter	ψ	Radial angle, amplitude ratio upon reflection in ellipsometry
Δe	Increase of coating thickness due to hydration	ρ	Liquid density
Δ	Quantity related to the Péclet number in air, NMR evolution time	ρ_p	Maltodextrin density
δ	Optical path length	τ	NMR encoding time
$\Delta\Phi$	Difference of phase	θ	Contact angle
$\Delta\phi$	Difference of hydration in volume fraction	θ_E	Equilibrium contact angle
η	Liquid viscosity	θ_S	Contact angle with the substrate
Γ	Contrast factor	ε	Nanometric cut-off
γ	Liquid surface tension	ϱ	Complex reflectance
γ_r	Gyromagnetic ratio	ξ	Experimental size of the diffusion/condensation region
γ_S	Solid surface energy	ξ_1	Experimental size of the concentration plateau
γ_{SL}	Solid/liquid interfacial energy	ζ_B	Normalized relative response the camera blue sensor
κ	Characteristic length of the diffusion/condensation region	ζ_G	Normalized relative response the camera green sensor
κ	Theoretical size of the diffusion/condensation region	ζ_R	Normalized relative response the camera red sensor
Λ	Extent of the evaporation along the y -axis	A	Amplitude of the wrinkles in gray value
λ	Wavelength of the wrinkles, Characteristic length of the diffusion/convection region	a_w	Water activity
μ_0	Chemical potential of pure liquid	a_w^g	Water activity at glass transition
μ_{st}	Standard chemical potential	b	Length of a monomer
		C	GAB fitting parameter
		c	Water concentration in air
		c_p	Mass fraction of polymer in solution
		c_0	Initial concentration of water in air
		c_{sat}	Maximal concentration of water in air
		d	Sphere diameter
		D_p	Diffusion coefficient of water in the solid coating
		D_v	Diffusion coefficient of water in air

GLOSSARY

D_{mutual}	Mutual diffusion coefficient of water in polymer	R	Radius (channel, droplet, sphere), Ideal gas constant
D_{self}	Self diffusion coefficient of water in polymer	R_g	Radius of gyration
e	Layer thickness	RH	Relative humidity of air
e^0	Initial layer thickness	T	Temperature
e_1	Frontier between thin and dry regimes	t	Time
e_2	Frontier between thin and thick regimes	T_1	NMR longitudinal relaxation time
e_3	Frontier between intermediary thick and thick regimes	T_2	NMR transverse relaxation time
e_c	Critical thickness of dewetting	U	Contact line velocity, Liquid speed
E_p	Young modulus of the polymer coating	U_c	Critical velocity between thick and dry regimes
e_{solid}^0	Initial dry solid thickness	U_g	Glass transition velocity
E_{sub}	Young modulus of the substrate	v_d	Dissolution speed
e_{water}^0	Initial water thickness	W	Width of the wrinkles
G	Magnetic field gradient	W_m	GAB fitting parameter
g	Gravitational acceleration	x_C	Characteristic length of the vertical gradient region
I	Intensity of the NMR signal	x_g	Extent of the melt layer ahead the contact line
I_0	initial intensity of the NMR signal	$\%wt$	Unit of mass fraction in percentage
I_B	Intensity measured by the camera blue sensor	AFM	Atomic Force Microscopy
I_G	Intensity measured by the camera green sensor	DE	Dextrose Equivalent; describes the degree of conversion of starch to dextrose. A higher DE means a smaller polymer.
I_m	Mean intensity of light	DMSO	Dimethyl sulfoxide; organic solvent
I_R	Intensity measured by the camera red sensor	DSC	Differential Scanning Calorimetry
J	Velocity of evaporation	K₂CO₃	Potassium carbonate; white salt used to set the humidity in experiments at 43%
j	Flux of evaporation	K₂SO₄	Potassium sulfate; crystalline salt used to set the humidity in experiments at 97%
K	Constant of hydration used to approximate $\Delta\phi$, GAB fitting parameter	LiCl	Lithium chloride; ionic compound used to set the humidity in experiments at 11%
k	Boltzmann constant	MD	Maltodextrin, carbohydrate polymer supplied by Roquette company
L	Extent of the evaporation along the x -axis	NaBr	Sodium bromide; inorganic compound used to set the humidity in experiments at 58%
M_w	Molecular weight	NaCl	Sodium chloride; ionic compound used to set the humidity in experiments at 75%
N	Number of monomers in a polymer	NMR	Nuclear Magnetic Resonance
n	Refractive index	rpm	Rounds Per Minute
n_s	Refractive index of the substrate		
p	Relative pressure of water in air		
p_0	Water pressure at saturation		
Q	Liquid flow in a channel		
q	Frequency in Fourier transforms		

1

Introduction

Many products from the food industry are sold in dehydrated powder. It is for example the case for dairy powders, chocolate beverages or soluble coffee. The required property for these powders is to mix with water and dissolve in a few tens of seconds avoiding lumps formation. Indeed, it can be very displeasing for the consumer to have to stir for long minutes and to nevertheless obtain undissolved powder in their beverage. The process of transforming a dehydrated powder into a beverage is called reconstitution. In order to improve the understanding of physico-chemical mechanisms at stake, it is common to dissociate in 4 steps the reconstitution process as presented in Fig. 1.1. We have:

- Wetting: Powder aggregates are wetted by the liquid.
- Capillarity/Immersion: Powder bed is impregnated by capillarity between the grains leading to immersion of the aggregates.
- Dispersion: Aggregates break up and the powder particles are dispersed in the liquid.
- Dissolution: Powder particles are progressively dissolved.

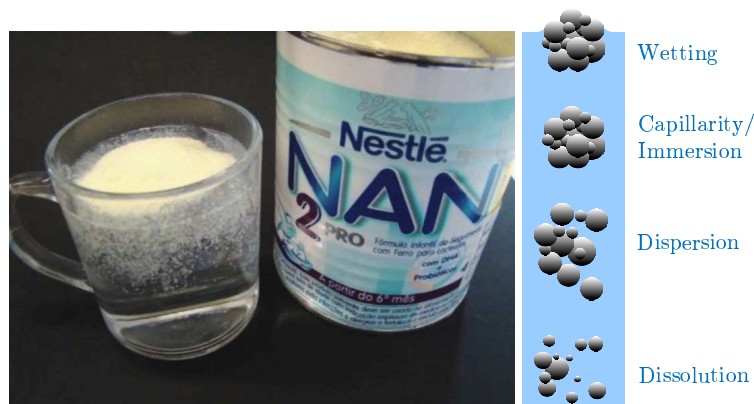


Figure 1.1: Beverage reconstitution process - (Picture) Reconstitution of a dehydrated dairy powder. (Scheme) Reconstitution process is often decoupled into 4 steps.

1. INTRODUCTION

The main issue is that this description is too simplistic. Indeed, the wetting of the aggregates occurs at the same time than the dissolution and the diffusion of water within the bulk. The understanding of these intricate phenomena is the object of this work. In this manuscript, we will focus on maltodextrins which are water-soluble polymers. Glassy and brittle when dry, they become molten and sticky upon hydration. That glass transition as a function of water content is linked to a dramatic increase of the water diffusion coefficient of about two orders of magnitude for 20% of water content variation. The surface properties of the maltodextrin particles are radically changed upon hydration and because wetting, dissolution and diffusion are coupled, the wetting dynamics is difficult to master. Hence, understanding the reconstitution process of carbohydrate powders requires a comprehension of the mechanisms influencing the wetting step and so the capillarity step. More precisely, all the mass transfers that control hydration of the surface are important to explain the differences observed between different powders.

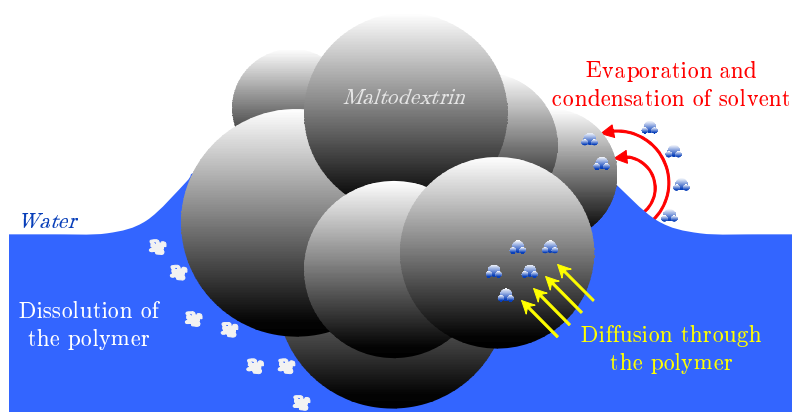


Figure 1.2: Mass transfers in carbohydrate aggregates - The wetting of carbohydrates particles is influenced by 3 mass transfers: evaporation/condensation, diffusion and dissolution.

We schematically represent in Fig. 1.2 a carbohydrate aggregate wetted by water. Since the hydration of the polymer is expected to modify the wetting properties of the surface, we can expect three transfers that require deep investigations:

- Evaporation/Condensation: Water can evaporate and further condensate into the carbohydrate
- Diffusion: Water molecules can diffuse into the polymer (directly from the droplet or indirectly after condensation).
- Dissolution: Water can dissolve the carbohydrate and the polymer chains diffuse into the solvent.

Tay *et al.* (2) were the first to study and evidence the important role of Evaporation/ Condensation during the wetting of soluble surfaces. They used thin layers of polymers prepared by spin-coating and performed free-spreading experiments of liquid droplets in order to study the wetting dynamics. Their work does not consider the two other mass transfers (diffusion and

dissolution) and a few divergences appear between their theoretical arguments and the experimental observations. We decided to use the same approach as the one they have developed, *i.e.* to focus on the hydration of the contact line through the different transfers in order to explain wetting dynamics on polymer layers. In this work, we will complete their results and suggest new explanations for the missing pieces of the puzzle.

In chapter 2, we will discuss the results from literature. Indeed, the 3 mass transfers presented above have been discussed in different scientific publications dealing with wetting or other physico-chemical experiments. We will see how the classical wetting theories cannot account for our experimental data and that some approximations in Tay *et al.* theory may be too drastic. In particular, the horizontal diffusion of water in the polymer layer, the dissolution of the polymer and the glass transition process that have not been taken into account in their study exhibit an important role in the wetting process of soluble materials.

Then, in chapter 3, we will explain how our different measurements were performed and what are the key parameters that can influence the wetting of soluble carbohydrates by water. In this work, we performed contact angle measurements to quantify the wetting on polymer layers prepared on silicon wafers (see Fig. 1.3b). We investigated the wetting dynamically, *i.e.* that the contact angle was measured over 6 decades of contact line velocities. In addition to the classical contact angle measurements, our experiments also characterized the hydration of the polymer layers during solvent motion. Indeed, the Newton hues that appear on the thin layers because of optical interferences were used to measure the thickness profile ahead the contact line (see Fig. 1.3a).

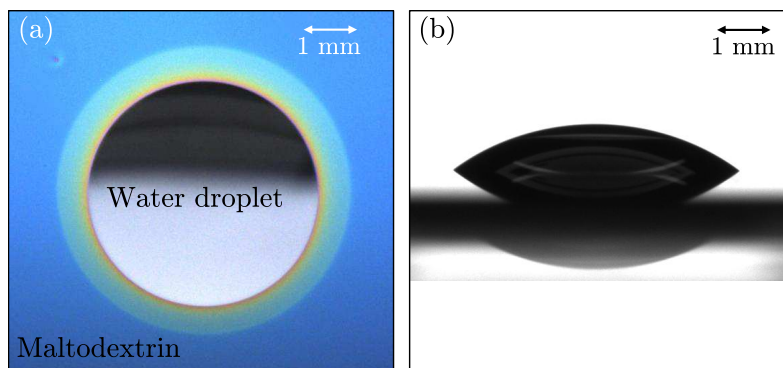


Figure 1.3: Wetting experiments - Water droplet spreading onto a 300 nm-thick layer of maltodextrin DE6 equilibrated at $a_w = 0.58$. (a) hydration characterization (top view) (b) Contact angle measurement (lateral view)

In chapter 4, we will discuss the hydration mechanisms of a maltodextrin layer wetted by water. We will show how evaporation/condensation and diffusion in the carbohydrate are both important to predict the behaviour of the contact line at different velocities and thicknesses of solid. We will introduce characteristic lengths that appear in our system ahead from the contact

1. INTRODUCTION

line and use Finite Element Method simulations to validate our theoretical arguments. Then, we will build a theoretical wetting diagram where different regimes can be identified depending on contact line velocity and sample thickness that explains our experimental data.

In chapter 5, we will study the influence of glass transition on wetting. We will show that the diffusion coefficient change has a dramatic role on the hydration behaviour observed in the vicinity of the glass transition. The wetting diagram will be used to discuss the experimental observations.

Finally, in chapter 6, we will focus on carbohydrates dissolution during wetting. We will characterize the wrinkling pattern that appears behind the contact line during water spreading onto maltodextrin layers.

2

State of the art

2.1 Wetting

2.1.1 Young's relation

In 1805, Thomas Young (3) proposed an equation describing the equilibrium state for a liquid droplet deposited on a solid smooth and homogeneous surface. It links the surface energy of the solid γ_S , the liquid surface tension γ , the solid/liquid interfacial energy γ_{SL} to the equilibrium contact angle θ_E between the droplet and the solid substrate as represented on Fig.2.1:

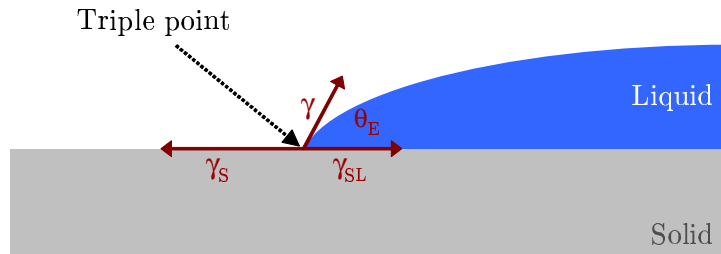


Figure 2.1: Energy parameters in Young's equation - The equilibrium contact angle of a liquid droplet deposited on a solid surface is according to Young's theory, linked to three energy parameters: surface energy, liquid surface tension and interfacial energy.

The equilibrium contact angle is given by the equilibrium of capillary forces:

$$\cos(\theta_E) = \frac{\gamma_S - \gamma_{SL}}{\gamma} \quad (2.1)$$

If θ_E is defined, we are in partial wetting situation. A liquid is said to be "mostly wetting" when $\theta_E < 90^\circ$ and "mostly non-wetting" when $\theta_E > 90^\circ$. If $\gamma_S > \gamma_{SL} + \gamma$, relation 2.1 has no solution. It corresponds to a "total wetting" situation. In that case, there is no equilibrium contact angle and the liquid spreads all over the substrate. In our study, we will always be in a partial wetting situation with contact angles ranging from 2° to 110° .

2. STATE OF THE ART

2.1.2 Spreading dynamics on a non-soluble surface

The spreading dynamics of a non-volatile liquid droplet on a non-soluble solid surface is governed by the competition between interfacial and dissipation forces. The classical hydrodynamic approach to describe the flow near a moving wetting line does not result in a physically acceptable solution. A divergence occurs close to the contact line and a cut-off length L_m has to be introduced. A description of this problem has been given by Cox and Voinov (4, 5). They used two different approaches to deal with this singularity:

- Truncate the solution artificially at the molecular scale (Voinov)
- Relax the no-slip condition in the vicinity of the contact line in order to obtain a finite force (Cox)

In both cases, capillary number $\frac{\eta U}{\gamma}$ and Reynolds number $\frac{\rho U L}{\eta}$ have to remain small (η is the liquid viscosity, ρ its density, γ , its surface tension and L a characteristic length). It is only on the mesoscale that viscous bending becomes important (see Fig. 2.2). θ_m , the microscopic contact angle is assumed to be governed by short-range intermolecular forces.

The dynamic contact angle θ_D depends on the contact line speed U . In its simplest form, the resulting formula describing the change in the dynamic contact angle due to viscous bending of the liquid-gas interface may be written as:

$$\theta_D^3 = \theta_m^3 + 9 \frac{\eta U}{\gamma} \ln \left(\frac{L}{L_m} \right) \quad (2.2)$$

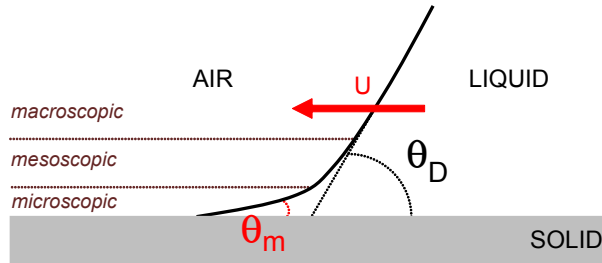


Figure 2.2: Hydrodynamic wetting theories - The Cox-Voinov law is based on a balance between interfacial and dissipation forces at the wedge of a liquid droplet onto a solid surface

Usually, the value of θ_m is chosen equal to θ_E , the equilibrium contact angle, but it is likely to be speed-dependent as θ_D . In practice, the term $\ln \left(\frac{L}{L_m} \right)$ is usually treated as an adjustable parameter. Voinov considers L_m as the distance from the solid at which the solution is truncated. Cox defines L_m as the scale of the inner region where slip is important. L is the approximate distance from the contact line at which the contact angle can be measured. Taking $L_m \sim 1$ nm and $L \sim 10$ μ m gives reasonable values.

The hydrodynamic models (4, 5, 6, 7, 8) correctly describe wetting onto classical solids. They are often used by experimentalists to account for their observations even if they present a few

drawbacks. For instance, there is no experimental proof of the viscous bending except for precursor thin film in a perfect wetting situation (9).

Other theories not based on hydrodynamics (10, 11) try to account for the speed-dependent contact angle. The motion of the contact line is determined by the statistical dynamics of the molecules within a three-phase zone where the solid, liquid and gas phases meet each other. Molecules displacements are ruled by processes of detachment and attachment to or from the solid surface. The dissipation channel is the dynamic friction. These models (called MKT for Molecular Kinetic Theories) are often criticised because they neglect hydrodynamics. Some papers (12, 13) try to develop comprehensive models taking into account dissipation through hydrodynamic channel and dissipation due to creation and destruction of interface. Nevertheless, they introduce several phenomenological coefficients that make the data analysis and understanding uncertain. Finally, most of wetting specialists will prefer the use of hydrodynamic models since Cox-Voinov law (Eq. 2.2) is successful in practice.

In our study, the food substrate is soluble in the chosen liquid, water, which is a volatile solvent. Therefore, water can evaporate quickly and further condensate ahead the contact line. This water uptake modifies spreading dynamics. We can not neglect this additional mass transfer.

2.1.3 Wetting in presence of evaporation

In most papers, drying is rather described in a receding situation where the evaporation of colloidal suspensions for instance leads to patterns formation (14, 15, 16), e.g. the coffee stain effect. Evaporation has also been discussed in the case of a polymer solution spreading onto a solid. It leads to an increase of viscosity at the contact line (17) which is known to modify the spreading process. Evaporation is limited by the diffusion of water molecules in air. We can theoretically describe the evaporation at the triple line with a 2D-model. Fig. 2.3 describes the geometry that is considered for the calculation. We assume that the droplet has a small contact angle θ_E with the solid surface. The evaporative flux $j(x)$ can be calculated at the surface of the droplet. At this liquid-air interface, the concentration in water is c_{sat} . This assumption is valid only in the presence of air. In the absence of air, different models like the Knudsen model has to be applied. Far from the droplet, we have the concentration c_0 . By doing a mirror image of the droplet relative to the x-axis, the problem has an equivalent in electromagnetics leading to Eq. 2.3 in the case of small contact angles.

$$j(x) = \tilde{j}_0 \cdot x^{-1/2} = j_0 \Lambda^{1/2} \cdot x^{-1/2} \quad (2.3)$$

Λ is a characteristic length. It corresponds to the boundary layer size in convective regime and to the droplet size in diffusive regime. Eq. 2.3 shows that evaporation is important in the vicinity of the triple line. Indeed, a divergence of the normal evaporative flux occurs in $x = 0$. The prefactor can be obtained with the help of the diffusion equation:

$$j_0 = D_v \frac{c_{sat} - c_0}{\Lambda} \quad (2.4)$$

2. STATE OF THE ART

The diffusion coefficient of water in air is $D_v \sim 2.7 \cdot 10^{-5} \text{ m}^2 \cdot \text{s}^{-1}$. Finally, we can divide $j(x)$ by the water density ρ in order to obtain a flux homogeneous to a velocity. $J(x)$ is thus the velocity of the liquid normal to the liquid-air interface:

$$J(x) = \frac{j(x)}{\rho} \quad (2.5)$$

$$J(x) = \frac{D_v}{\Lambda^{1/2}} \frac{c_{sat} - c_0}{\rho} \cdot x^{-1/2} \quad (2.6)$$

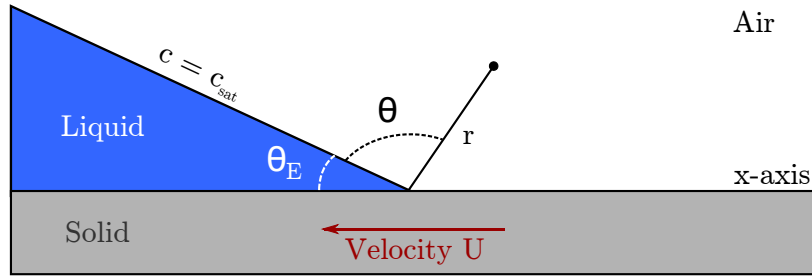


Figure 2.3: Geometry of the evaporation problem - The droplet vapour diffuses in air. The vapour is saturated at liquid-air interface.

For larger contact angles θ_E , the exponent is modified (18, 19). Indeed, we have the general formula $j(x) = j_0 x^{-\lambda} \Lambda^{1-\lambda}$, where $\lambda = \frac{\pi - 2\theta_E}{2\pi - 2\theta_E}$. Evaporation leads to a drawing up of water near the contact line but this loss of matter does not modify the apparent contact angle significantly (20).

The evaporation mass transfer becomes much more complex when the substrate ahead the contact line can absorb water from air, which is the case in our study. Therefore, we need to take into consideration the condensation of the evaporated water ahead the contact line.

2.1.4 Wetting of a soluble layer

Wetting onto soluble surfaces makes the dynamics of spreading much more complex. Besides classical hydrodynamical effects, hydration of the substrate modifies surface energy and the dissolution of the substrate modifies hydrodynamics. Hydration effects have been studied on gels surfaces (21, 22). They highlight a decrease of the contact angle with spreading time due to two mechanisms of hydration: direct diffusion of water in the gel and evaporation of water that further condensates into the substrate. The same approach can be adopted for soluble surfaces with an additional transfer: layer dissolution.

A description of the mass transfers at stake in the problem (evaporation/condensation, diffusion in the layer and dissolution, see Fig. 2.4) was performed by Tay *et al.* (2). The main finding of their work is that a coating of hydrosoluble material, although eventually dissolved in water,

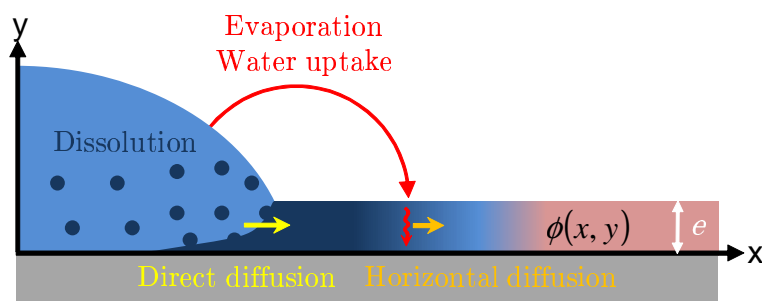


Figure 2.4: Mass transfers at stake during spreading onto a soluble surface - Three mass transfers are identified by Tay *et al.* during the spreading of water onto a soluble polymer: evaporation/condensation, diffusion in the layer (direct or indirect) and dissolution.

may be poorly wetted by water when dry. However, hydration of the coating causes an increase of its wettability (1, 23). As a consequence, the more hydrated, the more hydrophilic a soluble coating appears, and the spreading of a water droplet is accelerated compared to the dry case.

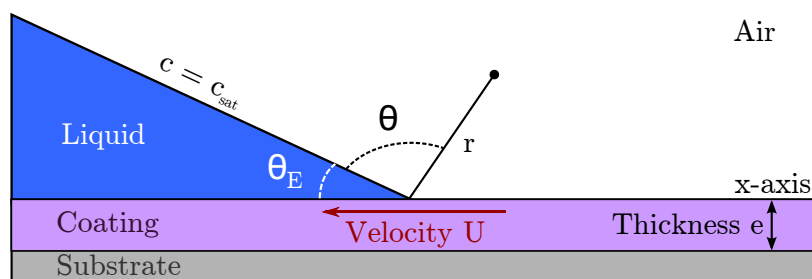


Figure 2.5: Geometry of the problem - In the frame of the liquid, a substrate with a coating of thickness e is moving at a constant velocity U . The solvent vapour diffuses in air. The vapour is saturated at liquid-air interface. We use cylindrical coordinates.

A theoretical analysis of this process (1) allowed for the derivation of a model describing solvent uptake of a coating of thickness e in front of a contact line advancing at a velocity U (geometry presented in Fig. 2.5). In Tay *et al.* papers, the hydration is assumed to occur only through water condensation and direct diffusion is neglected. Indeed, the diffusion coefficient of water in air ($D_v \sim 2.7 \cdot 10^{-5} \text{ m}^2 \cdot \text{s}^{-1}$) is much larger than the one of water in the coating ($D_v \sim 10^{-10} \text{ m}^2 \cdot \text{s}^{-1}$). Thus, the ratio of the mass transfer coefficient in air versus in the substrate $\frac{c_{sat} D_v}{\rho D_p}$ is larger than 1. The solvent - water in our case - evaporates from the drop and diffuses through gas phase ahead the contact line. It condensates into the polymer and modifies its water content $\phi(x, y)$. Spreading dynamics is influenced by the evolution of this water content, which itself depends on the contact line velocity U .

3 assumptions are made in Tay *et al.*'s approach:

- The contact angle θ is a function of the volume water content in the coating ϕ at the

2. STATE OF THE ART

contact line.

- Horizontal diffusion in the polymer coating is neglected.
- Motion of the contact line is quasi-stationary

Similarly to the approach of Cox-Voinov, a cut-off length ε has to be introduced (here $\varepsilon \sim 1$ nm). Once water molecules condensate on the coating, hydration of the layer across its thickness e is limited by the diffusion of water through the polymer. Away from the contact line, for distances larger than $x_C = \frac{Ue^2}{D}$, the coating has time to fully hydrate across the entire thickness, whereas close enough to the contact line, the hydration only penetrates at some depth into the coating, the penetration being limited by the diffusion coefficient of water in the polymer D_p . 3 different wetting regimes can be expected:

- Thin film regime: this regime corresponds to the absence of vertical concentration gradient at any distance from the contact line larger than the cut-off length ε (see Fig. 2.6a), *i.e.* $x_C < \varepsilon$.
- Thick film regime: in this regime, we have $x_C > \varepsilon$. A vertical concentration gradient is expected ahead the contact line (see Fig. 2.6b).
- Dry regime: at large velocities, the solvent uptake in the coating becomes negligible.

Let's call $c(r, \theta)$ the water concentration in air. In stationary conditions, c is independent of time and the equation $\Delta c = 0$ has to be solved. In the frame of the coating and assuming that the density of the liquid ρ does not depend on ϕ , the thickness increase of the substrate is equal to the flux of water downward, normalized in volume units:

$$\frac{de}{dt} = \frac{D_v}{\rho} \left. \frac{\partial c}{r \partial \theta} \right|_{\theta=\pi} \quad (2.7)$$

Assuming a linear water activity a_w , *i.e.* that the derivative of a_w relative to ϕ is constant, and a constant contact line velocity U , they obtain a differential equation that links the boundary conditions of c to the different parameters of the problem:

$$\begin{cases} U \frac{e}{c_{sat}} \frac{\partial c}{dr} = \frac{D_v}{\rho} \frac{\partial a_w}{\partial \phi} \frac{\partial c}{r \partial \theta} & \text{for } \theta = \pi \\ c = c_{sat} & \text{for } \theta = \theta_E \end{cases} \quad (2.8)$$

The solution of $\Delta c = 0$ with the boundary conditions of Eq. 2.8 allows one to obtain the expression of the concentration c at the surface of the coating:

$$c(r, \pi) = c_{sat} - (c_{sat} - c_0) \left(\frac{r}{L} \right)^k \quad (2.9)$$

$$\text{where } k = \frac{1}{\pi - \theta_E} \arctan \left(\frac{D_v c_{sat}}{\rho U e} \frac{\partial a_w}{\partial \phi} \right) \quad (2.10)$$

The macroscopic length L is the distance at which the water content is set by the humidity in the atmosphere (typically L is the size of the droplet). Thus, the concentration c and so the water content ϕ in the coating is expected to only depend on the quantity eU . The assumption that θ is a function of ϕ at the contact line only, leads to the result that θ is a function of eU only. Eq. 2.9 remains true as long as the equilibration of the coating in the vertical direction is very fast compared to the evaporation/condensation process, *i.e.* $x_C < \varepsilon$.

Further in the paper(1), they use a one-dimensional approximation to find a relation between the water fraction ϕ ahead the contact line and the quantity eU :

$$\int_{\phi(L)}^{\phi(\varepsilon)} \frac{d\phi}{(1-\phi)^2(1-a_w(\phi))} = \frac{D_v c_{sat}}{(\pi-\theta)\rho eU} \ln\left(\frac{\varepsilon}{L}\right) \quad (2.11)$$

When x_C becomes much larger than ε , the 1D-approximation simplifies the calculation and they are able to propose another expression where $\phi(\varepsilon)$ does not depend on the thickness any more but on $U^{-1/2}$:

$$\int_{\phi(L)}^{\phi(\varepsilon)} \frac{d\phi}{(1-\phi)^2(1-a_w(\phi))} \cong \frac{2D_v c_{sat}}{(\pi-\theta_E)D_p^{1/2}\rho U^{1/2}\varepsilon^{1/2}} \ln\left(\frac{\varepsilon}{L}\right) \quad (2.12)$$

Therefore, the three expected wetting regimes have the following properties:

- Thin film regime: at small eU , this regime corresponds to the absence of vertical concentration gradient ahead from the contact line. A scaling of θ with eU is expected in this regime.
- Thick film regime: in this regime where $x_C > \varepsilon$, θ becomes independent of the thickness. It is only a function of U .
- Dry regime: when solvent uptake in the coating is negligible, θ is expected to be constant. ϕ is independent of e and U and equal to the initial water content ϕ_0 .

The frontiers between these regimes can be expressed as a function of different liquid or coating parameters. We have:

$$e_1 \sim e_{thin/dry} = \frac{D_v c_{sat}}{\rho U} \quad (2.13)$$

$$e_2 = e_{thin/thick} = \sqrt{\frac{\varepsilon D_p}{U}} \quad (2.14)$$

$$U_c = U_{thick/dry} = \frac{D_v^2 c_{sat}^2}{D_p \rho^2 \varepsilon} \quad (2.15)$$

The spreading regimes can be summarized in a e - U diagram. An example is given in Fig.2.7.

2. STATE OF THE ART

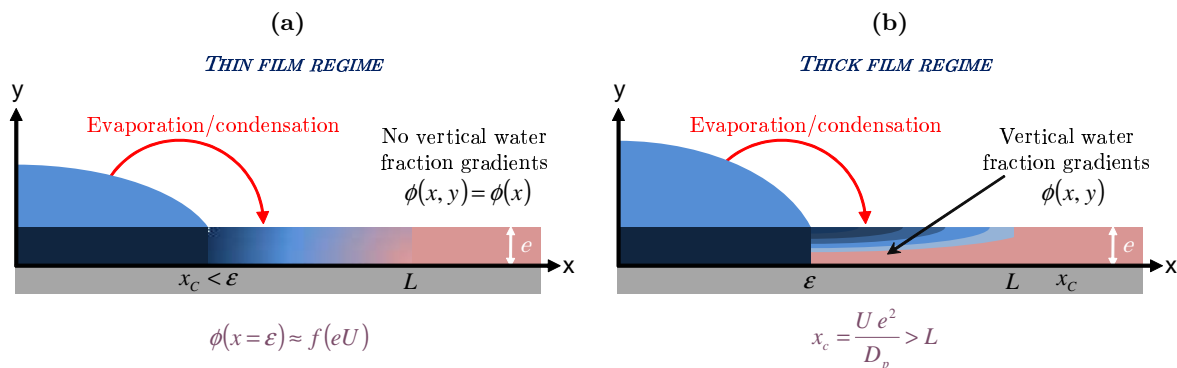


Figure 2.6: Schematic representation of wetting regimes according to Tay et al. - (a) Thin film regime. (b) Thick film regime.

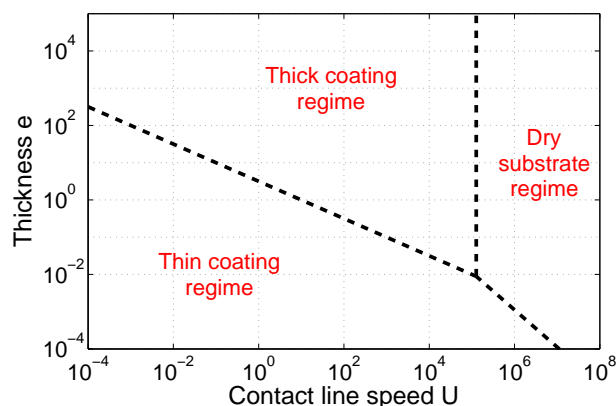


Figure 2.7: Wetting diagram according to Tay et al. - Three wetting regimes are identified in the diagram coating thickness versus contact line velocity. Frontiers depend on solvent and layer parameters (solvent density and vapour pressure, diffusion coefficients, sorption isotherm)

In conclusion, Tay *et al.* have shown that the wetting of a soluble substrate is controlled by evaporation/condensation. This mass transfer is the fastest one and depending on the values e and U , we can expect three wetting regimes from its action ahead the contact line. Especially, we should observe a scaling of ϕ in eU in the thin film regime.

2.2 Dissolution of polymers

Dissolution of the substrate is referred by Tay *et al.* as one of the three mass transfers controlling the spreading of a solvent onto a soluble surface. In the spreading experiment onto soluble layers, this transfer plays a role by modifying viscosity in the droplet wedge. Therefore, we need to understand how our materials - carbohydrates polymers - dissolve in water.

The dissolution of polymers is a complex process that have been studied in a few papers (24, 25, 26, 27, 28). De Gennes and Brochard (24) discussed about the dissolution of a semi-diluted polymer solution in pure solvent. They suggest the following picture:

- At the beginning of the hydration process, the polymer chains are swollen by the solvent. This first step is associated with a cooperative diffusion coefficient D_{coop} .
- The swelling of the entangled chains is then limited by chain stretching. The regime where the chain stretching equilibrates the osmotic pressure is called by the authors a gel.
- From this gel phase, the polymer chains have to escape from the entangled ones. This step is governed by the diffusion coefficient of reptation D_{rep} . Reptation mechanism makes dissolution process non-fickian.

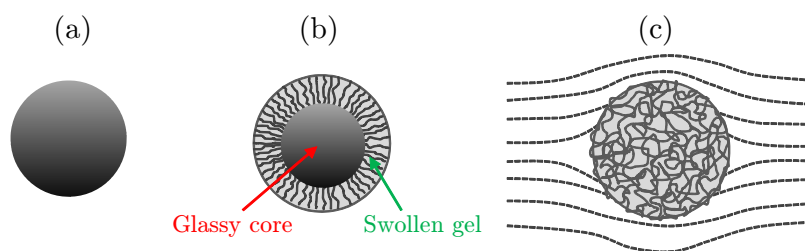


Figure 2.8: Mechanistic events in the dissolution of polymeric particle according to Ranade and Mashelkar - (a) Solid polymeric particle ($t = 0$). (b) Glass transition, swelling and reptation ($t < t_{rep}$) (c) Disengagement and diffusion in a flow field ($t > t_{rep}$)

Ranade and Mashelkar (25) worked on the dissolution process of a polymer sphere and proposed a mathematical model. They described the sphere as made of a glassy core and a swollen gel phase (Fig.2.8).

- After immersion in the solvent, the first step corresponds to an increase of the sphere diameter. The gel phase swells.
- The solvent penetrates in the glassy cores via the swollen gel layer. This step can be non-fickian. Case II diffusion is the term generally applied to a linear uptake of solvent in time (29, 30, 31).
- At the same time, the chains of the swollen gel leave the sphere by reptation.

These mechanisms lead to an initial swelling of the object and an erosion at longer times. Another theoretical study of the dissolution of free-falling solid spheres in liquid can be found in V.G. Levich books (32, 33). An expression for the total flow of matter leaving the sphere is proposed:

$$I = 7.98\phi_0 D_p^{2/3} U^{1/3} d^{4/3} \quad (2.16)$$

where d is the diameter of the sphere, U the rate of descent, D_p the diffusion coefficient of the solvent in the sphere and ϕ_0 the initial solvent fraction in the material.

2. STATE OF THE ART

A complete description of phenomena at stake during polymer dissolution will be found in Miller-Chou and Koenig review (27). We will show in this study that the dissolution of maltodextrin spheres is in agreement with Ranade and Mashelkar theory, and that the swelling of the non-dissolved polymer behind the contact line in the spreading experiment leads to wrinkles formation.

2.3 Water imbibition in porous media

Ultimately, our study aims at understanding the processes involved in the reconstitution of beverages from dehydrated food powders (34). Therefore, one objective is to use the wetting, swelling and dissolution experimental data to account for the strong differences of behaviour observed between different formulations starting with carbohydrates. Thus, we will have to discuss the water penetration in a soluble assembly of particles.

The hydration of a soluble powder bed can be compared to a simpler situation: capillary penetration in a cylindrical capillary. The dynamics of capillary rise was described by Washburn (35). When neglecting inertia and weight, the penetration length z in time depends on the pore radius r_p , the contact angle θ between the liquid and the solid, the liquid viscosity η or its surface tension γ . We have $z = \sqrt{\frac{\gamma r_p \cos(\theta) t}{2\eta}}$. If inertia is considered, this relation evolves in such way penetration speed does not diverge any more at short times (36). Different geometries are also considered in literature (patterned surfaces (37), spheres packing, tortuous channels...) and modify the imbibition speeds and the importance of parameters that influence the wetting.

If the capillary is made of soluble walls, the understanding of the imbibition process is intricate. Firstly, contact angle θ will be humidity and speed-dependent. Then, the dissolution of the solid material will involve an increase of viscosity and pore radius with time and space (38). Surface tension can also be modified. These modifications will strongly affect the dynamic process and may lead to contact line trapping. The swelling of the walls due to diffusion or condensation of gas has to be considered too since it can involve pore closure. As far as we know, very few literature data report this effect. We will discuss these effects in appendix F.

2.4 Open questions

In this manuscript, we will try to answer the following questions:

- The influence of horizontal diffusion: Tay *et al.* proposed a wetting diagram based on evaporation/condensation transfer and diffusion along the substrate thickness only. We will see how the horizontal diffusion in the coating modifies the diagram eU in chapter 4.
- Glass transition in carbohydrates: maltodextrin polymers present a strong variation of their properties when varying the water content, especially the diffusion coefficient D_p .

These polymers are glassy at low water content but the rubbery state is reached when ϕ increases. We will highlight the role of this glass transition in the wetting process in chapter 5.

- The influence of polymer dissolution: water dissolves maltodextrin. We will investigate the coupling of dissolution with the other hydration mechanisms and evaluate its importance in the wetting process (chapter 6 and outlooks).

2. STATE OF THE ART

3

Materials & Methods

3.1 Materials

3.1.1 From carbohydrates to lipids

Food powders often contain many ingredients going from carbohydrates to lipids through additives and surfactants. The approach chosen for this study was to work on a model system, that is known to exhibit most of the usual problems encountered in powder dissolution, more precisely lactose and maltodextrins.

3.1.1.1 Maltodextrins

Starch is a polysaccharide carbohydrate (density close to 1.5) consisting of a large number of glucose monosaccharide units joined together by glycoside bonds. Starch can be hydrolyzed into simpler carbohydrates by acids, various enzymes, or a combination of both, yielding smaller molecules: maltodextrins (see fig. 3.1). The extent of conversion is typically quantified by dextrose equivalence (*DE*) which is a measure of the amount of reducing sugars present in a sugar product, relative to glucose, expressed as a percentage on a dry basis. For example, a maltodextrin with a *DE* of 50 would have 50% of the reducing power of dextrose (which has a *DE* of 100, prepared by the complete hydrolysis of starch). The *DE* is roughly the fraction of the glycoside bonds in starch that have been broken. In this study, maltodextrin DE29, DE6 and DE2 were used (Roquette, France). The polydispersity index is always larger than 5. The density of maltodextrin is taken as $\rho_c=1.50 \text{ g}\cdot\text{mol}^{-1}$ (measured by pycnometry Helium). The same batches were used throughout the experiments and were stored under vacuum in a desiccator to avoid degradation.

- Maltodextrin DE29: intermediate molecular weight, $M_w \simeq 2500 \text{ g/mol}$, $M_n \simeq 735 \text{ g/mol}$
- Maltodextrin DE6: High molecular weight, $M_w \simeq 80\,000 \text{ g/mol}$, M_n unknown
- Maltodextrin DE2: Very high molecular weight, $M_w \simeq 343\,000 \text{ g/mol}$, M_n unknown

In food industry, maltodextrins are often used as bland-tasting fillers and thickeners. They are widely found in many formulations such as meal replacements and protein powders. The

3. MATERIALS & METHODS

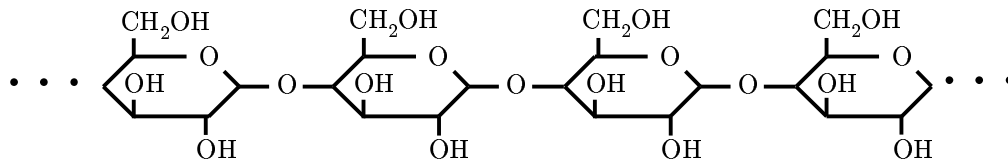


Figure 3.1: Maltodextrin molecule - Glucose polysaccharide. The length of the molecule chain determines the DE. The shorter the chain, the higher the DE.

inclusion of maltodextrin in weight gain formula allows the important nutrients such as protein to be delivered to muscle cells gradually rather than all at once.

3.1.1.2 Lactose

Lactose is one of the main ingredients in milk powder. It is a sugar whose systematic name is β -D-galactopyranosyl-(1 \leftrightarrow 4) β -D-glucopyranose. Indeed, lactose is a disaccharide : one fragment of α/β -D-glucose and another of β -D-galactose bonded through a β 1-4 glycosidic linkage. Thus, lactose powder can have two different crystalline forms : α or β . Its molecular weight is 342 g/mol.

The α -lactose is the most common crystalline form. In this crystal, each lactose molecule is associated with one molecule of water. In other words, α -lactose crystallizes as a monohydrate. The normal water content of α -lactose monohydrate is around 5 %. The α -lactose density is 1.53.

The β -lactose crystallizes as an anhydrous lactose. The formation of this crystal is possible with a highly concentrated solution of lactose at a temperature above 93.5 °C. The β -lactose density is around 1.59.

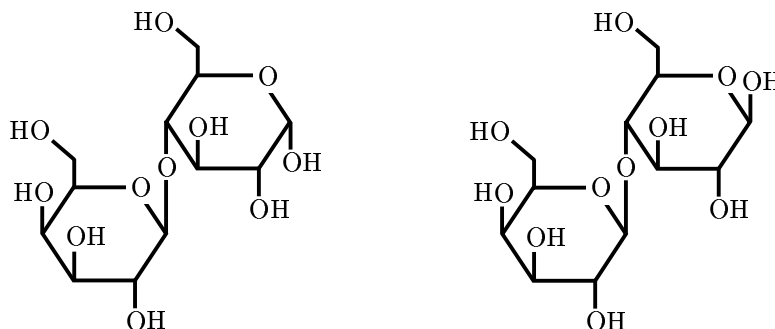


Figure 3.2: Lactose molecule - α (left) and β (right) forms of lactose

The solubility of lactose in water is around 189 g/L at 25 °C. When α -lactose (respectively β -lactose) is dissolved in water, a mutarotation phenomena can be observed leading to β -lactose apparition (respectively α -lactose). Both forms change into one another continuously. This change of specific rotation entails a precise ratio α/β which depends on temperature. β -lactose

dissolution is easier than α -lactose because of differences in initial solubility rates, but the final solubility is the same for α - and β -lactose because of this mutarotation equilibrium that is eventually reached in solution.

Lactose is obtained in an amorphous form by using freeze-drying or spin-coating. The freeze-drying consists in sublimating the water of a frozen lactose solution while the spin-coating consists in evaporating a solution by spinning a lactose solution onto a flat surface. In amorphous lactose, the arrangement of the molecules is more or less random. In our experimental conditions where we prepare thin layers by spin-coating, lactose is glassy since the drying step is very fast.

3.1.1.3 Lipids

Butterfat, the fatty portion of milk, belongs to the family of lipids. Chemically, butterfat consists essentially in a mixture of triglycerides, particularly those derived from fatty acids. These fatty acids are saturated acids (Palmitic acid, myristic acid, stearic acid...) and unsaturated acids (Oleic acid, palmitoleic acid, Linoleic acid...). The fatty acid composition of butterfat extracted from milk varies according to the producing animal's diet. All the different triglycerides have their own melting point and at room temperature, the butterfat appears highly viscous. Indeed, these melting points are on the range -25°C to 35°C and several of them remain liquid at 24°C . For health reasons, food industry tends to reduce the proportions of lipids in powders.

Even if lipids are usually present in powder formulations, we will not study their influence on wetting. Pure layers of lipids exhibits a contact angle of the order of 90° with water.

3.1.2 Materials characterization

3.1.2.1 The structure of a powder grain

A powder particle is a porous object. The pore size distribution depends on the powder preparation process. Powder can often be considered as a open network with two scales of porosity: large pores (10 to 100 μm) between agglomerated primary particles and small pores inside primary particles (below 1-10 μm).

3.1.2.2 Water activity

Water activity a_w is defined as the ratio of p , the vapour pressure of water at equilibrium to p_0 , the saturated vapour pressure of water at the same temperature. In the case of a system air/water, a_w can be approximated to the relative humidity RH . Considering air as a perfect gas, if we call c the water concentration in air and p the relative pressure of water in air, we can write $a_w = \frac{p}{p_0} = \frac{c}{c_{sat}} = RH$ where c_{sat} is the concentration at saturation ($c_{sat} \simeq 23 \text{ g.m}^{-3}$ at $T \simeq 25^{\circ}\text{C}$) and p_0 the water pressure at saturation.

The chemical potential, μ_0 , of pure liquid water in equilibrium with its vapour can be expressed as $\mu_0 = \mu_{st} + RT \ln(p_0/p_{st})$ where μ_{st} is the standard chemical potential, R is the gas constant, and T is the temperature. For a saturated aqueous solution at the same temperature,

3. MATERIALS & METHODS

which has a vapour pressure p_s which is less than p_0 , and a chemical potential μ , the difference in chemical potential between water in the solution and pure water can be expressed as $\mu - \mu_0 = RT \ln(p_s/p_0) = RT \ln(a_w)$. Thus, if we consider a thin film of solution (maltodextrin in water for instance), a driving force exists for evaporation/condensation of water when the vapour pressure p exceeds/is lower than p_s , or equivalently when the relative humidity of the surroundings exceeds/is lower than the water activity of the thin film.

3.1.2.3 Maltodextrin sorption isotherms

As explained in 3.1.2.2, carbohydrates equilibrate with water in surrounding atmosphere. For a given relative humidity RH (or water activity a_w), the material will absorb a given amount of water ϕ . The relation between a_w and ϕ is the sorption isotherm. In order to obtain sorption isotherms of different carbohydrates, powder samples may be equilibrated in a desiccator containing a salt solution that sets the water activity. When the weight of the sample does not vary any more, powder is equilibrated. Using thermogravimetric analysis (TGA), the precise amount of absorbed water can be measured. Measurements performed by Nestlé scientists on maltodextrin DE29 and DE6 are presented in Fig. 3.3. In this figure, the data points are fitted with the Guggenheim - Anderson - de Boer (GAB) model (Eq. 3.1), a classical model used to describe food sorption isotherms (39, 40). Data concerning amorphous lactose are more imprecise since several papers give different measurements. We chose to use the values extracted by Nestlé scientists from Lloyd *et al.* data (41) and Roos data (42).

$$\frac{\rho_w}{\rho_p} \frac{\phi}{1 - \phi} = \frac{W_m C K a_w}{(1 - K a_w)(1 + (C - 1)K a_w)} \quad (3.1)$$

where ρ_w and ρ_p are the densities of water and polymer respectively. W_m , C and K are fitting parameters.

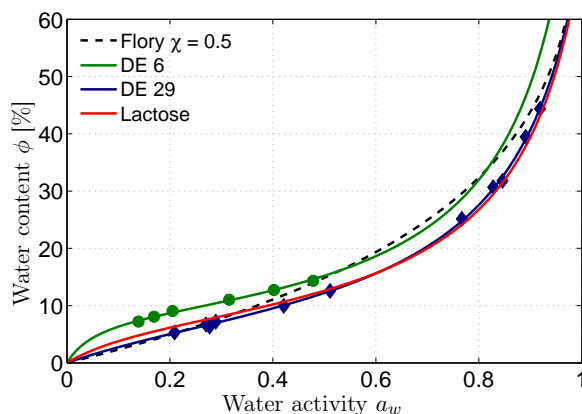


Figure 3.3: Sorptions isotherms - Considered water fractions ϕ versus water activity a_w for lactose, maltodextrin DE29 and maltodextrin DE6. The dotted line corresponds to Flory's theory with $\chi = 0.5$.

Otherwise, the theory of Flory (43, 44) is often used to describe the sorption isotherm of polymers (Eq. 3.2). It introduces an interaction parameter χ that quantifies the affinity between the solvent - water in our study - and the polymer. For instance, for maltodextrin DE29, a value of χ between 0.5 and 0.6 is in relative good agreement with experimental data (indeed the GAB model that comprises three adjusting parameters better fits the data). The advantage of the Flory approach is that it describes physically the relation from $a_w = 0$ to $a_w = 1$ with a single physical parameter:

$$a_w = \phi \cdot e^{(1-\phi)+\chi(1-\phi)^2} \quad (3.2)$$

In this study, we will use the Flory equation with $\chi = 0.5$ in order to describe the interaction of maltodextrin DE29 with water.

3.1.2.4 Glass transition

Glass transition refers to the transformation of a glass into a soft material able to flow. For polymers, it corresponds to a fast variation of the characteristic time scale with temperature T and solvent volume fraction ϕ . The main observable effect is the dramatic change in viscosity over a small range of temperature. The rigid and brittle amorphous glassy material becomes soft and flexible at this transition. The transition occurs when the molecule chains, motionless at temperatures below the glass transition range, become free to move.

Glass transition in maltodextrins is strongly dependent of the DE. For a given water content ϕ , T_g will be larger for long chains (*i.e.* small DE). In our study, we set temperature at 25 °C (room temperature). In these conditions, glass transition is crossed at a water activity a_w^g in the material. Nestlé data are obtained by Differential Scanning Calorimetry (DSC), *i.e.* that the evolution of the heat capacity with temperature is followed. The data are presented in table 3.1.

Table 3.1: Characteristics of maltodextrins by DE: molecular weight M_w , water activity a_w^g and water content ϕ_g at glass transition according to Nestlé DSC measurements (at 25 °C).

DE	M_w (g.mol ⁻¹)	a_w^g	ϕ_g
29	2500	0.50	12.2 %
6	80 000	0.68	22.2 %
2	343 000	-	-

The value of a_w^g considered in this manuscript in the case of maltodextrin DE29 will be $a_w^g = 0.6$. It is a little bit larger than the one given by Nestlé ($a_w^g = 0.5$). In our case, the important criterion is hydration dynamics rather than the heat capacity and we will define a_w^g in the glass transition chapter using the diffusion coefficient of water rather than DSC data. We have to keep in mind that glass transition is a smooth transition. The definition of a_w^g depends on the parameter that we decide to follow.

3. MATERIALS & METHODS

3.1.2.5 Diffusion coefficient

The diffusion coefficient of maltodextrin DE29 was measured in-situ by Nuclear Magnetic Resonance (NMR) with the help of Maxime Van Landeghem and Bruno Bresson using a pulsed field gradient technique (45, 46). The principle is the following: when spins are moving randomly or diffusing through a magnetic field gradient, they explore regions with various magnetic field amplitudes and acquire random phase shifts. These phase shifts lead to an additional attenuation of the signal and can be seen as an additional relaxation rate which adds to the relaxation rate measured in homogeneous field. There are several experimental factors limiting the applicability of this technique with respect to very low diffusion coefficients. In particular, the amplitude of the dephasing and rephasing gradients must be both accurate and stable, otherwise the accuracy of the measurement is altered (47). In addition to this, the transverse relaxation time (T_2) of the diffusing species must be long compared to the rising time of the field gradients. To overcome these problems, Kimmich et al. (48) proposed to make use of the high and stable constant magnetic field gradients that occur in the fringe field of superconducting magnets.

The stray field of the wide bore 7 T magnet equipped with a Bruker Avance III spectrometer was carefully mapped in order to determine the strength and orientation of the gradient. This part have already been described elsewhere (49). We found that at the position where the field is equal to 3.2 T on the axis of the magnet, the gradient can be considered as uniaxial and uniform with a strength of 47 T/m. The NMR sequence we used is a stimulated spin echo. It consists of three 90° pulses. The first pulse flips the magnetization into the xy plane. After a duration τ (encoding time), a second 90° pulse stores the magnetization along the z axis. Then, T_2 decay is stopped and the magnetization relaxes only with the longitudinal relaxation time (T_1) during a time Δ (evolution time). Finally a third 90° pulse flips the magnetization back into the xy plane and an echo arises at time τ following the last pulse. Due to their random motion through the magnetic field gradient, spins progressively loose their coherence and the amplitude of the stimulated spin echo is affected. This attenuation $\frac{I}{I_0}$ can be written as (50):

$$\frac{I}{I_0} = \frac{1}{2} \exp \left(-\gamma_r^2 G^2 D_{self} \tau^2 \left\{ \frac{2}{3} \tau + \Delta \right\} - \frac{2\tau}{T_2} - \frac{\Delta}{T_1} \right) \quad (3.3)$$

where γ_r is the gyromagnetic ratio, G the magnetic field gradient and D_{self} the self-diffusion coefficient.

For the condition $\Delta \ll T_1$ and $\tau \ll T_2$, the previous equation becomes independent of both T_1 and T_2 and we obtain Eq. 3.4.

$$\frac{I}{I_0} = \frac{1}{2} \exp \left(-\gamma_r^2 G^2 D_{self} \tau^2 \left\{ \frac{2}{3} \tau + \Delta \right\} \right) \quad (3.4)$$

This technique was used to evaluate the self-diffusion of water in maltodextrin at various volume water fractions. In each case, we plotted I as a function of $\gamma_r^2 G^2 \tau^2 \left\{ \frac{2}{3} \tau + \Delta \right\}$ and computed an exponential fit to obtain the diffusion coefficient. For instance in Fig. 3.4a, the measurements at $\phi = 39.1\%$ are presented. The exponential fit leads to $D_{self} = 7.5 \cdot 10^{-11} \text{ m}^2 \cdot \text{s}^{-1}$. Fig. 3.4b exhibits the diffusion coefficients obtained for various water fractions ϕ .

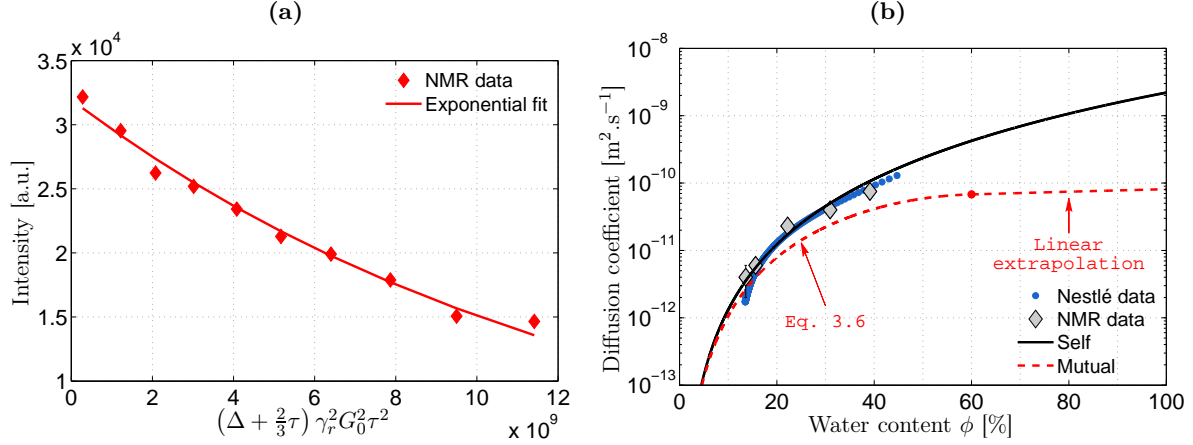


Figure 3.4: NMR measurement of maltodextrin DE29 diffusion coefficient - (a) NMR signal extraction and corresponding exponential fit ($I(x) = 31955.63 \exp(-7.510^{-11}x)$) to obtain D_p at $\phi = 39.1\%$. (b) Diffusion coefficient as a function of the water content of the polymer (Data and fit).

The diffusion coefficient measurements are fitted with a power law in order to get $D_{self} = 2.2 \cdot 10^{-9} \text{ m}^2 \cdot \text{s}^{-1}$ for pure water, i.e. the self-diffusion coefficient of water. We have $D_{self}(\phi) [\text{m}^2 \cdot \text{s}^{-1}] \simeq 1.9210^{-14} \left(\frac{\phi}{2.7}\right)^{3.224} + 10^{-15}$. The self-diffusion coefficient D_{self} corresponds to the diffusion of water molecules in a homogeneous sample. In our experiment where strong lateral gradients of water content are observed in the polymer coating, the mutual diffusion coefficient D_{mutual} must be used. Flory sorption isotherm (Eq. 3.2) can be used to obtain a relation between D_{self} and D_{mutual} :

$$D_{mutual} = D_{self} \cdot \frac{\partial \ln(a_w)}{\partial \ln(\phi)} \quad (3.5)$$

which yields, using Eq. 3.2 to:

$$D_{mutual} = D_{self} \cdot (1 - \phi)(1 - 2\chi\phi) \quad (3.6)$$

The values of the mutual diffusion coefficient are in relative good agreement with Nestlé Research Center. Those data were obtained using drying experiments in the range $\phi \in [0.1, 0.4]$ (Yamamoto method (51)). Nevertheless, Eq. 3.6 cannot be used at large water contents since the diffusion of the polymer itself becomes non-negligible when the concentration in water increases. At $\phi = 100\%$, we should have $D_{mutual} = D_{self}^{polymer}$. $D_{self}^{polymer}$ can be assessed using theories of polymer dynamics (52, 53):

$$D_{self}^{polymer} \sim \frac{kT}{6\pi\eta R_g} \quad (3.7)$$

3. MATERIALS & METHODS

$$R_g \sim N^{3/5}b \quad (3.8)$$

where R_g is the radius of gyration of the polymer chain, b the length of a monomer (or Kuhn segment) and N the number of monomers.

With maltodextrin DE29, we can estimate N using the ratio of monomer molecular weight (162.14 g.mol⁻¹) to the one of the polymer (2500 g.mol⁻¹) which yields to $N = 15.4$. With $b \sim 600$ pm, we obtain $R_g = 3.1$ nm and $D_{self}^{polymer} = 8.1 \cdot 10^{-11}$ m².s⁻¹. For our study, we will use Flory equation between $\phi = 0$ % and $\phi = 60$ %. For $\phi > 60$ %, we extrapolate the value of the diffusion coefficient with a linear evolution from $D_{mutual}(\phi = 0.6)$ to $D_{self}^{polymer}$. The final curve (dotted curve in Fig. 3.4b) will always be referred as $D_p(\phi)$ in this manuscript.

3.1.2.6 Dissolution speed

The dissolution speed of different maltodextrins in water or in a maltodextrin solution has been measured with the help of different home-made experiments. The most precise was the one using some spheres of polymer moulded with hands where we could obtain the dissolution speed as a function of the velocity U of the liquid in contact with the sphere. Other experiments use some channels of polymer, either rectangular with only one wall of maltodextrin and three of PDMS or cylindrical with maltodextrin only.

- Dissolution of polymer spheres

We design small dense spheres of maltodextrin by using a hot and very viscous solution of maltodextrin DE29 (obtained by heating a 50 % *wt* solution in a micro-wave oven). The sphere is moulded with hands and hardens as cooling. To decrease the water content, one can either put the sphere in a dry atmosphere (P₂O₅) or dry the sphere in an oven (not too hot to keep the spherical shape of the sphere and not to deteriorate the polymer). Fig. 3.5 shows a typical picture of obtained spheres. The radius R of the spheres ranges from 1 mm to 5 mm.



Figure 3.5: Maltodextrin spheres - Spheres of maltodextrin DE29 moulded with hands.

We measure the dissolution speed v_d with a home-made experimental set-up (Fig. 3.6). A syringe (diameter $d = 20$ mm) is cut along the length using an electric saw and a microscope glass slide is glued to the remaining part of the syringe. With the help of a needle stuck into the polymer, the maltodextrin sphere is hung inside the syringe. A hole is pierced at the top of

the system in order to evacuate the liquid which will arrive by the bottom part of the syringe. A micro-pump (small flows) or a peristaltic pump (large flows) is then used to inject the solvent in order to reach a large range of liquid speeds U . The size of the sphere decreases with time in the flow of solvent. The observation of the immersed sphere is performed through the glass slide using a video camera. It allows a precise measurement of the dissolution speed by extracting the outline of the object. We call C the center of the sphere and M the points of the outline.

For instance with a maltodextrin DE29 sphere immersed in static water, we can follow the sphere radius $R = \|\overrightarrow{CM}\|$ at a given radial angle ψ as a function of time ($\psi = 90^\circ$ corresponds to the top vertical direction). The result presented in Fig. 3.7a shows that the dissolution is characterized by an initial step of swelling, *i.e.* that R increases during the first seconds. Then, the radius linearly decreases with time. This curve is in good agreement with the predictions of Ranade and Mashelkar (25). The dissolution is non-fickian since $\frac{dR}{dt}$ is almost constant in the second step (a fickian dissolution would lead to $R(t) \sim -t^{1/2}$). A linear fit of $R(t)$ gives the value of v_d . Here, the presented curve corresponds to $v_d = 1.67 \mu\text{m.s}^{-1}$.

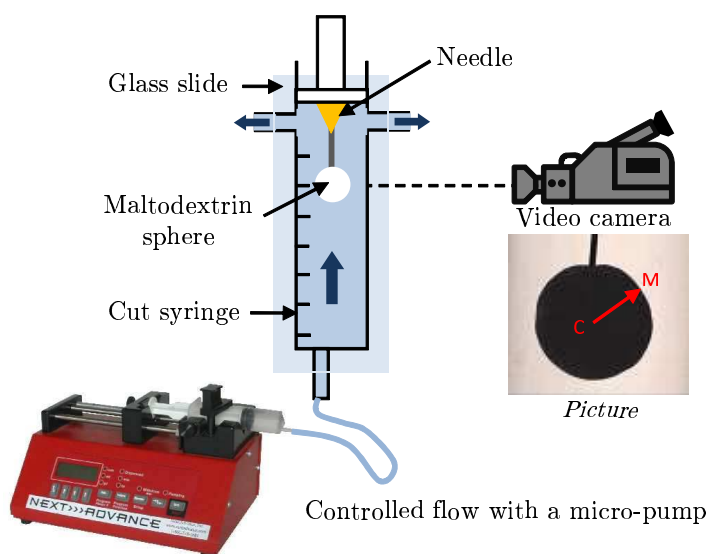


Figure 3.6: Dissolution of maltodextrin spheres: experimental set-up - Measurement of the dissolution speed v_d of maltodextrins using spheres of polymer exposed to a given flow of solution.

In Fig. 3.7b, we represent the dissolution speed v_d as a function of the radial angle ψ . We find that the dissolution speed is almost constant in the top part of the polymer sphere ($v_d \sim 1.6 \mu\text{m.s}^{-1}$) while it becomes larger in the bottom part ($v_d \sim 2 \mu\text{m.s}^{-1}$). This can also be seen in the pictures of Fig. 3.7c that represent the sphere at 4 different times of immersion. We clearly see the difference of shape evolution between the top and the bottom of the sphere. This effect is likely to be due to the gravity. The dissolved matter below the sphere falls down in the liquid bringing some fresh water by convection. In this manuscript, we will always refer to v_d in the sphere experiment as the average dissolution speed in the top part of the sphere.

3. MATERIALS & METHODS

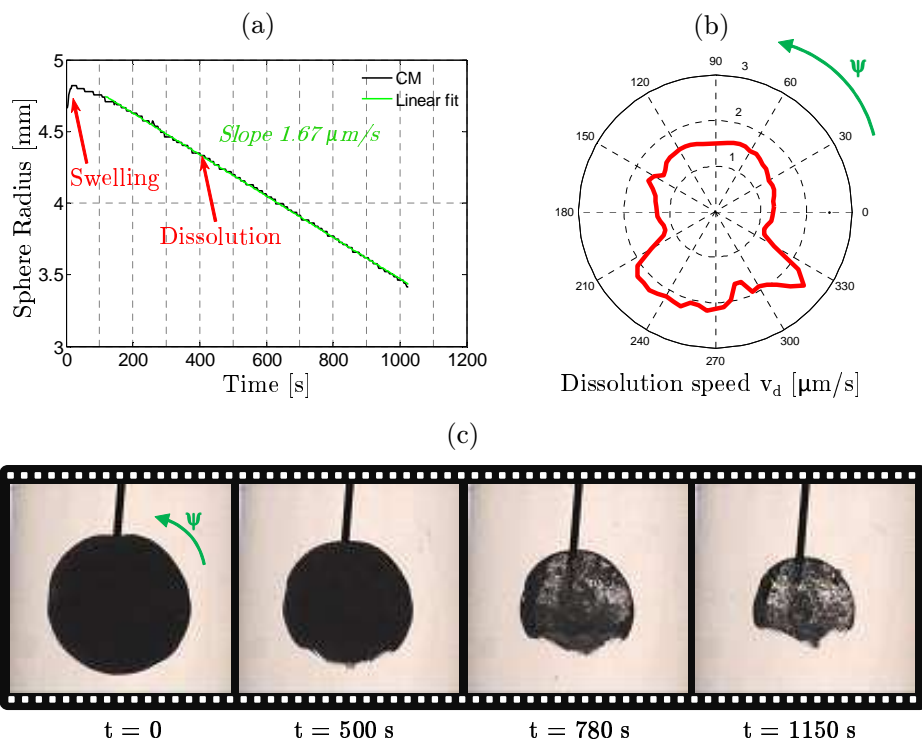


Figure 3.7: Dissolution of a maltodextrin DE29 sphere in water - Measurement of the dissolution speed of a maltodextrin DE29 sphere in static water ($R_0 = 4.7$ mm). (a) Extraction of the distance CM for $\psi = 45^\circ$ and linear fit in the dissolving part of the curve (9.4 mm sphere in pure water). (b) Polar plot of the dissolution speed $v_d(\psi)$ where ψ is the radial angle (in $\mu\text{m}\cdot\text{s}^{-1}$). v_d is increased by gravity in the bottom part of the sphere. (c) Raw pictures of a maltodextrin DE29 sphere in pure water at different times.

With this experimental set-up, we will show in chapter 6 or appendix E that we can measure the dissolution speed v_d relative to the liquid speed or the solution concentration in maltodextrin. Both have a non-negligible effect that will be related to the dissolution of the polymer coating during spreading experiments.

- Dissolution of channels

Other methods were developed in order to measure the dissolution speed v_d of maltodextrin. In these methods, the aim is to get close to the geometry of food powders, *i.e.* closed channels. With that kind of geometry, we can also study the effect of the viscosity increase in a channel due to the dissolution of the walls. Two fabrication methods were successful for these channels:

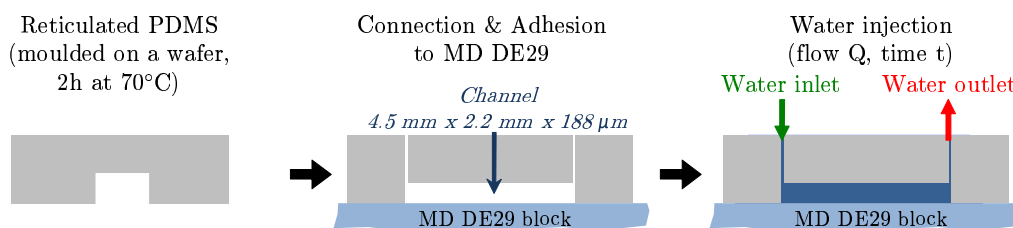
- Rectangular PDMS channels: We use a mould made with two pieces of Si wafer to obtain a PDMS block with a furrow at its surface (depth $\sim 150\text{-}200$ μm). PDMS is then glued by adhesion to a maltodextrin thick surface prepared using the method described in section

3.2.2. We obtain a closed channel with three walls of PDMS and one of polymer, where a solution can be injected (see Fig 3.8). The dissolution speed is measured with two techniques: measuring the refractive index of the outlet solution or measuring the depth of the furrow by profilometry (at the end of the experiment).

- Cylindrical channels: we use a Teflon pipe as a mould to prepare a block of maltodextrin. A viscous solution of maltodextrin is dried at 75°C and the pipe is removed in order to get a cylindrical channel (see Fig 3.8). Water is injected and the dissolution speed is measured using video acquisition through the polymer.

Both methods lead to a less precise measurement of v_d in comparison with the sphere experiment. The dissolution of the channel walls leads to a modification of both liquid speed and liquid concentration at the same time. Besides, some leaks of liquid appear due to the difficulty to connect the soluble polymer and the pipes. Nevertheless, the dissolution speeds obtained with both experiments are in good agreement.

Method 1: rectangular PDMS channels



Method 2: cylindrical channels

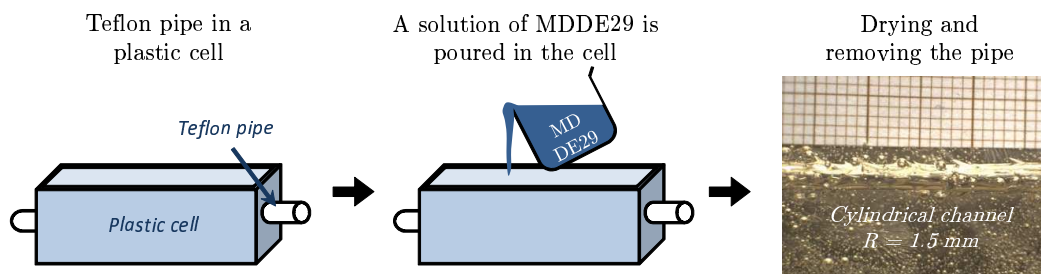


Figure 3.8: Preparation methods of maltodextrin channels - Method 1: rectangular PDMS channels. Method 2: cylindrical channels.

3.2 Preparation of carbohydrates samples

In this section, the methods of preparation of homogeneous layers of carbohydrate (lactose or maltodextrin) on a solid substrate are explained. Three different methods were used: spin-coating, dip-coating and moulding.

3. MATERIALS & METHODS

3.2.1 Thin layers

Most of our experiments were carried on thin layers, *i.e.* of thickness smaller than $3\ \mu\text{m}$. For the preparation of the layers, first, aqueous solutions of carbohydrates are prepared at concentrations ranging between 1 and 40 wt% depending on the coating thickness desired. The layers are then obtained by spin-coating of the solutions onto solid substrates at different speeds from 1500 rpm to 4000 rpm (see Fig. 3.9). As solid substrates, we use bare silicon wafers (ACM France), 2 inches in diameter, that were modified in some specific cases to vary their surface properties. In the general case, the wafers are first oxidized using a H_2O plasma treatment and immediately coated with the prepared solution. The plasma step leads to a contact angle between water and oxidized silicon of $\theta_S \simeq 0^\circ$. We sometimes used microscope glass slides instead of silicon wafers when transparency was required. The thickness of the resulting layers depends on the rotation speed, the acceleration, the solution concentration or the evaporation rate (solvent choice). Layers of thicknesses ranging between 1 nm and $3\ \mu\text{m}$ were obtained by adjusting the solution concentration and the spinning speed.

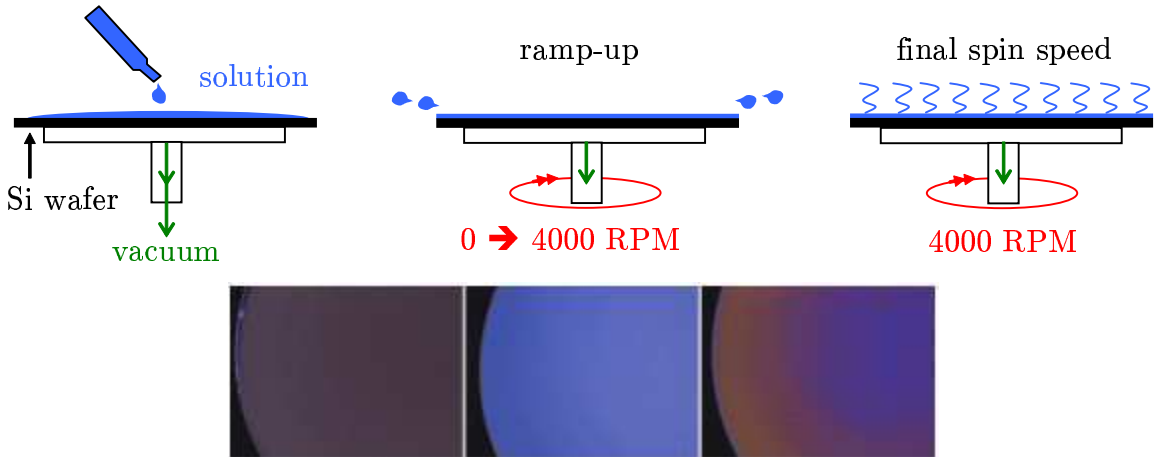


Figure 3.9: Schematic representation of the spin-coating process - A solution containing the soluble material to be investigated is spread onto a substrate by centrifugation. Evaporation occurs and a uniform layer of material is obtained (see the three example pictures obtained with lactose)

In specific cases we modify the surface properties of the solid underlying substrate by spin-coating a 250-nm thick layer of polystyrene (PS) in toluene solution on the silicon wafer. The PS layer is known to be hydrophobic and the contact angle of water is $\theta_S \simeq 90^\circ$. By exposing the PS layer to a H_2O plasma for two different exposure times, we tune its contact angle with water down to $\theta_S=32$ and 7° respectively. On these plasma-treated PS layers, maltodextrin solutions are spin-coated as before. We thus obtain maltodextrin coatings on solid substrates of lesser hydrophilicity compared to the bare Si wafers, as quantified by the values of θ_S .

Owing to optical interferences, the submicrometric layers obtained on silicon wafers exhibit Newton hues. The colour depends on the thickness (see the color scale in appendix A and theory

in 3.3.4). The thickness can be measured by ellipsometry or interferometric profilometry. Briefly, ellipsometry consists in illuminating the layer with a polarised laser beam. The polarization state of the incident light may be decomposed into a s and a p -component (the s -component is oscillating perpendicular to the plane of incidence and parallel to the sample surface, and the p -component is oscillating parallel to the plane of incidence). The amplitudes of the s and p -components, after reflection and normalized to their initial value, are denoted by r_s and r_p , respectively. Ellipsometry measures the complex reflectance ϱ which is the ratio of r_p over r_s (complex quantity):

$$\varrho = \frac{r_p}{r_s} = \tan(\psi) e^{i\Delta} \quad (3.9)$$

where $\tan \psi$ is the amplitude ratio upon reflection, and $\Delta\Phi$ is the phase shift.

Ellipsometry is an indirect measurement method. A model analysis must be performed using the values of ψ and Δ and the sample properties (different layers, known thicknesses or expected values, refractive index, ...) in order to obtain the optical constants of the sample. If the refractive index of the layer is unknown, it can be measured using varying incident angles of the laser beam. In our case, we obtain $n = 1.569$ for maltodextrin DE29 and $n = 1.567$ for lactose. The complex refractive index of the substrate was chosen equal to $n_s = 3.874 + i 0.016$ and an intermediate layer of SiO_2 was introduced ($n = 1.46$ and $e = 20\text{\AA}$). An incident angle of 70° was chosen.

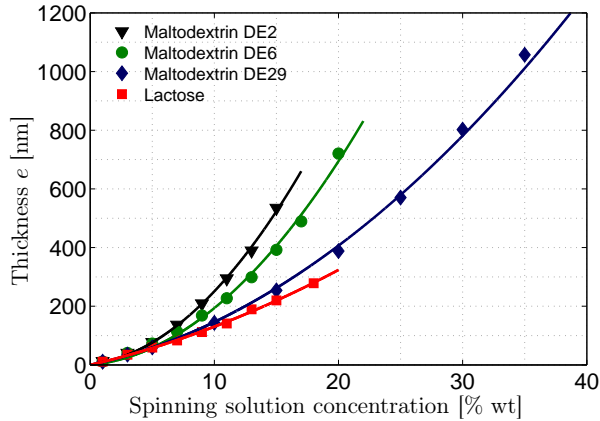


Figure 3.10: Spin-coating of carbohydrates - Thickness of spin-coated samples of carbohydrates (lactose, maltodextrin DE29, maltodextrin DE6 and maltodextrin DE2) measured by ellipsometry for a constant refractive index, as a function of mass fraction in the spinning solution. Polynomial fits of the 2nd order are also plotted.

Fig. 3.10 gives the measured thickness e of four different spin-coated compounds: lactose, maltodextrin DE29, maltodextrin DE6 and maltodextrin DE2. They are fitted with polynomial functions of the 2nd order. The spin-coating parameters are set to be: spinning speed of 4000 RPM, acceleration of 2 s and spinning time of 80 s which is enough to reach a constant thickness.

3. MATERIALS & METHODS

The curves show that the heavier carbohydrates such as maltodextrin DE2 have a thickness that increases faster with solution concentration. This behaviour is correlated to the viscosity of the solution. The higher the viscosity, the thicker the layer for the same spinning parameters. These curves were used to prepare layers of various thicknesses of soluble material. By reducing the spinning speed, thicker layers could be obtained but the homogeneity of the surface is reduced especially below 2000 rpm where stains of different colors are obtained at high concentrations (concentration between 20 % wt and 50 % wt). At 4000 rpm, the layers are homogeneous across the central area of the wafer, over around 4 cm. The thickness is always larger at the center of the sample but the relative difference between the center and the periphery of the wafer is below 8%. This difference is not a problem for the spreading experiment since only a few square millimetres of the surface are used and so the difference of thickness is negligible in comparison to the swelling. Finally, the roughness of the surfaces was measured by AFM to be subnanometric.

3.2.2 Thick layers

Spin-coated layers become heterogeneous for thickness larger than about 3 μm . The samples with a thickness between 3 μm and 10 μm were all prepared by dip coating. After making the substrate hydrophilic by applying H_2O plasma on a microscope glass slide, it is immersed into the maltodextrin solution. After removing it carefully from the bath, the sample is dried during several hours. This operation is performed on a hot plate at $T \sim 70^\circ\text{C}$. The samples obtained by dip-coating on glass are fully transparent. In that case, the best technique to measure their thickness is profilometry.

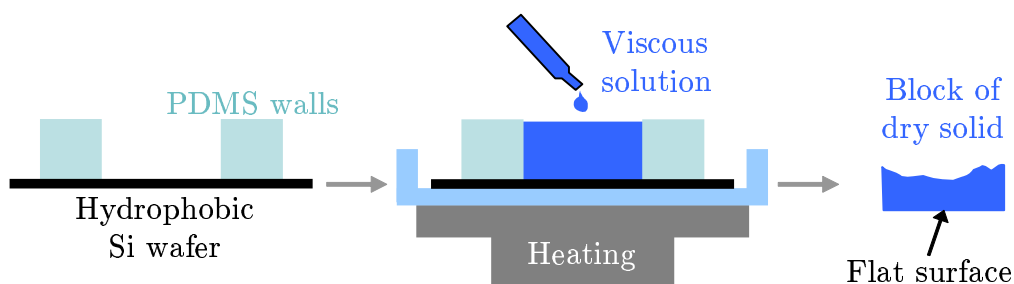


Figure 3.11: Preparation of maltodextrin thick blocks - A concentrated solution of maltodextrin in water is poured into a mould made with PDMS walls and a silanized wafer at the bottom. After drying a few days, the maltodextrin solid block is removed from the mould.

Another technique was used to get very large thicknesses of maltodextrin DE29. These were obtained by drying thick blocks of polymer. Therefore, a silicon wafer or a glass slide is silanized using trichloro(1H, 1H, 2H, 2H-perfluorooctyl)silane. Then a mould is made by spontaneous adhesion on the substrate of PDMS pieces (see Fig. 3.11). A highly concentrated solution of polymer (solid content between 50% and 70%) is poured inside the mould and the substrate is placed on a hot plate ($T \sim 70\text{-}80^\circ\text{C}$). After a few days, a dry solid block is obtained and easy to remove from the mould because of the hydrophobic coating that reduces maltodextrin adhesion.

The face which was on the substrate is very flat. We were able to obtain thicknesses in the range [0.5 mm - 5 mm]. For the spreading experiment, the equilibration at the desired water activity $a_w = 0.43$ was done for three days.

3.3 Spreading experiments

3.3.1 Experimental set-up

The coated substrates are placed in a home-made transparent chamber made out of PMMA (Fig. 3.12). The chamber is tightly closed at the top by a removable lid with soft paraffin. The lower level of the chamber is a drawer that contains a saturated solution of chosen salt which sets the humidity inside the box. A sensor (Rotronic HC2-C04) monitors the humidity and temperature at all times. Prior to any experiment, the coated wafer is allowed to equilibrate in the chamber. Equilibration is obtained when the water absorption saturates, that is when the coating thickness no longer varies. Depending on the initial thickness of the layer and the difference between room humidity and the imposed one, the equilibration can go from minutes to days. A small computer fan was installed inside the box in order to accelerate the equilibration process.

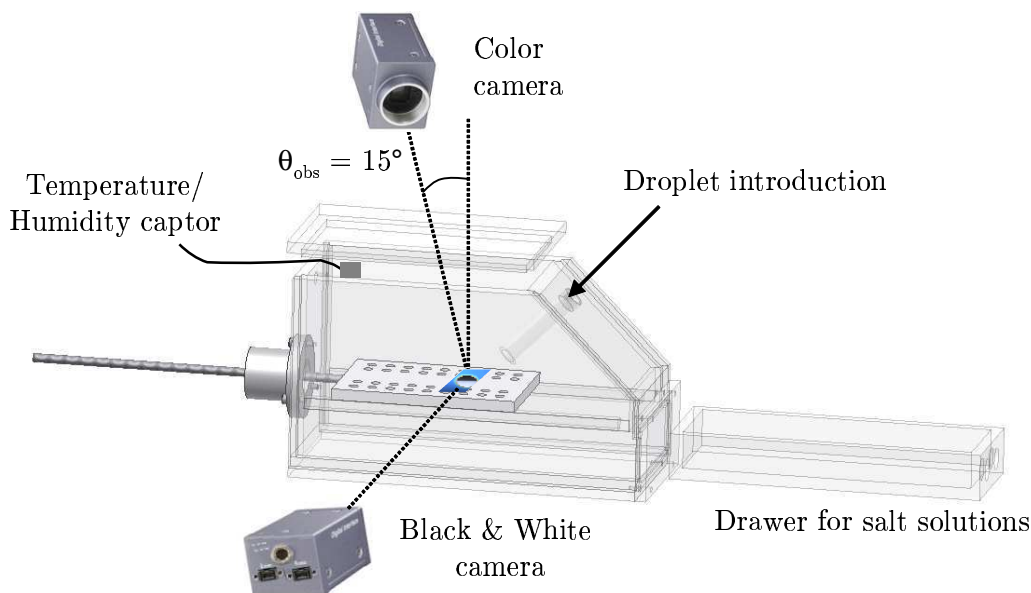


Figure 3.12: Experimental set-up for spreading experiment - A close box was designed for contact angle measurement and Newton hues detection using two cameras. Humidity is set using saturated salt solutions. Temperature and humidity are measured continuously.

The experiment consists in depositing a 3- μ L droplet on the coated substrate with a micropipette and monitoring its spreading from the side and the top at a frame rate of 1 to 30 Hz. The lateral views are acquired with a black & white camera (Sony XCD-SX90) set at about 1° from the horizontal axis. They show clear views of the droplet and its mirror image in the wafer, making accurate the determination of the dynamic contact angle θ at the triple line. We

3. MATERIALS & METHODS

verify experimentally that the droplet shape remains circular during the whole spreading, so we could use the radius R to compute the contact line velocity $U = \dot{R}$. The top view is acquired with a color camera (Sony XCD-SX90CR) placed at an angle $\alpha=15^\circ$ from the vertical direction. It records the Newton hues which enables thickness calculation, as detailed in the next section. Side illumination is provided by a white LED screen (Phlox). The macro-objectives used with the two cameras give the following resolutions: $8.3 \mu\text{m}/\text{pixel}$ for the lateral pictures and $5.3 \mu\text{m}/\text{pixel}$ for the color top-view pictures.

In the spreading experiment, the water activity a_w is set using saturated salt solutions. The sample is always equilibrated at this a_w before starting the experiment. The introduction of the droplet brings room air into the box but the change of water activity is negligible. The humidity measurement is performed 2 cm above the droplet. The maximum variation, observed at $a_w = 0.11$, was 0.02. For the other tested water activities, the disturbance is not larger than 0.01.

Six different water activities were tested for all the carbohydrates:

- P_2O_5 : sets the relative humidity to $a_w \sim 0$
- LiCl : sets the relative humidity to $a_w = 0.11$
- $\text{K}_2\text{CO}_3, 1.5 \text{H}_2\text{O}$: sets the relative humidity to $a_w = 0.43$
- NaBr : sets the relative humidity to $a_w = 0.58$
- NaCl : sets the relative humidity to $a_w = 0.75$
- K_2SO_4 : sets the relative humidity to $a_w = 0.97$

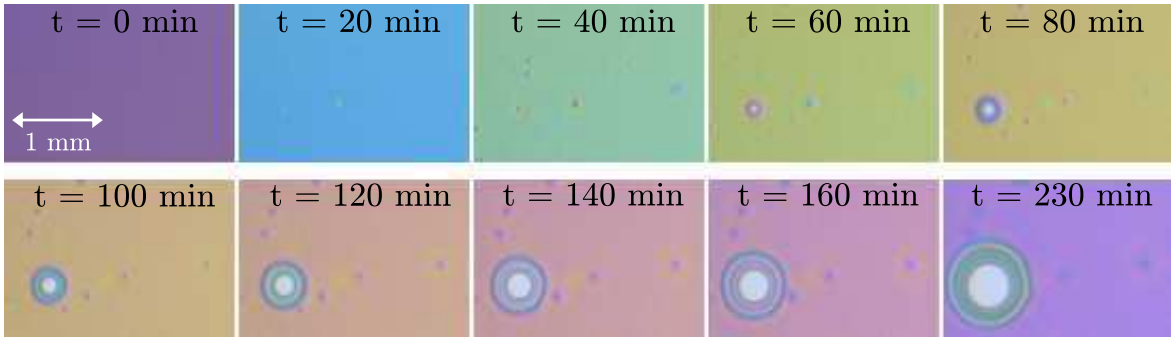


Figure 3.13: Dewetting of maltodextrin at high water activity - Opening of a hole by dewetting of a 240 nm-thick maltodextrin DE29 layer during equilibration at $a_w = 0.97$ from room humidity $a_w = 0.28$.

At $a_w = 0.97$, a dewetting is observed during equilibration of a 240 nm-thick maltodextrin DE29 layer. The large water content decreases the viscosity of the material leading to an unstable thin layer. Literature (54) describes this phenomenon of dewetting. A thin film of liquid has a critical thickness of dewetting e_c . It is unstable below this thickness given by:

$$e_c = 2\sqrt{\frac{\gamma}{\rho g}} \sin\left(\frac{\theta}{2}\right) \quad (3.10)$$

where θ is the contact angle of the liquid on the substrate, γ the surface tension, and ρ the density. In our case, the maltodextrin is no longer solid but can be considered as a viscous aqueous solution. After 4 hours at $a_w = 0.97$, the thin layer reaches 460 nm, *i.e* almost twice its initial thickness. With a surface tension equal to 72.8 mN/m and a contact angle around 10° , the equation leads to a theoretical critical thickness $e_c = 475 \mu\text{m}$. This is much larger than the measured layer thickness during swelling ($e < 1 \mu\text{m}$). Thus, dewetting occurs during water absorption in the thin layer and the substrate becomes visible as shown in Fig. 3.13.

3.3.2 Pulled substrate experiment or swollen droplet

The spontaneous spreading of the sessile droplet yields spreading velocities U ranging between $5 \cdot 10^{-4} \text{ mm.s}^{-1}$ and $8 \cdot 10^{-1} \text{ mm.s}^{-1}$. To explore faster contact line motion, we push the droplet relatively to the substrate by pulling the substrate at controlled speed U while holding the liquid droplet in place with a Teflon wiper tightly placed above the substrate (Fig. 3.14). For this, a motor is attached to the platform slider and a high speed monochrome camera monitors the side view (SVS340MUGE, 640x480 pixels, frame rate up to 260 Hz). Typical pictures are presented in Fig. 3.15. The contact line speeds relative to the substrate obtained this way approximately range between 1 mm.s^{-1} and 30 mm.s^{-1} but it is also possible to reach very large values of U by manually pulling the plate. Thus, we obtained velocities around 1 m.s^{-1} . This experiment will be referred to as pulled substrate experiment.

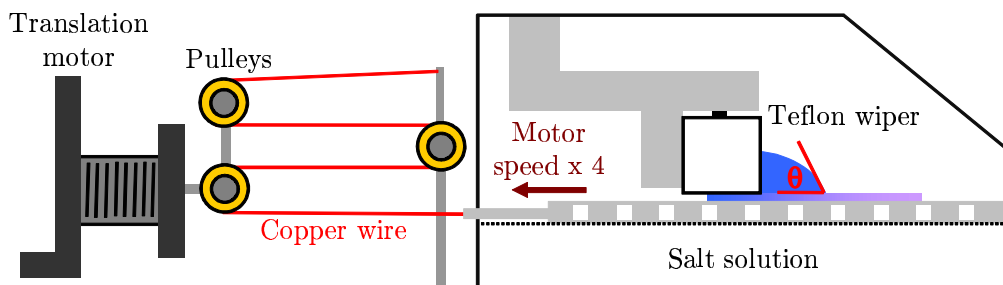


Figure 3.14: Experimental set-up for the pulled substrate experiment - A motor and a system of pulleys allow to pull the substrate while the drop is held in place with a Teflon wiper. Higher contact line speeds are obtained.

Finally, intermediate velocities can be obtained by feeding the droplet using a micro-pump. The contact line speeds obtained with this method approximately range between $3 \cdot 10^{-2} \text{ mm.s}^{-1}$ and 7 mm.s^{-1} . The precision on the speed measurement is better than the pulled substrate experiment but the contact line does not remain a long time within the field of view of the camera. This experiment will be referred to as the fed drop experiment.

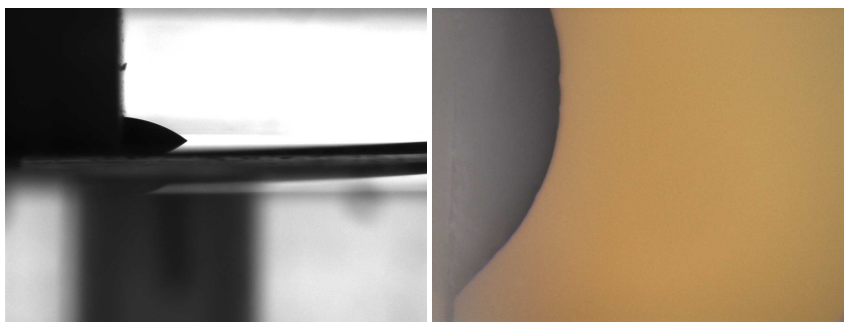


Figure 3.15: Typical pictures obtained during pulled substrate experiment - Left: Side view of the droplet. Right: Top view of the layer.

3.3.3 Contact angle measurement

The extraction of the contact angle is done on side view monochrome pictures. For each experiment, around 280 pictures are recorded with a variable frequency adapted to the velocity of the contact line. At the beginning of free spreading, a frame rate of 15 or 30 Hz is used while a frame rate of 1-2 Hz is used at the end. Each picture is binarized using ImageJ. Thus, the droplet appears black on a white background. Using a code written on Matlab, the coordinates of both extremities A and B are obtained ($\{x_A, y_A\}$ and $\{x_B, y_B\}$) that allows the calculation of the droplet radius R and the contact line speed U . Then, for each point C of the contour, not too close to the extremities A and B, the circle going through A, B and C is found. Thus, the equation of the average circle following the contour is obtained. The contact angle θ is then calculated using the slope at the triple point and the baseline slope. The error on θ measurement using this method was estimated between 0.2° and 0.5° depending on the picture quality. We show in Fig. 3.17a an example of spreading dynamics with maltodextrin DE29 at $a_w = 0.58$. θ decreases with time as the contact line speed U , leading to an increasing function $\theta(U)$.

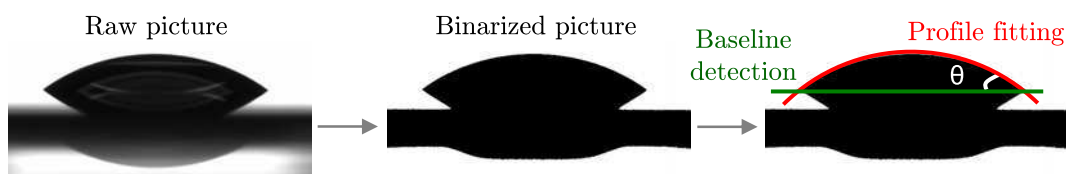


Figure 3.16: Contact angle measurement on black and white pictures - The measurement of the contact angle θ is performed on lateral pictures. The droplet image is binarized using ImageJ (constant threshold) and a mathematical fit is performed on the circular shape using Matlab.

As explained in section 3.2.1, we also performed spreading experiments on modified substrates. A layer of polystyrene was used to cover the silicon substrate. Using a plasma treatment, we varied the contact angle θ_S between the substrate and water and so the substrate energy. A 250 nm-thick layer of maltodextrin DE29 is then spin-coated onto the modified substrate. We extract the dynamic contact angle θ between water and the coating as a function of the droplet velocity U for the different samples. The result is presented in Fig. 3.17b. We observe that the

modified substrate does not have any effect on the contact angle showing that the triple line is above the layer. Water does not penetrate underneath the polymer coating.

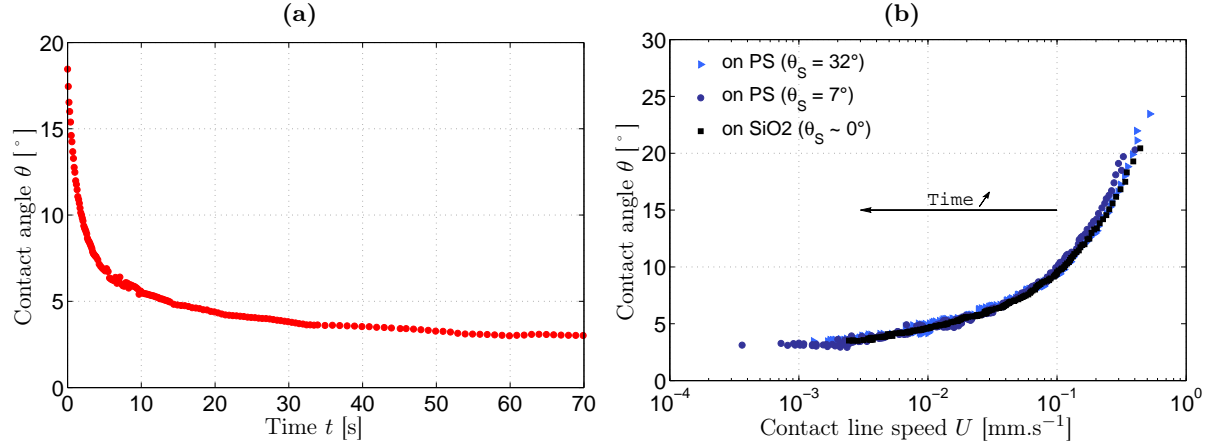


Figure 3.17: Contact angle measurement on maltodextrin layers - Measurement of the contact angle for a water droplet deposited onto a 250 nm-thick layer of maltodextrin DE29. (a) $\theta(t)$ at $a_w = 0.58$. (b) $\theta(U)$ at $a_w = 0.58$ for different substrates.

Finally, the stationarity of the measurement was investigated. Indeed, the theoretical arguments used in the following chapters consider a stationary contact line. Thus, we have verified that the contact line velocity does not vary too rapidly during spreading. We present in Fig. 3.18 the average ratio $\frac{U(x+\Delta x)-U(x)}{U(x)}$ during free-spreading (550 nm-thick maltodextrin DE29 layer equilibrated at $a_w = 0.75$) as a function of the contact line displacement Δx . We can notice that for a displacement Δx smaller than 100 μm , the velocity varies by less than about 20%.

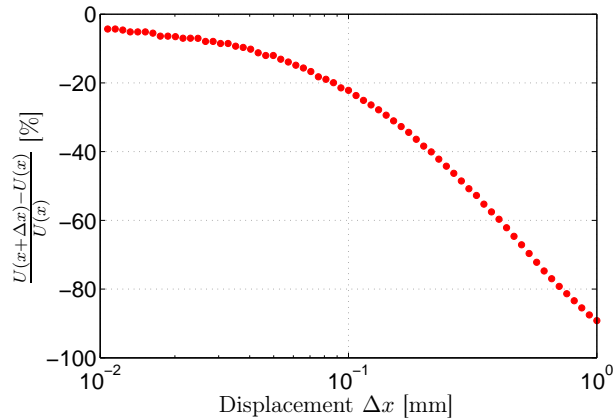


Figure 3.18: Validation of the stationarity approximation - Measurement of the average contact line speed variation for different contact line displacements Δx during water free-spreading onto maltodextrin (550 nm-thick maltodextrin DE29 layer equilibrated at $a_w = 0.75$).

3. MATERIALS & METHODS

3.3.4 Color analysis

3.3.4.1 Interferences theory

The observed color variations (Fig. 3.19) of a soluble thin film while being hydrated are due to changes of the thickness. This phenomenon is well-known to pedestrians who can observe colors on the road when a puddle is covered by petrol. Interferences occur in that kind of geometry where a sub-micrometric layer of transparent material is onto a very reflective surface (silicon wafer in our experiment). The color scale can be found in appendix A.

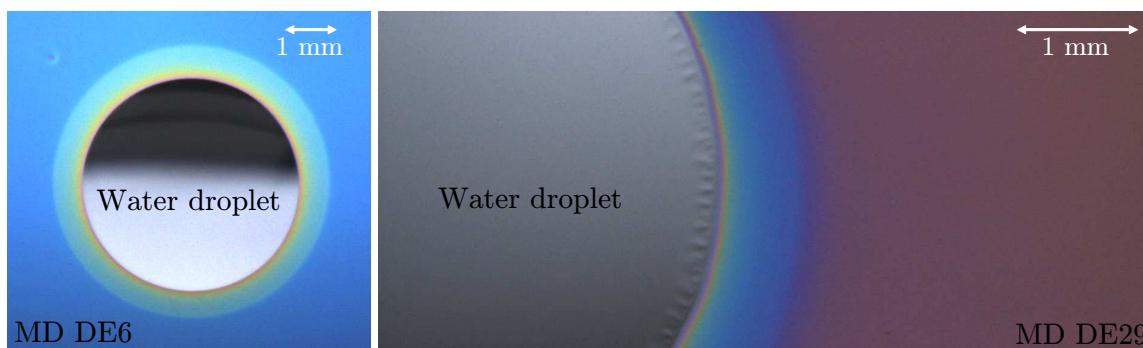


Figure 3.19: Color pictures obtained in spreading experiments - Typical pictures acquired by the color camera of spreading set-up. (left) Water droplet onto a 300 nm-thick maltodextrin DE6 layer equilibrated at $a_w = 0.58$. (right) Water droplet onto a 250 nm-thick maltodextrin DE29 layer equilibrated at $a_w = 0.43$.

These interferences depend on the refractive indexes of the different domains, on the observation angle and on the layer thickness. Light interferes constructively or destructively according to wavelength, leading to color variations if the layer is illuminated with white light.

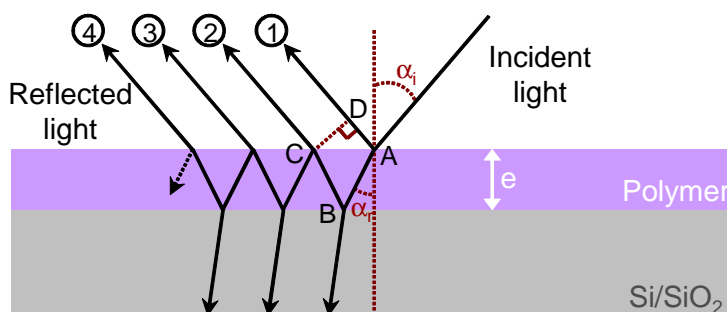


Figure 3.20: Interferences formation in a thin layer of polymer - The color of thin layers prepared by spin-coating is due to the interferences created in this sub-micrometric system.

On Fig. 3.20, a wave of wavelength λ arrives on a thin film (thickness e , refractive index $n = 1.569$). The substrate has a high reflective index $n_s = 3.874$. Let I_0 be the intensity of

the incident light arriving with an angle α_i to the perpendicular direction. The Snell-Descartes law gives a relation between α_i and α_r , the angle between the perpendicular direction and the refracted beam.

$$\sin(\alpha_i) = n. \sin(\alpha_r) \quad (3.11)$$

The reflected beam has a difference of phase $\Delta\Phi$ with the one transmitted through the layer, reflected on the substrate and transmitted in the air. Using Eq. 3.11, we can find:

$$\begin{aligned} \Delta\Phi &= \frac{2\pi\delta}{\lambda} = \frac{2\pi}{\lambda} (n(AB + BC) + AD) \\ &= \frac{4\pi ne \cos(\alpha_r)}{\lambda} \end{aligned} \quad (3.12)$$

Using the Fresnel reflection and transmission coefficients at a solid interface (here $n_{polymer} = 1.569$ and $n_{Si} = 3.874$), we can show that the intensity of the third reflected beam is negligible. Thus, the reflected intensity can be expressed as:

$$I(\lambda) = I_m \left[1 + \Gamma \cos \left(\frac{4\pi ne \cos(\alpha_r)}{\lambda} \right) \right] \quad (3.13)$$

where I_m is the mean intensity and Γ is a contrast factor.

With this relation, it is possible to link the recorded signal to the experimental color. A simple approach would consist in describing each camera sensor as a monochromatic sensor (red: λ_R , green: λ_G and blue: λ_B) but in this study, we decided to improve the color detection by considering the three densities of intensities ($\zeta_R(\lambda)$, $\zeta_G(\lambda)$ and $\zeta_B(\lambda)$) for the relative responses of each sensor (the density of probability is the relative response supplied by the device manufacturer normalized in order to have an integration equal to 1). These responses are functions of the wavelength and are known in the range [400 nm - 700 nm] as shown in Fig. 3.21a. Indeed, first analysis based on monochromatic responses showed some irregularities in thickness calculation close to the droplet. They were corrected using this improved description. Thus, the three sensors record the 3 following intensities:

$$\begin{cases} I_R = \int_{\lambda=400nm}^{\lambda=700nm} \zeta_R(\lambda).I_m \left[1 + \Gamma \cos \left(\frac{4\pi ne \cos(\alpha_r)}{\lambda} \right) \right] \\ I_G = \int_{\lambda=400nm}^{\lambda=700nm} \zeta_G(\lambda).I_m \left[1 + \Gamma \cos \left(\frac{4\pi ne \cos(\alpha_r)}{\lambda} \right) \right] \\ I_B = \int_{\lambda=400nm}^{\lambda=700nm} \zeta_B(\lambda).I_m \left[1 + \Gamma \cos \left(\frac{4\pi ne \cos(\alpha_r)}{\lambda} \right) \right] \end{cases} \quad (3.14)$$

The theoretical color is then defined by the hue function H which depends on I_R , I_G and I_B :

3. MATERIALS & METHODS

$$H = \begin{cases} \operatorname{atan} \left(\frac{\sqrt{3}/2(I_G - I_B)}{I_R^{-1/2}(I_G + I_B)} \right) & \text{if } I_R - \frac{I_G + I_B}{2} > 0 \\ \pi + \operatorname{atan} \left(\frac{\sqrt{3}/2(I_G - I_B)}{I_R^{-1/2}(I_G + I_B)} \right) & \text{else} \end{cases} \quad (3.15)$$

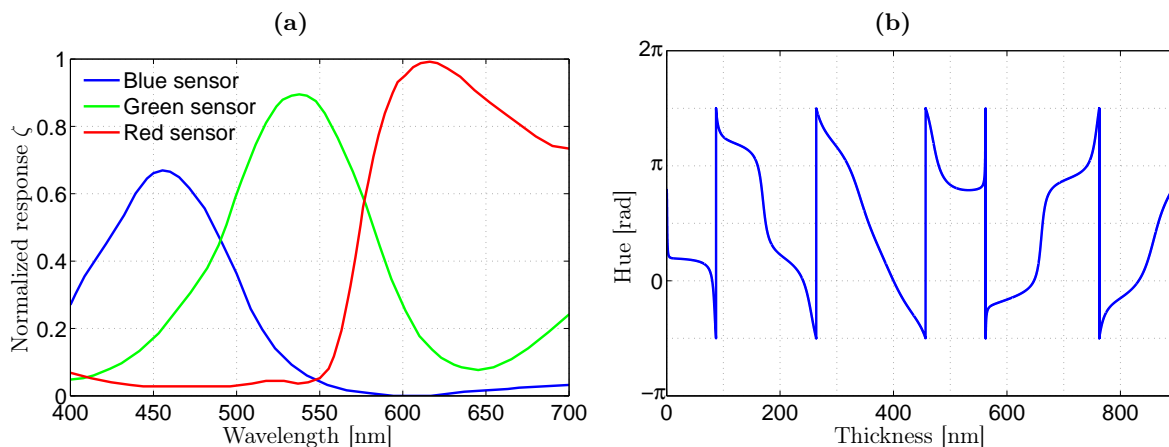


Figure 3.21: Camera sensors and hue - (a) Sensitivity of camera sensors. Normalized relative responses of the three camera sensors used for color detection and analysis. (b) Theoretical hue for a thin film of polymer ($n = 1.569$) observed with an angle $\alpha_i = 15^\circ$ is obtained by coupling theory of interferences with the properties of the camera.

By comparing the theoretical hue based on Eq. 3.14 and Eq.3.15 with the experimental hue based on RGB measurement in one point, it becomes possible to measure the thickness of the film at this point. The experimental values of I_R , I_G and I_B are firstly calibrated to ensure the white balance of the camera. A surface of TiO_2 is used as a white reference and we impose the constraint $I_R = I_G = I_B$ for this surface. The calculation of the thickness must be done carefully since the hue function is not bijective. For one hue, there are several solutions for the thickness as shown in Fig. 3.21b. But knowing the initial thickness of the layer before swelling and so the initial hue, it becomes possible to obtain the thickness evolution as a function of time in any point since the swelling is continuous. Without an initial value, the color determination does not allow the measurement of the thickness via the hue function. Literature (55) shows that the use of the saturation function can help to have only one solution but we did not use it since it was referred to as a very sensitive method.

3.3.4.2 Color analysis and thickness

We have validated the color analysis with direct measurements of the thickness of maltodextrin layers. By tuning the concentration of the solution at constant spinning speed (4000 rpm), one can obtain a large range of thickness using spin-coating. With maltodextrin DE29 for instance, the range [0 nm - 1200 nm] is easily reachable. Ellipsometry measurements give an increasing

thickness when increasing the concentration gradually from 1% to 40%. The color measurement can be performed with the same principle. We can measure the experimental hue and explore the theoretical curve (Fig. 3.21b) by increasing the thickness.

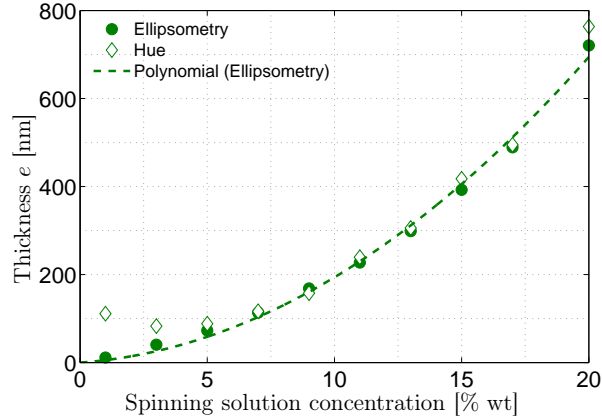


Figure 3.22: Ellipsometry versus Hue measurement - Thickness of spin-coated samples of maltodextrin DE6 measured by ellipsometry or hue determination. The method based on colors deviates under a thickness of 50 nm.

The comparison between the color determination of the thickness and the ellipsometry measurement is presented in Fig. 3.22 for maltodextrin DE6. We have a good agreement between both values. Nevertheless, below 50 nm the color method overestimates the thickness. The thin layer, which is brown around 50 nm, becomes transparent if the thickness decreases leading to a reflection of the light source onto the Si wafer. With maltodextrin DE29, the same observation was made.

The upper limit of the color analysis was found around 550 nm. Despite color is intense enough between 550 nm and 1200 nm to visually guess a thickness using a color scale, the precise measurement using color analysis shows its limits in this range. The error on the thickness measurement becomes non negligible. We can highlight this upper limit with a swelling experiment. We initially prepare maltodextrin DE29 layers of different thicknesses. These layers are equilibrated at $a_w = 0.008$. Color analysis is performed on each layer for various values of a_w . We represent the evolution of the colors with humidity variation in Fig. 3.23. Then, we plot in Fig. 3.24 the measured thickness for each sample and each humidity versus the expected thickness obtained considering $\phi = f(a_w)$ and ellipsometry measurements as a reference.

We can notice in Fig. 3.24 that the color analysis fails above $e = 600$ nm and that the points corresponding to large a_w may give a slight underestimated measured thickness in the range [50 nm-600 nm]. Different sources of error can be involved:

- The sensitivity of camera sensors is unknown at wavelengths larger than 700 nm which can lead to large errors on $H(e)$ for large thicknesses.

3. MATERIALS & METHODS

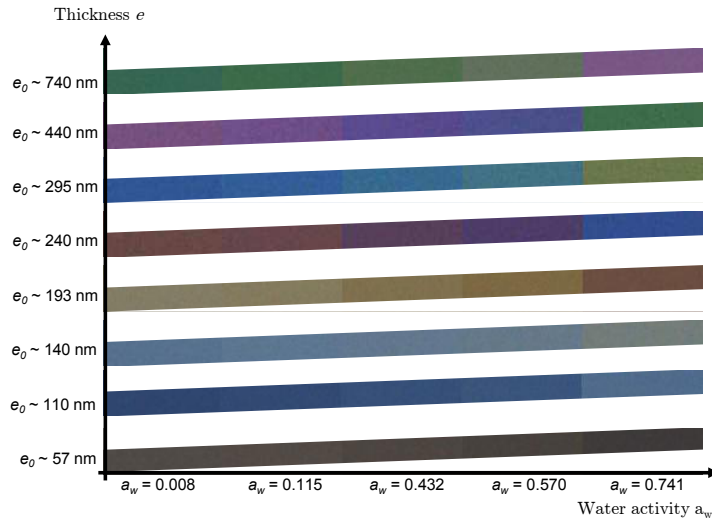


Figure 3.23: Color evolution with thickness and humidity - Equilibration of different layers of maltodextrin DE29 at various water activities. Effect of the thickness and humidity on the sample color.

- The refractive index is probably not linear with ϕ . Linearity is valid at large ϕ but the measured increment does not correspond to the dry refractive index measured by ellipsometry.
- The assumption of volume additivity between water and the hydro-soluble polymer may not be valid for large water contents.

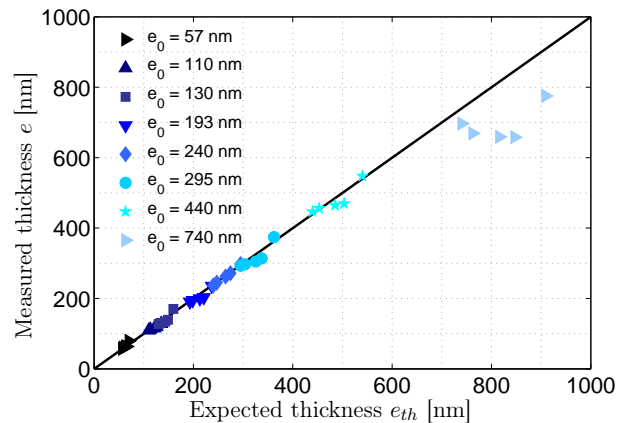


Figure 3.24: Validation of the color analysis - Equilibration of different layers of maltodextrin DE29 at various water activities. Comparison between the thickness measurement using the color analysis and the expected one obtained with the sorption isotherm.

3.3.4.3 Swelling and water content

In the theory presented above, we have considered a constant refractive index n for the color analysis. Nevertheless, as the polymers swells, the refractive index decreases. The calculation of the thickness using the comparison between experimental and theoretical hues is still possible by doing some approximations.

The easiest approximation is that the index of the solution n is the average of the index of water n_{water} and maltodextrin n_{solid} (Eq. 3.16). The initial layer thickness e^0 is considered to be the sum of an equivalent thickness of water e_{water}^0 and of solid e_{solid}^0 such ϕ_0 , the initial volume water content, is given by Eq. 3.17. During swelling, the thickness increases of Δe such as $(n.e) = (n.e)^0 + n_{water}\Delta e$. Thus, we are able to calculate the thickness e and the water content ϕ for any variation in time of the water content.

$$(n.e)^0 = n_{solid}.e_{solid}^0 + n_{water}.e_{water}^0 \quad (3.16)$$

$$\phi^0 = \frac{e_{water}^0}{e_{solid}^0 + e_{water}^0} = \frac{e_{water}^0}{e^0} \quad (3.17)$$

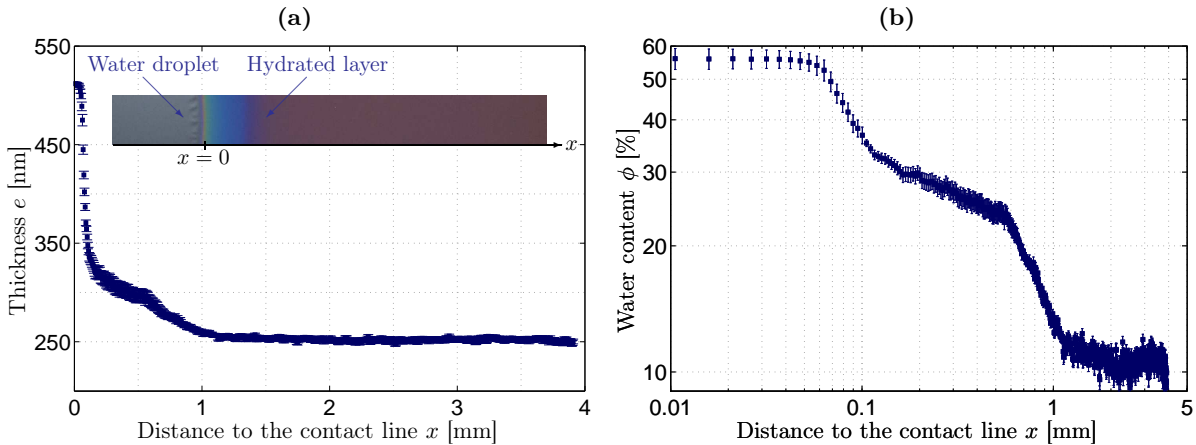


Figure 3.25: Color analysis on a hydrated maltodextrin thin layer - Determination of the swelling profile close to the contact line for a water droplet deposited onto a 250 nm-thick layer of maltodextrin DE29. The contact line speed is equal to 0.05 mm/s and the water activity is 0.43. (a) Thickness calculation using the theory of interferences with error bars. (b) Water content calculated using the thickness profile.

For instance, let's have a look at a color picture obtained with maltodextrin DE29 at the contact line speed $U = 0.05$ mm/s for and a water activity of 0.43. All the color analysis were performed on Matlab using a code that calculates the mean hue on 7 pixels taken on the azimuthal direction in order to reduce the noise. In the given example (Fig. 3.25a), we obtain a

3. MATERIALS & METHODS

thickness $e \sim 250$ nm. With $\phi_0 \sim 10$ %, we get $e_{solid}^0 \sim 225$ nm and $e_{water}^0 \sim 25$ nm. The error on thickness measurement is calculated using the differentiation of the previous equations and an estimation of the error on the hue using the initial picture without water droplet. Fig. 3.25b shows the evolution of the water content ϕ with the distance to the contact line x , including the error bars.

In conclusion, color analysis provides an accurate measurement of the thickness in the range [50 nm - 600 nm]. Assuming a simple law for the average refractive index of the swollen layer, those thickness measurements provide a good estimation of the water content of the layer.

3.4 Conclusions

Key messages

- The main physical parameters are known for the considered carbohydrates: the diffusion coefficient $D_p(\phi)$, the sorption isotherm $a_w(\phi)$, the viscosity $\eta(\phi)$, the dissolution speed $v_d(\phi, U)$...
- We have an experimental set-up that allows us to obtain the contact angle θ and the contact line velocity U over 6 decades during water spreading onto the polymer thin layers.
- We can measure the water content ϕ of the thin layers using color analysis.

4

Wetting regimes

4.1 Introduction

In this chapter, we will study the spreading of a water droplet on a water-soluble carbohydrate layer. As mentioned earlier, water is transferred to the layer by an evaporation/condensation process, as well as by direct diffusion from the droplet. We will start by showing the limits of Tay *et al.* theory and the necessity to consider water diffusion in the horizontal direction. We will evidence the characteristic lengths at stake and validate our approach using FEM simulations. Then, we will establish a new thickness vs velocity diagram. We will show that the horizontal diffusion in the layer is important because it modifies the wetting regimes, we will demonstrate that the scaling in eU remains nevertheless valid in the thin film regime. The wetting diagram will be confronted to the experimental data in order to validate it.

4.2 Preliminary observations

4.2.1 The failure of hydrodynamics theories

We start this study with the effect of the contact line velocity on contact angle. We consider a 250 nm-thick layer of maltodextrin DE29 equilibrated at $a_w = 0.58$. We measure the contact angle using the free-spreading experiment and the pulled substrate experiment. The results of these measurements are presented in Fig. 4.1 where we plot the contact angle θ versus the contact line velocity U . The full red circles have been obtained from only one experiment of free spreading. In that case, θ and U decrease with time leading to an increasing $\theta(U)$. The hollow red circles originate from several pulled substrate experiments. We can notice that we are able to reach large values of θ with $\theta \sim 110^\circ$ for velocities close to 10^3 mm.s⁻¹. The hydro-soluble coating behaves as a hydrophobic material at large U .

The wetting dynamics illustrated in Fig. 4.1 highlights a strong increase of the contact angle θ with contact line velocity U . Hydrodynamic theories such as Cox-Voinov law (Eq. 2.2) predict an important increase of θ when the capillary number $\frac{\eta U}{\gamma}$ becomes larger than 1. In our experimental conditions, it corresponds to velocities larger than 10 m.s⁻¹. We represent

4. WETTING REGIMES

hydrodynamic curves with black lines on Fig. 4.1 for different equilibrium contact angle θ_E . In our experiments, a significant increase of θ is observed for velocities larger than 10^{-2} mm.s $^{-1}$. Clearly, that increase cannot be described by a Cox-Voinov law.

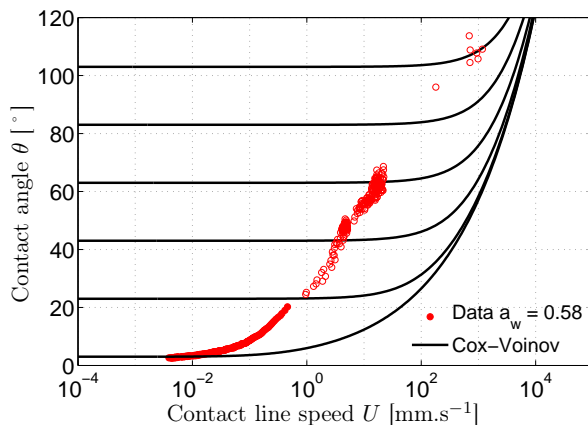


Figure 4.1: Contact angle measurement and hydrodynamics theory - Contact angle measurement versus contact line speed during water spreading onto a 250 nm-thick layer of maltodextrin DE29 equilibrated at $a_w = 0.58$ (Full circles: free spreading, hollow circles: Pulled substrate experiment). Comparison with Cox-Voinov theory plotted for different equilibrium contact angles ($\eta=0.87$ mPa.s).

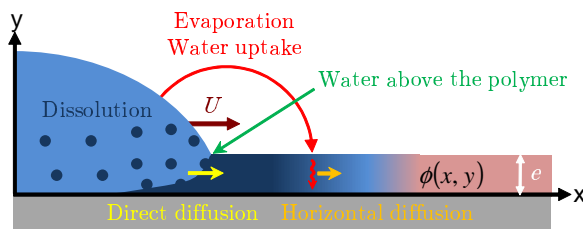


Figure 4.2: Wetting of a soluble layer of maltodextrin - Recall of the mass transfers at stake during spreading onto a soluble surface. Water is advancing on the top of the polymer layer.

As mentioned earlier in the materials and methods chapter, our experiments demonstrate hydration of the coating ahead the contact line during the spreading of water onto maltodextrins. Different hues appear in the coating that result from its swelling. Hydration is a key phenomenon to explain the wetting dynamics. Two hypotheses can be made: (i) the coating swells with water or (ii) water penetrates between the layer and the silicon substrate. In the latter case, the polymer would be peeled off the substrate and the moving contact line would actually connect the peeled polymer layer, the silicon wafer and water. Therefore, the dynamic contact angle should be affected by a change in the silicon wafer surface energy. To check this hypothesis, we used the modified substrates where a layer of polystyrene covers the silicon substrate, thus modifying the substrate energy. The result of this measurement was shown in Fig. 3.17b where we clearly find that the different substrates do not have any effect on the contact angle. We conclude here that

the polymer layer is not peeled off the substrate. This proves that the water is advancing on the top of the polymer layer as illustrated in Fig. 4.2, where we recall the transfers at stake in the problem, and that the hypothesis that the contact angle θ is a function of the water content in the layer ϕ is likely to be correct. Thus we can discuss the different mass transfers that will lead to the hydration of the coating.

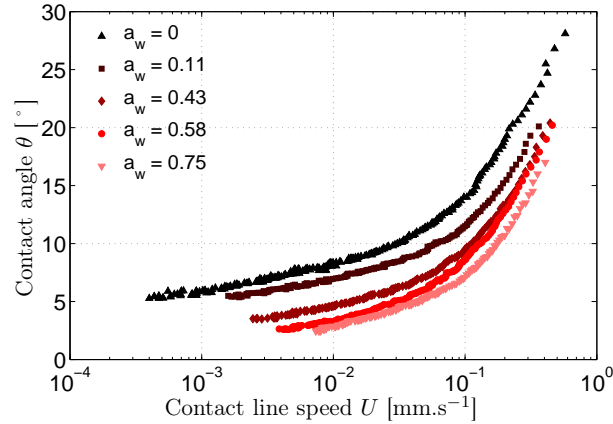


Figure 4.3: Contact angle measurement and water activity - Contact angle measurement versus contact line speed during water spreading onto a 250 nm-thick layer of maltodextrin DE29 equilibrated at five different water activities.

Tay *et al.* showed that the main process influencing contact angle variation with contact line velocity is evaporation/water uptake (see section 2.1.4). The solvent - water in our case - evaporates from the drop and diffuses through gas phase ahead the contact line. It condensates into the polymer and modifies its water content. Spreading dynamics is influenced by the evolution of this water content. The smaller the contact line velocity U , the more water absorbed which results in a decrease of the contact angle θ , as observed in Fig. 4.1. Fig. 4.3 shows how the humidity of the surrounding atmosphere modifies spreading dynamics. The maltodextrin 250 nm-thick layers are initially equilibrated at five different water activities a_w . The larger the water activity a_w , the smaller the contact angle θ . Thus, this indicates again the importance of the hydration on the contact angle value.

4.2.2 Discrepancy with the Tay *et al.* wetting diagram

We presented in section 2.1.4 how Tay *et al.* predicted the existence of three wetting regimes in a thickness vs velocity diagram. Their study introduces a characteristic length x_C such that a vertical gradient of water content is observed ahead from the contact line for $x < x_C$. When x_C is smaller than the nanometric cut-off ε , it corresponds to the thin film regime. In this regime, they predict a water content ϕ at the contact line that depends on the quantity eU . When x_C is larger than ε , it corresponds to the thick film regime where ϕ only depends on U . When the layer is dry at large U , they define a dry regime.

4. WETTING REGIMES

The frontier between thin film regime and thick film regime was demonstrated to depend on the diffusion coefficient of water in maltodextrin DE29 D_p . The NMR data and their transformation in a mutual diffusion coefficient yield D_p of the order of $10^{-11} \text{ m}^2.\text{s}^{-1}$ for intermediate water contents (see section 3.1.2.5). Fig. 4.4a represents the wetting diagram for this diffusion coefficient. We indicate the range of thickness and velocity we can reach using the free-spreading experiment or the pulled substrate one by color domains. Thus, we should be able to distinguish thin and thick film regime. We expect a scaling of θ in eU in the thin film regime. Fig. 4.4b represents the iso-contact angles in the wetting diagram. The scaling in eU in the thin film regimes involves iso θ curves with an exponent -1 in the diagram. In the thick film regime, the contact angle no longer depends on the thickness e but only on the velocity U . In the dry regime, a constant θ is expected.

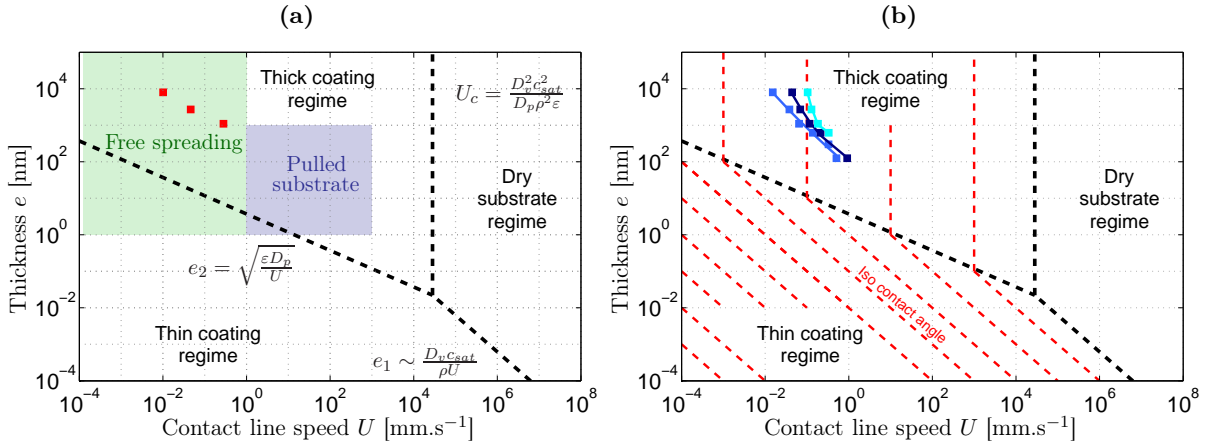


Figure 4.4: Wetting diagram according to Tay et al. - Wetting diagram built with the following parameters: $D_p = 1.4 \cdot 10^{-11} \text{ m}^2.\text{s}^{-1}$, $D_v = 2.7 \cdot 10^{-5} \text{ m}^2.\text{s}^{-1}$, $\rho = 997.05 \cdot 10^3 \text{ g.m}^{-3}$, $c_{sat} = 23 \text{ g.m}^{-3}$, $\varepsilon = 1 \text{ nm}$, $L = 5 \text{ mm}$. (a) Frontier equations and experimental domains (b) Theoretical iso contact angle lines, some experimental points are represented in blue ($\theta = 15^\circ$, 20° and 25° for maltodextrin DE29)

We will show in section 4.4.3 that the scaling in eU works very well for small values of eU . Nevertheless, the frontier between thin coating regime and thick coating regime was found to be much higher in the experimental diagram than in the one above. We represent three experimental points with red squares in Fig. 4.4a. They correspond to the experimental frontier between regions where a scaling in eU is respectively observed and non-observed. The experimental frontier is shifted toward larger thicknesses by about 2 orders of magnitudes. Similarly, some experimental iso-contact angle points are represented in blue in Fig. 4.4b for maltodextrin DE29 ($\theta = 15^\circ$, 20° and 25°). The experimental iso- θ do not correspond to Tay *et al.* theory represented by red dotted lines. Thus, it is likely that an additional mechanism has to be considered to explain this larger thin film regime. The role of the water diffusion within the layer and in the horizontal direction has to be studied. With the help of Finite Element Method simulations, we are going to discuss about the effect of the horizontal diffusion within the film or direct diffusion from the

water droplet. Furthermore, we have found that for larger eU , in the thick film regime according to Tay *et al.*, the contact angle still shows a dependence on the coating thickness e . This effect was not predicted in their theory and we will have to introduce a new regime.

NB: In all the wetting diagrams presented in this manuscript, the considered experimental thickness e is always the initial thickness of the coating and not the one of the once swollen layer. At most, the latter is twice the initial thickness for small values of eU .

4.3 The role of diffusion: FEM simulations

We present in this section the results of Finite Elements Method simulations in 2D, *i.e.* that we will represent the polymer layer and the water droplet with a sectional view and do not consider the cylindrical geometry of the system (the curvature of the contact line is small enough to make this approximation). We use this tool in order to go beyond the limits of the theoretical approach. Indeed, Tay *et al.* theory only considers evaporation/water uptake process. They predict the water content ϕ in the case of thin layers where horizontal diffusion is not allowed. Finite Elements Methods allows us to introduce a new transfer: diffusion within the film and from the droplet to the layer. We thus allow horizontal diffusion everywhere in the layer. Furthermore, we can easily modify the boundary conditions and study their effect on the 2D-water content $\phi(x, y)$ (x being the axis in the horizontal direction and y in the vertical direction). The software COMSOL is used to perform the simulations.

We use a step-by-step approach where we progressively introduce complexity in the system and try to evidence the characteristic lengths at stake in the hydration processes. In particular, our aim was to decouple the effects of the different sources of non-linearity in the problem, namely:

- The relation between the water activity in air a_w and the water content in the layer ϕ . Simulations with $a_w = \phi$ and $a_w \neq \phi$ were performed.
- The strong dependence of the water diffusion coefficient in the layer D_p with its water content ϕ . Simulations with D_p constant and $D_p = f(\phi)$ were performed.

The geometry and the boundary conditions used for the simulations are represented in 4.5. The droplet is simulated using a edge of water having an angle $\theta = 25^\circ$ with the layer. We use two diffusion equations in order to describe water diffusion (Eq. 4.1 and 4.2), with c the concentration of water in air (the maximal concentration is c_{sat}) and ϕ the water content in the polymer (ϕ cannot exceed 100%). D_v is the diffusion coefficient of water in air and D_p in the polymer. In addition, a motion at a speed U of the coating and air domains is introduced.

$$\frac{\partial c}{\partial t} = D_v \left(\frac{\partial^2 c}{\partial x^2} + \frac{\partial^2 c}{\partial y^2} \right), \quad 0 \leq x \leq L, \quad e \leq y \leq L, \quad t \geq 0 \quad (4.1)$$

$$\frac{\partial \phi}{\partial t} = D_p \left(\frac{\partial^2 \phi}{\partial x^2} + \frac{\partial^2 \phi}{\partial y^2} \right), \quad 0 \leq x \leq L, \quad 0 \leq y \leq e, \quad t \geq 0 \quad (4.2)$$

4. WETTING REGIMES

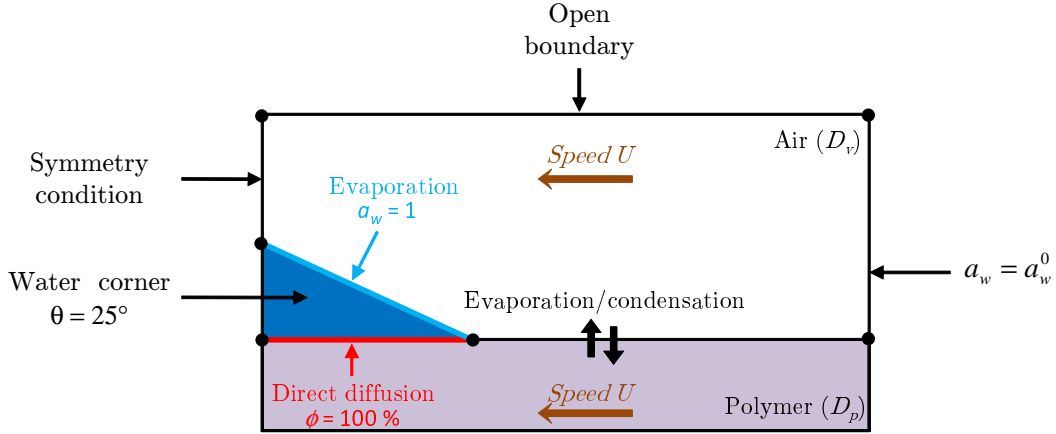


Figure 4.5: Schematic representation of COMSOL geometry and boundary conditions
- The box has a dimension $L \times L$ with $L = 5$ mm. The water edge has a length $R = 0.1$ mm. Two domains of diffusion are considered: air and polymer.

The boundary condition between air and maltodextrin is set using a flux condition. The flux J is set to be proportional to the difference of water activity between air and the solid with α the constant of proportionality (Eq. 4.3). We chose to use $\alpha = 100 \text{ mol.m}^{-2}.\text{s}^{-1}$. We have checked that the value of α does not change the final result of the simulation but it has to be large enough otherwise the simulation time is too long. A larger value of α leads to an endless simulation.

$$J = \alpha \left(a_w^{polymer} - a_w^{air} \right) \quad (4.3)$$

The mesh size is chosen very small close to the contact line, and coarser far from the coating in the air. The units range from 2 nm to 100 μm . We make sure that decreasing the mesh size does not modify the results in order to validate our choice. The choice must be intermediate to have a good compromise between calculation time and accuracy of the result. The time-dependent simulation is performed until reaching an equilibrium state where $J_{air} \simeq J_{polymer}$.

In the following subsections, we will discuss the following points:

- The characteristic lengths at stake will be evidenced considering the simplest case, which corresponds to $a_w = \phi$ and D_p constant.
- We will consider the evaporation/condensation transfer and show how a vertical concentration gradient can appear ahead the contact line. The water content profiles obtained in the thin film regime will be compared to Tay *et al.* theory and the predicted characteristic lengths of diffusion will be validated.
- We will focus on the influence of water direct diffusion from the droplet. The influence of the Péclet number on the water content profiles ahead the contact line will be investigated.
- We will see how the direct diffusion process couples with the evaporation/condensation process.

- The scaling law in eU will be checked in the condensation/convection region and in the diffusion/condensation region.
- Finally, other sources of non-linearity will be introduced: the non-linear sorption isotherm $a_w(\phi)$ and the concentration-dependent diffusion coefficient $D_p(\phi)$.

4.3.1 Characteristic lengths

4.3.1.1 Thin films

We begin the discussion with some theoretical considerations. In this subsection, we consider that wetting occurs in the thin film regime, *i.e.* that x_C is very small and no vertical concentration gradient is observed ahead from the contact line. Tay *et al.* theory is based on the competition between evaporation/water uptake and motion at the velocity U . They do not take into account the diffusion along the horizontal direction that occurs in the coating. They make the assumption that the inward amount of water at a distance x quickly equilibrates in the layer along the vertical direction. Practically, water can also diffuse along the x -axis all the more that the diffusion coefficient is large. We derive a diffusion equation in order to describe this secondary process and consider an additional term to account for the inward condensation flux of water j_v in the coating in a 1D-approximation (Eq. 4.4). In the frame of the contact line that moves at the velocity U , it writes:

$$\frac{\partial \phi}{\partial t} = \frac{\partial}{\partial x} \left(D_p \frac{\partial \phi}{\partial x} \right) + U \frac{\partial \phi}{\partial x} + \frac{j_v}{e} \quad (4.4)$$

In order to discuss the characteristic lengths at stake in the problem, it is convenient to use the Fourier transform of Eq. 4.4. The Fourier transform will be indicated by the notation $\hat{\cdot}$. The Fourier transform of j_v can be expressed as a function of the water activity Fourier transform (see appendix B).

$$\hat{j}_v = \frac{c_{sat}}{\rho} D_v \hat{a}_w(q) \cdot q \frac{ch(q\Lambda)}{sh(q\Lambda)} \quad (4.5)$$

Λ is the distance above the layer where the water activity in the air is not modified by the droplet. Typically, Λ is of the order of a few millimetres. In stationary regime, with a constant diffusion coefficient and a linear sorption isotherm ($a_w = \phi$), we obtain Eq. 4.6;

$$0 = -q^2 D_p \hat{\phi}(q) + iqU \hat{\phi}(q) + \frac{c_{sat}}{\rho e} D_v \hat{\phi}(q) \cdot q \frac{ch(q\Lambda)}{sh(q\Lambda)} \quad (4.6)$$

We are interested in the concentration profile for distances to the contact line smaller than L which is millimetric. Thus, the term $q\Lambda$ is much smaller than 1 and $\frac{ch(q\Lambda)}{sh(q\Lambda)} \simeq 1$. We can rewrite Eq. 4.6 with an adimensional form using the Péclet number in the polymer $(Pe)_p = \frac{eU}{D_p}$. and the quantity related to the Péclet number in air $\Delta = \frac{\rho(Pe)_v}{c_{sat}} = \frac{\rho e U}{D_v c_{sat}}$.

4. WETTING REGIMES

$$0 = q\hat{\phi}(q) \left(-qe + i(Pe)_p + \frac{(Pe)_p}{\Delta} \right) \quad (4.7)$$

The first term corresponds to diffusion, the second to convection and the third to condensation. The ratio of the second and third terms only depends on Δ . Thus, for small q , there is no characteristic length scale when diffusion in the polymer is negligible. This case corresponds to the case described by Tay *et al.* who found that the water content in the polymer is given by $\phi(x) \sim \left(\frac{x}{L}\right)^k$ with k given by Eq. 2.10. As the exponent depends on the product eU , the water content is expected to scale with eU . For large q , diffusion can dominate depending on the value of Δ . New characteristic lengths can be found by comparing the different terms of Eq. 4.7:

- if $\Delta \ll 1$, the two dominant terms are diffusion and condensation. Convection is negligible. The characteristic length is $\kappa = \frac{e\Delta}{(Pe)_p}$. Diffusion/condensation dominates at $x < \kappa$ and condensation/convection at $x > \kappa$. κ depends on the thickness but not on the velocity. In the following, we will show that if $\Delta \ll 1$, $\phi(x)$ presents a plateau before decreasing.
- if $\Delta \gg 1$, the two dominant terms are diffusion and convection. Condensation is negligible. The characteristic length is $\lambda = \frac{e}{(Pe)_p} = \frac{D_p}{U}$. This length characterizes the exponential decrease of ϕ . The solution is $\phi \sim e^{-xU/D_p}$.

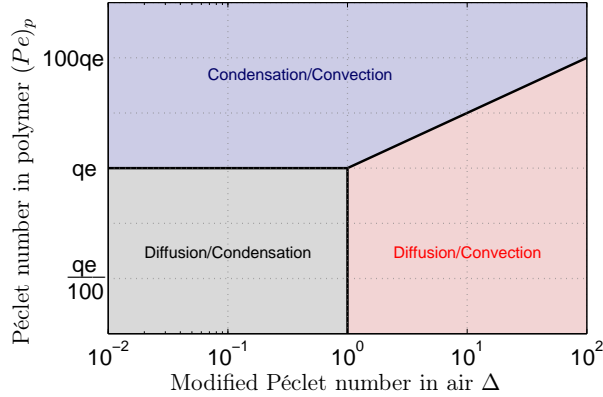


Figure 4.6: Mass transfers and Péclet numbers - 3 regions have been identified depending on the value of the modified Péclet number in air Δ and the Péclet number in the polymer $(Pe)_p$. Each region corresponds to two mass transfers among condensation, diffusion and convection.

We summarize the different regions that we have identified in a diagram $(Pe)_p$ - Δ (Fig. 4.6). The Condensation/Convection region corresponds to large values of $(Pe)_p$, the Diffusion/Condensation to small values of Condensation $(Pe)_p$ and Δ , and the Diffusion/Convection regions to small values of Condensation $(Pe)_p$ and large values of Δ .

4.3.1.2 Effect of vertical gradient

The previous calculation was based on the thin film regime approximation. For large thicknesses (or small D_p), vertical concentration gradient can exist in the layer ahead from the contact line. As shown by Tay *et al.*, the horizontal length over which that gradient exists is given by $x_C = \frac{Ue^2}{D_p}$. Thus, even if Δ is smaller than 1, if the characteristic length x_C becomes larger than κ , we expect κ not to be a characteristic length any more.

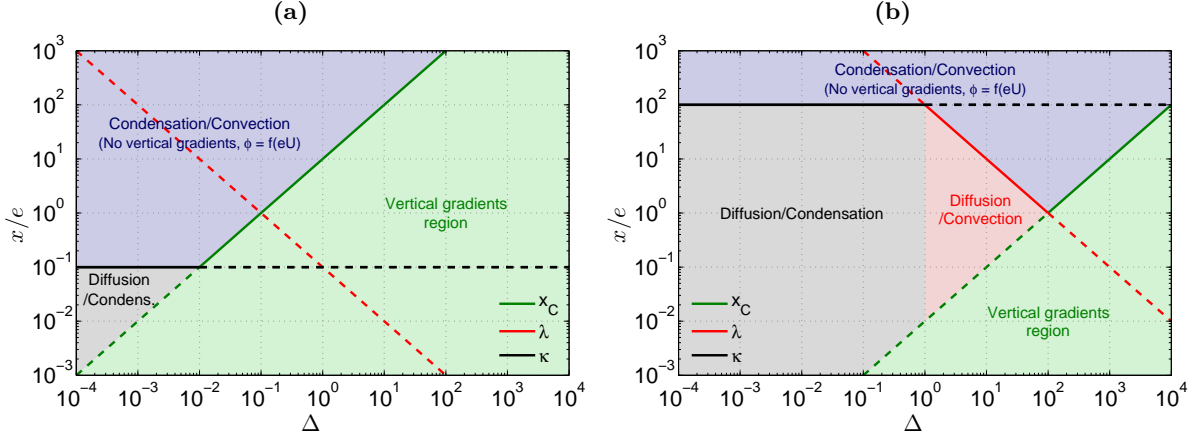


Figure 4.7: Normalized characteristic lengths of the condensation/diffusion equation - κ/e , λ/e and x_C/e versus Δ (a) Case with 3 domains: $\Delta/(Pe)_p = 10^{-1}$ (b) Case with 4 domains: $\Delta/(Pe)_p = 10^2$

For the sake of simplicity, we will present two typical situations in Fig. 4.7a and Fig. 4.7b. Fig. 4.7a presents the three different lengths at stake in the process for a ratio $\Delta/(Pe)_p$ of 10^{-1} : κ , the characteristic length of the diffusion plateau at small Δ , λ , the length of diffusion in the moving frame and x_C the characteristic distance at which vertical concentration gradient disappears. The lengths are normalized by the layer thickness and plotted versus Δ in order to obtain a diagram $x/e = f(\Delta)$ where x is the distance to the contact line. For Δ smaller than 1, κ is the characteristic length as long as there is no vertical gradient. Here x_C becomes larger than κ at $\Delta \sim 0.01$ so κ dominates for $\Delta < 0.01$ and x_C for $\Delta > 0.01$. We can define three regions in the diagram:

- Condensation/Convection region: At large x , above the full lines (blue domain).
- Diffusion/Condensation region: At small x when x_C is smaller than κ (gray domain).
- Vertical gradients region: At small x when x_C is larger than κ (green domain).

Fig. 4.7b corresponds to a larger diffusion coefficient in the layer, such as to obtain a ratio $\Delta/(Pe)_p$ of 100. The diagram is modified. A new region appears: the Diffusion/Convection one. κ is the characteristic length only for $\Delta < 1$. Then we have a regime where λ is larger than x_C for $\Delta \in [1-100]$. κ does no longer dominate since Δ is larger than 1. Above $\Delta = 100$, x_C becomes predominant. The four regions that appear from this higher ratio $\Delta/(Pe)_v$ are:

4. WETTING REGIMES

- Condensation/Convection region: At large x , above the full lines (blue domain).
- Diffusion/Condensation region: At small x and for $\Delta < 1$ (gray domain).
- Diffusion/Convection: At small x for $\Delta > 1$ and when x_C is smaller than λ (red domain).
- Vertical gradients region: At small x when x_C is larger than λ (green domain).

We will see in the next section how these considerations on the relevant length scales (summarized in Table 4.1) can be related to the water content gradients of the problem.

Table 4.1: Characteristic lengths at stake in the wetting problem.

Length	Expression	Region
κ	$\frac{e\Delta}{(Pe)_p}$	Diffusion/Condensation
λ	$\frac{D_p}{U}$	Diffusion/Convection
x_C	$\frac{Ue^2}{D_p}$	Vertical Gradients

4.3.2 Evaporation/water uptake (no direct diffusion)

4.3.2.1 Thin and thick layers: simulations vs. theory

In this section, we aim at evidencing the characteristic length x_C below which vertical gradients are expected using FEM simulations. As in the theoretical section, we do not consider the direct diffusion process. Thus, let us replace the boundary condition below the droplet $\phi = 100\%$ by a zero-flux condition (Fig. 4.8). Water can only come into the layer from the air by condensation and then diffuse vertically and horizontally. As previously, a simple linear sorption isotherm is chosen ($a_w = \phi$). Finally, we use the initial water activity $a_w = 0$.

We chose the parameters in order to reach two very different values of the length x_C . In a first simulation, we set the contact line speed to $U = 1 \text{ mm.s}^{-1}$ and the diffusion coefficient to $D_p = 10^{-11} \text{ m}^2.\text{s}^{-1}$. With $e = 1 \text{ }\mu\text{m}$, we obtain a large x_C : $100 \text{ }\mu\text{m}$. In a second simulation, we use $U = 0.01 \text{ mm.s}^{-1}$ and $D_p = 10^{-9} \text{ m}^2.\text{s}^{-1}$. It leads to $x_C = 0.01 \text{ }\mu\text{m}$. Then, we extract the water content ϕ in the coating and especially the one at the surface and at the bottom of the layer ($y = e$ and $y = 0$). According to Tay *et al.* theory, we expect to observe a vertical concentration gradient from the contact line to the distance $x_C = \frac{e^2 U}{D_p}$.

Simulation results are in agreement with our arguments concerning the presence of a vertical concentration gradient in the layer. Fig. 4.9a and 4.9b show the results of the simulation for the two different cases. We plot the resulting water content profiles at the top of the coating (black) and at its bottom (blue). On Fig. 4.9a, the length x_C is large enough to be clearly visible. There is a difference of water content between the top border and bottom one for $x < x_C$ demonstrating the presence of gradients. Other simulations confirmed the very good

agreement with theory concerning the value of x_C . On Fig. 4.9b, both borders have the same profile in the considered range of x . In that case, x_C is too small to be observed in the simulation.

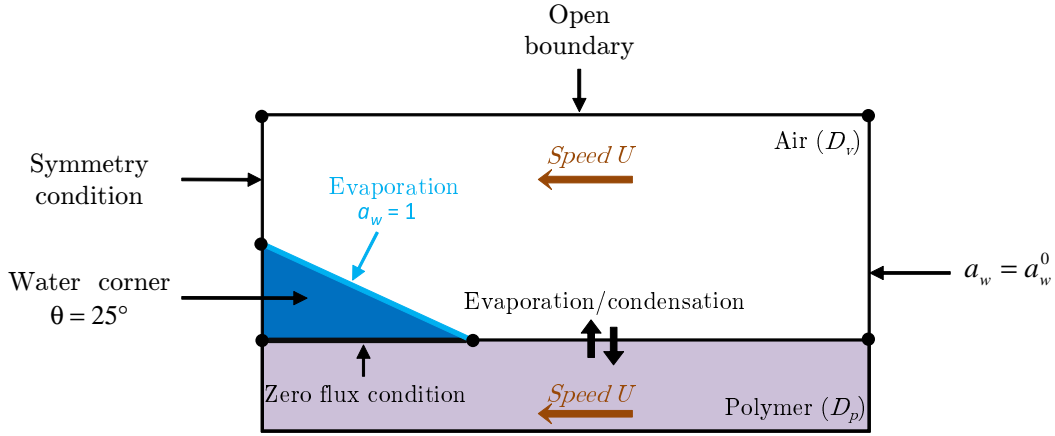


Figure 4.8: Schematic representation of COMSOL geometry and boundary conditions in the case of condensation only - The box has a dimension $L \times L$ with $L = 5$ mm. The water edge has a length $R = 0.1$ mm. Two domains of diffusion are considered: air and polymer. A zero flux condition replaces the direct diffusion condition.

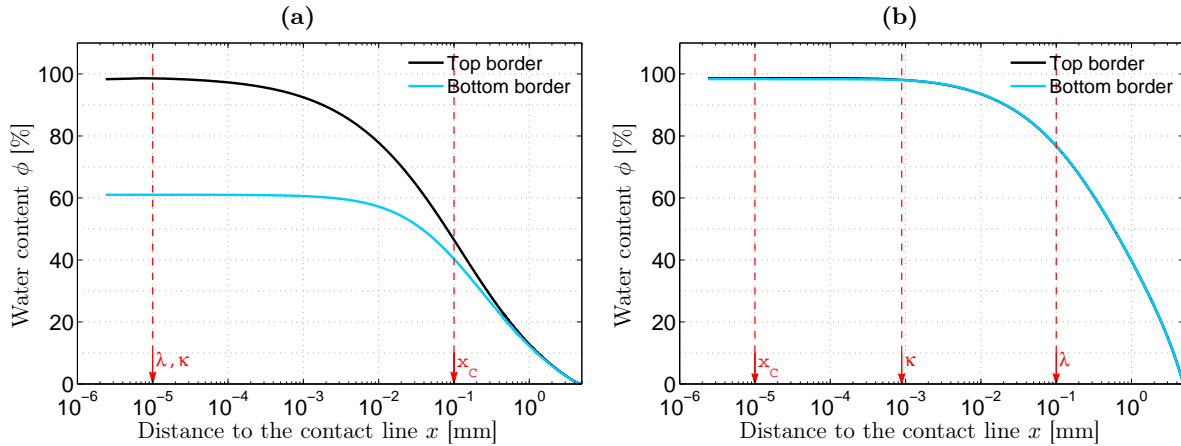


Figure 4.9: COMSOL simulation of evaporation/water uptake mass transfer - Water content profiles for a $1 \mu\text{m}$ -thick layer having a constant diffusion coefficient and a linear sorption isotherm ($a_w = \phi$). Top and bottom borders of the coating are represented. (a) $U = 1 \text{ mm}\cdot\text{s}^{-1}$ and $D_p = 10^{-11} \text{ m}^2\cdot\text{s}^{-1}$. (b) $U = 0.01 \text{ mm}\cdot\text{s}^{-1}$ and $D_p = 10^{-9} \text{ m}^2\cdot\text{s}^{-1}$.

In the two following figures, we plot the corresponding 2D-representations of the previous water content profiles. Fig. 4.10a highlights the shape of the gradients at small distances while in Fig. 4.10b, no gradients are observed. Fig. 4.10b corresponds to the thin film regime *i.e.*

4. WETTING REGIMES

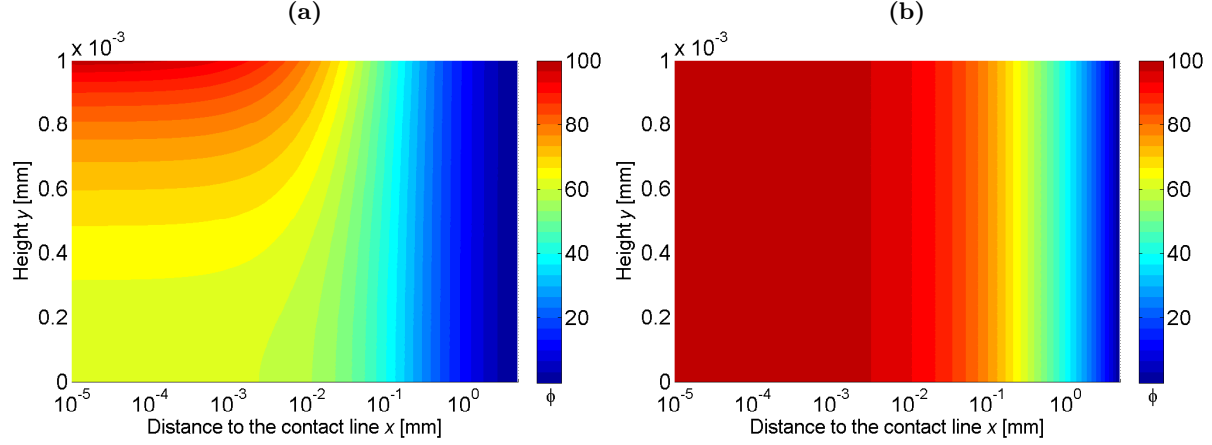


Figure 4.10: Schematic 2D view of water content calculated by simulation - Water content obtained in the case of evaporation/water uptake only. The layer thickness is $1 \mu\text{m}$ and the sorption isotherm of the coating is $a_w = \phi$. (a) $U = 1 \text{ mm.s}^{-1}$ and $D_p = 10^{-11} \text{ m}^2.\text{s}^{-1}$. (b) $U = 0.01 \text{ mm.s}^{-1}$ and $D_p = 10^{-9} \text{ m}^2.\text{s}^{-1}$.

$\phi(x, y) = \phi(x)$. The simulations are therefore in qualitative agreement with the theoretical findings of Tay *et al.* We will show in the following that the agreement is also quantitative.

4.3.2.2 Water content profiles in the thin film regime

Tay *et al.* predicted that in the thin film regime, the polymer content $\phi_p(x) = 1 - \phi(x)$ can be written as a power law: $\log(\phi_p) \sim k \log(x)$. They gave an expression for the exponent k (Eq. 4.8) as a function of different parameters: the contact angle θ , the diffusion coefficient of water in air D_v , the density of water ρ , the saturated concentration of water in air c_{sat} , the contact line speed U , the coating thickness e and the variation of the water activity with the water content $\frac{\partial a}{\partial \phi}$, following:

$$k = \frac{1}{\pi - \theta} \arctan \left(\frac{D_v c_{sat}}{\rho U e} \frac{\partial a}{\partial \phi} \right) \quad (4.8)$$

We plot in Fig. 4.11a the polymer content profiles obtained at $e = 500 \text{ nm}$ for a diffusion coefficient $D_p = 10^{-11} \text{ m}^2.\text{s}^{-1}$. By increasing the speed, we vary the value of x_C from $x_C^{min} = 50 \text{ nm}$ to $x_C^{max} = 50 \mu\text{m}$. Thus the condensation/convection region is reduced at high speed while the vertical gradients region becomes larger. Firstly, we observe the effect of the speed on the profile. The faster the contact line the drier the coating. Then, we observe that at intermediate distances from the contact line, the curve can be fitted with a power law (with an exponent k) over more than two decades in x . This is not true when we are too close to the borders in $x = 0$ or $x = L$. We extract the value of k from simulation in the intermediate region and represent its comparison with theory in Fig. 4.12a. We used $\theta = 25^\circ$, $c_{sat} = 25 \text{ g.m}^{-3}$, $D_v = 4.5 \cdot 10^{-5} \text{ m}^2.\text{s}^{-1}$ and $\rho = 10^6 \text{ g.m}^{-3}$. At small velocities, the agreement between both values of k is good.

When x_C becomes too large (at large U), the theoretical value of k no longer corresponds to the one obtained by simulation. The gradients of concentration modify the value of ϕ at the surface of the coating.

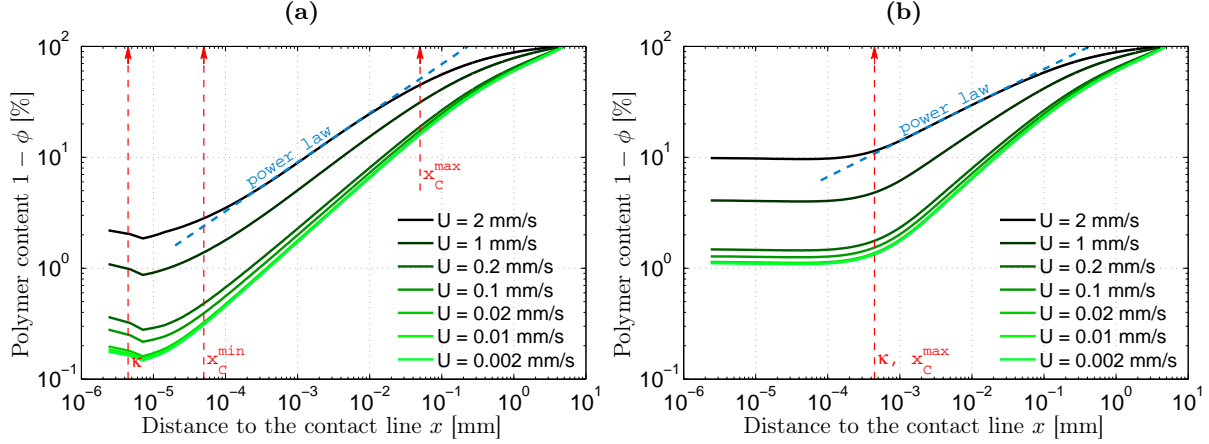


Figure 4.11: Influence of speed and diffusion coefficient on evaporation/water uptake profiles obtained by simulation - Polymer content profiles for a 500 nm-thick layer having a constant diffusion coefficient and a linear sorption isotherm ($a_w = \phi$). Different contact line speeds are represented. (a) $D_p = 10^{-11} \text{ m}^2 \cdot \text{s}^{-1}$: vertical gradients region and condensation/convection region are highlighted. (b) $D_p = 10^{-9} \text{ m}^2 \cdot \text{s}^{-1}$: diffusion/condensation and condensation/convection regions are highlighted.

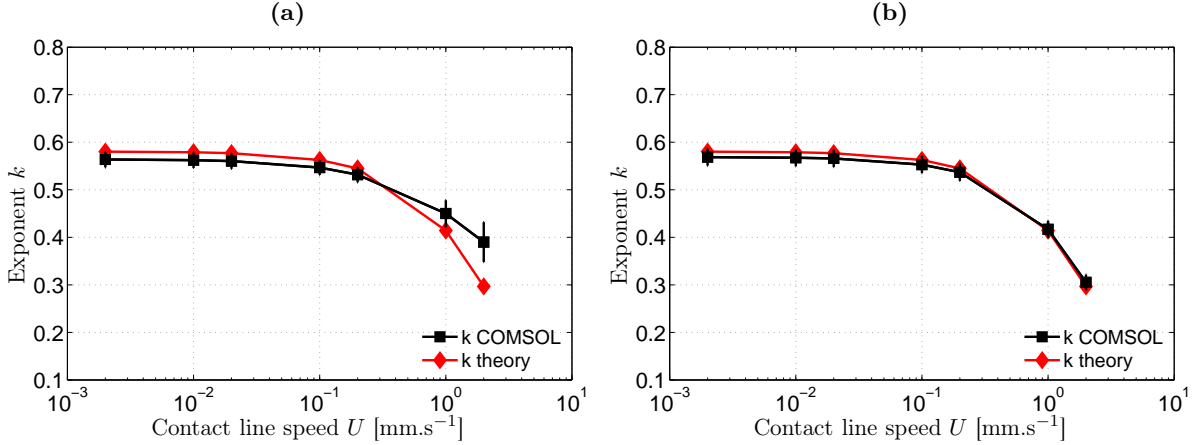


Figure 4.12: Exponent k : comparison between theory and simulation - Comparison between Tay et al. value of the exponent k and its calculation via polymer content profiles (at $e = 500 \text{ nm}$). (a) $D_p = 10^{-11} \text{ m}^2$. (b) $D_p = 10^{-9} \text{ m}^2 \cdot \text{s}^{-1}$.

The same study is performed with a larger diffusion coefficient ($D_p = 10^{-9} \text{ m}^2 \cdot \text{s}^{-1}$) in Fig. 4.11b and Fig. 4.12b. In that case κ is larger than x_C and we observe a concentration plateau.

4. WETTING REGIMES

This plateau is set by the characteristic length κ which is of the order of the thickness e in the case considered here. Indeed, Δ is lower than 1 and x_C is smaller than κ , which leads to dominant diffusion/condensation process. It is a consequence of the horizontal diffusion in the coating at small distances from the contact line. When D_p becomes too large, water diffuses significantly along the horizontal direction, especially in the regions where the concentration of water strongly varies. We thus have two regions: diffusion/condensation region and condensation/convection region. The slope of the polymer content $1 - \phi$ is measured in the condensation/convection region. The agreement between theory and simulation is very good as shown in Fig. 4.12b. Thus, we validate Tay *et al.* theory in the condensation/convection region.

Finally, the comparison between top and bottom water content profiles highlight an interesting result which will be discussed in section 4.4.2.1. When $x_C \sim \kappa$, we do not have vertical concentration gradients in the diffusion/condensation region. Diffusion along the horizontal direction therefore results in the smoothing of vertical concentration gradients.

4.3.2.3 The characteristic length κ

Finally, in order to complete the validation of our theoretical arguments of evaporation/water uptake, we test the agreement between the predicted characteristic length $\kappa = \frac{e\Delta}{(Pe)_p}$ and the length of the plateau measured from the simulations. We denote that length ξ since we will show it can slightly differ from the length κ . We performed simulations using different diffusion coefficients D_p (range $[10^{-9} \text{ m}^2.\text{s}^{-1} - 10^{-5} \text{ m}^2.\text{s}^{-1}]$), velocities U (range $[0.001 \text{ mm}.\text{s}^{-1} - 100 \text{ mm}.\text{s}^{-1}]$) and thicknesses e (range $[100 \text{ nm} - 2 \text{ }\mu\text{m}]$). All the simulations are performed in the thin film regime, *i.e.* when x_C is smaller than or close to κ , in order not to be disturbed by vertical concentration gradient. We thus expect a region in which diffusion/condensation dominate at small distances from the contact line and a region in which condensation/convection dominate at large x .

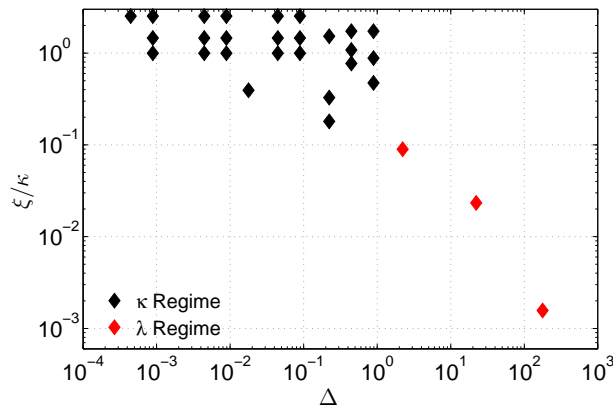


Figure 4.13: COMSOL simulations: validation of the characteristic lengths - Simulations of the evaporation/water uptake process for various D_p , U and e . Extraction of the plateau length ξ and comparison with κ value for different Δ .

We extract the values of the plateau length ξ and plot in Fig. 4.13 the ratio $\frac{\xi}{\kappa}$ as a function of the quantity $\Delta = \rho(Pe)_v/c_{sat}$. We observe that the ratio $\frac{\xi}{\kappa}$ remains in the range [0.2 - 3] when $\Delta < 1$. It is in good agreement with our theoretical arguments that predict a concentration plateau with a characteristic length κ at small contact line speeds. When Δ becomes larger than 1, the size of the observed plateau drops. Diffusion/convection processes then dominate and the characteristic length becomes λ . The concentration plateau disappears at larger Δ . x_C will end up being the characteristic length as shown in Fig. 4.7b.

In conclusion, we have shown with qualitative arguments that considering the diffusion along the horizontal axis introduces new characteristics lengths. In particular, for small Péclet numbers in air (*i.e.* small Δ), a concentration plateau is expected ahead from the contact line for $x < \kappa$ where diffusion and condensation dominate the convection. In our experiments, Δ ranges between 0.001 and 1 and x_C is of the order of κ in some situations which means we may be able to observe this plateau. Nevertheless, in the experiment, another diffusion process occurs. Water can diffuse directly from the water droplet to the coating. Before looking at the experimental data, we need to understand the role of this additional mass transfer.

4.3.3 Direct diffusion without condensation

Direct diffusion corresponds to the diffusion of water from the droplet to the coating. In the following simulations, we do not consider the exchange of matter between the layer and the air as presented in Fig. 4.14 in order to focus on the effect of direct diffusion alone. We thus keep the diffusion and the convection term in the transfer equation.

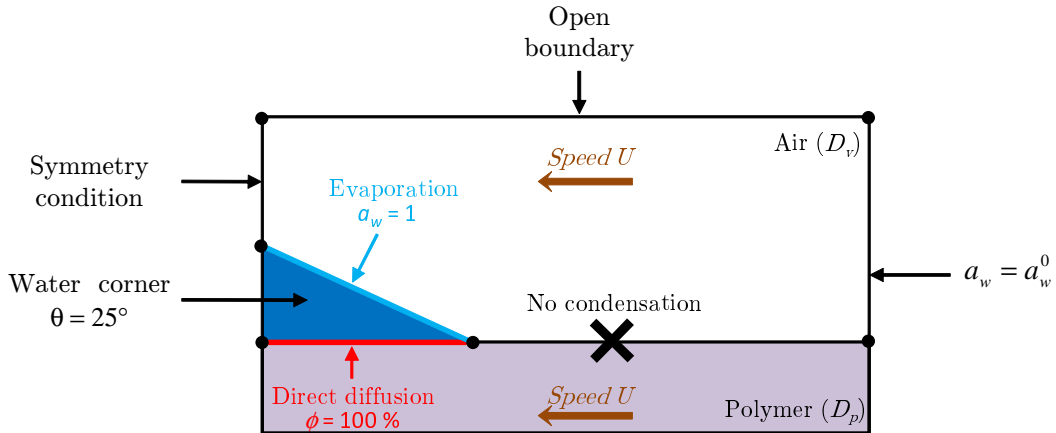


Figure 4.14: Schematic representation of COMSOL geometry and boundary conditions in the case of direct diffusion only - The box has a dimension $L \times L$ with $L = 5$ mm. The water edge has a length $R = 0.1$ mm. Two domains of diffusion are considered: air and polymer. The flux condition at the interface polymer/air is suppressed.

In a first analysis, we present the effect of the dimensionless Péclet number in the layer

4. WETTING REGIMES

$(Pe)_p = \frac{eU}{D_p}$ on direct diffusion. As explained in Fig. 4.14, the simulation of the direct diffusion process is performed by setting $\phi = 100\%$ at the border below the edge of water. When considering a motion at speed U , the diffusion equation in the coating can be rewritten such as:

$$\frac{\partial \phi}{\partial t} - U \frac{\partial \phi}{\partial x} = D_p \left(\frac{\partial^2 \phi}{\partial x^2} + \frac{\partial^2 \phi}{\partial y^2} \right) \quad (4.9)$$

Considering the changes of variable $x' = \frac{xU}{D_p}$ and $y' = \frac{yU}{D_p}$, and a stationary regime, we obtain:

$$0 = \left(\frac{\partial^2 \phi}{\partial x'^2} + \frac{\partial^2 \phi}{\partial y'^2} \right) + \frac{\partial \phi}{\partial x'} \quad (4.10)$$

This equation is solved with the following boundary conditions:

$$\begin{cases} \phi(x, y) = 1 & \text{for } x \leq 0 \text{ and } y = e \\ \nabla_y \phi(x, y) = 0 & \text{for } x > 0 \text{ and } y = e \\ \nabla_y \phi(x, y) = 0 & \text{for } y = 0 \end{cases} \quad (4.11)$$

We set the initial water content in the layer to $\phi = 0\%$. We vary the Péclet number in the coating $(Pe)_p$ and we extract the water content profiles in $y = e$ (top of the layer) and $y = 0$ (bottom of the layer). Then we plot both water contents as a function of the adimensional variable x' for different Péclet numbers (Top border in Fig. 4.15a and bottom border in Fig. 4.15b). $x' = 0$ corresponds to the contact line.

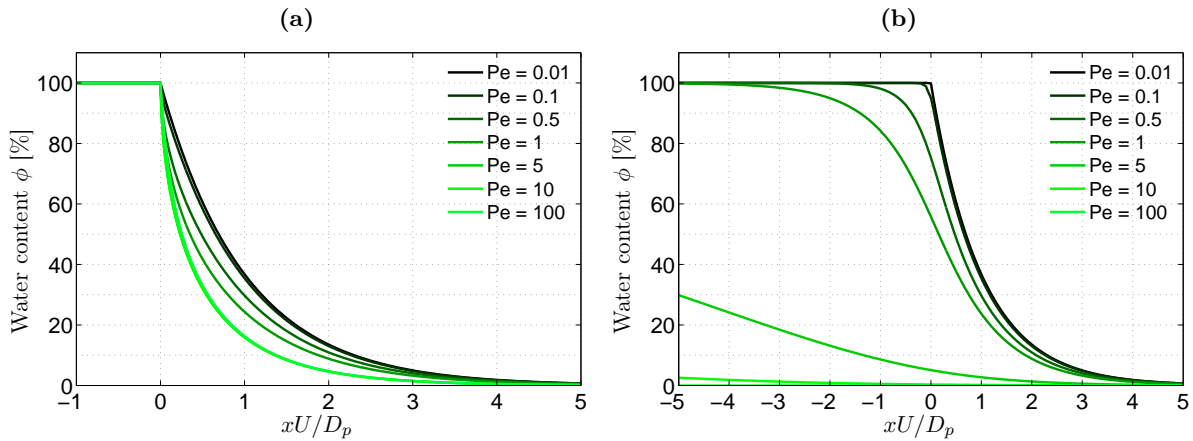


Figure 4.15: COMSOL simulations: influence of Péclet number on direct diffusion - Water content profiles versus the dimensionless distance $\frac{xU}{D_p}$ obtained by simulation of direct diffusion process at different Péclet numbers. The simulation is performed at $U = 0.01 \text{ mm.s}^{-1}$ and $D_p = 10^{-10} \text{ m}^2.\text{s}^{-1}$ for different thicknesses. (a) Top of the layer. (b) Bottom of the layer.

For small $(Pe)_p$, the top border profile corresponds to a classical 1D-diffusion process with an exponential decrease of $\phi \sim e^{-xU/D_p}$ (obtained by solving the diffusion equation without the term in y'). In that case, the bottom border profile is the same as the top one. At larger $(Pe)_p$, the profile decreases faster with x' and the bottom border starts to differ from the top border. At very large $(Pe)_p$, we reach a limit profile where the thickness is very large compared to the diffusion length. Thus the profile is not any more influenced by the bottom border. The bottom profile is equal to the initial water content. In this situation, the surface profile is an *arcsin* function (close to $1 - \sqrt{x'}$).

Let's now look at the direct diffusion profiles more precisely. We set the thickness e to 250 nm and the diffusion coefficient to $D_p = 10^{-9} \text{ m}^2 \cdot \text{s}^{-1}$. We vary the contact line speed U in order to modify the diffusion length $\lambda = \frac{D_p}{U}$. We plot the polymer content ahead the contact line in Fig. 4.16 for four different speeds. Firstly, we can check that the extent of the direct diffusion scales as λ . Secondly, it can be noticed that the profiles can be split up into three parts. At $x > D_p/U$, the curve does not fit with a power law. At $e < x < D_p/U$, the curve can be fitted with a power law with an exponent $k \sim 1$ (especially at small velocities). Then we observe a crossover in $x = e$. For $x < e$, the curve can be fitted with a power law with an exponent $k \sim 1/2$. The problem is similar to drying near the contact line. We have the same geometry with $\phi = 1$ for $x \leq 0$ and $\nabla\phi = 0$ for $x > 0$ and the air has an infinite "thickness" (2D problem). It leads to $\phi(x) \sim 1 - \sqrt{x}$. Thus, we have an exponent 1/2 at small x . For $x > e$, the substrate plays a role and the exponent $k \sim 1$ is the one corresponding to 1D free diffusion.

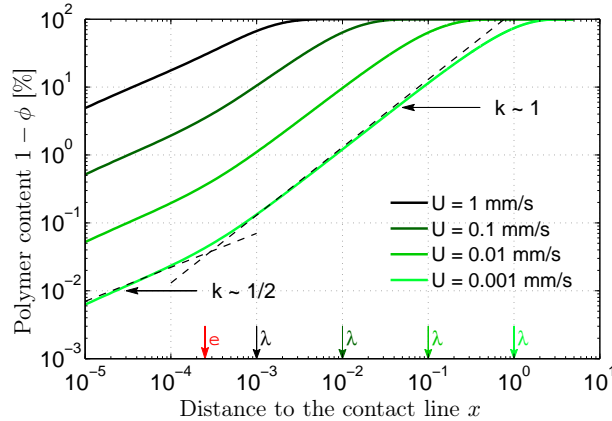


Figure 4.16: COMSOL simulations: direct diffusion profiles at different speeds - Polymer content as a function of the distance to the contact line x extracted from simulation of direct diffusion. Layer thickness e is 250 nm and diffusion coefficient $D_p = 10^{-9} \text{ m}^2 \cdot \text{s}^{-1}$. Four different values of the velocity are represented. The exponent of the power law is called k .

Finally, we can notice that the exponent 1/2 observed for $x < e$ in the case of direct diffusion only is close to the one observed in the condensation/convection region in the previous sections. Indeed, the values of k obtained in 4.3.2.2 range from 0.3 to 0.58. This property will be important in the section 4.3.5 dealing with the scaling in eU .

4.3.4 Condensation and direct diffusion

We have showed that the simulations considering evaporation/water uptake only, in the case of a linear sorption isotherm, are in good agreement with the theoretical arguments. In that section, we study the coupling of the evaporation/condensation and direct diffusion processes. We introduce the effect of direct diffusion in the FEM simulations, *i.e.* water diffusing from the droplet to the layer. Thus, we now consider the boundary condition $\phi = 100\%$ below the water edge as shown in Fig. 4.17. We will compare simulations with evaporation/water uptake only (Fig. 4.8), simulations with direct diffusion only (Fig. 4.14) and finally, simulations with both mass transfers.

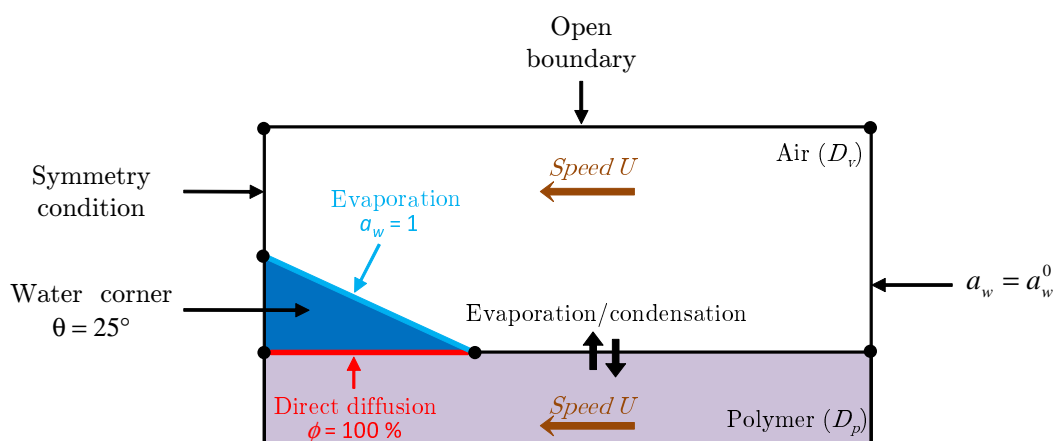


Figure 4.17: Schematic representation of COMSOL geometry and boundary conditions in the case where condensation and direct diffusion are considered - The box has a dimension $L \times L$ with $L = 5$ mm. The water edge has a length $R = 0.1$ mm. Two domains of diffusion are considered: air and polymer.

Fig. 4.18 presents the comparison between the three cases for $e = 250$ nm and $D_p = 10^{-9}$ $\text{m}^2 \cdot \text{s}^{-1}$ at two different speeds ($U = 10^{-3}$ $\text{mm} \cdot \text{s}^{-1}$ in Fig. 4.18a and $U = 1$ $\text{mm} \cdot \text{s}^{-1}$ in Fig. 4.18b). The first speed corresponds to $\lambda = 1$ mm and the second one to $\lambda = 1$ μm . The polymer content profiles in the case of direct diffusion only are plotted in red (we name it "Direct diffusion"). The polymer content profiles in the case of evaporation/water uptake only are plotted in blue (we name it "Evaporation/Condensation"). The simulation that takes into account both mass transfers is represented in black (we name it "Evap./Cond. + Direct diffusion"). For the comparison, we also add the "Evaporation/Condensation" profile obtained at $D_p = 10^{-11}$ $\text{m}^2 \cdot \text{s}^{-1}$ (dotted curve) and the characteristic lengths (obtained at $D_p = 10^{-9}$ $\text{m}^2 \cdot \text{s}^{-1}$).

The red curves correspond to the situation described in 4.3.3 with a crossover at $x = e$. The blue profiles evidences the two regions discussed in 4.3.1: a diffusion/condensation region at $x < \kappa$ and a condensation/convection region at $x > \kappa$. Let's now focus on the influence of the direct diffusion. In comparison to the blue profile, the black profile is only different at small

distances from the contact line, between $x = 0$ and $x \simeq 5\kappa$. The plateau disappears when direct diffusion is activated. The effect of the velocity on this modification is weak. The characteristic length λ that controls direct diffusion alone does not appear in the simulations but κ still seems to control the diffusion/condensation region. In this region, instead of having a plateau, a power law with an exponent close to 1/2 is observed, *i.e.* almost the same exponent as the one in the condensation/convection region. Direct diffusion brings more water and prevents horizontal diffusion to average the profile. At longer distances, even if the direct diffusion profile shows a higher water content than the Evaporation/Condensation profile (see in Fig. 4.18a), the black profile is similar to the blue one.

We can conclude that there is no additivity of condensation and direct diffusion. The total amount of water is almost unchanged when direct diffusion is added for both velocities. The differences of water content that stem from the additional direct diffusion are localised close to the contact line. The plateau of the diffusion/condensation region is replaced by a power law with an exponent 1/2.

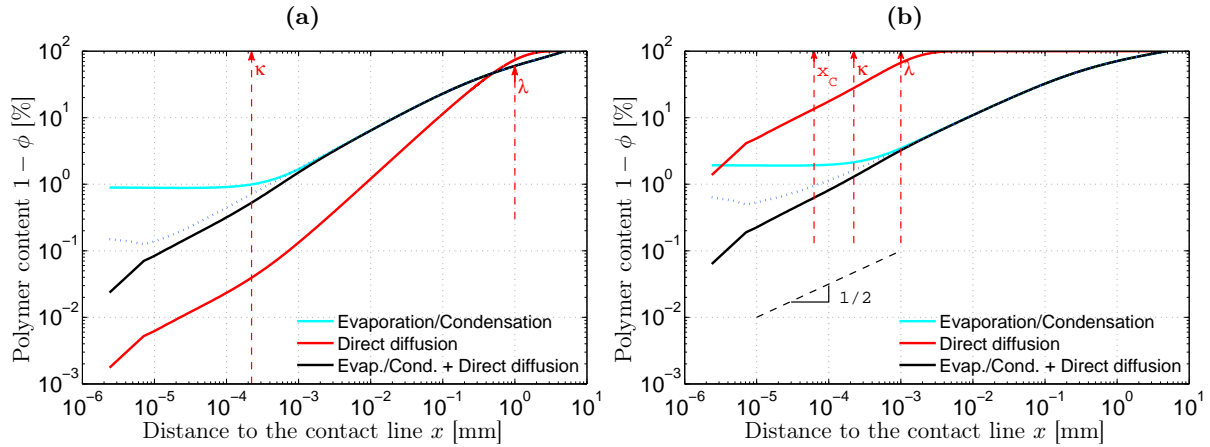


Figure 4.18: COMSOL simulations: influence of direct diffusion on evaporation/water uptake profiles - Polymer content profiles at the surface of a 250 nm-thick layer having a constant diffusion coefficient ($D_p = 10^{-9} \text{ m}^2.\text{s}^{-1}$) and a linear sorption isotherm ($a_w = \phi$). Dotted curves correspond to "Evaporation/Condensation" profile at $D_p = 10^{-11} \text{ m}^2.\text{s}^{-1}$. (a) $U = 0.001 \text{ mm.s}^{-1}$. (b) $U = 1 \text{ mm.s}^{-1}$.

4.3.5 Scaling $\phi(eU)$

Let's now discuss about the scaling $\phi = f(eU)$ expected in the thin film regime. As we have shown, the scaling is expected when evaporation/condensation is the only process at stake, however it should not stand any more when direct diffusion occurs. Indeed, the amount of water brought by direct diffusion alone does not depend on the thickness e but only on U . In the case of evaporation/condensation alone in the thin film regime, doubling the velocity or the thickness brings half water uptake and ϕ is a function of eU . We will firstly verify the scaling in the case

4. WETTING REGIMES

of evaporation/condensation only and secondly see the influence of direct diffusion on this scaling.

- Condensation/convection region:

We first look at the variations of ϕ with eU in the simulations of evaporation/condensation only. We extract the value of ϕ at the surface of the coating from simulations. We do this for simulations at different thicknesses e and velocities U . We look at the value of ϕ at a distance x to the contact line. We perform this study for a constant diffusion coefficient.

Fig. 4.19a shows the scaling $\phi = f(eU)$ at $D_p = 10^{-9} \text{ m}^2.\text{s}^{-1}$. It corresponds to a ratio $\Delta/(Pe)_p$ of $8.9 \cdot 10^{-1}$. The extraction is performed for two different distances from the contact line: $x = 1 \mu\text{m}$ (top points) and $x = 100 \mu\text{m}$ (bottom points). These distances are larger than the length κ (diffusion/condensation region) and the length x_C (vertical gradients regions). It means that all the points correspond to the condensation/convection region. As expected, the scaling in eU is perfect in this region.

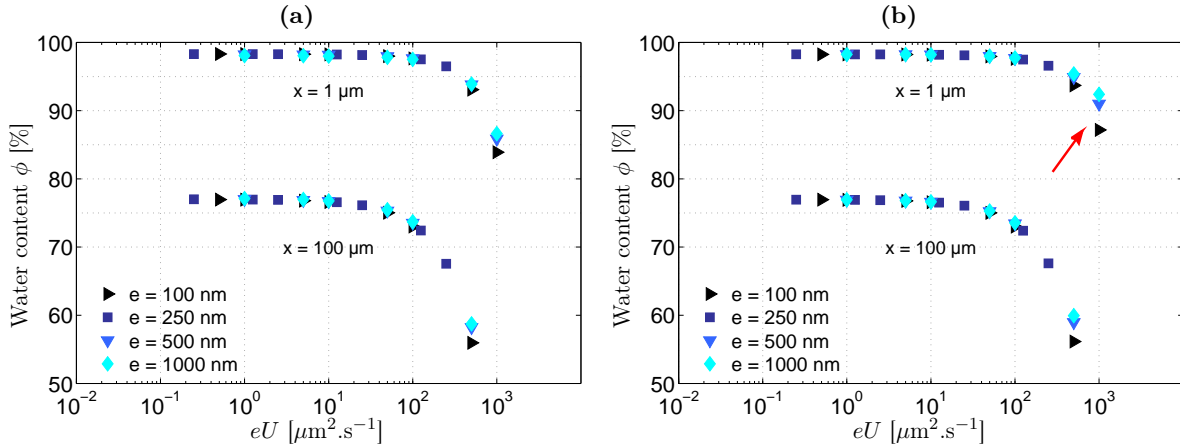


Figure 4.19: COMSOL simulations: scaling - Water content extracted from simulation at different speeds U and thicknesses e at $x = 1 \mu\text{m}$ (top) and $x = 100 \mu\text{m}$ (bottom) from the contact line. The values are plotted versus the product eU . (a) $D_p = 10^{-9} \text{ m}^2.\text{s}^{-1}$. (b) $D_p = 10^{-11} \text{ m}^2.\text{s}^{-1}$.

- Vertical concentration gradients:

Let's now see how the vertical concentration gradient modifies the scaling property. In Fig. 4.19b, the diffusion coefficient is now $D_p = 10^{-11} \text{ m}^2.\text{s}^{-1}$ which leads to $(Pe)_v/(Pe)_p$ of $8.9 \cdot 10^{-3}$. In this situation, we still focus on the condensation/convection region since κ is very small but x_C becomes larger than $1 \mu\text{m}$ for large velocities. Vertical concentration gradients are obtained. For instance, at $U = 0.5 \text{ mm}.\text{s}^{-1}$ and $e = 100 \text{ nm}$, x_C is $50 \mu\text{m}$. Thus, for $x = 1 \mu\text{m}$, the scaling does not work any more at large U . This is pointed by the red arrow that shows the three points that do not overlap any more. We show that, as expected in the thick film regime, the scaling

in eU is not valid.

- Diffusion/condensation region in the thin film regime:

In this paragraph, we discuss the water content evolution when diffusion and condensation are dominant, *i.e.* at $x_C \ll x < \kappa$. As explained before, a concentration plateau is observed in this region. We plot with dotted lines in Fig. 4.20a the polymer content for three simulations where eU is a constant ($eU = 1.25 \mu\text{m}^2.\text{s}^{-1}$). We considered the following thicknesses: $e = 25$ nm, $e = 250$ nm and $e = 2500$ nm. D_p is equal to $10^{-9} \text{m}^2.\text{s}^{-1}$ such as x_C remains negligible in comparison with κ . Since eU is constant, we observed similar profiles at $x > \kappa$ confirming what was said about the condensation/convection region. Close to the contact line, we see that the vertical position of the plateau is modified with the thickness. Thus, we do not have a scaling in eU in the diffusion/condensation region.

- Adding direct diffusion:

In Fig. 4.20a, we also represent the profiles obtained when direct diffusion is activated (full lines). As shown in the previous section, the concentration plateau disappears and the polymer content approximately varies as $\phi_p \sim x^{1/2}$ close to the contact line. Surprisingly, the curves obtained at different thicknesses tend to superimpose. The relative small difference between the power law exponent in the diffusion region and the one in the condensation/convection region allows to preserve the scaling in eU .

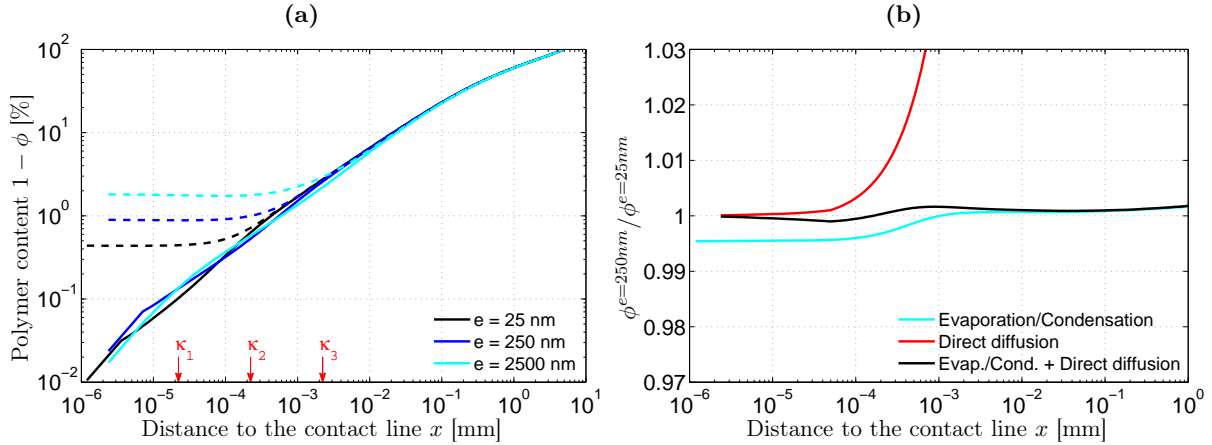


Figure 4.20: COMSOL simulations: scaling of the water content profiles - Simulations at $D_p = 10^{-9} \text{m}^2.\text{s}^{-1}$ and $eU = 1.25 \mu\text{m}^2.\text{s}^{-1}$ (a) Polymer content. Comparison between 3 thicknesses considering evaporation/condensation only (dotted lines) or evaporation/condensation + direct diffusion (full lines) (b) Ratio of the water contents at $e = 250$ nm and $e = 25$ nm.

We plot in Fig. 4.20b the ratio $\phi^{e=250\text{nm}}/\phi^{e=25\text{nm}}$ of the water contents at $e = 250$ nm and

4. WETTING REGIMES

$e = 25$ nm presented in Fig. 4.20a. We also include the ratio of the direct diffusion profiles (in red). The blue curve (evaporation/condensation only) shows that the scaling is verified at intermediary distances as the ratio is close to 1. For smaller distances x , *i.e.* in the plateau region, the ratio is smaller than 1. When direct diffusion is added (black curve), the ratio is increased in this region and always remains close to 1.

In conclusion, diffusion along the horizontal axis (without direct diffusion) modifies deeply the shape of $\phi(x)$ by allowing the water to migrate upstream, which leads to a concentration plateau. Nevertheless, when water is allowed to directly diffuse from the droplet, the effect of upstream migration is compensated by the migration from the droplet itself. Both effects cancel in practice, leading to the non-intuitive result that the scaling in eU is valid even in the presence of horizontal diffusion.

4.3.6 Non-linearities

4.3.6.1 Sorption isotherm $a_w = f(\phi)$

In the previous simulations, we have simplified the study by using a linear relation $a_w = \phi$. However, our experimental conditions are really different since for instance our main polymer - maltodextrin DE29 - contains only 7% of water at 43% of humidity. Indeed, $a_w(\phi)$ is very non-linear and the object of this section is to understand what are the consequences of this non-linearity. In order to understand how the modification of the sorption isotherm influences the evaporation/condensation profiles, we chose to use a Flory equation as sorption isotherm with χ the Flory parameter:

$$a_w(\phi) = \phi \cdot \exp\left(\left(1 - \phi\right) + \chi(1 - \phi)^2\right) \quad (4.12)$$

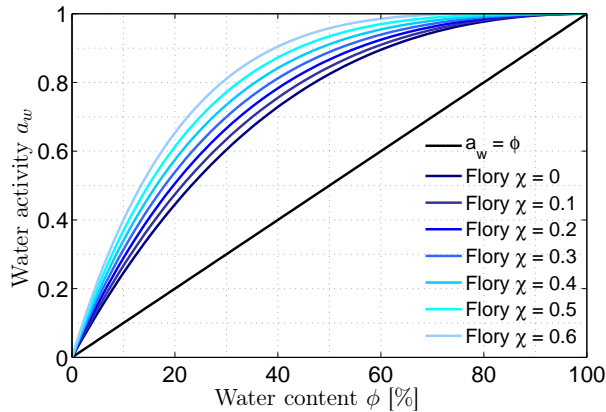


Figure 4.21: Sorptions isotherms used in FEM simulations - Considered functions $a_w(\phi)$ in simulations: linear case or Flory sorption isotherm.

We vary χ from 0 to 0.6 (see the sorption isotherms in Fig. 4.21) knowing that our experimental conditions are close to $\chi \sim 0.5-0.6$. We perform the simulations using the conditions of

Fig. 4.8 (evaporation/condensation without direct diffusion) with a contact line speed $U = 0.01$ mm.s⁻¹ and a diffusion coefficient $D_p = 10^{-9}$ m².s⁻¹. The layer thickness e is 250 nm. Fig. 4.22a represents the obtained polymer profiles. We compare the linear case ($a_w = \phi$, black curve) with the Flory case at different χ . The influence of this new water activity function is important. The layer is less and less hydrated when χ increases. Nevertheless, the diffusion plateau is always set by the length κ showing that characteristic lengths are not significantly modified. Finally, the polymer content at the plateau increases with χ .

In a second figure (Fig. 4.22b), we show the effect of the derivative of the water activity $\frac{\partial a_w}{\partial \phi}$ on the theoretical polymer content predicted by Tay *et al.*. We use Eq. 2.9 with $c = c_{sat} \cdot a_w = c_{sat} \cdot \frac{\partial a_w}{\partial \phi} \cdot \phi$. With $a_w(x = L) = \frac{c_0}{c_{sat}} = 0$, it yields:

$$\phi(x) = \frac{1}{\frac{\partial a_w}{\partial \phi}} \left[1 - \left(\frac{r}{L} \right)^k \right] \quad (4.13)$$

We plot this theoretical profile for three values of $\frac{\partial a_w}{\partial \phi}$. We can notice that a decrease of this term leads to smaller polymer content and respectively an increase leads to a larger polymer content. With the Flory water activity ($\chi = 0.5$), $\frac{\partial a_w}{\partial \phi}$ is larger than 1 for $\phi \sim 35$ % and smaller than the one at larger water contents. Thus, the FEM simulations in Fig. 4.22a show that far from the contact line, we obtain a larger polymer content than the case $a_w = \phi$, with small $\frac{d\phi_p}{dx}$. Then when ϕ increases and $\frac{\partial a_w}{\partial \phi}$ becomes smaller than 1, the slope of the polymer content $\frac{d\phi_p}{dx}$ tends to increase.

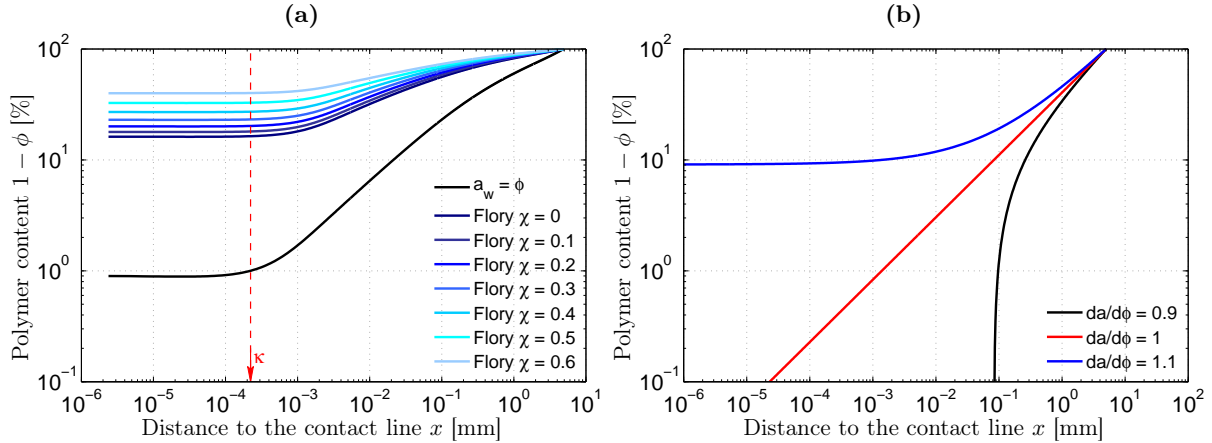


Figure 4.22: COMSOL simulations: influence of the sorption isotherm - (a) Influence of the Flory parameter χ on polymer content profiles for $e = 250$ nm, $U = 0.01$ mm.s⁻¹ and $D_p = 10^{-9}$ m².s⁻¹. (b) Influence of the term $\frac{\partial a_w}{\partial \phi}$ on theoretical profiles in the case of a linear sorption isotherm (following Eq. 9 in (1)).

If we add the direct diffusion to the previous study, we obtain a similar result that the one

4. WETTING REGIMES

obtained with $a_w = \phi$ (see the difference between Fig. 4.23a and 4.18a). On the black curve (corresponding to Fig. 4.17), the plateau disappears and the variations are close to the ones of a power law with an exponent $1/2$ in the vicinity of the contact line. At larger distances ($x > 50\kappa$), the condensation/convection profile dominates. In Fig. 4.23b, the diffusion coefficient is smaller ($D_p = 10^{-10} \text{ m}^2.\text{s}^{-1}$). Thus λ and κ are both 10 times smaller. It gives a slight larger polymer content for the total profile close to the contact line but the same observations can be done.

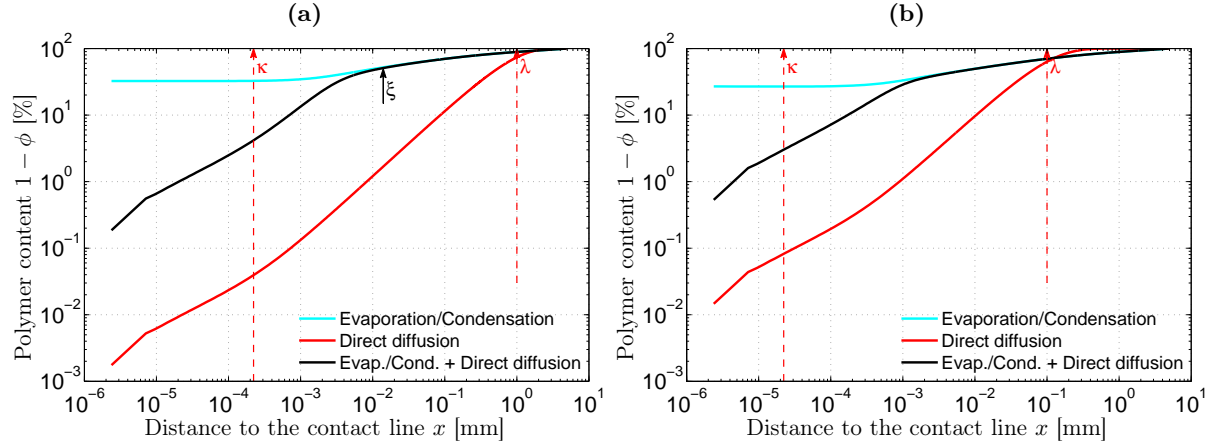


Figure 4.23: COMSOL simulations: influence of direct diffusion on evaporation/water uptake profiles using Flory sorption isotherm - Polymer content profiles at the surface of the coating for a 250 nm-thick layer having a constant diffusion coefficient and a Flory sorption isotherm ($\chi = 0.5$). $U = 0.001 \text{ mm}.\text{s}^{-1}$. (a) $D_p = 10^{-9} \text{ m}^2.\text{s}^{-1}$. (b) $D_p = 10^{-10} \text{ m}^2.\text{s}^{-1}$.

We show that the addition of the direct diffusion does not introduce a new characteristic length if $a_w(\phi)$ is not linear. It was already the case with the linear sorption isotherm. The length κ still represents a crossover between the diffusion/condensation region and the condensation/convection region. Nevertheless, we can observe larger extents of the diffusion/condensation regions in the simulation than what the scaling analysis indicates. For instance, we measure plateau lengths $\xi \sim 100\kappa$ in Fig. 4.23a whereas $\xi \sim 5\kappa$ with $a_w = \phi$. Several reasons can explain these differences:

- In the linear case, the difference can be due to the scaling approach that uses the Fourier Transform equation. Indeed, we assimilate $\frac{\partial\phi}{\partial x}$ to $q\phi$ and q to $\frac{1}{x}$. This scaling arguments can lead to differences between the predicted characteristic length κ and the observed one ξ especially when $\frac{\partial\phi}{\partial x}$ quickly varies.
- For a non-linear water activity, the inward flux term \hat{j}_v used in Eq. 4.6 is modified. It is proportional to the derivative of the water activity $\frac{\partial a_w}{\partial\phi}$. The characteristic length of the diffusion/condensation region should thus be modified. At large ϕ , when $\frac{\partial a_w}{\partial\phi}$ is small, we expect a larger region (size inversely proportional to $\frac{\partial a_w}{\partial\phi}$).
- In addition, we also expect a velocity effect coming from $\frac{\partial a_w}{\partial\phi}$ and $\frac{\partial\phi}{\partial x}$. Indeed, both terms

are modified in the crossover region when the velocity is changed. We observe a slight decrease of ξ with U in simulations.

In conclusion, κ underestimates the length of the diffusion/condensation region. With a non-linear sorption isotherm and in presence of direct diffusion, the observed size of the diffusion/condensation region ξ is approximately increased by two orders of magnitude and speed-dependent.

4.3.6.2 Concentration-dependent diffusion coefficient $D_p(\phi)$

In the previous simulations, we have considered a constant diffusion coefficient D_p . In practice, as explained in the materials and methods chapter, the diffusion coefficient in maltodextrin strongly depends on the water content ϕ . The mutual diffusion coefficient $D_p(\phi)$ was estimated with the help of NMR measurements and diffusion theories, showing that D_p increases by several orders of magnitude between $\phi = 0\%$ and $\phi = 100\%$. With the chosen function (see section 3.1.2.5), we have $D_p(0) = 10^{-15} \text{ m}^2.\text{s}^{-1}$ and $D_p(1) = 8.1 \cdot 10^{-11} \text{ m}^2.\text{s}^{-1}$.

The implementation of this concentration-dependent diffusion coefficient in the FEM simulations was found to be quite difficult. The simulation of a simple process such as direct diffusion only is straightforward but the simulation of evaporation/condensation transfers was found to be time consuming in that case. Owing to a lack of time, we only provide qualitative data on that effect. In particular, we have found that the size of the diffusion/condensation region, characterized by the concentration plateau, was consistent with a simulation performed at the maximum value of $D_p(\phi)$. In brief, we expect the varying diffusion coefficient to result in an increase of the theoretical size of the diffusion/condensation region.

4.3.7 Conclusions

In this section, we have used the theoretical description of Tay *et al.*, to which we have included diffusion in the horizontal direction. Our main findings are:

1. Water transfers to the layer occur through condensation, diffusion and convection. We have shown that the leading processes are condensation and convection far from the contact line whereas condensation and diffusion dominate for small modified Péclet numbers in air Δ . The crossover length is κ .
2. Introducing non-linearities such as $a_w = f(\phi)$ or a concentration-dependent diffusion coefficient $D_p(\phi)$ increases the value of κ by two or three orders of magnitude.
3. We have showed that the scaling $\phi(eU)$ predicted by Tay *et al.* is valid in the condensation/convection region. At first view, in the diffusion/condensation region, the $\phi(eU)$ rule should not hold. However, diffusion effects cancel each other out, leading to a scaling even in the diffusion/condensation region:

4. WETTING REGIMES

- diffusion towards large x due to the gradient of concentration generated by the condensation/convection effect
- diffusion from the water droplet (direct diffusion)

With this more complete approach of the hydration, we can now establish a new wetting diagram and compare experimental results to the theory.

4.4 New wetting diagram and confrontation with experimental data

In this section, we will compare the experimental data to the prediction of the leading mechanisms presented in section 4.3. We will see that, as expected, the experimental diffusion/condensation region is much larger than κ because of strong non-linearities. We will use this experimental diffusion/condensation region to build the new wetting diagram. It will modify the position of the frontiers and a new regime will be introduced to explain the contact angle dependence on the thickness e outside of the thin film regime. We will also validate the scaling of the contact angle in eU in the thin film regime.

4.4.1 Diffusion/Condensation region in hydration profiles

4.4.1.1 Experimental profiles $\phi(x)$

Up to that point, we have shown the results of FEM simulations as polymer content profiles $1 - \phi(x)$ plotted in log-log scale. It was convenient in order to compare with Tay *et al.* theory that predicts power laws for that quantity. In the following paragraphs, the experimental profiles will be presented in water content $\phi(x)$ plotted in lin-log scale. Thus, the results will be more readable.

In section 4.3, we predicted the existence of a diffusion/condensation region ahead the contact line. When vertical concentration gradients are negligible, this region should be observed for $x < \xi$. Because of the different sources of non-linearity (sorption isotherm $a_w = f(\phi)$ and diffusion coefficient $D_p(\phi)$), ξ is expected to be two or three orders of magnitude larger than the characteristic length $\kappa = \frac{e\Delta}{(Pe)_p}$. For instance, Fig. 4.24a represents the expected water content profile if we consider the Flory sorption isotherm at $e = 250$ nm, $D_p = 10^{-10}$ m².s⁻¹ and $U = 0.001$ mm.s⁻¹ (the inset corresponds to the polymer content as it was represented in previous sections). The observed length of the diffusion/condensation region ξ is approximately 100 times larger than κ . This larger size, of the order of a few micrometers, indicates us that we should be able to observe this region experimentally.

In our experimental conditions, the diffusion coefficient is concentration-dependent. Here, in this section, most of the data come from samples equilibrated at $a_w = 0.75$. It corresponds to wet layers with an initial mutual diffusion coefficient of $D_p = 1.4 \cdot 10^{-11}$ m².s⁻¹. We will use this diffusion coefficient to plot the diagrams. Fig. 4.24b represents the wetting regions as it was performed in section 4.3.1. We have $\Delta/(Pe)_p = 2.2 \cdot 10^{-2}$. The experimental velocity range that

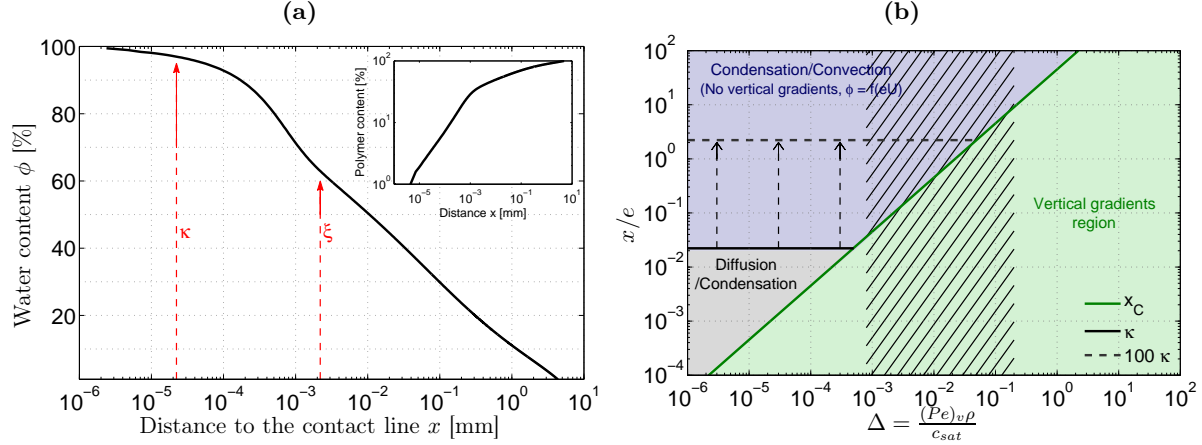


Figure 4.24: The diffusion/condensation region in water content profiles - (a) Simulated water content profile $\phi(x)$ at the surface of the coating for a 250 nm-thick layer having a constant diffusion coefficient ($D_p = 10^{-10} \text{ m}^2 \cdot \text{s}^{-1}$) and a Flory sorption isotherm ($\chi = 0.5$) for $U = 0.001 \text{ mm} \cdot \text{s}^{-1}$. Evaporation/condensation and direct diffusion are both considered in the simulation. The inset recalls the shape of the polymer content $1 - \phi(x)$ in log-log scale. (b) Normalized characteristic lengths of the condensation/diffusion equation: κ/e and x_C/e versus Δ . $\Delta/(Pe)_p = 2.2 \cdot 10^{-2}$. The hatched area corresponds to the velocity range in free-spreading experiment. The arrows and the dotted horizontal line represents the larger diffusion/condensation region that comes from nonlinearities with $\xi \sim 100\kappa$

is reachable with the free-spreading experiment is represented with hatches. Thus, if we consider a diffusion/condensation region of 100κ instead of κ (dotted line), this region may be observed in our experiments.

- Experimental profiles at intermediate velocities:

We plot in Fig. 4.25 the experimental water content profiles $\phi(x)$. They are obtained by extraction of the thickness from the color analysis of the layer. We use a 250 nm-thick layer of maltodextrin DE29 equilibrated at $a_w = 0.75$ and perform a free-spreading experiment. The color analysis is done for three different contact line speeds: $U = 0.05 \text{ mm} \cdot \text{s}^{-1}$, $U = 0.1 \text{ mm} \cdot \text{s}^{-1}$ and $U = 0.2 \text{ mm} \cdot \text{s}^{-1}$. These velocities correspond to different values of Δ that are given in Table 4.2. If we consider the dotted line $\xi = 100\kappa$ in Fig. 4.24b, it corresponds to profiles where the diffusion/condensation region exists. Finally, the initial value of the water content ϕ_0 is represented with a black line at large x . We have $\phi_0 \sim 24.7 \%$.

Various observations can be done on Fig. 4.25. First, it evidences an effect of the velocity on the water content. The larger the speed U , the smaller the water content ϕ as it was observed in the simulations (Fig. 4.11b). Second, the experimental water content at the contact line is smaller than the one obtained in the FEM simulations of Fig. 4.24a. It might be a consequence of coating dissolution. Indeed, the concentration of polymer in the droplet is probably not

4. WETTING REGIMES

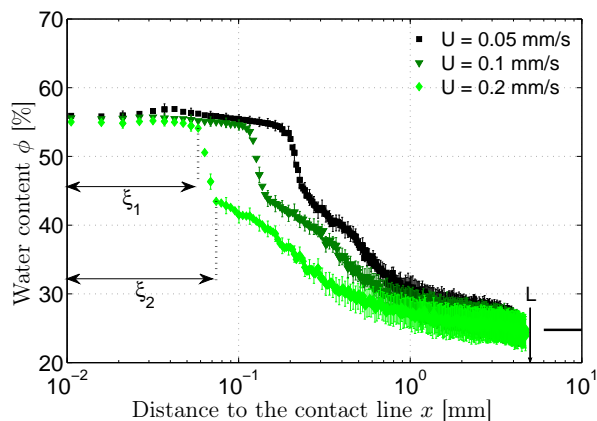


Figure 4.25: Speed influence on water content profiles ahead the contact line - Water content extraction from color pictures during water spreading onto a 250 nm-thick layer of maltodextrin DE29 equilibrated at $a_w = 0.75$. Three different contact line velocities U are represented. The full black line indicates the equilibrium water content in the layer, ϕ_0 , at this water activity a_w .

negligible in the edge and it modifies the boundary condition with $\phi(x < 0, y = e) < 1$ instead of $\phi(x < 0, y = e) = 1$. Third, we observe different regions in the profiles:

- In the immediate vicinity of the contact, for x smaller than a length we denote ξ_1 , there is a plateau in water content.
- Then, a sharp decrease of ϕ occurs between ξ_1 and a distance we denote ξ_2 .
- If we call L the extent of the hydration where $\phi = \phi_0$, we observe a smooth decay of ϕ from $x = \xi_2$ to $x = L$.

The profile shape is approximately similar to the curve of Fig. 4.24a but it seems more complex. The region from $x = 7 \mu\text{m}$ (the resolution) to $x = \xi_2$ may be a signature of direct and/or horizontal diffusion. For instance at $U = 0.2 \text{ mm}\cdot\text{s}^{-1}$, we measure $\xi_1 = 58 \mu\text{m}$ and $\xi_2 = 74 \mu\text{m}$. The theoretical length κ for the chosen diffusion coefficient is around 6 nm. With non-linearities added to the simulation, it corresponds to a theoretical distance ξ of the order of 10 μm which is not that far from ξ_1 and ξ_2 . Besides, the chosen diffusion coefficient, which corresponds to the initial one of the layer, may be underestimated. Indeed, we could have chosen the maximum value of $D_p(\phi)$ instead, value which is rather imprecise since we do not have direct measurements of the mutual diffusion coefficient. In that case, ξ would increase and get close to the experimental lengths ξ_1 and ξ_2 .

Table 4.2: Péclet numbers in the free spreading experiments: approximate experimental values of Δ and $(Pe)_p$ during water spreading onto a 250 nm-thick layer of maltodextrin DE29 equilibrated at $a_w = 0.75$.

Velocity [mm.s ⁻¹]	Δ	$(Pe)_p$
0.005	0.002	0.089
0.01	0.004	0.179
0.05	0.020	0.893
0.1	0.040	1.786
0.2	0.080	3.571

- Experimental profiles at small velocities:

In the previous paragraph, we presented intermediate velocities in the free-spreading process. At long times, the contact line velocity becomes very small and the water content profiles are modified. In Fig. 4.26, we present the water content profiles $\phi(x)$ for two small velocities: $U = 0.005 \text{ mm.s}^{-1}$ and $U = 0.01 \text{ mm.s}^{-1}$.

Fig. 4.26 shows that even if the water content profiles exhibit some features that are consistent with the ones of Fig. 4.25, we observe a bump ahead the contact line. Instead of having a plateau, the water content increases in the vicinity of the contact line to reach a maximum value. This bump was also observed with lactose layers at small velocities. We will come back later in this chapter on the possible origin of this bump.

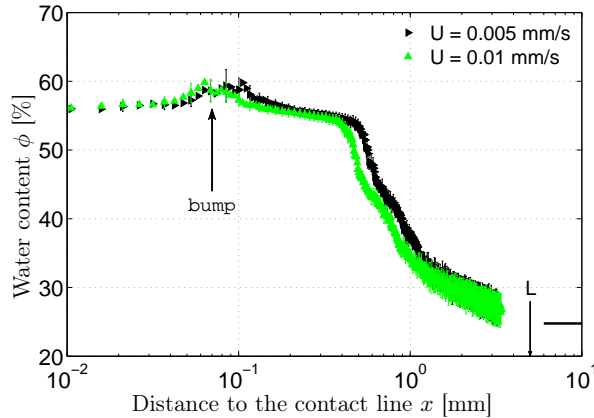


Figure 4.26: Water content profiles at small velocities - Water content extraction from color pictures during water spreading onto a 250 nm-thick layer of maltodextrin DE29 equilibrated at $a_w = 0.75$. Two different contact line velocities U are represented. The full black line indicates the equilibrium water content in the layer, ϕ_0 , at this water activity a_w .

4. WETTING REGIMES

We have shown in this subsection that the experimental water content profiles exhibit shapes in agreement with the FEM simulations even though they present additional features. A concentration plateau is observed ahead the contact line which could correspond to the diffusion/condensation region. In order to evidence the role of horizontal diffusion, we used another experiment that is presented in the next subsection.

4.4.1.2 The broken wafer experiment

In the previous subsection, we have showed that the experimental water content profiles $\phi(x)$ present a plateau close to the contact line. This plateau is suspected to be a consequence of diffusion. In the FEM simulations, we also observe a similar shape in the profile ahead the contact line (see Fig. 4.24a).

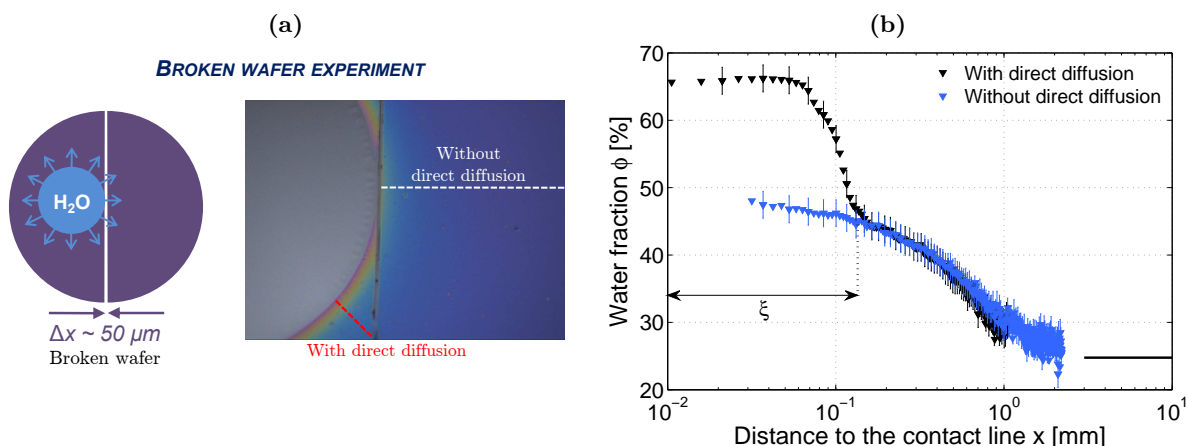


Figure 4.27: Direct diffusion validation with the broken wafer experiment - Water content extraction from color pictures during water spreading onto a 250 nm-thick layer of maltodextrin DE29 equilibrated at $a_w = 0.75$. Comparison between normal case and broken wafer experiment where direct diffusion is suppressed. $U = 0.08 \text{ mm.s}^{-1}$.

In order to validate this part of the profile as a signature of horizontal diffusion in the coating, we imagined a simple experiment that allows us to suppress direct diffusion and also modifies the horizontal diffusion in the layer without changing the condensation process. To achieve this, we break the wafer coated by maltodextrin into two parts. We put side to side both parts in order to obtain a very small gap Δx between them ($\Delta x \sim 50 \mu\text{m}$). Then, a free-spreading experiment is performed on one side as described in the scheme of Fig. 4.27a. A picture is taken at which the contact line reaches the gap. Indeed, beyond the gap the water uptake results only from condensation, and not from direct diffusion. Besides, horizontal concentration gradients in the layer are modified beyond the gap, and thus the effects of diffusion in that direction. Indeed, at shorter times and in the contact line frame of reference, the gap is moving towards the drop preventing some water molecules to horizontally diffuse at larger x . Finally, that experiment

provides a qualitative way to characterize the influence of diffusion effects in the layer.

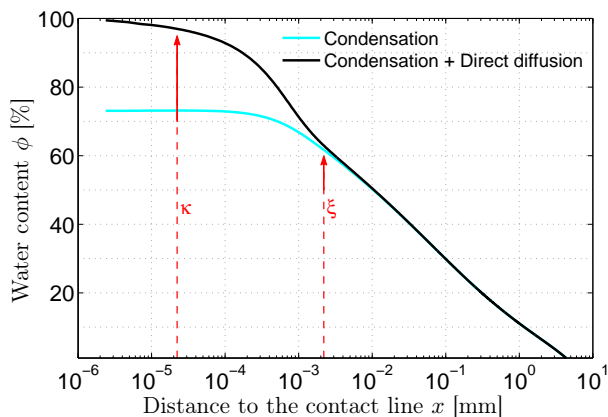


Figure 4.28: Simulation of coating hydration with or without direct diffusion - Simulated water content profiles at the surface of the coating for a 250 nm-thick layer having a constant diffusion coefficient ($D_p = 10^{-10} \text{ m}^2 \cdot \text{s}^{-1}$) and a Flory sorption isotherm ($\chi = 0.5$) for $U = 0.001 \text{ mm} \cdot \text{s}^{-1}$. Case with and without direct diffusion.

We plot in Fig. 4.27b a comparison between the profile obtained in this experiment and the one obtained without any gap. Both color extractions are performed on the same picture as presented on Fig. 4.27a. The contact line velocity is $U = 0.08 \text{ mm} \cdot \text{s}^{-1}$. We observe similar profiles at distances larger than the length ξ defined on the graph. For $x < \xi$, the plateau disappears in the broken wafer experiment. A smooth decrease of ϕ with x is observed close to the contact line. We recall in Fig. 4.28 the result of the simulation with the Flory water activity, to which we add the same simulation without direct diffusion (blue curve). We observe a strong decrease of the water content ahead the contact line that is similar to the one observed in the broken wafer experiment. Thus, the first part of the experimental curves (between $x = 0$ and $x = \xi$) is likely to be the signature of diffusion.

Finally, the same experiment performed with different carbohydrates (not shown here) confirmed the presence of a diffusion/condensation region ahead the contact line. With amorphous lactose, a very short molecule compared to maltodextrin DE29, we obtained larger ξ (4 to 5 times larger for the same U and a_w). It is in agreement with the scaling arguments since water diffuses faster in lactose. On the opposite side, maltodextrin DE6, which contains larger chains of polymer, presented very small diffusion domains at the limit of the resolution for large speeds and small humidities (ξ below $10 \mu\text{m}$) and up to $100 \mu\text{m}$ at high a_w and small U . Finally, no diffusion/condensation region was observed with maltodextrin DE2. This polymer has very long chains (140 times larger than maltodextrin DE29) and water diffuses slowly in it. The values of $D_p(\phi)$ are much smaller in that case and the diffusion/condensation region has a size which is not observable in our experimental conditions.

4. WETTING REGIMES

4.4.1.3 Measurement of the diffusion/condensation region size

The broken wafer experiment have demonstrated that the large water uptake, observed close to the contact line in experimental water content profiles, is a signature of diffusion effects. According to theory, the size of the diffusion/condensation region ξ should weakly depend on the contact line velocity U . We do not have a quantification of the speed-dependence but as explained in section 4.3.6, the Fourier transform approach and the non-linear water activity may lead to a decrease of ξ with U .

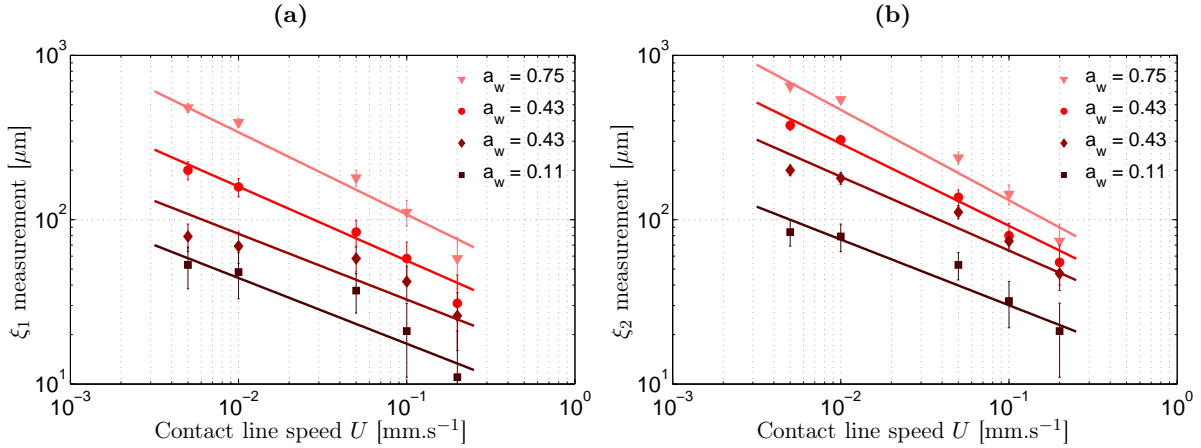


Figure 4.29: Measurement of the diffusion/condensation region size - power law fitting - ξ_1 (a) and ξ_2 (b) measurement on $\phi(x)$ profiles at different water activities a_w . Curves are fitted with power laws $\xi = a.U^b$.

We measured the experimental lengths ξ_1 and ξ_2 as a function of the contact line velocity U and the surrounding humidity a_w (respectively Fig. 4.29a and Fig. 4.29b). Curves are fitted with power laws $\xi = a.U^b$. It can be checked that the evolution of the measured lengths is not in U^{-1} . It confirms that the region between $x = 0$ and $x = \xi_2$ is not a diffusion/convection region controlled by $\lambda = \frac{D_p}{U}$ as it would be the case if evaporation/condensation would not be present (see Appendix C). In Fig. 4.30a and Fig. 4.30b, we fit the same data points with logarithmic curves $\xi = a.\ln(U/U^*)$ in order to obtain a better agreement. On these figures, we can notice a speed and humidity dependence. ξ_1 and ξ_2 decrease with U and increase with a_w . It is in agreement with the evolution of the diffusion/condensation region size ξ observed in FEM simulations. The velocity effect was noticed while the humidity influence was found in the value of D_p . Indeed, the effective diffusion coefficient is an increasing function of humidity, leading to increasing values of ξ . Furthermore, the term $\frac{\partial a_w}{\partial \phi}$ close to $x = \xi_2$ is smaller at large humidity. ξ being inversely proportional to this term, it also corresponds to increasing values of ξ from small a_w to large a_w .

We have showed that the diffusion/condensation region predicted in the wetting theory was observable with the system water/maltodextrin DE29. The size of this region ξ was found to be three orders of magnitude larger than the predicted characteristic length κ . We know that

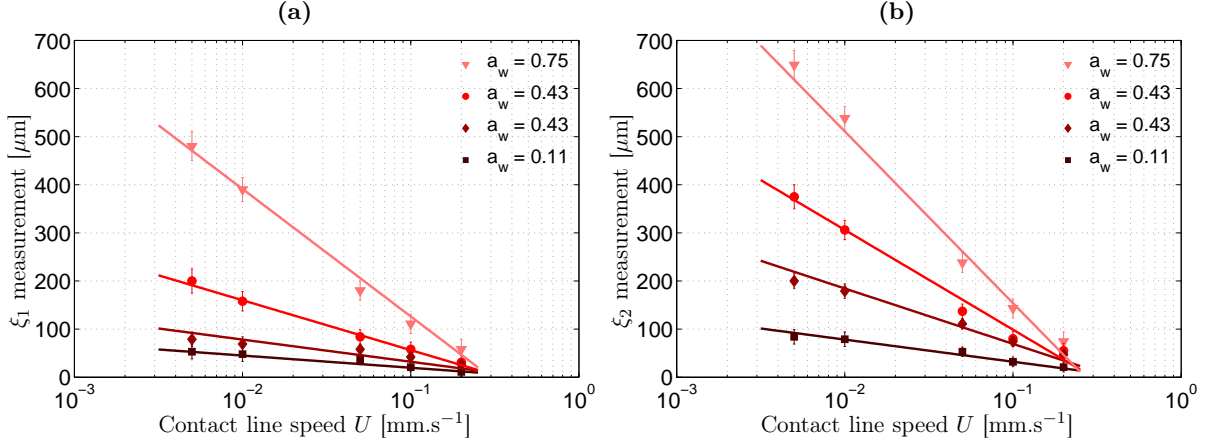


Figure 4.30: Measurement of the diffusion/condensation region size - logarithmic fitting - ξ_1 (a) and ξ_2 (b) measurement on $\phi(x)$ profiles at different water activities a_w . Curves are fitted with logarithmic curves $\xi = a \cdot \ln(U/U^*)$.

this discrepancy results from the non-linearities at stake in the problem (sorption isotherm and diffusion coefficient). Besides, ξ is difficult to define experimentally since 2 lengths ξ_1 and ξ_2 are observed on the profiles that are more complex than the one obtained by simulation. ξ_1 and ξ_2 are of the same order of magnitude and evolve similarly with U and a_w . In the following, we choose to use ξ_2 as a measure of ξ .

With this experimental measurement of the diffusion/condensation region, we are now able to propose a new wetting diagram. We have to take into account the length ξ in the building of the diagram.

4.4.2 Building the new wetting diagram

4.4.2.1 A new cut-off length

The frontier between thin film regime and thick film regime was defined by Tay *et al.* as being dependent of a molecular cut-off ε . They consider that as long as there are no vertical gradients ahead the nanometric distance to the contact line ε , the coating is equilibrated over the whole coating thickness and the scaling $\phi(eU)$ is valid. It corresponds to the condition $x_C < \varepsilon$ where $x_C = \frac{U\varepsilon^2}{D_p}$ what leads to a frontier in $U^{-1/2}$ in the eU diagram.

We have showed in the simulation section (4.3) that a diffusion/condensation region exists ahead the contact line. This region was characterized by the length κ . When x_C is smaller than κ , we have seen in 4.3.2.2 that no vertical concentration gradients are observed even for $x < x_C$. We present below the results of two different simulations (in the case where $a_w = \phi$): the first one with $x_C \sim \kappa$ and a second one with $x_C \sim 10\kappa$.

- We plot in Fig 4.31a an example of 2D water content profile for which $x_C \sim \kappa$ (obtained

4. WETTING REGIMES

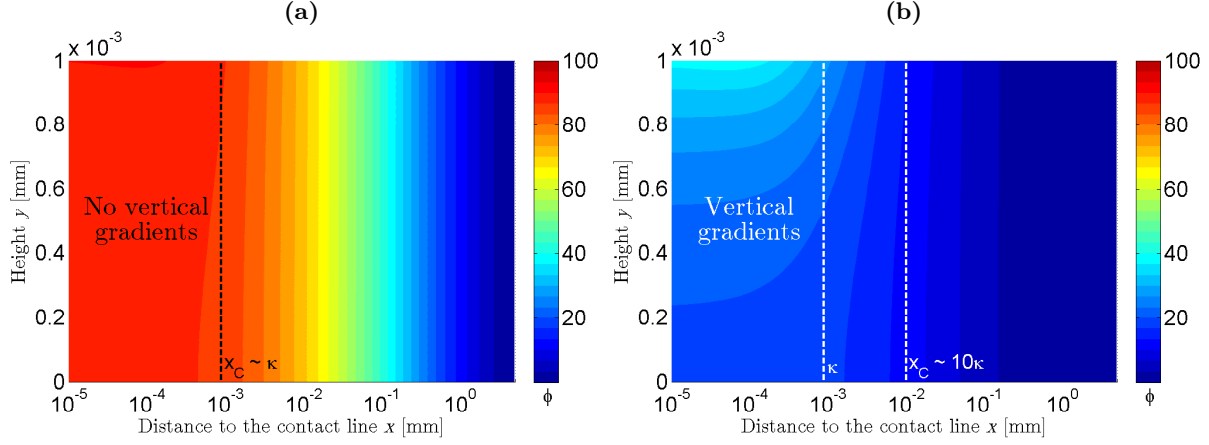


Figure 4.31: Schematic 2D view of water content calculated by simulation - Water content obtained in the case of evaporation/water uptake only. The layer thickness is $1 \mu\text{m}$ and the sorption isotherm of the coating is $a_w = \phi$. (a) Case $x_C \sim \kappa$: $U = 1 \text{ mm.s}^{-1}$ and $D_p = 10^{-9} \text{ m}^2.\text{s}^{-1}$. (b) Case $x_C \sim 10\kappa$: $U = 10 \text{ mm.s}^{-1}$ and $D_p = 10^{-9} \text{ m}^2.\text{s}^{-1}$.

using the conditions of Fig 4.8 in the case of evaporation/condensation with no direct diffusion). We can notice that there are no vertical concentration gradients in the diffusion/condensation region. As explained in section 4.3.5, the scaling $\phi(eU)$ remains valid in the diffusion region when direct diffusion is considered. Thus, the cases with $x_C < \kappa$ correspond to a thin film regime.

- In Fig 4.31b, the velocity was taken to be 10 times larger, such that $x_C \sim 10\kappa$. Here, we can clearly see the strong concentration gradient ahead the contact line at $x < x_C$. There is still a plateau observed for the surface water content but is shorter than κ . When x_C is larger than κ , the size of the diffusion/condensation region is reduced and vertical gradients appear in this region the scaling $\phi(eU)$ is no longer valid.

We summarize both situations ($x_C < \kappa$ and $x_C > \kappa$) in the schemes of Fig 4.32a and Fig 4.32b. In conclusion, the thin film regime is expected to be much larger than the one predicted by Tay *et al.* The cut-off length that has to be considered is not ε but κ . As long as $x_C < \kappa$, there are no vertical gradients of water content ahead in the diffusion/condensation region and the scaling $\phi(eU)$ works. When non-linearities are considered, as in the experiments, the same considerations can be done with the length ξ instead of κ .

In Tay *et al.*'s approach, there is a singularity at the contact line. The strong variation of water content in a few nanometers at the contact line theoretically leads to an infinite flux in $x \sim \varepsilon$. Nevertheless, in the situation in which a diffusion/condensation region exists, the flux is expected to be modified. We can calculate the flux using an experimental water content profile where the characteristic length ξ is observed (the droplet is considered at $\phi = 1$ and a fit of the profile is used) as presented in Fig. 4.33a. Using the approximations of Appendix B, we obtain the vertical water flux at the surface of the layer (Fig. 4.33b). We find that the droplet is not

4.4 New wetting diagram and confrontation with experimental data

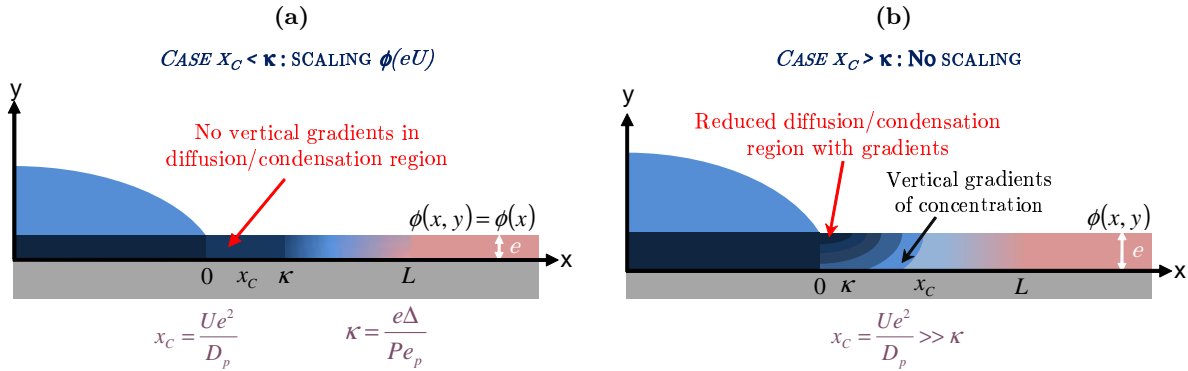


Figure 4.32: Schematic representation of the cut-off length - (a) Case without vertical gradients of ϕ : $x_C < \kappa$. (b) Case with vertical gradients of ϕ : $x_C > \kappa$

the only place where evaporation occurs. Far from the contact line, the water flux is negative and condensation occurs but just ahead the contact line, in the diffusion/condensation region, the vertical water flux becomes positive. Thus, a new divergence of the condensation flux occurs around $x = \xi$ as if the condensation flux was translated from the contact line. This observation is in agreement with the new cut-off length ξ .

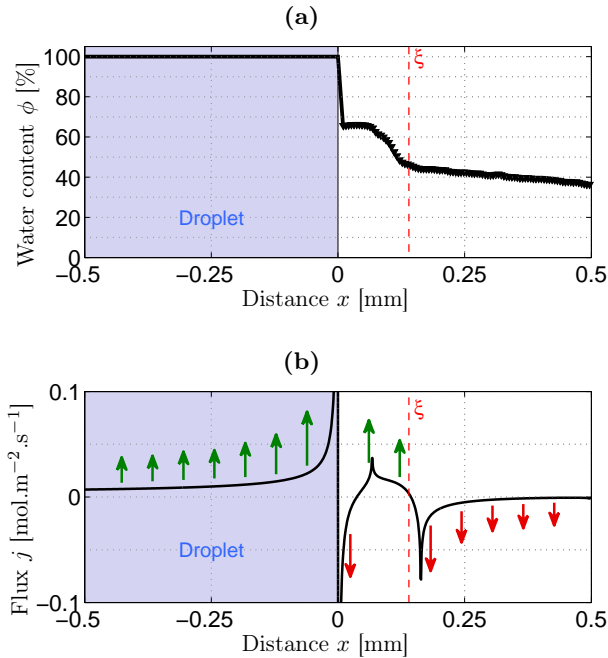


Figure 4.33: Flux calculation on an experimental water content profile - (a) Water content behind and ahead the contact line corresponding to the spreading of water onto a maltodextrin DE29 layer at $U = 0.08 \text{ mm.s}^{-1}$ and $a_w = 0.75$. (b) Vertical water flux obtained at the surface of the layer and droplet by analytical calculation.

4. WETTING REGIMES

4.4.2.2 A larger thin film regime

We demonstrated in the previous paragraphs that the cut-off length of the problem is not ε but the size of the diffusion/condensation region, *i.e.* ξ . Thus, we are now able to define the transitions and the frontiers between the various wetting regimes.

With this new experimental cut-off length, the frontiers of the wetting diagram will be strongly modified. Indeed, the order of magnitude found for ξ ranges from 10 to 500 μm , *i.e.* ξ has an intermediate value between the nanometric lengthscale ε and the macroscopic length L . If we focus on the frontier between the thin film regime and the thick film regime, the condition $x_C < \varepsilon$ is replaced by $x_C < \xi$. This defines a new frontier:

$$e_2 = \sqrt{\frac{\xi D_p}{U}} \quad (4.14)$$

The consequence on the eU diagram is that this frontier is shifted toward larger thickness values. We expect to observe a larger thin film regime. Horizontal diffusion in the coating enlarges the domain where the scaling $\phi(eU)$ works (schematic representation of the layer in Fig. 4.34). Furthermore, the equation of the frontier is not in $U^{-1/2}$ any more. Indeed, we have seen that ξ is speed-dependent. In order to be able to plot this frontier, we used power laws to fit the experimental $\xi(U)$ (see Fig. 4.29b).

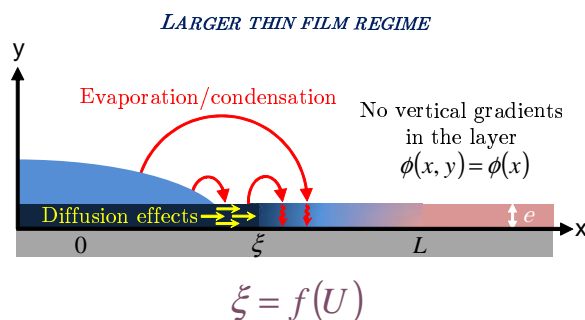


Figure 4.34: New schematic representation of the thin film regime - Horizontal diffusion introduces a new cut-off length: ξ . The thin film regime is larger than the one predicted by Tay *et al.*

4.4.2.3 Intermediary thick regime

In the preliminary section of this chapter, we have showed in Fig. 4.4b that in some cases, the experiments evidence iso- θ curves which shape is not predicted in the thin film regime or the thick film regime. At the frontier of the thin film regime, when the scaling $\phi(eU)$ fails, the contact angle θ still depends on the thickness e . This behaviour is not expected in the thick film regime where we only have a dependence in U . Thus, a new regime can be thought of, where the scaling in eU is not valid any more but the thickness still has an effect on ϕ . This regime

corresponds to the situation where the extent of the vertical gradients ahead the contact line reaches some intermediate distance to the contact line, that is $\xi < x_c < L$. L corresponds to the horizontal extent of the hydration. It defines the intermediary thick regime schematically represented in Fig. 4.35.

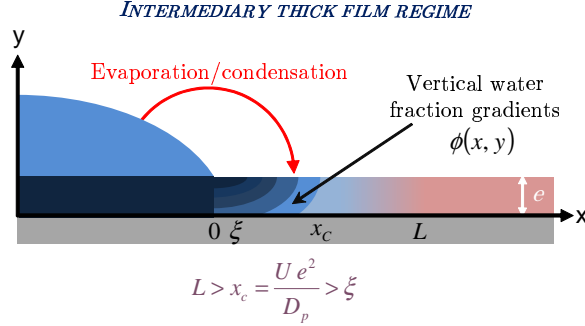


Figure 4.35: Schematic representation of the intermediary thick film regime - Vertical concentration gradients exist such x_C ranges between ξ and L .

In the intermediary thick regime, the scaling in eU is not valid any more, but the contact angle still keeps a dependence in e and U . In the thick film regime when x_C becomes larger than L , ϕ no longer depends on the thickness e . The equation of the frontier between the intermediary thick regime and the thick film regime can thus be expressed as:

$$e_3 = e_{int/thick} = \sqrt{\frac{LD_p}{U}} \quad (4.15)$$

4.4.2.4 Other frontiers

The other frontiers in the eU diagram, *i.e.* the frontiers between the dry substrate regime and the hydrated regimes (thin coating regime or thick coating regime) can be obtained with the same arguments as used by Tay *et al.* We can write the amount of water $\Delta\phi$ absorbed in the layer by condensation and compare this quantity to a characteristic value of $\Delta\phi$. Indeed, the dry substrate regime corresponds to a negligible amount of solvent in the coating. Let's first write the expression of $\Delta\phi$ in each regime.

- Thin film regime:

At small velocities, in the thin film regime, we can express the fraction of solvent ϕ in a coating of thickness e with the help of a one-dimensional approximation of evaporation/condensation process. A detailed calculation of the increase in water fraction $\Delta\phi$ for a thin coating is derived by Tay *et al.* (1) by integrating the flux of solvent arriving on the coating by absorption of the evaporated water from the droplet at a distance from the contact line comprised between the macroscopic length L and the microscopic cut-off ξ (see Eq.(21) in that paper). The result is:

4. WETTING REGIMES

$$\Delta\phi^{thin} = K \frac{D_v c_{sat}}{\rho U} \frac{1}{e} \ln \frac{e_3}{e_2} \quad (4.16)$$

We define $h = \ln \frac{e_3}{e_2} = \frac{1}{2} \ln \frac{L}{\xi}$. The scaling in $1/eU$ is explicit in this equation. Note that the expression of $\Delta\phi$ involves a prefactor K that depends on the adsorption isotherms of water in the polymer¹. Therefore, we are limited to scaling laws.

- Thick film regime:

The same assumption holds for thick coating regimes as well. The water content being independent on the coating thickness in this regime, so is expected to be the contact angle. Also, for thick coatings, the relevant length scale for the hydration is no longer the coating thickness e , but the distance over which water has diffused into the polymer that involves the diffusion coefficient of water into the polymer D_p . The increase in water content in this situation is calculated using Eq.(23) in the paper by Tay *et al.* and reads, with $e \gg e_2$:

$$\Delta\phi^{thick} = K \frac{D_v c_{sat}}{\rho U} \left(\frac{1}{e_2} - \frac{1}{e} \right) = K \frac{D_v c_{sat}}{D_p^{1/2} \rho U^{1/2} \xi^{1/2}} \quad (4.17)$$

We verify in Eq. 4.17 that for what we called thick coatings, the theoretical volume fraction of water uptake is independent of the thickness e .

- Intermediary regime:

The water fraction in the intermediary regime can also be derived using the equations of the paper by Tay *et al.* It involves two distinct terms, the first describing the part of the layer that is fully hydrated and the second, the partially hydrated layer, yielding a combination of Eq. 4.16 and Eq. 4.17. We find:

$$\Delta\phi^{int} = K \frac{D_v c_{sat}}{\rho U} \frac{1}{e} \left(\ln \frac{e_3}{e} + \frac{e}{e_2} - 1 \right) \quad (4.18)$$

- Dry regime:

Now we recall the main arguments defining the limits separating the dry regime and the hydrated regimes. The dry regime corresponds to a negligible amount of solvent in the coating. Using Eq. 4.16, we show that we stay in the thin wet regime as long as $\Delta\phi$ is small. We arbitrarily choose this limit to be 1 %, and the frontier between dry and thin regimes is obtained:

$$e_1 \sim e_{thin/dry} = \frac{K \ln \left(\frac{L}{\xi} \right)}{2} \frac{D_v c_{sat}}{0.01 \rho U} \quad (4.19)$$

¹K will be discussed in the glass transition chapter (p. 94). We have $\frac{1}{K} \sim \frac{(\pi-\theta)}{\phi(L)-\phi(\xi)} \int_{\phi(L)}^{\phi(\xi)} \frac{d\phi}{(1-\phi)^2(1-a_w(\phi))}$

4.4 New wetting diagram and confrontation with experimental data

The frontier between the dry substrate regime and the thick film regime is obtained as before when $\Delta\phi^{thick}$ is negligible, taken as 1 %, that is for velocities larger than U_c with:

$$U_c = U_{thick/dry} = \frac{K^2 D_v^2 c_{sat}^2 \ln\left(\frac{L}{\xi}\right) 2}{4 D_p \rho^2 \xi 0.01^2} \quad (4.20)$$

The range of velocities experimentally accessible is 10^{-3} to 10^3 mm.s⁻¹ at most, combining both spontaneous spreading and pulled substrate experiments. Thus, the dry regime is hardly observed. The dry regime is theoretically obtained when no significant hydration occurs in the coating. Therefore, the substrate energy is a constant and the contact angle is expected to be only affected by the hydrodynamics. Looking at Fig. 4.1 where high velocities were explored with the pulling substrate method, we find that the dynamic contact angle θ keeps increasing with U with a steep slope, reaching as much as 110° for velocities close to 1 m.s⁻¹. Thus, it may still correspond to the thick film regime rather than the dry regime.

- New diagram:

The equations of the wetting regime frontiers are now all expressed and we can plot the new wetting diagram (Fig. 4.36) corresponding to our experimental conditions, *i.e.* the system water/maltdextrin DE29 at $a_w = 0.75$. The value of the constant K is chosen equal to 0.006. We will explain this choice later in the report (glass transition chapter).

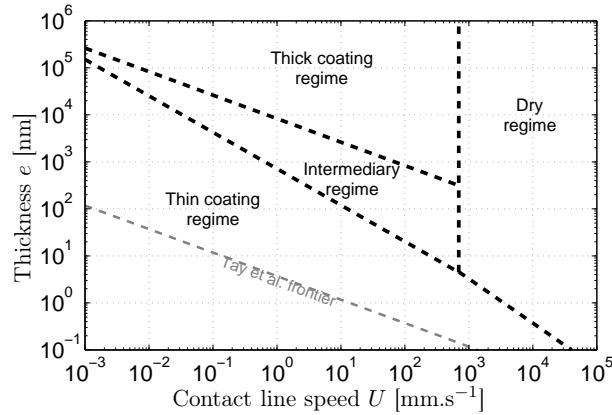


Figure 4.36: New wetting diagram - Wetting diagram taking into account the experimental diffusion/condensation region and the intermediary thick regime. The following parameters are used: $D_p = 1.4 \cdot 10^{-11}$ m².s⁻¹, $D_v = 2.7 \cdot 10^{-5}$ m².s⁻¹, $\rho = 997.05 \cdot 10^3$ g.m⁻³, $c_{sat} = 23$ g.m⁻³, $\xi[\mu\text{m}] = 37 U[\text{mm.s}^{-1}]^{-0.55}$, $\varepsilon = 1$ nm, $L = 5$ mm and $K = 0.006$. Tay et al. thin/thick frontier is also plotted (gray dotted line).

Thus, we have established a new wetting diagram based on the same approach that Tay *et al.*, but considering a new cut-off length ξ that results from diffusion effects. As a consequence, the

4. WETTING REGIMES

thin film regime is larger than their predictions. Besides, we have introduced a new intermediary regime that corresponds to $\xi < x_C < L$. We can now compare this diagram to our experimental data.

4.4.3 Experimental validation of wetting regimes

4.4.3.1 Validation of the scaling $\theta(eU)$ in the thin film regime

In the previous section, we have built a new wetting diagram. In comparison with the one of Tay *et al.*, one main result is the larger extent of the thin film regime. As a consequence of diffusion effects, it involves a scaling $\phi(eU)$ in a larger range of speeds and thicknesses. Let's try to evidence this scaling in our experiments from which we measure the contact angle θ . A scaling law in eU for the water content ϕ should lead to the same property for the contact angle θ .

We prepare thin layers of maltodextrin DE29 by spin-coating or dip-coating in order to obtain various thicknesses e . The free-spreading experiment is performed at $a_w = 0.75$ and $\theta(U)$ is extracted from lateral pictures as explained in section 3.3.3. We observe an increase of θ with the thickness e (Fig. 4.37a). It is in agreement with theory that predicts less hydration below the contact line if we have a thicker coating. Similarly, a contact line speed increase leads to larger contact angles. The shorter the time of hydration, the drier the layer. Plotting θ versus eU (Fig. 4.37b) shows that the scaling is very good at small eU . Thus, we evidence the thin film regime. At larger eU , the scaling $\theta(eU)$ is not valid any more. Nevertheless, the contact angle θ still depends on the layer thickness e . It validates the existence of the intermediary thick regime.

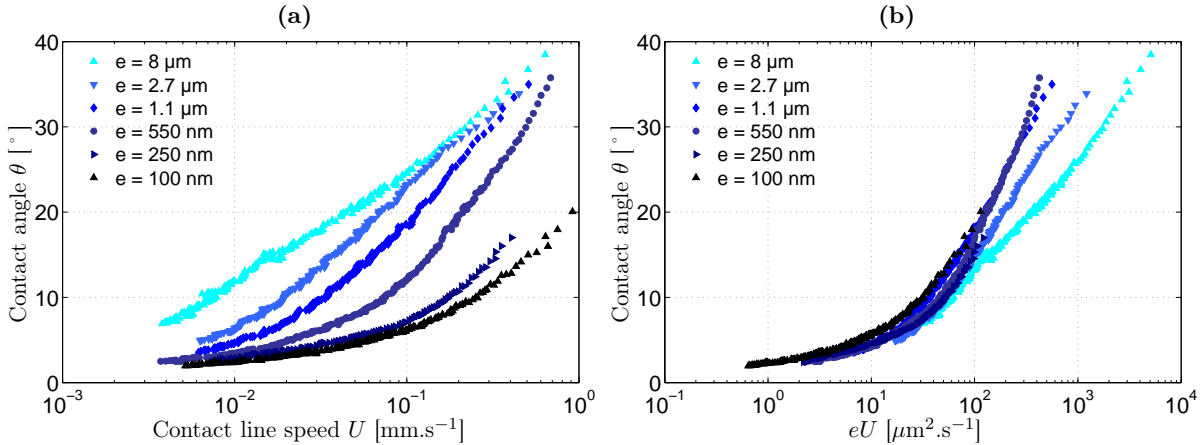


Figure 4.37: Thickness and speed effects on contact angle - Contact angle measurement versus contact line speed during water spreading onto maltodextrin DE29 layers. Influence of the thickness at $a_w = 0.75$. (a) $\theta(U)$ (b) scaling $\theta(eU)$.

In Fig. 4.38, a more precise representation of the scaling is presented. At different water activities a_w , we plot the thickness of the sample as a function of the contact line speed for a

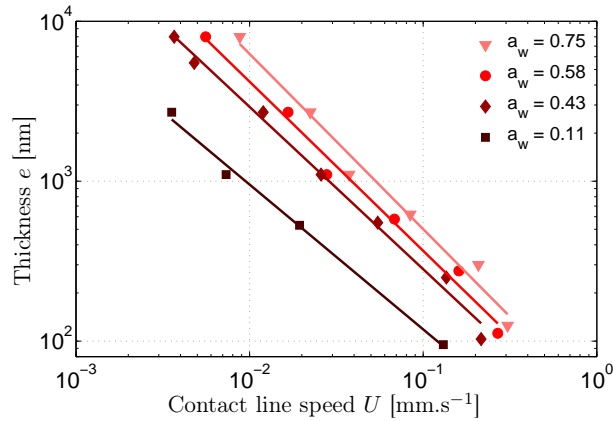


Figure 4.38: Scaling $\theta(eU)$ for a given contact angle - Extraction of the thickness e and speed U at $\theta = 11^\circ$ during water spreading onto layers of maltodextrin DE29 equilibrated at different a_w . Data were fitted to a power law with exponent $\beta = -0.90, -1.02, -1.05$ and -1.09 for $a_w = 0.11, 0.43, 0.58$ and 0.75 .

given contact angle $\theta = 11^\circ$. By fitting with power laws, we obtain exponents very close to -1. It perfectly validates the scaling in eU and iso-contact angle lines (or iso- θ) in the thin film regime. As humidity increases, the iso- θ curves are shifted toward larger thickness values. That effect results from the increase of the diffusion coefficient D_p with increasing humidity.

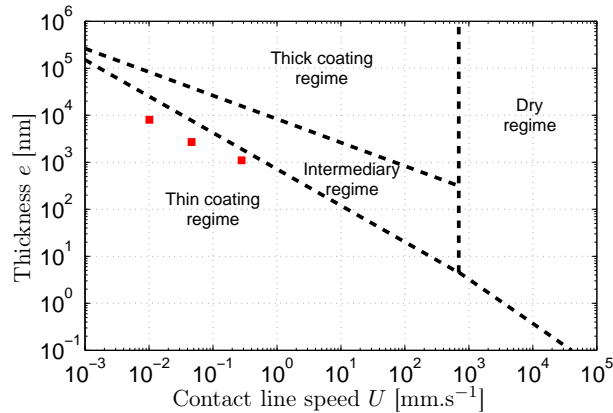


Figure 4.39: Experimental frontier in the wetting diagram - Experimental determination of the frontier between thin film regime and intermediary thick regime. Wetting diagram built with the following parameters: $D_p = 1.4 \cdot 10^{-11} \text{ m}^2 \cdot \text{s}^{-1}$, $D_v = 2.7 \cdot 10^{-5} \text{ m}^2 \cdot \text{s}^{-1}$, $\rho = 997.05 \cdot 10^3 \text{ g} \cdot \text{m}^{-3}$, $c_{sat} = 23 \text{ g} \cdot \text{m}^{-3}$, $\xi[\mu\text{m}] = 37 U[\text{mm} \cdot \text{s}^{-1}]^{-0.55}$, $L = 5 \text{ mm}$ and $K = 0.006$. Experimental frontier points are represented in red for $a_w = 0.75$.

We can use the graph of Fig. 4.37b to obtain experimental points at the frontier between thin film regime and intermediary thick regime. We extract the coordinates (e, U) of the points where the scaling starts to fail. We represent these points in the wetting diagram of Fig. 4.39

4. WETTING REGIMES

with red squares. This wetting diagram is plotted with the parameters corresponding to $a_w = 0.75$ ($D_p = 1.4 \cdot 10^{-11} \text{ m}^2 \cdot \text{s}^{-1}$ and $\xi[\mu\text{m}] = 37 U[\text{mm} \cdot \text{s}^{-1}]^{-0.55}$). We have a fairly good agreement between the diagram frontier and the experimental data points. It shows that the choice of the new cut-off length ξ is relevant.

4.4.3.2 Observation of the thick film regime

In the previous subsection, we have presented the contact angle evolution with velocity for water onto maltodextrin DE29 at $a_w = 0.75$. In Fig. 4.37a, we could observe that at large velocities U , the curve for the $8 \mu\text{m}$ -thick sample gets close to the curve for the $2.7 \mu\text{m}$ -thick sample. Nevertheless, we do not reach the thick film regime. Using the very thick sample prepared with the method described in Materials & Methods (section 3.2.2), we could evidence the thick film regime at the water activity $a_w = 0.43$.

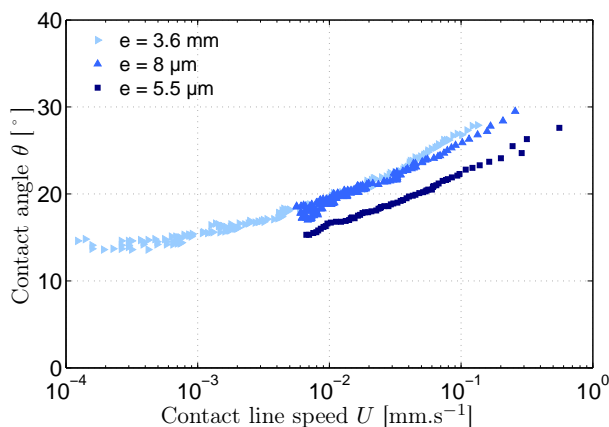


Figure 4.40: Thick film regime evidence in contact angle measurements - Contact angle measurement versus contact line speed during water spreading onto maltodextrin DE29 layers. Influence of the thickness at $a_w = 0.43$.

We show in Fig. 4.40 the measurement of θ versus U for three samples equilibrated at $a_w = 0.43$. We can notice that the thicker coating, *i.e.* the one at $e = 3.6 \text{ mm}$, follows a $\theta(U)$ curve that superimposes at high speeds ($U > 10^{-2} \text{ mm} \cdot \text{s}^{-1}$) with the curve obtained for a coating 450 times thinner, *i.e.* $e = 8 \mu\text{m}$ (NB: the smaller velocities and thicknesses are not plotted here). We will come back on these data later in the glass transition chapter). This observation is the last missing piece of the hydrated regimes discussed previously. It corresponds to the thick film regime in which thickness e does not influence the hydration at the contact line any more. At very large eU , θ only depends on the contact line velocity U .

4.4.3.3 Iso- θ in the wetting diagram

We have shown that the scaling $\phi(eU)$ in the thin film regime is confirmed experimentally by the contact angle measurements. In that regime, the iso- θ curves (such as the ones of Fig. 4.38)

vary as U^{-1} . We can therefore plot systematically those curves for different values of θ in order to probe the extent of the thin film regime.

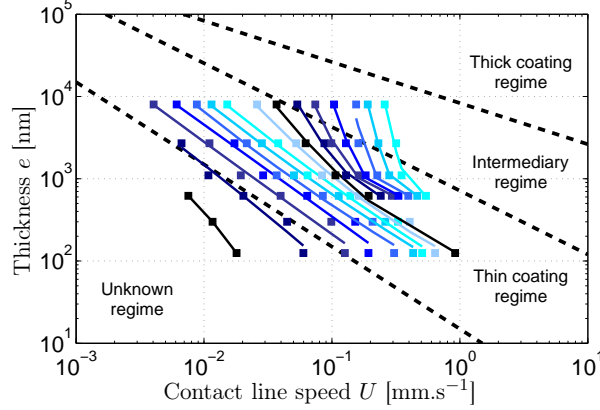


Figure 4.41: Final wetting diagram and isotheta - Wetting diagram built with the following parameters: $D_p = 1.4 \cdot 10^{-11} \text{ m}^2 \cdot \text{s}^{-1}$, $D_v = 2.7 \cdot 10^{-5} \text{ m}^2 \cdot \text{s}^{-1}$, $\rho = 997.05 \cdot 10^3 \text{ g} \cdot \text{m}^{-3}$, $c_{sat} = 23 \text{ g} \cdot \text{m}^{-3}$, $\xi[\mu\text{m}] = 37 U[\text{mm} \cdot \text{s}^{-1}]^{-0.55}$, $L = 5 \text{ mm}$ and $K = 0.006$. Experimental iso- θ are represented at $a_w = 0.75$ (θ from 3° to 31° , every 2°)

We use the data of Fig. 4.37a in order to extract the iso- θ . We plot these lines in the wetting diagram for θ from 3° to 31° by step of 2° (Fig. 4.41). We zoom in the zone of interest. We notice the signature of the scaling in eU in the thin film regime where the iso- θ curves are straight lines in U^β with β close to -1. We can also notice the transition to the intermediary regime for large e and U where we loose this scaling property. The iso- θ bend and the dependence on the thickness e is reduced. For small thicknesses and velocities, the scaling also seems not to be valid any more. A new regime (named "Unknown regime"), materialized by the another dotted line, must be thought of for this part of the diagram.

In order to improve the precision on the range of θ within which the scaling is observed, we fit all the iso- θ points with power laws $e \sim U^\beta$ and plot the exponent β as a function of the contact angle (Fig. 4.42). We observe that β is close to -1 for intermediate contact angles and is smaller than -1 at small and large contact angles (values of β at small θ are less precise because fewer data points are available). It is a confirmation of the diagram presented in Fig. 4.41 where the power law $e \sim U^{-1}$ is observed at intermediate contact angles. In this figure, we also vary the humidity to see if it modifies the range where scaling is valid. We observe a similar shape for $\beta(\theta)$. The humidity slightly modifies the value of β . At large a_w , β is larger in absolute value and the contact angle range within which the exponent is close to -1 is shifted to slightly smaller values.

Thus, as suspected, the scaling $\theta(eU)$, expected in the thin film regime, fails at small contact angles. It is characterized by a plateau of contact angle that appears at small velocities in $\theta(U)$ curves. One possibility is that the droplet edge becomes much more viscous for small velocities.

4. WETTING REGIMES

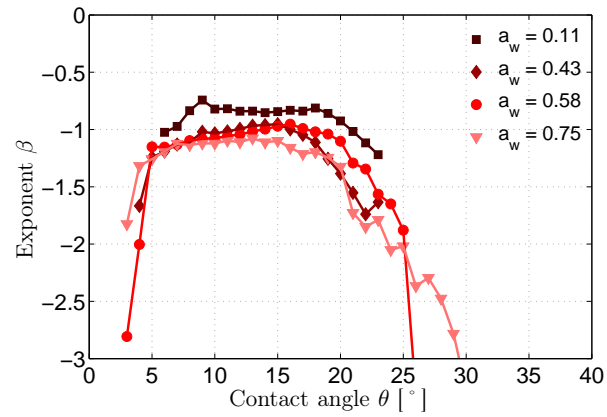


Figure 4.42: Exponent of $e(U)$ function at various water activities - Extraction of the exponent β for different contact angles and water activities such as $e = \alpha U^\beta$ during water spreading onto layers of maltodextrin DE29.

Dissolution would modify the spreading process by creating a viscosity increase at the contact line. Furthermore, other observations at small speeds remain unexplained such as the "bump" in the diffusion/condensation region of the profile (*i.e.* the increase of ϕ with x close to the contact line).

4.5 Conclusions

In this chapter, we have studied the water transfers to a soluble layer during the spreading of a water droplet. We have shown that hydration results from three different mechanisms: condensation, diffusion and convection. Depending on the Péclet numbers in air and polymer, we can observe different situations as represented in Fig. 4.43. The main results are summarized here below:

- At small Péclet number in air, two regions have been identified ahead the contact line: diffusion/condensation region for $x < \kappa$ (grey region in Fig. 4.43) and a condensation/convection region for $x > \kappa$ (blue region in Fig. 4.43). The non-linearities ($a_w(\phi)$ and $D_p(\phi)$) increase the value of κ by two or three orders of magnitude. Using free-spreading experiments, we have validated the existence of both these regions with an experimental cut-off length we denote ξ .
- At larger Péclet number in air, vertical concentration gradients appear in the layer. They are characterized by the length x_C . When x_C becomes larger than the size of the diffusion/condensation region, the gradients can be observed at $x < x_C$ as represented in Fig. 4.43 (green area).

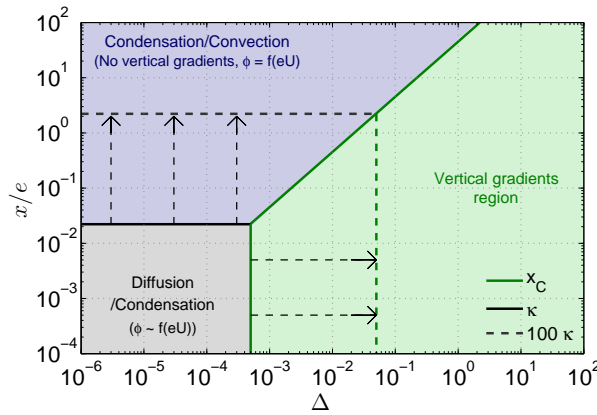


Figure 4.43: Diagram of existence of different mass transfers - Normalized characteristic lengths of the condensation/diffusion equation: κ/e and x_C/e versus the normalized Péclet number in air Δ . The ratio $\Delta/(Pe)_p = 2.2 \cdot 10^{-2}$ leads to three different regions. Non-linearities increase the value of κ . We also represent the extent of the diffusion/condensation region with dotted lines if κ is 100 times larger.

- When no gradients are observed, *i.e.* when $x_C < \xi$, a scaling of the contact angle in eU was predicted and confirmed experimentally. It corresponds to a larger thin film regime than the one predicted by Tay *et al.*. Instead of being nanometric, the cut-off length is micrometric. The scaling with eU is still valid in the diffusion/condensation region because the effects of direct diffusion and horizontal diffusion cancel each other out.
- A new wetting diagram has been established with the new cut-off length ξ . An intermediary regime has been considered to account for the dependence of θ on the thickness e when

4. WETTING REGIMES

gradients are localized at $\xi < x < L$. An unknown regime appears at small e and U , which remains to be interpreted.

With this new wetting diagram, we are now able to discuss more precisely the effect of hydration in the case of very dry layers of maltodextrin being wetted by water. In that case, the diffusion coefficient D_p strongly varies during the spreading process and the material crosses its glass transition.

Key messages

- At small Péclet number in air, horizontal diffusion leads to a new region ahead the contact line, with an extent set by κ . Non linearities ($a_w(\phi)$ and $D_p(\phi)$) increase the value of κ .
- The scaling $\phi(eU)$, characteristic of the condensation/convection region, is also valid in the diffusion/condensation region.
- At large eU , vertical gradients of concentration appear ahead the contact line and the scaling in eU does not work any more.
- A new quantitative wetting diagram has been established, based on a cut-off length ξ set by diffusion effects.

5

Glass transition effect in wetting dynamics

5.1 Introduction

In this chapter, we explore experimentally the situation where hydration induces a sharp change in the diffusion coefficient of water in the polymer: this is what happens when the polymer undergoes a glass transition in water content. The diffusion coefficient of water changes by orders of magnitude upon glass transition, and we show that it results in a sharp effect on the course of the spreading, as the hydration will be affected by the change in diffusion in the coating. We expand the modelling of the previous chapter to account for glass transition effects.

5.2 Wetting dynamics

In this section, we focus our attention on wetting dynamics onto a dry layer of maltodextrin. When the relative humidity RH above the layer is very small, the initial water content ϕ is small too. Thus, the coating is in a glassy state at the beginning of the spreading experiment. In that case, the diffusion coefficient of water in maltodextrin DE29 is of the order of 10^{-12} - 10^{-13} $\text{m}^2.\text{s}^{-1}$. We recall in Fig. 5.1 the water content dependent diffusion coefficient $D_p(\phi)$ (see section 3.1.2.5). When hydration occurs through condensation and direct diffusion, D_p strongly increases with water content ϕ and the coating finally enters its melt state. Using the expression of the mutual diffusion coefficient D_p , we can assess an approximate value of the water content at glass transition ϕ_g . Indeed, the glass transition is ill-defined, and those values are approximate. After an increase phase, the second-derivative of $D_p(\phi)$ reaches a plateau around $\phi_g = 18$ %. It means that the glassy state corresponds to water activities below $a_w^g = 0.6$. Thus, we will consider the diffusion coefficient $D_p = 6 \cdot 10^{-12}$ $\text{m}^2.\text{s}^{-1}$ at glass transition.

5. GLASS TRANSITION EFFECT IN WETTING DYNAMICS

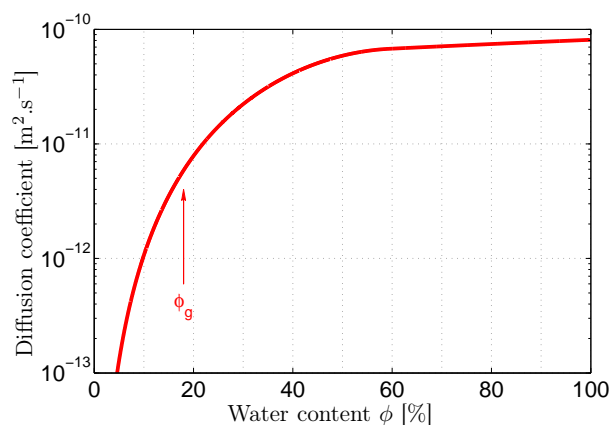


Figure 5.1: Diffusion coefficient of water in maltodextrin DE29 - Mutual diffusion coefficient D_p as a function of the water content ϕ as presented in section 3.1.2.5.

5.2.1 Contact angle measurements

In Fig. 5.2a, we show again the $\theta(U)$ curves for different thicknesses we have presented in section 4.4.3. The curves were obtained at $a_w = 0.75$, *i.e.* well above the glass transition. In that case, the hydration of the maltodextrin layer does not strongly modify the value of D_p since the polymer is initially in its melt state.

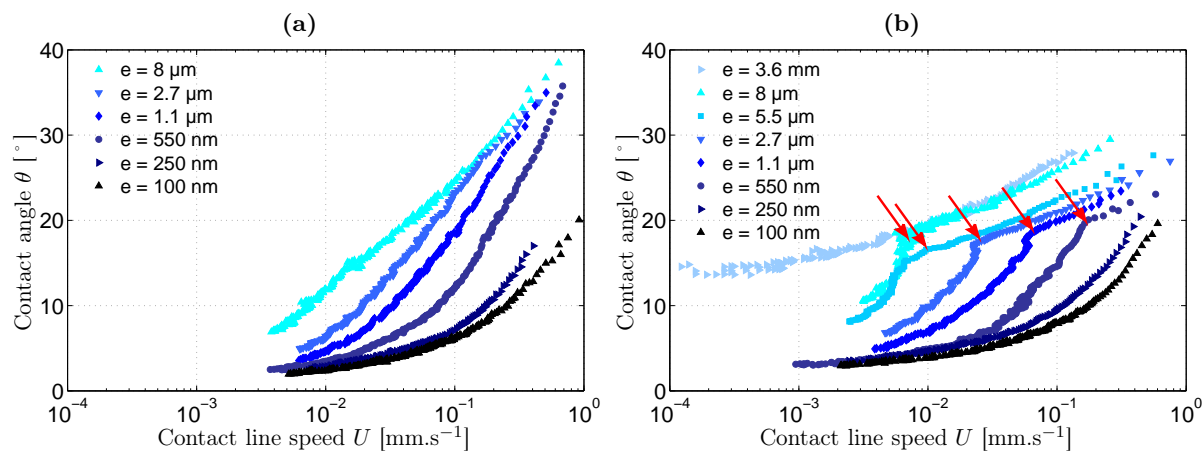


Figure 5.2: Glass transition and contact angle - Contact angle measurement versus contact line speed during water spreading onto maltodextrin DE29 layers. Influence of the thickness at two different water activities. Kinks are observed at $a_w = 0.43$. (a) $a_w = 0.75$. (b) $a_w = 0.43$.

We present in Fig. 5.2b the same study performed at $a_w = 0.43$. At smaller humidity, a new feature appears on the $\theta(U)$ curves that was never seen before. The $\theta(U)$ curves are similar at small velocities and small contact angles for both water activities (θ is slightly smaller at $a_w = 0.75$), but at $a_w = 0.43$, a kink shows up towards higher speeds for all the thicknesses except the

larger one ($e = 3.6$ mm). The slope of the $\theta(U)$ curves is strongly lessened after the kinks. The kink is observed experimentally for every a_w smaller than 0.6 (not shown), which is the water activity at glass transition. We show in the following that it results from glass transition effects in the coating. Qualitatively, the velocity U decreases with spreading time and the layer initially glassy at large U becomes melt at small U . We denote θ_g and U_g the coordinates of the kink. We have found that U_g decreases with e and increases with a_w (not shown), whereas θ_g remains roughly constant at a given humidity.

We represent in Fig. 5.3 the evolution of the critical velocity U_g where the kink is observed as a function of layer thickness. We include in this plot the experiments performed at all the water activities and also a data point obtained at $e = 250$ nm with the swollen drop experiment. We can notice that U_g approximately varies according to a power law with an exponent -1 (dotted line). We will show later in this chapter that this variation of U_g as $1/e$ can be predicted.

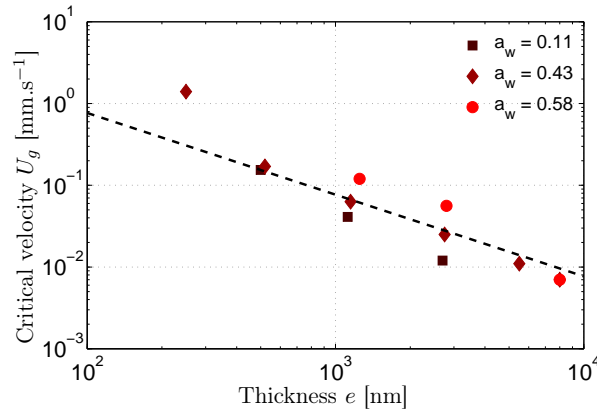


Figure 5.3: Kink coordinates in contact angle data - Extraction of the critical velocities at the kink in $\theta(U)$ curves and representation versus sample thickness e in the case of water spreading onto maltodextrin DE29 layers. Three different water activities are represented. The black dotted line represents a power law with an exponent -1.

5.2.2 Water content profiles

We now report the hydration profiles $\phi(x)$: we also observe a modification of the hydration process ahead the contact line for substrates initially in the glassy state. Fig. 5.4a presents the color analysis results at different water activities a_w for a 250 nm-thick layer of maltodextrin DE29. At $a_w = 0.75$, as shown in section 4.4.1.1, we observe a plateau followed by a sharp drop of ϕ (diffusion/condensation region), and a decrease of ϕ at larger x (condensation/convection region). At $a_w = 0.11$ and $a_w = 0.43$, we also observe the diffusion region ahead the contact line. The plateau of water content close to the contact line shows that diffusion effects in the layer still play a role at small humidities. The size of the diffusion region ξ decreases with the water activity a_w . It is in agreement with the finding that the plateau length varies proportionally with D_p . Indeed, D_p is smaller at small a_w .

5. GLASS TRANSITION EFFECT IN WETTING DYNAMICS

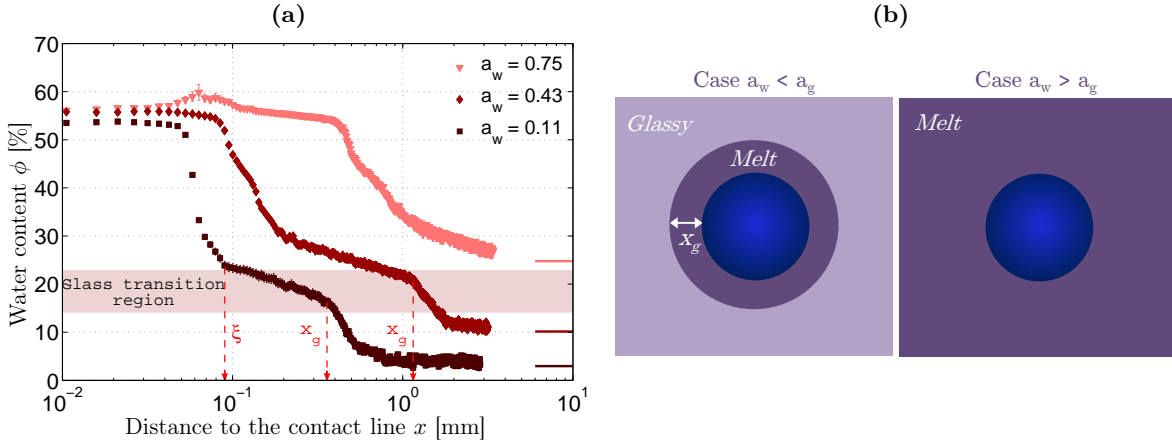


Figure 5.4: Glass transition and hydration profiles - (a) Determination of the water content ahead the contact line during water spreading onto 250 nm-thick layers of maltodextrin DE29. Influence of water activity. $U = 10^{-2}$ mm.s $^{-1}$. (b) Schematic top view of the drop at small or high water activity.

Let's now look at the profiles at larger distances for $x > \xi$. The curves at $a_w = 0.11$ and $a_w = 0.43$ present an additional kink for $x = x_g$ (for instance, at $a_w = 0.11$, $x_g \simeq 360$ μm). At $x > x_g$, the water content decreases faster with x . This region corresponds to a glassy layer. Thus, the strong variation in the slope of the water content results from the strong variation of D_p (by two orders of magnitude) at glass transition.

We summarize the two different kinds of profiles in Fig. 5.4b with a schematic top view of the drop at a water activity below or above glass transition. At large a_w , the layer is always in melt state. At small a_w , the melt zone is limited. The size of the melt zone x_g depends on the contact line velocity. It is large at small U . At $U = U_g$, x_g becomes negligible.

The kink in $\theta(U)$ curves is observed for the thicker samples where the color analysis is not possible ($e > 1.1$ μm). We therefore cannot measure the water content profiles for $U = U_g$. Nevertheless, with the swollen droplet experiment, we were able to evidence the kink in $\theta(U)$ for a 250 nm-thick sample at $U_g \sim 1.4$ mm.s $^{-1}$. We present the obtained water content profile in Fig. 5.5. The incertitude on ϕ is not negligible since the colors of the layer quickly vary in the vicinity of the contact line in a short range of speed. The curve is compared to the profile obtained at $U = 10^{-2}$ mm.s $^{-1}$, *i.e.* at $U < U_g$. As expected, the water content is much smaller at $U \sim U_g$. The fraction at the contact line gets closer to ϕ_g . The pronounced kink that is observed at $U < U_g$ is smoothed.

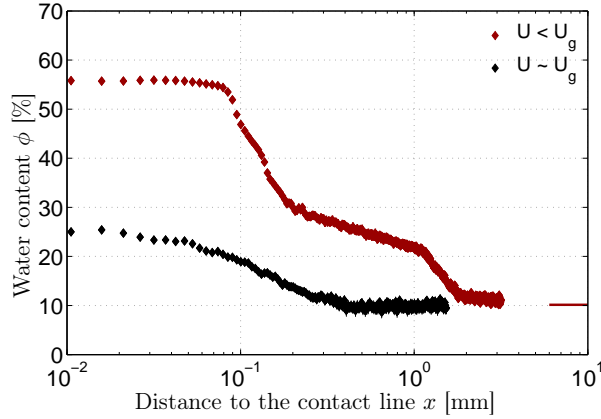


Figure 5.5: Hydration profile at the critical glass transition speed - Determination of the water content ahead the contact line during water spreading onto 250 nm-thick layers of maltodextrin DE29. Influence of the speed: comparison between $U = 10^{-2} \text{ mm.s}^{-1}$ ($U < U_g$) and $U = 1.4 \text{ mm.s}^{-1}$ ($U \sim U_g$).

5.3 Consequences of glass transition on hydration mechanisms

In the previous sections, we have evidenced an effect of the humidity on the $\theta(U)$ curves as well as on the $\phi(x)$ profiles. In both measurements, we have identified a kink, *i.e.* a sharp variation of the derivatives of θ and ϕ with respectively U_g and x_g . The water content profiles indicate that the kink in $\phi(x)$ curves corresponds to the transition from a glassy coating at large x to a melt one at small x . We are going to show that the kink in $\theta(U)$ also corresponds to glass transition.

In the previous chapter, we have demonstrated that wetting is controlled by a cut-off length ξ , which represents the size of the diffusion/condensation region. Two different cases can happen depending on the contact line velocity U . At small U , the hydration of the coating leads to two distinct regions: a glassy one at $x > x_g$ and a melt one at $x < x_g$. As long as x_g remains larger than ξ , the droplet experiences a hydrated melt substrate and the contact angle is small. When the velocity increases, there is a critical speed U_g where the size of the melt region x_g becomes comparable to the cut-off length ξ , both being of the order of the nanometer. This critical point means that the hydration of the layer is reduced significantly for $U > U_g$. The consequence is the fast increase of the contact angle at $U \sim U_g$ because the droplet experiences a glassy substrate with a small diffusion coefficient D_p . We present both cases in Fig. 5.6 with schematic representations of the droplet (top view) spreading onto a melt substrate (picture on the left) or glassy substrate (picture on the right), and the corresponding position in the $\theta(U)$ curve.

We come back to the modelling of hydration presented in section 4.4.2.4. If we focus on the unusual kink observed in the $\theta(U)$ curves, it is possible to predict the critical velocity U_g . The results of the contact angle measurements show that the kinks correspond to the intermediary thick regime where the scaling in eU is not valid any more. At $U = U_g$, the quantity of water

5. GLASS TRANSITION EFFECT IN WETTING DYNAMICS

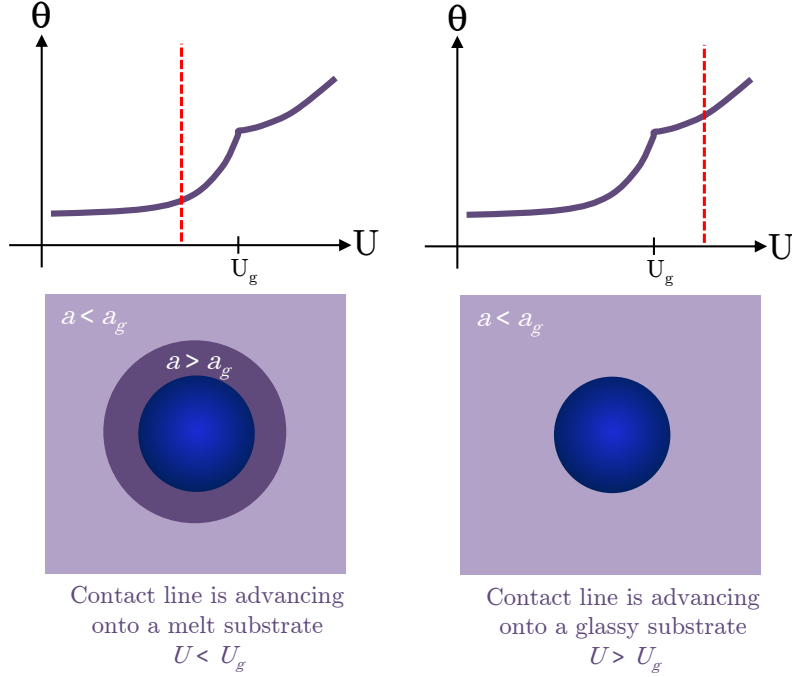


Figure 5.6: Schematic representation of hydration below and above glass transition - Link between contact angle measurement and hydration of the layer. The drop experiences a melt substrate below U_g and a glassy one above U_g .

coming from condensation corresponds to a water fraction at the contact line $\phi = \phi_g$, *i.e.* $\Delta\phi^{int} = \phi_g - \phi_0$. Thus, the critical velocity U_g at which the glass transition occurs can be obtained using Eq. 4.18 and setting $\Delta\phi^{int} = \phi_g - \phi_0$. The kinks being close to the frontier thin/intermediary, we have $e_2 \sim e$ and we can use the approximation $\Delta\phi^{int} \sim K \frac{D_v c_{sat}}{\rho U} \frac{1}{e} \left(\ln \frac{e_3}{e} \right)$. We obtain the following relation:

$$\phi_g - \phi_0 \sim K \frac{D_v c_{sat}}{2\rho e U_g} \ln \left(\frac{L D_p}{U_g e^2} \right) \quad (5.1)$$

If we assume a constant logarithmic term, we therefore obtain an evolution of U_g in $1/e$. This dependence is in agreement with experimental observations as it was shown in Fig. 5.3. Finally, as explained earlier in this manuscript, the constant K is introduced to approximate the value of $\Delta\phi$. If we refer to Tay *et al.* theory, we should use an implicit integral. Therefore, the value of K can also be obtained with:

$$\frac{1}{K} \sim \frac{(\pi - \theta)}{\phi(L) - \phi(\xi)} \int_{\phi(L)}^{\phi(\xi)} \frac{d\phi}{(1 - \phi)^2 (1 - a_w(\phi))} \quad (5.2)$$

Thus, we can predict qualitatively the amount of water at the contact line using eq. 5.1. In theory, we should calculate the water content at $x = x_g = \xi$. However, ξ is very small at the

transition since the diffusion coefficient is strongly reduced and U much larger than the one considered in the profiles of Fig. 5.4a. Moreover, the diffusion region is characterized by a plateau of ϕ . The calculation of $\Delta\phi$ at $x = 0$ instead of ξ therefore leads to an error that remains small.

With this expression of U_g , we are able to assess the constant K . Indeed, we can compare the experimental values of U_g to the theoretical $\frac{U_g}{K}$. Fig. 5.7a gives this comparison in the case of water spreading onto maltodextrin DE29 and with $\phi_g = 18\%$. We approximate the logarithmic term $\ln\left(\frac{LD_p}{U_g e^2}\right)$ using the value of the experimental U_g . The slope of a linear fit provides a value of $K = 0.006$. This value, which is quite sensitive to the choice of ϕ_g , was used to build all the wetting diagrams of this manuscript.

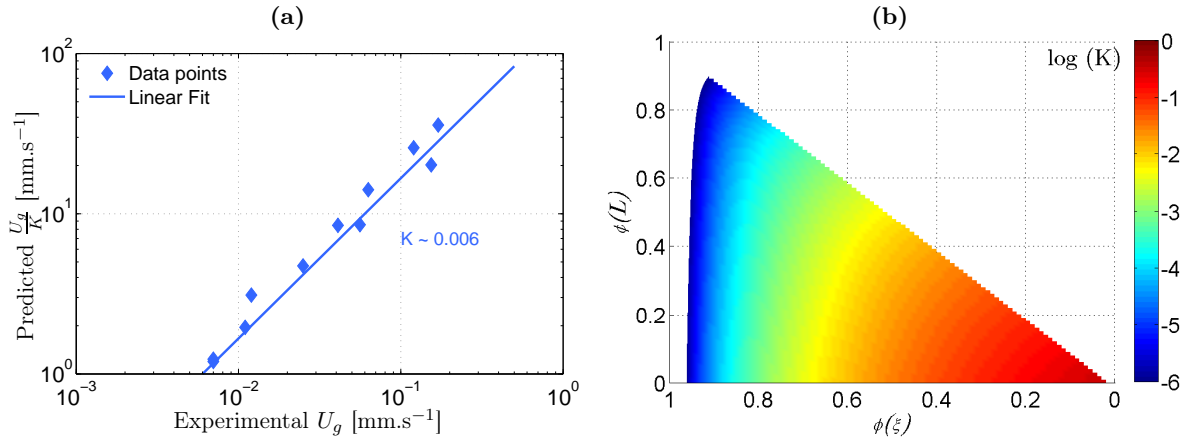


Figure 5.7: Assessment of the constant K - (a) Comparison between predicted U_g/K and experimental U_g . The slope of the linear fit gives the inverse of the constant K . (b) Theoretical calculation of K using Flory sorption isotherm with $\chi = 0.5$. $\theta = 20^\circ$.

In Fig. 5.7b, we represent the calculation of K using Eq. 5.2 and a Flory sorption isotherm with $\chi = 0.5$. Some slight differences are observed between the experimental value of K and the theoretical one. Nevertheless, the choice of K is not crucial in our study. Indeed, K does not modify the important frontiers of the wetting diagram used in our discussions (thin/intermediary and intermediary/thick) but only the dry regime frontiers. In the following section, we will discuss the link between this wetting diagram and the kink observed in $\theta(U)$ curves.

5.4 Link with the wetting diagram

As explained previously, the diffusion coefficient D_p increases by one to two orders of magnitude when the water volume fraction ϕ reaches its glass transition value ϕ_g . As a consequence, the water content ϕ of the coating abruptly increases at glass transition because the diffusion process becomes suddenly faster. Hence, the observed kinks can be attributed to a sudden transition to the thin regime where the layer is completely hydrated due to a fast increase in D_p , when the

5. GLASS TRANSITION EFFECT IN WETTING DYNAMICS

polymer undergoes a transition from glassy to melt state.

Going back to the description developed in the preceding chapter, this effect can be viewed in the eU diagram as a shift of the frontier limiting the intermediary thick regime and the thin film regime (we recall the expression of the frontier in Eq. 5.3). With the strong increase of the diffusion coefficient D_p occurring at glass transition, the e_2 increases within a very small range of water absorption by the layer. Increasing D_p by two orders of magnitude shifts this frontier upward, by one order of magnitude.

$$e_2 = \sqrt{\frac{\xi D_p}{U}} \quad (5.3)$$

In our typical experiment, we start with a coating of given thickness e and small diffusion coefficient D_p , so the trajectory depicting our experiments is given by a horizontal line in the eU diagram, starting in the high velocity region, in the intermediary thick regime, and moving towards smaller velocities. In the meantime, the fraction of solvent at the contact line increases until it reaches the glass transition ϕ_g value at $U = U_g$ where it abruptly homogenizes across the whole thickness. The e_2 and e_3 frontiers then move upward and the remaining of the spreading experiences a thin film regime. We summarize the history of hydration in the three wetting diagrams of Fig. 5.8:

- Glassy contact line: In Fig. 5.8a, we show that at U larger than U_g , the drop experiences the intermediary thick regime. The diffusion coefficient is small ($D_p = 1.1 \cdot 10^{-12} \text{ m}^2 \cdot \text{s}^{-1}$) and the iso- θ are not in U^{-1} in the eU diagram.
- Glassy transition: In Fig. 5.8b, we show that at $U = U_g$, the kinks coordinates (extracted from $\theta(U)$ curves) are localized at the frontier between intermediary and thin regimes. The diffusion coefficient is the one at glass transition.
- Melt contact line: At $U < U_g$ (Fig. 5.8c), the frontier e_2 is moved upward due to the larger diffusion coefficient $D_p = 4 \cdot 10^{-11} \text{ m}^2 \cdot \text{s}^{-1}$. The iso- θ are straight lines in the eU diagram, power laws such $e \sim U^{-1}$, characterizing the thin film regime where we observed a scaling $\theta(eU)$.

In conclusion, we have shown that:

- Glass transition involves a kink in $\theta(U)$ curves.
- The kink can be related to the distance to the contact line x_g where glass transition is crossed such that $x_g = \xi \sim 1 \text{ nm}$.
- The wetting diagram thickness vs velocity can be used to explain the abrupt change of contact angle at the kink. A displacement of the frontier thin/intermediary is induced by the strong variation of the diffusion coefficient D_p at glass transition.

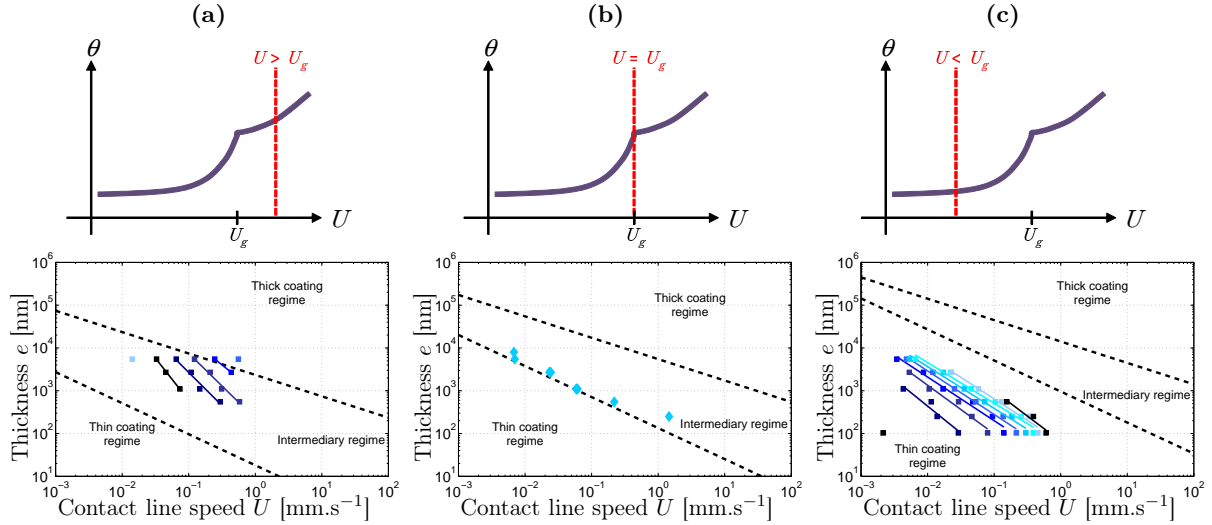


Figure 5.8: Wetting diagram built for maltodextrin DE29 equilibrated at $a_w = 0.43$.

Following parameters are used: $D_v = 2.7 \cdot 10^{-5} \text{ m}^2 \cdot \text{s}^{-1}$, $\rho = 997.05 \cdot 10^3 \text{ g} \cdot \text{m}^{-3}$, $c_{sat} = 23 \text{ g} \cdot \text{m}^{-3}$, $L = 5 \text{ mm}$ and $K = 0.006$. - (a) Iso- θ in glassy state ($\phi < \phi_g$). $D_p = 1.1 \cdot 10^{-12} \text{ m}^2 \cdot \text{s}^{-1}$ and $\xi[\mu\text{m}] = 0.3 U[\text{mm} \cdot \text{s}^{-1}]^{-0.45}$. (b) Coordinates of the kinks at glass transition ($\phi = \phi_g$). $D_p = 6 \cdot 10^{-12} \text{ m}^2 \cdot \text{s}^{-1}$ and $\xi[\mu\text{m}] = 3 U[\text{mm} \cdot \text{s}^{-1}]^{-0.45}$. (c) Iso- θ in melt state ($\phi > \phi_g$). $D_p = 4 \cdot 10^{-11} \text{ m}^2 \cdot \text{s}^{-1}$ and $\xi[\mu\text{m}] = 23 U[\text{mm} \cdot \text{s}^{-1}]^{-0.45}$.

5.5 Confirmation with various polymers and solvents

We have investigated different systems coating/solvent for which the glass transition occurs at different solvent concentrations. In a first series of experiments, we have tested maltodextrin DE6 instead of the DE29. That maltodextrin with a larger molecular weight presents a glass transition at a larger a_g . As a consequence, the intermediary thick regime frontier is shifted downwards in the wetting diagram. For similar U_g , the thickness of the coating required to cross the glass transition is smaller. We plot in Fig. 5.9a the results of the contact angle measurement at $a_w = 0.43$ for respectively 79 nm-thick, 41 nm-thick and 27 nm-thick layers. Kinks are also observed even if they are less pronounced than with maltodextrin DE29. In addition, we also observe the kinks in $\phi(x)$ profiles (not shown) confirming the existence of a glassy region at large distances from the contact line and a melt one ahead the contact line.

Finally, solvents with different volatility were tested. Indeed, according to Eq. 5.1, varying c_{sat} should modify the transition velocity U_g . The contact angles curves are plotted in Fig. 5.9b for water, DMSO and ethylene glycol on 250 nm-thick coatings of maltodextrin DE29 at a water activity $a_w = 0$. For all solvents, the $\theta(U)$ curves present a kink. We observe that the critical velocity U_g decreases with the volatility of the solvent represented by its vapour concentration at saturation c_{sat} as shown in Table 5.1. In our case, c_{sat} varies by two orders of magnitude. This decrease of U_g is in agreement with Eq. 5.1. Besides, smaller variations of D_v and ρ are also expected when changing the solvent.

5. GLASS TRANSITION EFFECT IN WETTING DYNAMICS

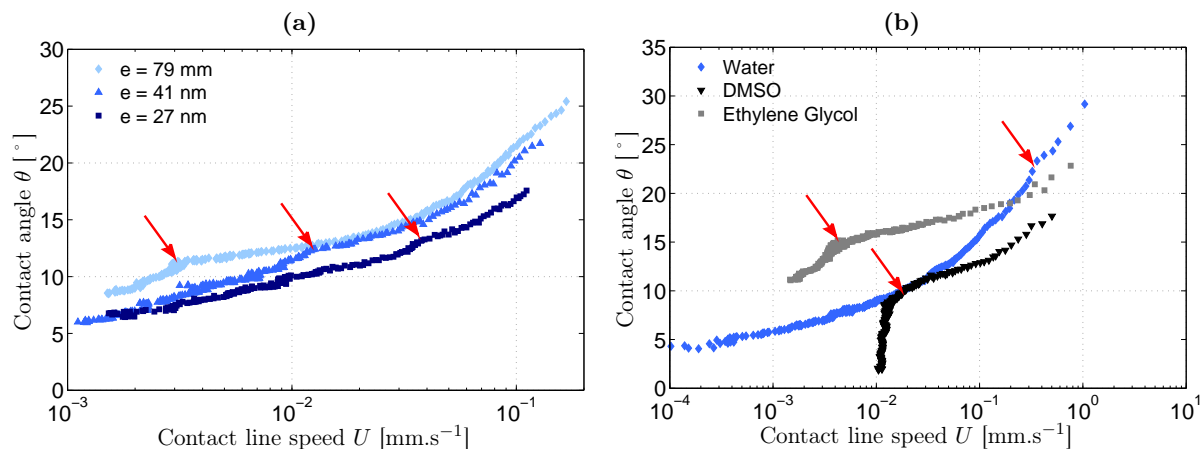


Figure 5.9: Kink on contact angle measurements for different systems - (a) Contact angle measurement versus contact line speed during water spreading onto layers of maltodextrin DE6. (b) Contact angle measurement versus contact line speed during spreading onto 250 nm-thick layers of maltodextrin DE29. Three different solvents are presented.

Table 5.1: Critical velocities U_g for different solvents spreading onto a 250 nm-thick maltodextrin DE29 layer equilibrated at $a_w = 0$, and saturation concentration c_{sat} of these solvents at 25 °C

Liquid	U_g [$\text{mm}\cdot\text{s}^{-1}$]	c_{sat} [$\text{g}\cdot\text{m}^{-3}$]
Water	1.4	23.0
DMSO	0.025	1.75
Ethylene Glycol	0.0013	0.23
1,3 propanediol	0.083	4.24
2,3 butanediol	0.068	1.18

We plot in Fig. 5.10 the evolution of the critical velocity U_g versus the layer thickness e for the five different solvents of maltodextrin we have tested. All the lines are power laws with an exponent -1. As shown previously with water, the values of U_g also follow a dependence in $1/e$. Even if we don't know the precise value of ϕ_g , this representation confirms the good agreement with Eq. 5.1 and that c_{sat} is the main parameter that influences the values of U_g . The value of $\phi - \phi_g$ probably does not strongly vary from one solvent to another and K remains the only unknown parameter in the equation. However, if we consider that the value of ϕ_g remains close to its value for water, we can assess the value of K for the various solvents. The results are presented in Table 5.2. We observe a strong variation of K with the solvent. K being a function of the sorption isotherm, this result is logical.

In conclusion, all the results of experiments using different solvents or different maltodex-

trins confirmed the effects of glass transition observed with the system water/maltodextrin DE29.

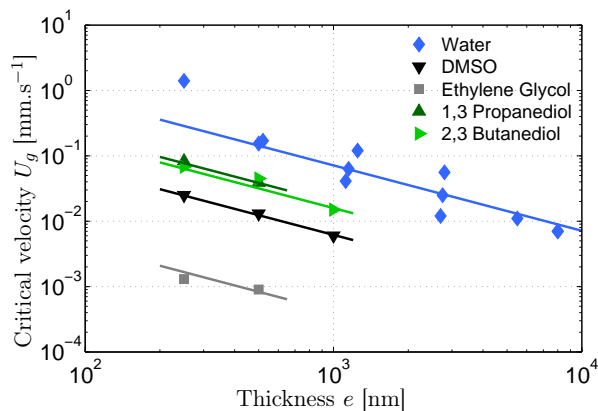


Figure 5.10: Kink coordinates for different solvents of maltodextrin - Extraction of the critical velocities at the kink in $\theta(U)$ curves and representation versus sample thickness e . Different solvents spreading onto maltodextrin DE29 layers are considered. The lines represent power laws with an exponent -1.

Table 5.2: Calculation of the constant K via Eq. 5.1 using $\phi_g = 18$ % for different solvents of maltodextrin.

Liquid	K
Water	0.006
DMSO	0.017
Ethylene Glycol	0.021
1,3 propanediol	0.162
2,3 butanediol	0.378

5.6 Conclusions

We have shown how glass transition effects in a coating can tune the wettability of the coating during the course of a spreading experiment, in the particular case where the glass transition itself is caused by the absorption of the spreading liquid. This effect is attributed to the drastic changes in the value of the diffusion coefficient of the solvent in the coating at glass transition, which varies by one to two orders of magnitude when the water content varies from 2 to 30 %. We have shown how the glass transition causes an abrupt change in the hydration process by accelerating it, thus increasing the wettability of the drop. This effect is clearly evidenced by our experimental data, as kinks are observed in $\theta(U)$ curves and in $\phi(x)$ profiles. Furthermore, we were able to derive a model accounting for our experimental observations and to link these

5. GLASS TRANSITION EFFECT IN WETTING DYNAMICS

observations to the wetting diagram presented in the previous chapter. We finally show that the same effect is observed with different solvents and molecular weights of the polymer.

Key messages

- Glass transition in maltodextrin modifies spreading dynamics through the diffusion coefficient change.
- A kink appears in $\theta(U)$ and $\phi(x)$ curves when glass transition is crossed.
- The kink in $\theta(U)$ can be related to the distance to the contact line x_g where glass transition is crossed such $x_g = \xi$.
- The modification of spreading dynamics at glass transition can be explained by a shift of the thin/intermediary frontier in the wetting diagram.

6

Dissolution and wetting

6.1 Introduction

Among the mass transfers discussed in chapter 4, there is still one which has not been considered yet: the dissolution of the polymer coating. Maltodextrin is soluble in water and during the spreading process, the coating below the water droplet is partially dissolved. For instance, we can observe that after complete evaporation of the droplet, the coating is dissolved since there are no more colors below the droplet due to optical interferences. At large contact line velocities, we can notice that Newton hues are still visible under the droplet in the vicinity of the contact line. These observations demonstrate that the coating dissolution depends on the contact line velocity. The consequence of dissolution is that it leads to an increase of the local concentration in the liquid edge that may modify the spreading dynamics, especially at small contact line velocity or with high molecular weights polymers. In this chapter, we present preliminary results about dissolution effects. We will show that the polymer layer wrinkles behind the contact line. We will discuss those observations with regards to the results of dissolution experiments in order to elucidate the origin of these wrinkles.

6.2 Wrinkles behind the contact line

6.2.1 Characterization

The spreading of water onto maltodextrin DE29 or lactose leads to a curious phenomenon. We give in Fig. 6.1 a picture of the spreading process onto a maltodextrin DE29 layer. Behind the contact line, we observe the formation of wrinkles perpendicular to the contact line. The wavelength λ of these wrinkles increases with the distance to the contact line. The width W of the ribbon where wrinkles are observed in the radial direction is of the order of $100 \mu\text{m}$ from the contact line. Let us characterize precisely those wrinkles.

- Existence of the wrinkles:

The observed wrinkles appear within a given range of contact line speed U and thickness e .

6. DISSOLUTION AND WETTING

In Fig. 6.2a, we show how the velocity range within which wrinkles can be observed decreases with the coating thickness. If we refer to the wetting diagram built in chapter 4, the wrinkles only exist in the thin film regime. Furthermore, a larger water activity a_w tends to slightly extend those ranges.

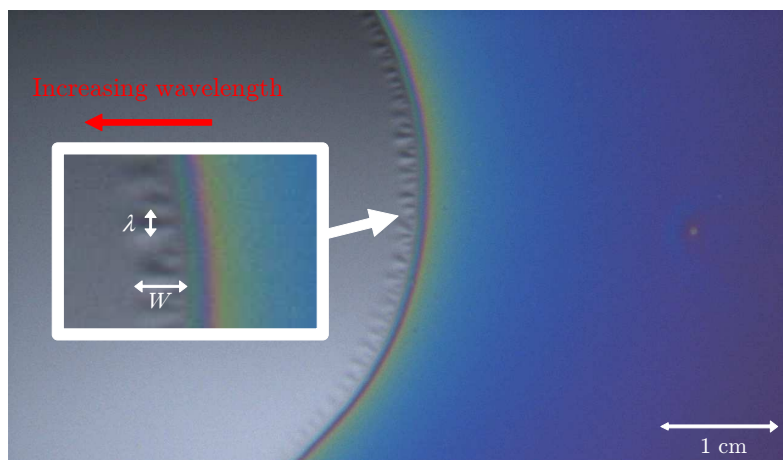


Figure 6.1: Wrinkles behind the contact line - Wrinkles appearing during the spreading of water onto a 250 nm-thick layer of maltodextrin DE29 equilibrated at $a_w = 0.58$. $U = 0.036 \text{ mm.s}^{-1}$

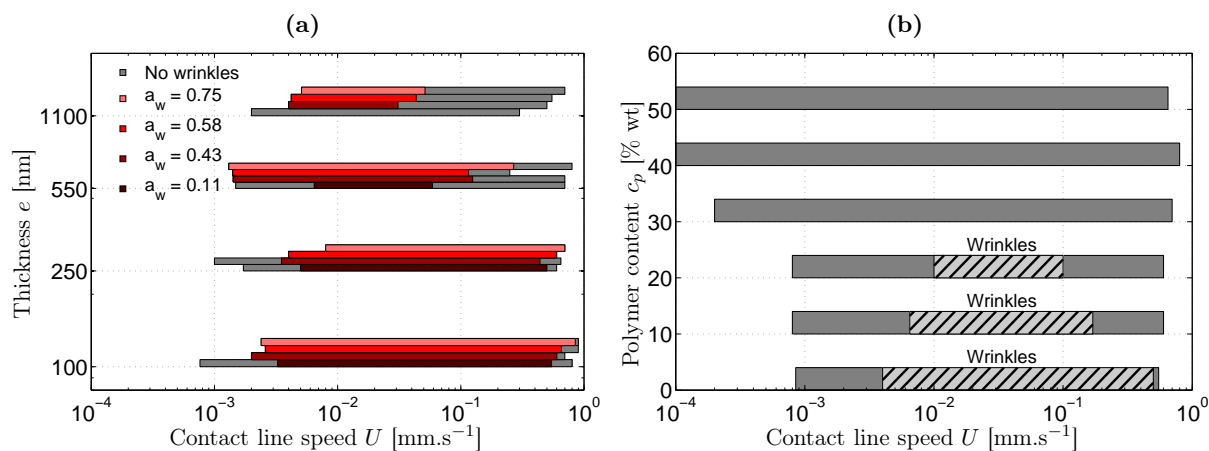


Figure 6.2: Domains of observation of the wrinkles behind the contact line - (a) Increase of the coating thickness at different a_w . Wrinkles are represented at each water activity with red shades. (b) Increase of the droplet concentration at $a_w = 0.43$. Hatches represent the wrinkles.

When the drop is a solution of maltodextrin that has been dissolved in water prior to the spreading experiment at a concentration c_p (between 0 and 50 % *wt*), we observe that the wrinkles disappear at larger concentrations (above 30 % *wt*) as represented in Fig. 6.2b. The velocity range within which wrinkles appears gets smaller when the polymer concentration increases. In-

deed, the swelling of the substrate and its dissolution are phenomena that depend on the polymer concentration, as well as on the contact line velocity. Thus, we suggest that the wrinkles are a consequence of swelling and dissolution.

- Dimensions of the wrinkles:

In our experiments, the wavelength λ ranges from 10 to 500 μm . We plot in Fig. 6.3a the measured wavelengths $\lambda(U)$ of the wrinkles at $e = 250$ nm for different water activities a_w (we choose to measure λ at mid-width of the wrinkled ribbon). We find a decrease of λ with the contact line speed U which follows a power law with an exponent close to $-1/2$. No significant variation trend with humidity can be inferred from the data.

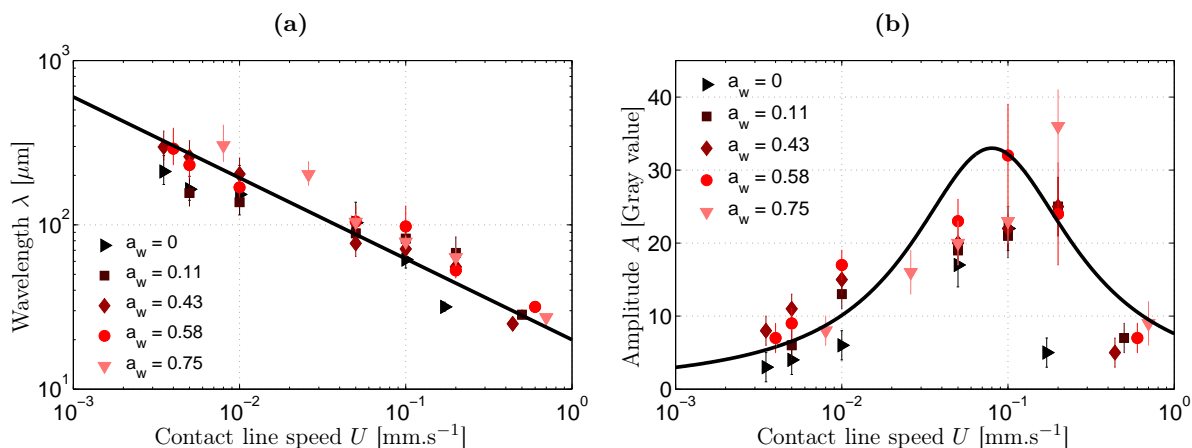


Figure 6.3: Characterization of wrinkle dimensions - (a) Wavelength of the wrinkles for a 250 nm-thick layer of maltodextrin DE29 at different a_w and measured at mid-width of the wrinkled ribbon. The black line corresponds to a power law with an exponent -0.49. (b) Amplitude of the wrinkles in gray value. The black line is a guide for the eye.

We plot in Fig. 6.3b the amplitude of the wrinkles measured by color analysis on pictures. We extract the gray values corresponding to a line that follows the center of wrinkles and calculate the difference between minima and maxima. The data points confirm that the wrinkles are visible in a range of contact line speed, and that they disappear because the amplitude decreases.

Finally, in Fig. 6.4, we plot the width W of the wrinkles for maltodextrin DE29 at $e = 250$ nm. We observe a rather constant width at small U and then a slight drop of W . Let us now discuss the origin of these wrinkles.

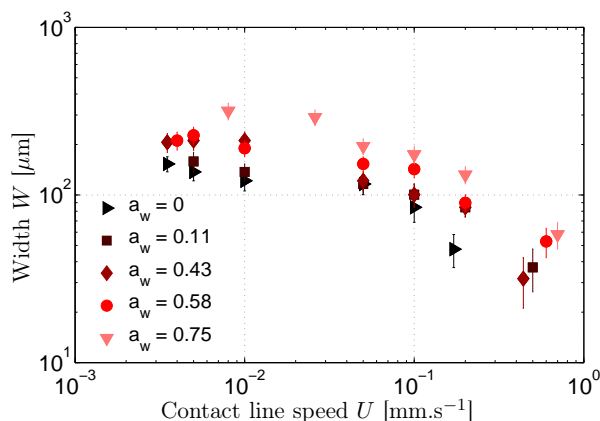


Figure 6.4: Measurement of wrinkles width - Width of the wrinkles from the contact line for a 250 nm-thick layer of maltodextrin DE29 at different a_w .

6.2.2 Origin of the wrinkles

We have made different hypotheses in order to explain the origin of the wrinkles (see Fig. 6.5). From our observations, we just know that the wrinkles are localised behind the contact line either inside or outside the water droplet. We also assume that dissolution process is probably a key phenomenon to explain the size of the wrinkled ribbon. Indeed, as mentioned earlier, all the polymer has been dissolved in water at the end of spreading since no more colors are observed when the droplet is evaporated. In consequence, far enough from the contact line, no coating remains. Thus, during the spreading process, the dissolution of the polymer layer leads to a gel-like ribbon that may lie in different positions. We assume that the swelling by hydration of this ribbon leads to a wrinkling pattern. We will examine three different hypotheses in the frame of that assumption, and compare the expected wavelengths to the one we have measured.

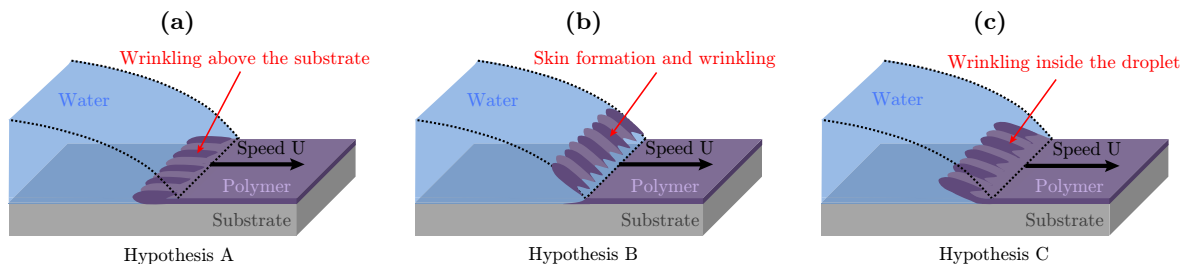


Figure 6.5: Hypotheses on the origin of wrinkles. (a) Wrinkling above the substrate. (b) Skin formation. (c) Wrinkling inside the droplet (curtain effect).

- Hypothesis A: Wrinkling above the substrate

The first hypothesis considers that the coating remains attached to the substrate. As the coating swells, there is a competition between the compression in the polymer and in the sub-

strate, *i.e.* the silicon wafer. Above a given threshold of compression, wrinkles appear in the layer above the substrate (see Fig. 6.5a). The wavelength of such wrinkles depends on the ratio of the Young moduli of the materials: the substrate (E_{sub}) and the polymer (E_p):

$$\lambda = e \left(\frac{E_p}{E_{sub}} \right)^{1/3} \quad (6.1)$$

With $e = 250$ nm, $E_p \sim 1$ MPa and $E_{sub} \simeq 107$ GPa, we obtain $\lambda \sim 5$ nm. Guvendiren *et al.* (56) use a similar approach but they introduce an intermediate layer of polymer. According to them, the solvent absorption in a polymer coating leads to a first layer with strong gradients of concentration and an intermediate one with a uniform concentration. Instead of considering E_{sub} , the Young modulus of this intermediate layer E_{int} has to be chosen. In our situation, with $\frac{E_p}{E_{int}} \sim 0.1$, it leads to $\lambda \sim 116$ nm. More generally, whatever the choice of the elastic modulus, the exponent 1/3 in Eq. 6.1 leads to expected values of the wavelength that are of the same order as the thickness, and therefore remain much smaller than the ones we measure, as shown in Fig. 6.3a where λ is of the order of 100 μ m. We can therefore conclude that it is not likely that the coating remains attached to the substrate.

- Hypothesis B: Skin formation

In that situation, the polymer dissolved in the drop would form a skin at the surface of the liquid as a result of water evaporation (see Fig. 6.5b). In the edge of the droplet, the solvent evaporation is efficient and the amount of dissolved polymer maximal. The evaporation would lead to an elastic floating free film. The excess of skin could lead to wrinkling. According to J.Huang *et al.* (57), the wrinkles wavelength for that kind of floating free film is given by:

$$\lambda = R^{1/2} \left(\frac{e^3 E_p}{\gamma} \right)^{1/4} \quad (6.2)$$

where R is the radius of the water drop. With $R = 2$ mm, $\gamma = 72.8$ mN.m⁻¹, $e = 250$ nm and $E_p \sim 1$ MPa, we obtain $\lambda \sim 1$ μ m. This value is smaller by at least one order of magnitude than the experimental data. More generally, the results of the experiment presented in Fig. 6.2b with the increase of the droplet concentration are not in agreement with this hypothesis. Increasing the amount of available polymer would help skin formation. We can therefore conclude that the wrinkles do not result from a skin formation at the surface of the droplet.

- Hypothesis C: Wrinkling inside the droplet (curtain effect)

In that last hypothesis, the non-dissolved polymer ribbon would be peeled off the substrate for mechanical reasons. Then, the swelling of the polymer inside the droplet leads to wrinkles formation (see Fig. 6.5c). That kind of wrinkling corresponds to the one observed on curtains (see Fig. 6.6) with a boundary confinement (here the contact line) and a free boundary. It leads

6. DISSOLUTION AND WETTING

to an increasing wavelength with the distance to the contact line x that can be estimated with a balance between bending and stretching energies. According to Vandeparre et al. (58), we have:

$$\lambda = \frac{e}{\Omega^{1/6}} \left(\frac{x}{e}\right)^{2/3} \quad (6.3)$$

where x is the distance to the boundary confinement, e the sheet thickness, $1 - \Omega$ is the ratio between the projected length of the sheet and its curvilinear length. With $x = 100 \mu\text{m}$, $e = 250 \text{ nm}$ and $\Omega = 0.6$ (the choice of Ω is not important because of the exponent $1/6$), we obtain $\lambda \sim 15 \mu\text{m}$ which is in agreement with the wavelengths we measure. The increase of λ with x is also observed in the experiments, although it is difficult to measure (see Fig. 6.1), giving credence to this hypothesis.

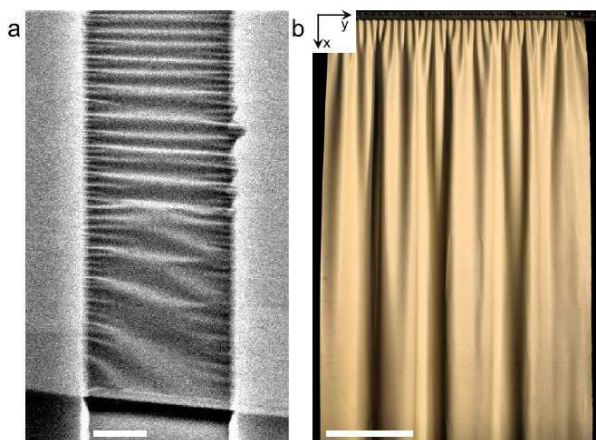


Figure 6.6: The curtain effect in different systems - Characteristic pictures of the curtain effect as found in (58). (a) Scanning electron microscopy image of suspended graphene bilayer (scale bar is $1 \mu\text{m}$). (b) Pattern of folds obtained for a rubber curtain (scale bar is 25 cm).

In conclusion, a gel-like ribbon appears behind the contact line. The characterization of this ribbon through its wrinkling pattern and additional experimental results show that it is detached from the substrate but does not float at the surface of the droplet. The swelling of the ribbon results in its wrinkling. Those wrinkles are the same that the ones observed on curtains with a free boundary and a confined one, here the contact line. In what follows, we discuss the conditions of formation of the wrinkled ribbon with regard to the contact line velocity.

6.3 Preliminary study on dissolution

6.3.1 Wrinkles: what is the link with the dissolution speed ?

We have shown in the previous section that the wrinkles observed behind the contact line are likely to be a consequence of the swelling of the coating that has detached from the substrate. The

detached ribbon exists in a given range of contact line speed and it results from the dissolution of the polymer layer. Therefore, knowing the dissolution speed v_d of the polymer is essential. In Fig. 6.7, we represent a schematic representation of the ribbon formation. The width of the ribbon can be expressed by equating the quantities e , U and v_d . The time to dissolve an element of thickness e is $\Delta t = e/v_d$. During that time, the contact line moves over a distance $U\Delta t$. Thus, the ribbon width W can be expressed as:

$$W \simeq \frac{eU}{v_d} \quad (6.4)$$

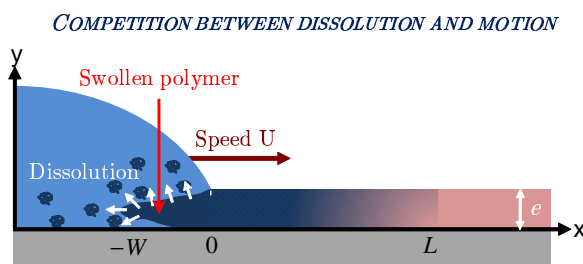


Figure 6.7: Dissolution at the contact line - Formation of a gel-like ribbon behind the contact line with width W that depends on e , U and v_d .

For instance, a width of $100 \mu\text{m}$, a thickness of 250 nm and a contact line velocity of 0.1 mm.s^{-1} lead to $v_d = 0.25 \mu\text{m.s}^{-1}$. Nevertheless, the experimental values of W do not show a dependence in U :

- At small contact line velocities U , we should observe the disappearance of the ribbon. In Fig. 6.4, we observe that W does not tend to 0 at small U . It is the amplitude of the wrinkles that decreases to 0. However, the expected increase of concentration in the edge reduces a lot the dissolution speed v_d and probably tends to limit that disappearance.
- At large velocities, the variation of W with U does not correspond to a dependence in U . In addition to a possible variation of v_d with U , we suggest that the ribbon is not peeled off the substrate. As mentioned earlier, at large U , attenuated Newton hues are still visible under the droplet in the vicinity of the contact line.

In conclusion, measuring the width of the wrinkles should give a rough estimate of the dissolution speed in the edge for a given contact line speed U . To further elucidate the observed behaviour, we have performed experiments to measure the dissolution velocity. We present the corresponding results in the following section.

6.3.2 Dissolution of a maltodextrin sphere

In the previous paragraph, we have given a simple expression that relates the dissolution speed of maltodextrin v_d to the width of the observed wrinkles W . However, it is important to get insight

6. DISSOLUTION AND WETTING

in the dissolution mechanism and in this subsection, we will measure the dissolution speed v_d with the techniques presented in the Materials & Methods chapter (see 3.1.2.6).

V.G. Levich (32, 33) described the dissolution of a free-falling soluble sphere in a liquid with a convective diffusion equation. He obtained an expression for the total flow of matter leaving the sphere:

$$I = 7.98(1 - c_p)D_p^{2/3}U^{1/3}d^{4/3} \quad (6.5)$$

where d is the diameter of the sphere, U the rate of descent, c_p the polymer concentration in the solution, and D_p the diffusion coefficient of the solvent in the sphere.

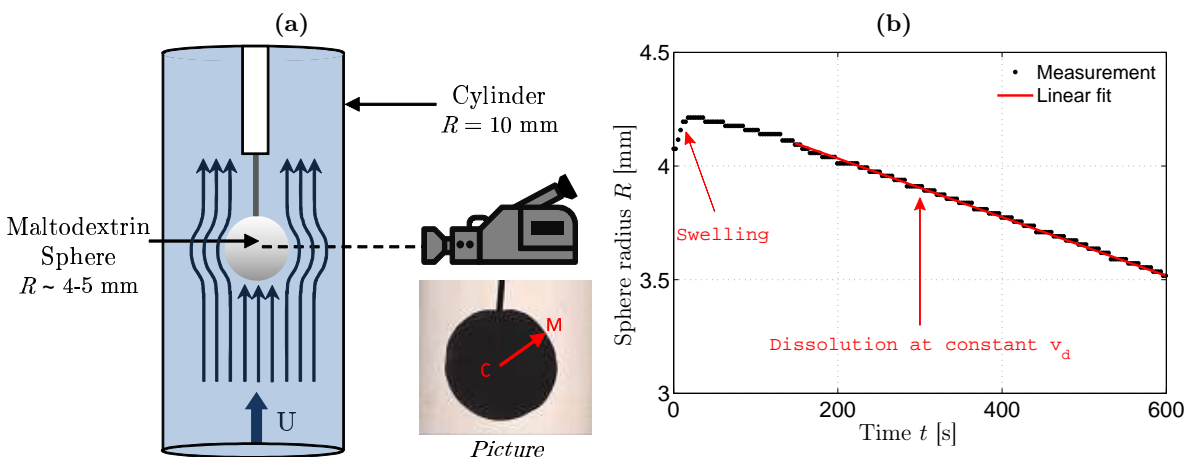


Figure 6.8: Dissolution of maltodextrin spheres - (a) Experimental set-up. (b) Radius evolution of a maltodextrin DE29 sphere immersed in static water. Initial radius is 4 mm.

We reproduced this geometry in order to measure the dissolution rate of maltodextrin. We used spheres made of polymer that we placed in a flow of velocity U . The polymer spheres have a radius between 4 and 5 mm. They are hung in a cylinder of radius $R = 10$ mm as represented in Fig. 6.8a. Thus, it is the liquid that moves and the sphere is static. The video camera allows a precise measurement of the sphere radius evolution in time. We plot in Fig. 6.8b the typical evolution of the sphere radius in the case of maltodextrin DE29 spheres. The radius first increases corresponding to the swelling of the polymer. The swelling of the entangled chains leads to a gel shell at the surface of the sphere. Then a linear decrease of the sphere radius with time is observed corresponding to a constant dissolution speed v_d (in the presented case $v_d = 1.67 \mu\text{m}\cdot\text{s}^{-1}$). By tuning the liquid velocity U and the solution concentration c_p , we have studied the influence of these parameters on v_d (see Appendix E). Our measurements show that the values of v_d slightly vary with U with values in the range $[0.5 \mu\text{m}\cdot\text{s}^{-1} - 20 \mu\text{m}\cdot\text{s}^{-1}]$. We thus obtain the same order of magnitude than the estimation made with the wrinkles width which was $0.25 \mu\text{m}\cdot\text{s}^{-1}$ at $U = 0.1 \text{ mm}\cdot\text{s}^{-1}$.

6.3.3 Dissolution at the contact line

The values for v_d we have estimated in the spreading experiment and the one directly measured are therefore in qualitative agreement. However, the geometry is expected to play a role in the dissolution process. For instance, the dissolution rate of a plate (32, 33) in a liquid was also discussed by V.G. Levich. The following expression for the dissolution rate is given:

$$I = 0.68(1 - c_p)D_p b \left(\frac{\eta}{\rho D_p} \right)^{1/3} \sqrt{\frac{\rho U L}{\eta}} \quad (6.6)$$

where U is the liquid velocity far from the plate, b the plate width, L its length along the flow direction (L and b being much larger than the thickness e) and η the liquid viscosity.

We can notice a dependence with the square root of the plate length whereas it was a dependence with the diameter to the power of 4/3 in the case of the sphere. The velocity dependence is also different. Thus, differences of dissolution behaviour are expected between a sphere and a plate. As a consequence, the dissolution velocity of a maltodextrin coating wetted by an edge of water may differ from the values we have measured. Other experiments are therefore to be conducted in order to better understand the conditions leading to the wrinkling of the coating.

6.4 Conclusions

In this chapter, we have discussed the dissolution process that occurs inside the water droplet during spreading onto the soluble polymer layer.

In a first part, we have shown that the dissolution of maltodextrin occurs behind the contact line possibly leading to the formation of a gel-like ribbon that detaches from the substrate. This ribbon wrinkles because of the swelling of the polymer. The wavelength of these wrinkles is of the order of 100 μm . The wrinkling pattern is of same origin as the one observed on curtains.

In a second part, we have linked the dissolution speed to the size of the gel-like ribbon behind the contact line. We have quantified the dissolution speed of maltodextrin and found a value of the order of 1 $\mu\text{m}\cdot\text{s}^{-1}$.

6. DISSOLUTION AND WETTING

Key messages

- A detached ribbon of polymer is formed in the droplet edge by the action of dissolution.
- The gel-like ribbon wrinkles due to swelling.
- The size of the ribbon can be linked to the dissolution speed.
- The dissolution speed of maltodextrin DE29 is of the order of $1 \mu\text{m}\cdot\text{s}^{-1}$.

Conclusions and open questions

In this study, we have investigated the hydration mechanisms that influence the wetting of a soluble polymer layer by one of its solvents. Starting from Tay *et al.* theory, we have introduced new theoretical arguments concerning the contact angle evolution and the hydration ahead the contact line. We validated our predictions with experimental observations on a system water/carbohydrate.

The experimental data confirmed the idea developed by our predecessors: hydrodynamics alone cannot explain spreading dynamics when dealing with a soluble layer. The water content ϕ at the contact line is the relevant parameter. 3 mass transfers were considered in our theoretical analysis, which are involved in the wetting of a soluble layer having a thickness e at a contact line velocity U :

- Evaporation of the solvent that can further condensate into the polymer layer.
- Diffusion of the solvent into the polymer layer (directly from the droplet or indirectly after condensation)
- Dissolution of the polymer in the solvent

We have confirmed that the main transfer influencing the contact angle value θ is evaporation/condensation but we have shown that diffusion effects in the layer (direct diffusion and horizontal diffusion) cannot be neglected. Using some theoretical arguments, we have built a new wetting diagram thickness-velocity. That diagram evidences different regimes as represented in Fig. 7.1. We have:

- Thin film regime: In the film thin regime, the water content ϕ at the contact line depends on the quantity eU . We experimentally observe the same scaling with $\theta(eU)$ showing that θ is a function of ϕ at the contact line.
- Intermediary regime: In the intermediary thick regime, vertical concentration gradients appear along a distance x_C from the contact line. The scaling of θ in eU is not valid any more.

7. CONCLUSIONS AND OPEN QUESTIONS

- Thick film regime: In the thick film regime, vertical concentration gradients are everywhere ahead the contact line where hydration occurs. The contact angle only depends on U and not e .
- Dry regime: the dry regime is expected at large contact line velocities where no more hydration occurs (region in red in Fig. 7.1). θ is expected constant. This regime was not observed.
- Unknown regime: At small eU , we observe an unknown regime where the scaling in eU is not valid (region in blue in Fig. 7.1). θ is found to reach a plateau and the dependence on e is weak. This regime may be a consequence of the dissolution transfer. We suggest that the viscosity significantly increases in the drop edge as a result of polymer dissolution.

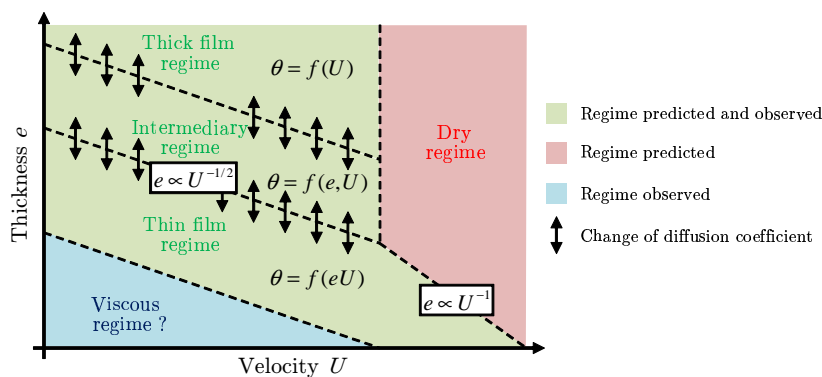


Figure 7.1: Wetting diagram - Diagram thickness - velocity built with theoretical arguments on hydration.

The position of the frontiers between the regimes observed experimentally (green regions) strongly depends on experimental conditions. They are shifted upwards when the layer is more hydrated because of the increase of the water diffusion coefficient in the polymer (e.g. for larger humidities). They are shifted downwards when the diffusion coefficient is reduced (e.g. for larger molecular weights).

Contrary to the wetting diagram from Tay *et al.*, the new diagram accounts for all experimental observations. One important modification is the new position of the frontier between thin film and intermediary thick regimes. We have found that the size of the thin film regime is extended. In our theory, the position of the frontier is proportional to the square root of a microscopic cut-off length ξ rather than a nanometric one. Indeed, using theoretical arguments, we have evidenced the characteristic lengths of the system and we have found those lengths using FEM simulations. One of those lengths is the size of a diffusion/condensation region ξ . This region of hydration appears ahead the contact line in the thin film regime because of the horizontal diffusion in the polymer layer. We summarize in Fig. 7.2 the different kinds of hydration profiles that can be observed ahead the contact line depending on the Péclet numbers in air and in the polymer layer.

- In the film thin regime, a diffusion/condensation region of size ξ appears ahead the contact line. Further from ξ , we have a condensation/convection region. Both regions are characterized by a scaling of the water fraction with the quantity eU . This scaling already predicted in the condensation/convection region is indeed still valid in the diffusion/condensation region because of two diffusion effects that cancel each other out.
- In the intermediary thick regime, vertical concentration gradients can be observed from the contact line to the distance x_C . ϕ is not a function of eU in this region but the scaling is still valid in the condensation/convection region
- In the thick film regime, the layer presents vertical concentration gradients such that x_C is larger than the extent the hydration zone. It leads to a dependence of ϕ with U only.

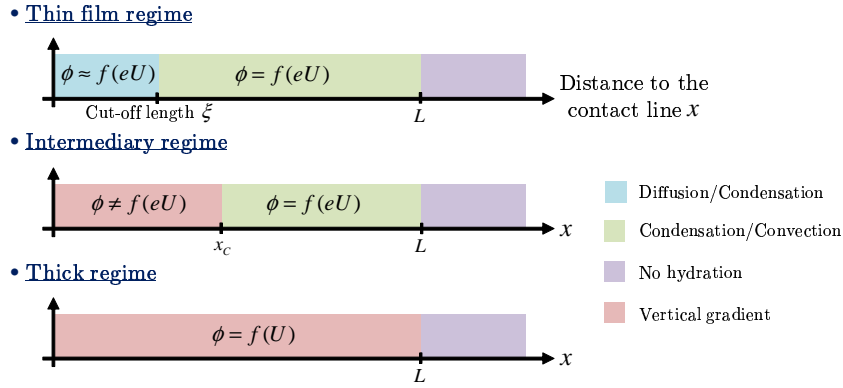


Figure 7.2: Different kinds of hydration profiles - Various hydration regions ahead the contact line moving at the velocity U can be evidenced depending on the considered wetting regime. A new cut-off length ξ appears in the thin film regime while the vertical concentration gradients can be observed at $x < x_C$ in other regimes.

The water fraction profiles were characterized experimentally by analysing the Newton hues that evolve upon hydration in our thin layers. Although they were found to be more complex than the ones obtained from simulation, they present similar features. For instance, the cut-off length ξ was validated experimentally. That length was found to be larger than the one found in FEM simulations when a linear sorption isotherm ($a_w = \phi$) and a constant water diffusion coefficient D_p are considered. In the experiments, those are two sources of non-linearity ($a_w = f(\phi)$ and $D_p = f(\phi)$) and the value of ξ is increased.

In the glass transition chapter, we have evidenced a kink in $\theta(U)$ curves that appears at $U = U_g$ corresponding to the advance of the contact line on a substrate at its glass transition (see Fig. 7.3). At $U > U_g$, the hydration of the layer is very slow because of the small water diffusion coefficient in the layer. Therefore, the droplet experiences a glassy substrate. At $U < U_g$, the hydration is efficient enough for a melt region to form ahead the contact line. The drop experiences that melt region and the contact angle is much smaller. We showed that the kink can be related to the wetting diagram and the upward shift of the frontier between thin

7. CONCLUSIONS AND OPEN QUESTIONS

film and intermediary thick regimes when U is decreased.

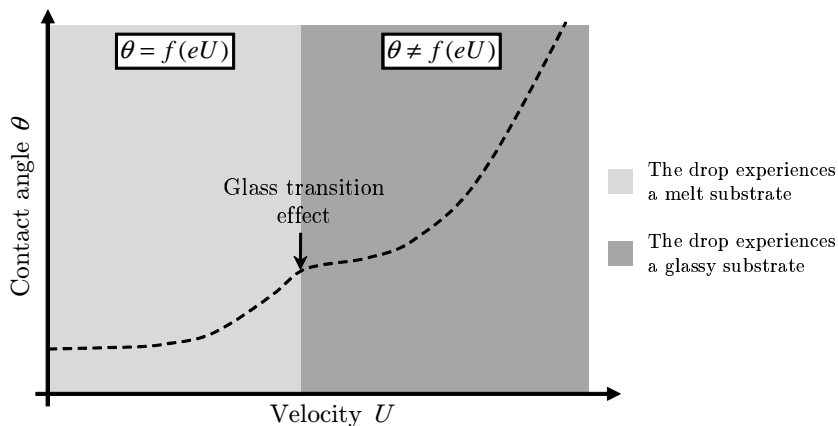


Figure 7.3: Contact angle and glass transition - Characteristic dynamic contact angle curve observed in our study.

Finally, some questions are still under debate. In particular, this is the case of the dissolution process. We do not know clearly how the dissolution, characterized by the concentrated region behind the contact line, influences the wetting. Secondly, we have observed this unknown regime in the wetting diagram that might be related to this dissolution effect.

◇ open question 1 : what is the role of dissolution during wetting onto soluble surfaces ?

The first enigma is the precise role of dissolution on wetting. As explained in chapter 6, dissolution kinetics is responsible for a layer of concentrated solute behind the contact line. That gel-like layer wrinkles because of its swelling prior to its dissolution. Indeed, some matter may be dissolved and accumulate in the liquid edge. We know from hydrodynamic equations that increasing the viscosity of the edge should affect the contact angle ($\theta^3 \propto \eta$). During the spreading of water onto maltodextrin, three mechanisms tend to increase the viscosity of the liquid edge: dissolution of matter, solute transport to the edge (14, 15, 16) and evaporation (17). We therefore need to quantify the importance of this viscosity increase.

We present in Fig. 7.4a an effect of viscosity increase in the droplet. We plot $\theta(U)$ in the case of a maltodextrin DE29 solution spreading onto a maltodextrin layer ($e = 250$ nm, $a_w = 0.43$). The larger the concentration c_p of polymer in the droplet, the larger the contact angle θ . At $c_p = 60$ % wt, the viscosity is 200 times larger than the one of water. In that case, we can see that the hydrodynamic theory of Cox-Voinov (full lines) gets closer to the data (the equilibrium contact angle is adjusted to obtain the right θ at small U). It means that hydration mechanisms (direct diffusion, evaporation/condensation) become less important and that the viscosity effects begin to dominate the contact line motion.

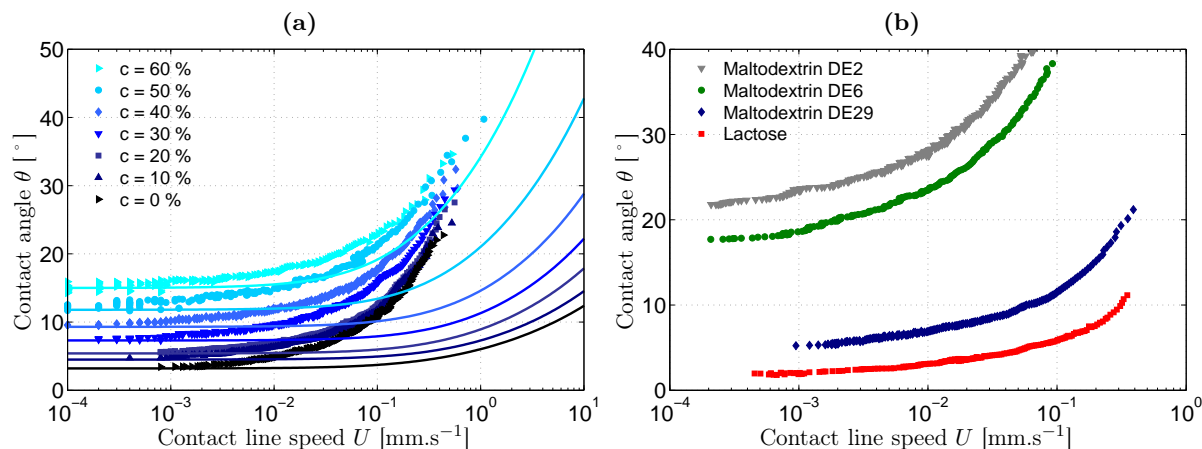


Figure 7.4: Contact angle and viscosity increase - (a) Effect of an increase of the polymer concentration in the droplet. Spreading of a maltodextrin solution onto a 250 nm-thick layer of maltodextrin DE29 ($a_w = 0.43$). Cox-Voinov theory is represented with full lines. (b) Effect of an increase of the molecular weight of the carbohydrate. Spreading of water onto a 250 nm-thick layer of carbohydrate ($a_w = 0.11$).

For a different molecular weight M_w of the carbohydrate, the contact angle θ is expected to vary since the water diffusion coefficient and the viscosity concentration dependence are modified. Nevertheless, the effect is intricate with the shift of the glass transition with M_w . We observe in Fig. 7.4b that θ strongly varies with M_w (using lactose and three different maltodextrins). We can also observe at small velocities that the contact angle tends to reach a plateau at different values. That plateau value might correspond to the increase of viscosity behind the contact line that varies from one compound to another.

◇ open question 2 : what is the origin of the unknown regime ?

In chapter 4, we have showed that the scaling fails at small eU . We introduced an "unknown" regime. At the time of writing, the debate on the origin of this regime is still open.

One could invoke a visco-elastic effect. When hydration is intense, maltodextrin behaves like a swollen gel. Literature (22, 59) shows that the wetting of a visco-elastic substrate is characterized by a deformation of the material below the contact line. It is known that the resulting out-of-plane displacement may affect the wetting dynamics. This hypothesis cannot be confirmed by our color analysis that does not have the required resolution to observe the nanometric deformation.

Our main hypothesis is that we have an effect of viscosity increase in the vicinity of the contact line as described in the previous open question. Hydration alone would lead to a decrease of θ at small U towards 0 but experimentally, we observe a plateau-like region in $\theta(U)$ curves. Thus, the scaling in eU of the contact angle is not valid any more. Nevertheless, if we consider

7. CONCLUSIONS AND OPEN QUESTIONS

hydration mechanisms, we expect a dependence on the quantity eU for the water content ϕ at small eU . It means that θ is no longer a function of ϕ only. We believe that the the viscosity increase starts to become non-negligible relative to the hydration mechanisms (condensation and diffusion). This effect strongly depends on the carbohydrate since dissolution velocity v_d and viscosity are modified.

We can summarize the possible effect of dissolution:

- Large Velocities: almost no matter is dissolved. Hydration through evaporation/condensation and diffusion dominate.
- Intermediate Velocities: the amount of dissolved matter in the droplet edge is likely to depend on the quantity eU . So even if the viscosity increase at the contact line becomes non negligible, the hydrodynamical contribution does not modify the scaling of θ in eU (see Fig. 7.5a).
- Small Velocities: we think that immediately behind the contact line, all the polymer layer is dissolved. The amount of dissolved matter in the droplet edge does no longer depend on eU . The large viscosity increase at the contact line involves a hydrodynamic contribution which is not negligible. The scaling of θ in eU expected from evaporation/condensation is not valid any more (see Fig. 7.5b).

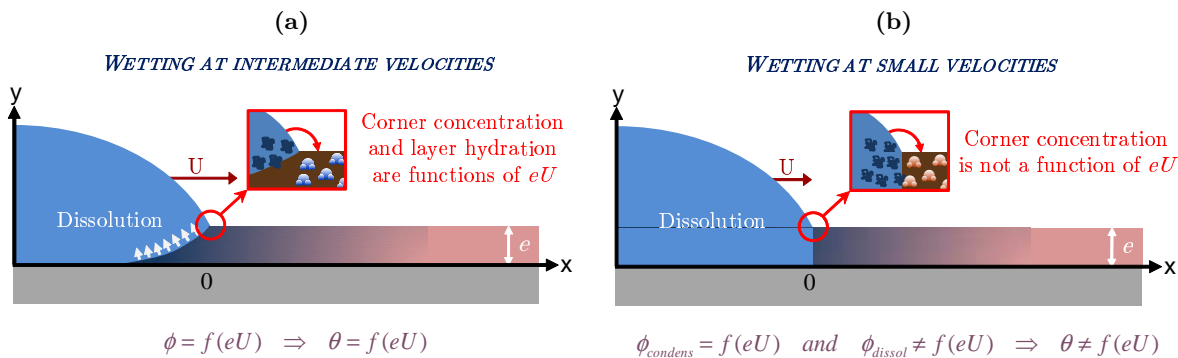


Figure 7.5: Possible effect of dissolution on the eU scaling - Schematic representation of spreading onto the soluble layer. Effect of dissolution on polymer concentration the droplet edge. (a) Intermediate velocities: dissolved matter is expected to be a function of eU . (b) Small velocities: dissolved matter no longer depends on eU .

Finally, this study allowed to improve our understanding of the wetting on soluble materials. The hydration mechanisms at stake were described and quantified with theoretical arguments that account for experimental data. However, a couple of open questions remain unresolved such as the quantification of the dissolution process.

Appendix A

Color scale

The color analysis based on interferences theory can be done visually by comparing the color of the thin layer coated on a Si wafer (under a constant observation angle $\theta = 15^\circ$) and the theoretical color given by the scale of Fig.A which links the product $n.e$, where n is the refractive index of the thin layer and e its thickness in nm, to the color of the layer.

	75.0		255.0		412.5		570.0		795.0		1065
	82.5		262.5		420.0		577.5		810.0		1080
	90.0		270.0		427.5		585.0		825.0		1095
	97.5		277.5		435.0		592.5		840.0		1110
	105.0		285.0		442.5		600.0		855.0		1125
	112.5		292.5		450.0		607.5		870.0		1140
	120.0		300.0		457.5		615.0		885.0		1155
	127.5		307.5		465.0		622.5		900.0		1170
	135.0		315.0		472.5		630.0		915.0		1185
	142.5		322.5		480.0		645.0		930.0		1200
	150.0		330.0		487.5		660.0		945.0		1215
	157.5		337.5		495.0		675.0		960.0		1230
	165.0		345.0		502.5		690.0		975.0		1245
	172.5		352.5		510.0		697.5		990.0		1290
	180.0		360.0		517.5		705.0		1005		1305
	187.5		367.5		525.0		712.5		1020		1320
	195.0		375.0		532.5		720.0		1027		1335
	210.0		382.5		540.0		727.5		1035		1350
	225.0		390.0		547.5		735.0		1042		1380
	232.5		397.5		555.0		750.0		1050		1410
	240.0		405.0		562.5		780.0		1057		1470

Figure A.1: Color scale for thickness measurement - Scale of colors and the corresponding product $n.e$ where n is the refractive index of the thin layer and e its thickness in nm, for an observation angle $\theta = 15^\circ$

A. COLOR SCALE

Appendix B

Water flux in spreading experiment

In this part, we will describe the spreading experiment using a "flat" droplet having a radius R and with a 2D-approach for the diffusion in the air. The contact line has a velocity U and we call Λ be the distance from the x -axis where the water activity a_w in the air is not modified by the evaporation process. Direct diffusion from water to the layer is not considered as the diffusion of polymer towards the droplet. Definitions are presented in Fig.B.1.

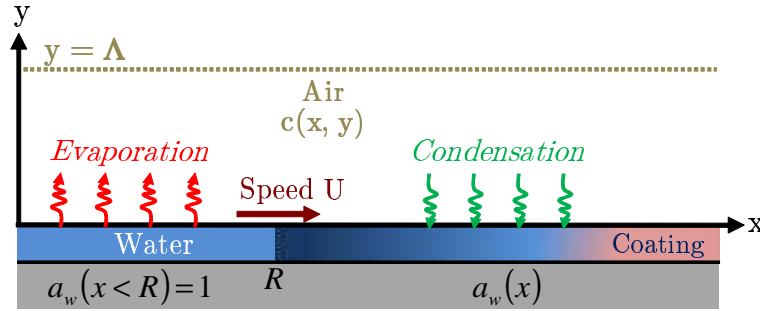


Figure B.1: Schematic representation for water flux calculation - A 2D-space is considered with a flat water droplet moving at the speed U . The distance Λ represents the distance above the droplet where the water concentration in air is not influenced by the experiment ($c = 0$)

Considering a diffusion coefficient D_v , the diffusion equation for a water concentration $c(x, y)$ in the air can be written:

$$\frac{\partial c}{\partial t} = D_v \Delta c \quad (\text{B.1})$$

In the stationary state, previous equation becomes:

$$\frac{\partial^2 c}{\partial x^2} + \frac{\partial^2 c}{\partial y^2} = 0 \quad (\text{B.2})$$

The chosen boundary conditions for this system are:

B. WATER FLUX IN SPREADING EXPERIMENT

$$\begin{cases} c(x, 0) = a_w(x)c_{sat} \\ c(x, \Lambda) = 0 \end{cases} \quad (\text{B.3})$$

where c_{sat} is the maximal concentration of water in air when equilibrium vapour pressure is reached (at 25 °C, $c_{sat} = 25 \text{ g/m}^3$).

In this 2D-representation, $c(x, y)$ is an odd function solution of a Laplace equation. We can assume that $c(x, y)$ can be written as a Fourier cosine development relative to x , with the coefficients c_q and a function $g_q(y)$:

$$c(x, y) = \int_0^\infty c_q \cos(qx) g_q(y) dq \quad (\text{B.4})$$

$g_q(y)$ is of exponential type. We will choose $sh(q(\Lambda - y))$ to respect boundary conditions. Thus:

$$c(x, y) = \int_0^\infty c_q \cos(qx) sh(q(\Lambda - y)) dq \quad (\text{B.5})$$

Using boundary conditions, a relation between c_q Fourier coefficients and $a_w(x)$ can be obtained:

$$\int_0^\infty c_q \cos(qx) sh(q\Lambda) dq = a_w(x)c_{sat} \quad (\text{B.6})$$

The odd function $a_w(x)$ can also be developed as a Fourier cosine transform:

$$a_w(x) = \int_0^\infty a_q \cos(qx) dq \quad (\text{B.7})$$

B.6 and B.7 lead to:

$$a_q = \frac{c_q}{c_{sat}} sh(q\Lambda) \quad (\text{B.8})$$

where a_q represents the Fourier coefficient in surface and c_q the Fourier coefficient in the air.

Let's now have a look to the water flux j . The interesting water flux for understanding the exchanges between the air and the thin layer can be obtained from the water gradient of concentration in the air at the height $y = 0$:

$$j(x) = -D_v \left. \frac{\partial c}{\partial y} \right|_{y=0} \quad (\text{B.9})$$

$$\begin{aligned} j(x) &= D_v \int_0^\infty c_q \cdot q \cos(qx) ch(q\Lambda) dq \\ j(x) &= c_{sat} D_v \int_0^\infty a_q \cdot q \cos(qx) \frac{ch(q\Lambda)}{sh(q\Lambda)} dq \end{aligned} \quad (\text{B.10})$$

Or a_q can be written as a function of a_w :

$$a_q = \int_0^\infty a_w(x') \cos(qx') dx' \quad (\text{B.11})$$

Introducing B.11 in B.10 leads to:

$$j(x) = c_{sat} D_v \int_0^\infty \int_0^\infty a_w(x') \cos(qx') \cos(qx) \left[q \frac{ch(q\Lambda)}{sh(q\Lambda)} \right] dx' dq \quad (\text{B.12})$$

Thus the flow can be calculated if $a_w(x)$ is known. Nevertheless, integration by parts can be performed on a_q in order to simplify the problem and obtain an integral that can be calculated:

$$\begin{aligned} a_q &= \int_0^\infty a_w(x') \cos(qx') dx' \\ &= \left[a_w(x') \frac{\sin(qx')}{q} \right]_{x'=0}^{x'=\infty} - \int_0^\infty \frac{da_w}{dx'} \frac{\sin(qx')}{q} dx' \\ &= - \int_0^\infty \frac{da_w}{dx'} \frac{\sin(qx')}{q} dx' \quad \text{if } a_w(x' \rightarrow \infty) = 0 \end{aligned} \quad (\text{B.13})$$

Thus, the new flow depends on the derivative of the water activity profile:

$$j(x) = -c_{sat} D_v \int_0^\infty \int_0^\infty \frac{da_w}{dx'} \sin(qx') \cos(qx) \left[\frac{ch(q\Lambda)}{sh(q\Lambda)} \right] dx' dq \quad (\text{B.14})$$

Using Mathematica to solve the integral and the following writing trick $\frac{ch(q\Lambda)}{sh(q\Lambda)} = \left[\frac{ch(q\Lambda)}{sh(q\Lambda)} - 1 \right] + 1$, we finally obtain:

$$j(x) = -c_{sat} D_v \int_0^\infty \frac{da_w}{dx'} \left[\sqrt{\frac{2}{\pi}} \frac{|x'|}{x'^2 - x^2} + \frac{1}{\sqrt{2\pi}} \left(\frac{-2x'}{x'^2 - x^2} + \frac{\pi \cdot sh\left(\frac{\pi x'}{\Lambda}\right)}{\Lambda \cdot ch\left(\frac{\pi x'}{\Lambda}\right) - \Lambda \cdot ch\left(\frac{\pi x}{\Lambda}\right)} \right) \right] dx' \quad (\text{B.15})$$

Eq.B.15 is difficult to calculate since the integrated function diverges in $x' = x$. A development at order 2 close to $x' = x$ can be used to approximate the final result. Let ε be a small variation around $x' = x$.

$$j(x) = -c_{sat} D_v \int_0^\infty \frac{f(x', x)}{x' - x} dx' \quad (\text{B.16})$$

$$f(x' = x + \varepsilon) = f(x) + \left. \frac{df}{dx'} \right|_x (x' - x) + \frac{1}{2} \left. \frac{d^2 f}{dx'^2} \right|_x (x' - x)^2 \quad (\text{B.17})$$

$$j(x) = -c_{sat} D_v \left[\int_{x'=0}^{x'=x-\varepsilon} \frac{f(x', x)}{x' - x} dx' + \int_{x'=x-\varepsilon}^{x'=x+\varepsilon} \frac{f(x', x)}{x' - x} dx' + \int_{x'=x+\varepsilon}^{x'=\infty} \frac{f(x', x)}{x' - x} dx' \right] \quad (\text{B.18})$$

The second term is the one to approximate. Using Eq.B.17, a simplification is possible by neglecting terms of the 2nd order and knowing that the integration of the even function is zero:

$$\int_{x'=x-\varepsilon}^{x'=x+\varepsilon} \frac{f(x', x)}{x' - x} dx' = 2\varepsilon \left. \frac{df}{dx'} \right|_x \quad (\text{B.19})$$

Thus

$$j(x) = -c_{sat} D_v \left[\int_{x'=0}^{x'=x-\varepsilon} \frac{f(x', x)}{x' - x} dx' + 2\varepsilon \left. \frac{df}{dx'} \right|_x + \int_{x'=x+\varepsilon}^{x'=\infty} \frac{f(x', x)}{x' - x} dx' \right] \quad (\text{B.20})$$

B. WATER FLUX IN SPREADING EXPERIMENT

Where:

$$f(x', x) = \frac{da_w}{dx'} \left[\sqrt{\frac{2}{\pi}} \frac{x'}{x' + x} + \frac{1}{\sqrt{2\pi}} \left(\frac{-2x'}{x' + x} + \frac{(x' - x)\pi.sh\left(\frac{\pi x'}{\Lambda}\right)}{\Lambda.ch\left(\frac{\pi x'}{\Lambda}\right) - \Lambda.ch\left(\frac{\pi x}{\Lambda}\right)} \right) \right] \quad (\text{B.21})$$

Knowing the water activity at the surface of the thin layer and so everywhere on the x -axis ($a_w(x < R) = 1$), the flow can be calculated using Eq.B.20 and Eq.B.21. This calculation was performed on Matlab where we use an experimental water content profile $\phi(x)$ to obtain an experimental $j(x)$ (the sorption isotherm is used to calculate $a_w(x)$). An example is given in Fig. B.2b. The flux is calculated using the water fraction profile of Fig. B.2a corresponding to a 250 nm-thick maltodextrin DE29 layer at $U = 0.01 \text{ mm.s}^{-1}$ and $a_w = 0.11$. We set R to 1 mm. The obtained flux is also compared to a FEM simulation on COMSOL that calculates the flux directly from the boundary condition $\phi(x)$.

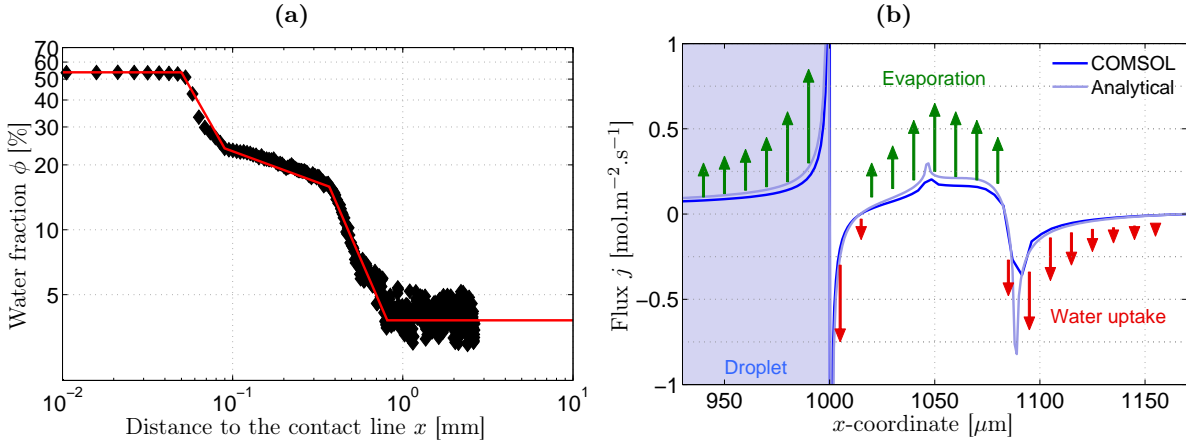


Figure B.2: Flux calculation on an experimental water content profile - (a) Water fraction ahead the contact line corresponding to the spreading of water onto a maltodextrin DE29 layer at $U = 0.01 \text{ mm.s}^{-1}$ and $a_w = 0.11$. (b) Vertical water flux obtained at the surface of the layer and droplet, either by FEM simulation or by analytical calculation using Eq.B.20 and Eq.B.21. The red profile of water fraction is considered.

We find that the droplet is not the only place where evaporation occurs. Far from the contact line, the water flux is negative and we have condensation but just ahead the contact line, in the diffusion/condensation region, the vertical water flux becomes positive.

Appendix C

Direct diffusion: 1D-theory

Let's consider a water droplet deposited on a soluble substrate having a thickness e_0 . Water dissolves the coating under the droplet and diffuses from the droplet to the coating. We make the hypothesis that the source of water is directly under the contact line. In the following calculation, we assume a constant contact line speed U and water diffusion through the air is not considered.

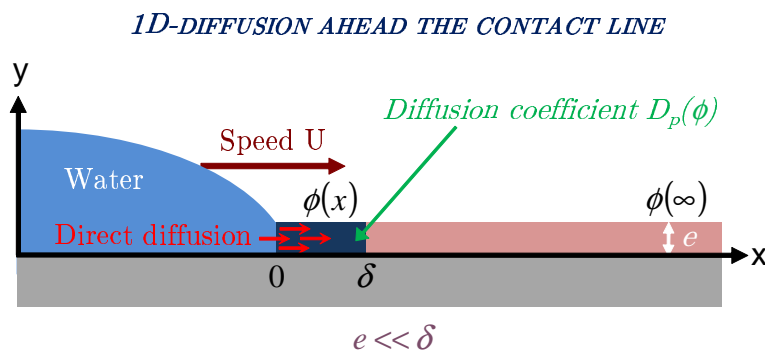


Figure C.1: Theoretical diffusion close to the contact line - Schematic representation of a droplet moving at a speed U on a thin layer of polymer. Water diffuses in the polymer and has a concentration ϕ at a distance x of the droplet.

For a water content in polymer ϕ , the mass conservation equation and Fick's law are respectively given by C.1 and C.2:

$$\frac{\partial \phi}{\partial t} + \vec{\nabla} \cdot \vec{j} = 0 \quad (\text{C.1})$$

$$\vec{j} = -D_p(\phi) \vec{\nabla} \phi \quad (\text{C.2})$$

where $D_p(\phi)$ is the diffusion coefficient of water in the thin layer (depending on water content) and \vec{j} is the water flux.

C. DIRECT DIFFUSION: 1D-THEORY

In 1D-geometry, both previous equations lead to [C.3](#):

$$\frac{\partial \phi}{\partial t} = \frac{\partial}{\partial x} \left[D_p(\phi) \cdot \frac{\partial \phi}{\partial x} \right] \quad (\text{C.3})$$

In the contact line frame of reference, we obtain the following relation:

$$\frac{\partial \phi}{\partial t} - U \frac{\partial \phi}{\partial x} = \frac{\partial}{\partial x} \left[D_p(\phi) \cdot \frac{\partial \phi}{\partial x} \right] \quad (\text{C.4})$$

If a stationary state is assumed, we suppress of the temporal term. The integration of [C.4](#) gives the final equation [C.5](#):

$$\begin{aligned} -U \frac{\partial \phi}{\partial x} &= \frac{\partial}{\partial x} \left[D_p(\phi) \cdot \frac{\partial \phi}{\partial x} \right] \\ \int_{\infty}^x \frac{\partial}{\partial x} (-U \phi) dx &= \int_{\infty}^x \frac{\partial}{\partial x} \left[D_p(\phi) \cdot \frac{\partial \phi}{\partial x} \right] dx \\ -U [\phi(x) - \phi(\infty)] &= D_p(\phi) \cdot \frac{\partial \phi}{\partial x} \quad \text{because } \left. \frac{\partial \phi}{\partial x} \right|_{\infty} = 0 \\ -\int_0^r U &= \int_0^r \left[\frac{D_p(\phi)}{\phi(x) - \phi(\infty)} \cdot \frac{\partial \phi}{\partial x} \right] dx \\ -U \cdot r &= \int_1^{\phi(r)} \frac{D_p(\phi)}{\phi - \phi(\infty)} d\phi \end{aligned} \quad (\text{C.5})$$

where r is the distance to the droplet.

Thus, an implicit equation is obtained. If $D_p(\phi)$ is known, a given water content ϕ corresponds to a distance to the droplet r . The resolution of the integral (right-hand term in [C.5](#)) for different r allows obtaining $\phi(r)$. Applying this equation to our experimental conditions leads to an overestimated theoretical size of the diffusion region δ in comparison to the experimental size ξ of the diffusion/condensation region.

Appendix D

Diffusion in a semi-infinite media

In this section, we consider water diffusing from a static source in a semi-infinite media with a diffusion coefficient $D_p(\phi)$. D_p can vary by several orders of magnitude as a function of the water fraction. The diffusion equation writes:

$$\frac{\partial \phi}{\partial t} = \frac{\partial}{\partial x} \left[D_p(\phi) \cdot \frac{\partial \phi}{\partial x} \right] \quad (\text{D.1})$$

Considering the change of variables $\phi(x, t) = \phi(u)$ with $u = \frac{x^2}{t}$, we can obtain a new differential equation. There is no characteristic length in the problem except the front size, therefore the diffusion equation can be fully expressed as a function of the new variable u . The change of variable gives:

$$\left\{ \begin{array}{l} \frac{\partial \phi}{\partial t} = -\frac{x^2}{t^2} \frac{\partial \phi}{\partial u} \\ \frac{\partial \phi}{\partial x} = \frac{2x}{t} \frac{\partial \phi}{\partial u} \\ \frac{\partial^2 \phi}{\partial x^2} = \frac{2}{t} \frac{\partial \phi}{\partial u} + \frac{4x^2}{t^2} \frac{\partial^2 \phi}{\partial u^2} \end{array} \right. \quad (\text{D.2})$$

And finally:

$$[u + 2D_p(\phi)] \frac{\partial \phi}{\partial u} + 4u \frac{\partial D_p(\phi)}{\partial \phi} \left(\frac{\partial \phi}{\partial u} \right)^2 + 4uD_p(\phi) \frac{\partial^2 \phi}{\partial u^2} = 0 \quad (\text{D.3})$$

The previous linear differential equation is solved numerically on Mathematica using the function *NDSolve*. The diffusion coefficient $D_p(\phi)$ is chosen either constant (e.g. $D_p = 8 \cdot 10^{-11} \text{ m}^2 \cdot \text{s}^{-1}$) or variable (diffusion coefficient of maltodextrin DE29 introduced in 3.1.2.5). The derivative of the function $\phi(u)$ close to $u = 0$ is adjusted in order to have water fractions from 1 to 0 (we want $\phi(\infty) = 0$). Fig. D.1 presents the obtained water fraction profiles. We can notice a difference in curve shape: a sharp front appears when D_p varies with ϕ .

The profile $\phi\left(\frac{x^2}{t}\right)$ obtained for maltodextrin DE29 was used to calculate the swelling of

D. DIFFUSION IN A SEMI-INFINITE MEDIA

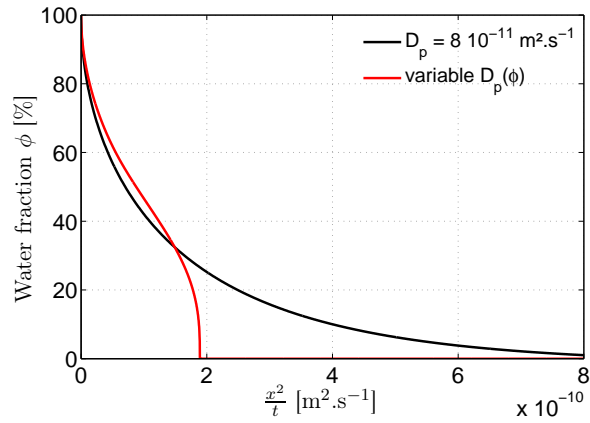


Figure D.1: Diffusion profiles in a semi-infinite media - Comparison between a constant diffusion coefficient ($D_p = 8 \cdot 10^{-11} \text{ m}^2 \cdot \text{s}^{-1}$) and a variable one $D_p(\phi)$ (maltodextrin DE29)

walls during capillary penetration in soluble channels. Knowing the contact time between the liquid and the wall, we can deduce how much water diffused in maltodextrin and so the expected swelling S of the wall:

$$S = \frac{\langle \phi \rangle}{1 - \langle \phi \rangle} \quad (\text{D.4})$$

Appendix E

Dissolution of maltodextrins

In order to quantify the dissolution speed v_d of maltodextrins in water, different experiments were performed. We used either spheres of polymer or channels to measure v_d as a function of the liquid velocity U or the solution concentration c_p .

E.0.1 Dissolution of a maltodextrin sphere

In a first series of experiments, we used spheres made of maltodextrin to obtain the dissolution speed v_d . As explained in section 3.1.2.6, we measure the radius R of the sphere in time and calculate the dissolution speed using $\dot{R}(t)$.

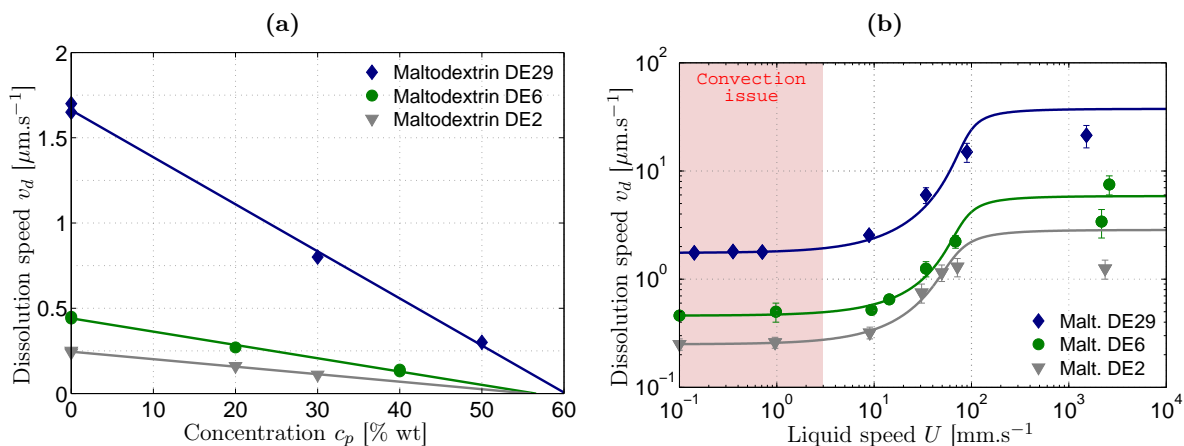


Figure E.1: Dissolution speed of maltodextrin spheres - Measurement of v_d using some spheres of different maltodextrins (a) for different concentrations c_p in a static liquid (b) for different liquid velocities U . The points at $U > 1 \text{ m/s}$ are obtained using a water tap. The full lines are guides to the eye.

We represent in Fig. E.1a the effect of polymer addition to the liquid. For instance, the dissolution speed of maltodextrin DE29 in pure static water is close to $1.6\text{-}1.7 \mu\text{m}\cdot\text{s}^{-1}$ (slope in Fig. 6.8b) while it drops to $0.3 \mu\text{m}\cdot\text{s}^{-1}$ at $c_p = 50 \text{ \% wt}$. A decrease of the dissolution

E. DISSOLUTION OF MALTODEXTRINS

speed with c_p is observed for all tested maltodextrins. As expected, the dissolution speed of high molecular weight maltodextrins is smaller. In Fig. E.1b, we show how the dissolution speed v_d of the spheres evolves with the liquid velocity U . At small U , v_d is almost constant and v_d starts increasing around $U = 5\text{-}10 \text{ mm.s}^{-1}$. This plateau of v_d could be a consequence of natural convection around the sphere. Thus, the data points obtained at small imposed U are imprecise and v_d probably overestimated.

NB: the points at large U ($U > 1 \text{ m/s}$) are obtained by simple dissolution under a water tap. We used smaller spheres to perform this experiment ($R \simeq 5 \text{ mm}$ against $R \simeq 9 \text{ mm}$ before) which could explain the unexpected small v_d obtained. Indeed, Levich theory predicts a dependence of v_d for a sphere in $R^{4/3}$.

E.0.2 Dissolution of a soluble channel

The dissolution speed v_d was also measured in maltodextrin capillaries. We used both methods of preparation presented in section 3.1.2.6 to obtain either rectangular channels made of one wall of polymer and three of PDMS, or cylindrical channels made of polymer only. Then we inject liquid in these channels using a micro-pump.

In the case of rectangular channels, we measured dissolutions speeds for different flow rates using a micro-pump. The liquid velocity range we investigated was [0.1 mm.s^{-1} - 35 mm.s^{-1}]. v_d was measured using the refractive index of the outlet solution and confirmed with profilometry by measuring the dimensions of the channel at the end of the experiments. We obtain the red data points presented in Fig. E.2. The results are in relative good agreement with the previous experiment. Unlike as with the sphere, there is no plateau of v_d in the channel. We could not reach very small velocities to confirm this observation more precisely.

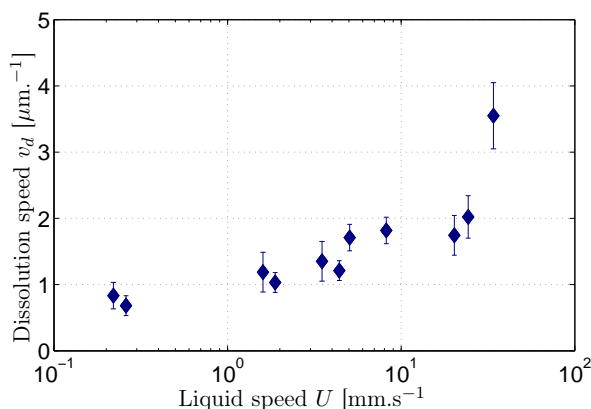


Figure E.2: Dissolution speed of maltodextrins channels - Dissolution speed of maltodextrin DE29 channels during water penetration at different velocities. v_d is measured using the refractive index of the outlet solution.

In the case of cylindrical channels, we were not able to precisely study the velocity effect because of important leaks near connectors. Nevertheless, we could obtain one data point for the liquid velocity $U = 1.7 \text{ mm.s}^{-1}$. The evolution of the channel radius with time was recorded using a video camera. We obtain a linear increase of channel radius with $v_d = 1.54 \text{ }\mu\text{m.s}^{-1}$. This dissolution speed is in relative good agreement with the one obtained with the sphere dissolution experiment.

E. DISSOLUTION OF MALTODEXTRINS

Appendix F

Preliminary study of the imbibition in a soluble media

In Nestlé Research Center, carbohydrate dehydrated powders exhibit radically different behaviour during the reconstitution process in water. By playing on the molecular weight or the preparation method of the powder, some powders dissolve very quickly while others lead to lumps formation. Even with the same maltodextrin, the differences can be important. Thus, the structure of the powder aggregates seem to control the reconstitution. In this appendix, we will perform a preliminary study to describe the penetration of water in a soluble capillary. We will consider dissolution and swelling and show that the dimensions of the maltodextrin capillary are key to predict why and where the water penetration stops through two mechanisms: viscosity increase of the contact line and pore closure.

F.0.3 Water penetration in soluble capillary

We consider a cylindrical capillary made of maltodextrin (Fig. F.1). Water penetrates by capillarity into the channel and dissolves the polymer, increasing both the capillary radius and the liquid viscosity. Moreover, hydration of the walls leads to a swelling that decreases the radius. Let R be the radius of the capillary at the coordinate z (initial pore radius is r_p). The flow at height z can be written as:

$$Q(z) = \int_0^R U(r, z) 2\pi r dr \quad (\text{F.1})$$

In the frame of a lubrication assumption, the speed profile $U(r, z)$ is given by:

$$U(r, z) = a(z) (R^2 - r^2) \quad (\text{F.2})$$

If we inject Eq. F.2 in Eq. F.1, we obtain:

$$Q(z) = a(z) R^4 \frac{\pi}{2} \quad (\text{F.3})$$

F. PRELIMINARY STUDY OF THE IMBIBITION IN A SOLUBLE MEDIA

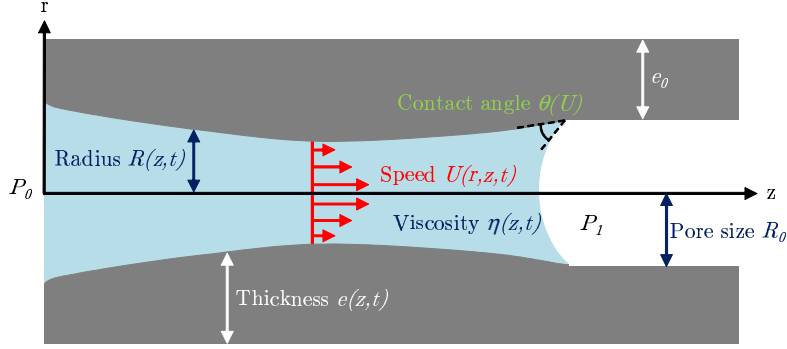


Figure F.1: Schematic representation of capillary penetration - Water penetration by capillarity in a maltodextrin soluble channel. Definition of the parameters.

The fluid incompressibility imposes that for small variations of R along z , Q can be considered as constant at a time t along the channel such $Q(z, t) \sim Q(t)$. The pressure gradient writes then:

$$\frac{dP}{dz} = \eta(z) \Delta \vec{U} \Big|_z = 4\eta(z)a(z) \quad (\text{F.4})$$

where $\eta(z)$ is the viscosity profile along the z -axis.

The capillary pressure is the motor for the imbibition leading to $\int \frac{dP}{dz} dz = \frac{2\gamma \cos(\theta)}{r_p}$. The integration of Eq. F.4 using Eq. F.3 allows obtaining an expression of Q :

$$Q(t) = \frac{\pi \gamma \cos(\theta)}{4r_p \int_0^L \frac{\eta(z,t)}{R(z,t)^4} dz} \quad (\text{F.5})$$

For a time step dt , the corresponding displacement is $dz = \frac{Q dt}{\pi R_0^2}$ and the average speed $U = \frac{Q}{\pi R_0^2}$ where $R_0 = R(t = 0)$. The implementation of the liquid displacement is performed using Matlab. At each step we calculate Q , to deduce dz and U . We use the dynamic contact angle of maltodextrin $\theta(U)$ which slightly reduces the penetration speed at short times. Dissolution and swelling processes are then considered as explained below:

- Dissolved matter is calculated using the measured $v_d(\phi, U)$ in sphere experiments. The polymer fraction in the liquid $\phi_p(z)$ along the capillary is calculated at each step as the resulting viscosity $\eta(z)$ (the relation $\eta(\phi_p)$ was obtained with rheology measurements). We assume that this polymer fraction is homogeneous in the tube for any given z . At each step, the dissolved matter is translated of dz and fresh water is injected between $z = 0$ and $z = dz$.
- Swelling is calculated using the contact time between the liquid and the wall. This contact time allows the calculation of the amount of water that has penetrated into the wall at the height z . We used the theory of diffusion in a semi-infinite solid described in appendix D.

The water fraction in the wall $\phi^w(z)$ can be obtained using the variable diffusion coefficient $D_p(\phi)$. The swelling is deduced from the average ϕ^w . With regards to experimental observations (for instance, the hydration of thin layers), we also impose a maximal swelling. Indeed, in practice the swelling saturates due to polymer chains stretching. Here, we choose to limit the swelling to 1, *i.e.* that the wall of thickness e cannot become thicker than $2e$.

F.0.4 Viscosity increase at the contact line

We begin the discussion by considering a maltodextrin capillary where only dissolution can occur and not swelling. In that case, the radius of the channel can only increase with time. At the beginning of the capillary penetration, the liquid velocity is large and the polymer concentration small what leads to a larger dissolution speed. Dissolution increases the viscosity of the liquid and modifies the dynamics of imbibition. When the viscosity close to the contact line reaches large values, the liquid front is stopped.

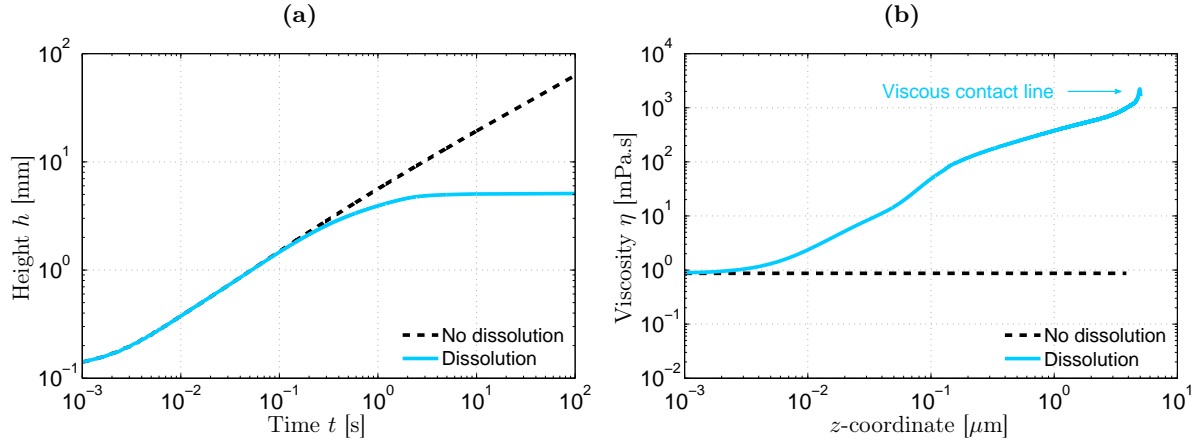


Figure F.2: Effect of dissolution on capillary penetration - Imbibition of a maltodextrin DE29 capillary by water ($r_p = 10 \mu\text{m}$, $e = 50 \mu\text{m}$). Comparison between a case without swelling and dissolution, and a case with dissolution. (a) Height of the liquid as a function of time. (b) Viscosity of the liquid at $t = 10$ s.

We show an example of dissolution effect in Fig. F.2a. We simulate the entrance of water in a maltodextrin DE29 capillary with $r_p = 10 \mu\text{m}$ and $e = 50 \mu\text{m}$. We plot the distance covered by water h as a function of time. The black dotted line represents the case without dissolution (and without swelling which is not considered in this subsection). We find that h is close to the Washburn law, *i.e.* $h \sim \sqrt{t}$. The slight differences result from the contact angle which depends on U in the simulation. In blue, we give the distance h when dissolution is activated. We observe that h curves separates from the black line around $t \sim 0.2$ s and finally reaches a plateau at $h \sim 5$ mm. This plateau is due to the increase of viscosity, especially at the contact line, that slows down the dynamics and eventually traps the contact line. We plot in Fig. F.2b the viscosity profile in the channel at $t = 10$ s. The viscosity has been multiplied by 1000 at the contact line.

F. PRELIMINARY STUDY OF THE IMBIBITION IN A SOLUBLE MEDIA

We have shown that the contact line in a carbohydrate channel can be trapped by viscosity increase. This process is especially intense for small capillary radii since the dissolved matter quickly saturates the water in the channel. Besides, long polymer chains lead to larger viscosities and so reduced distances of imbibition.

F.0.5 Effect of swelling behind the contact line

In this subsection, we now activate the swelling of the maltodextrin but we suppress dissolution. These conditions lead to a decrease of the capillary radius with time. It modifies the dynamics of capillary rise and if the swelling becomes too important, the channel eventually closes preventing the hydration of the remaining part of the capillary.

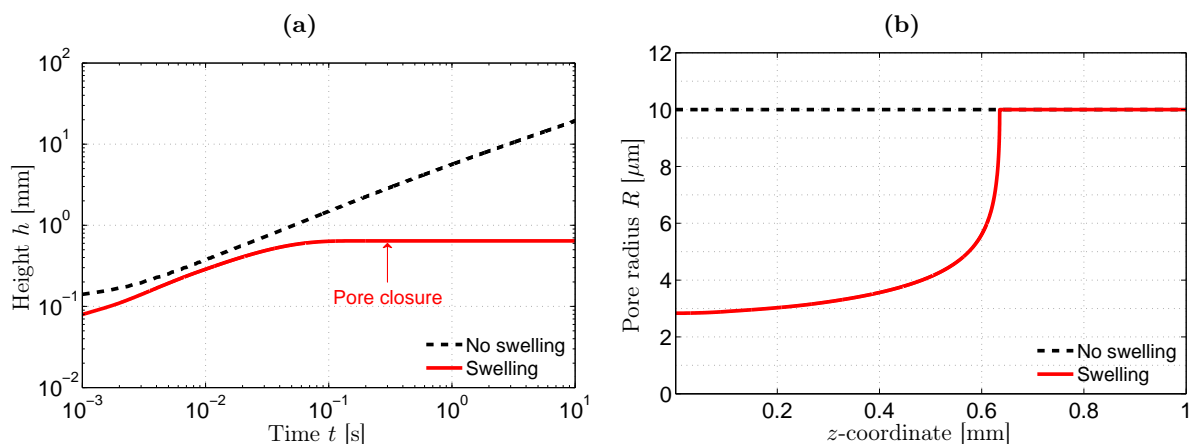


Figure F.3: Effect of swelling on capillary penetration - Imbibition of a maltodextrin DE29 capillary by water ($r_p = 10 \mu\text{m}$, $e = 50 \mu\text{m}$). Comparison between a case without swelling and dissolution, and a case with swelling. (a) Height of the liquid as a function of time. (b) Pore radius at $t = 0.1$ s.

We present in Fig. F.3a the effect of the swelling on the same maltodextrin DE29 capillary as in the previous subsection ($r_p = 10 \mu\text{m}$ and $e = 50 \mu\text{m}$). The distance covered by the liquid in the case where no swelling occurs (and no dissolution) is still represented in black. The case with swelling is plotted in red. We observe that at $t > 0.2$ s, the liquid does not move any more in the channel. h plateaus at 0.64 mm. This plateau comes from the closure of the channel. We plot in Fig. F.3b the pore radius at $t = 0.1$ s. We can see that it has decreased a lot especially at the entrance of the channel.

We have shown that swelling of the walls in a maltodextrin capillary can lead to a pore closure. This swelling that comes from diffusion of water through the walls reduces the capillary radius and if there is enough matter to swell, the contact line can be trapped. Thus, this process is important if the diffusion coefficient D_p is large (short carbohydrates) and if the walls are

thicker enough.

F.0.6 Dissolution and swelling

Let's now have a look to the case where dissolution and swelling are both considered. With the previous conditions ($r_p = 10 \mu\text{m}$ and $e = 50 \mu\text{m}$), adding dissolution almost does not modify the profile $h(t)$. Swelling dominates in that case. Dissolution becomes not negligible compared to swelling when the wall thickness e is of the same order of magnitude than the pore size r_p . The maximum swelling that the polymer can undergo is a key parameter to precisely define this transition.

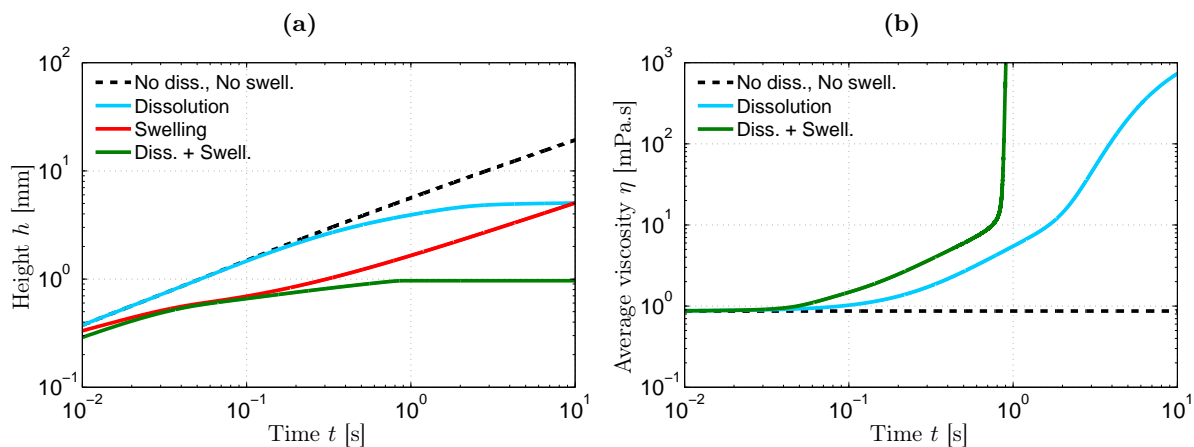


Figure F.4: Effect of dissolution and swelling on capillary penetration for small walls - Imbibition of a maltodextrin DE29 capillary by water ($r_p = 10 \mu\text{m}$, $e = 5 \mu\text{m}$). Comparison between different cases with or without swelling and dissolution. (a) Height of the liquid as a function of time. (b) Average viscosity in the channel as a function of time.

We present in Fig. F.4a a simulation performed with the same pore radius $r_p = 10 \mu\text{m}$ but with a smaller wall thickness $e = 5 \mu\text{m}$. The height of the liquid is compared for the four different cases: without dissolution and swelling (black dotted curve), with dissolution (blue curve), with swelling (red curve) and with both (green curve). We can see the corresponding average viscosity increase in the channel in Fig. F.4b. As explained in subsection F.0.4, the dissolution alone can lead to a viscosity increase that traps the contact line at $h \sim 5 \text{ mm}$. Here swelling alone cannot imply the closure of the pore because the walls are too thin. But when we combine dissolution and swelling, we observe a earlier viscosity increase of the channel that leads to a smaller covered distance by the liquid ($h < 1 \text{ mm}$). Thus, the effects are coupled and synergetic.

In conclusion, we have shown that two mechanisms can lead to the worsening of the imbibition process in a soluble capillary. Firstly, the increase of viscosity due to the dissolution can trap the contact line much sooner that expected with a non-soluble capillary. Then, the swelling of the polymer can lead to the closure of the channel. It would be interesting to develop a precise

F. PRELIMINARY STUDY OF THE IMBIBITION IN A SOLUBLE MEDIA

analysis in order to investigate in which situation one of these two mechanisms dominates.

F.0.7 Towards powder imbibition

The structure of a powder aggregates can considerably vary from one method of fabrication to another. For instance, Nestlé often used two kinds of maltodextrins: the DE and the IT. DE have smaller particles ($R \sim 40\text{-}50 \mu\text{m}$) what leads to intermediate pore sizes $r_p \sim 6\text{-}10 \mu\text{m}$. IT powders are made of bigger particles ($R \sim 200\text{-}350 \mu\text{m}$) and the pore size is also larger ($r_p \sim 40\text{-}50 \mu\text{m}$). The structure parameters will lead to strong differences of imbibition. Water will penetrate further in a powder bed of maltodextrin IT29 than in one of maltodextrin DE29. It is confirmed by the simulation that predicts a distance approximately divided by 10 for maltodextrin DE29.

Nevertheless, powder aggregates are much more complex objects than a single soluble capillary. The particles are spherical and even present and a wide range of pore sizes is observed. Our simulation is not precise enough to predict quantitatively the differences between aggregates. The order of magnitude for the critical covered distance is rather good but we know that the model has to be improved:

- Structure: tortuosity should be introduced.
- Pore size: a distribution of pore size would be better or at least two pore sizes.
- Dissolution: more dissolution speed measurements would be necessary to improve the precision of the simulation.
- Swelling: the limit of swelling is still rather unknown. Besides, we should couple swelling and dissolution since the most hydrated parts of the walls are surely dissolved. In fact, the boundary between the walls and the channel is a soft boundary with a continuity of the water content.

References

- [1] A. Tay, C. Monteux, D. Bendejacq, and F. Lequeux. How a coating is hydrated ahead of the advancing contact line of a volatile solvent droplet. *The European Physical Journal E*, 33(3):8, 2010. [i](#), [v](#), [9](#), [11](#), [65](#), [79](#), [143](#)
- [2] Astrid Tay and François Lequeux. *Dynamique du mouillage et du séchage d'une goutte d'eau sur un film de polymère hydrosoluble*. Thèse de doctorat, UPMC, Paris, 2009. [2](#), [8](#)
- [3] Thomas Young. An essay on the cohesion of fluids. *Philosophical Transactions of the Royal Society of London*, 95:65–87, January 1805. [5](#)
- [4] O. V. Voinov. Hydrodynamics of wetting. *Fluid Dynamics*, 11(5):714–721, 1976. [6](#)
- [5] R. G. Cox. The dynamics of the spreading of liquids on a solid surface. part 1. viscous flow. *Journal of Fluid Mechanics*, 168:169–194, 1986. [6](#)
- [6] E B Dussan. On the spreading of liquids on solid surfaces: Static and dynamic contact lines. *Annual Review of Fluid Mechanics*, 11(1):371–400, 1979. [6](#)
- [7] P. G. de Gennes. Wetting: statics and dynamics. *Reviews of Modern Physics*, 57(3):827–863, July 1985. [6](#)
- [8] J. Snoeijer and B. Andreotti. Moving contact lines: Scales, regimes and transitions. *Annual Review of Fluid Mechanics*, 2012. [6](#)
- [9] Oleg V. Voinov. Meniscus and precursor film in steady-state wetting. *Journal of Colloid and Interface Science*, 201(2):127–131, May 1998. [7](#)
- [10] T.D Blake and J.M Haynes. Kinetics of liquidliquid displacement. *Journal of Colloid and Interface Science*, 30(3):421–423, July 1969. [7](#)
- [11] T D Blake and J. De Coninck. The influence of solid-liquid interactions on dynamic wetting. *Advances in Colloid and Interface Science*, 96(1-3):21–36, 2002. [7](#)
- [12] Y.D. Shikhmurzaev. The moving contact line on a smooth solid surface. *International Journal of Multiphase Flow*, 19(4):589–610, August 1993. [7](#)
- [13] P. Petrov and I. Petrov. A combined molecular-hydrodynamic approach to wetting kinetics. *Langmuir*, 8(7):1762–1767, 1992. [7](#)
- [14] Robert D. Deegan. Pattern formation in drying drops. *Physical Review E*, 61(1):475–485, January 2000. [7](#), [114](#)
- [15] Tadashi Kajiya, Daisaku Kaneko, and Masao Doi. Dynamical visualization of coffee stain phenomenon in droplets of polymer solution via fluorescent microscopy. *Langmuir*, 24(21):12369–12374, 2008. [7](#), [114](#)
- [16] Kara L Maki and Satish Kumar. Fast evaporation of spreading droplets of colloidal suspensions. *Langmuir: The ACS Journal of Surfaces and Colloids*, 27(18):11347–11363, September 2011. [7](#), [114](#)
- [17] C. Monteux, Y. Elmaalem, T. Narita, and F. Lequeux. Advancing-drying droplets of polymer solutions: Local increase of the viscosity at the contact line. *EPL (Europhysics Letters)*, 83(3):34005, August 2008. [7](#), [114](#)
- [18] R. D Deegan, O. Bakajin, T. F Dupont, G. Huber, S. R Nagel, and T. A Witten. Capillary flow as the cause of ring stains from dried liquid drops. *Nature*, 389(6653):827–829, 1997. [8](#)
- [19] Emmanuelle Rio. *Gouttes, Flaques et Arches sèches : des lignes de contact en présence d'un écoulement*. PhD thesis, UPMC, Paris, 2005. [8](#)
- [20] G. Berteloot, C.-T. Pham, A. Daerr, F. Lequeux, and L. Limat. Evaporation-induced flow near a contact line: Consequences on coating and contact angle. *EPL (Europhysics Letters)*, 83(1):14003, July 2008. [8](#)
- [21] Katarzyna Hänni-Ciunel, Gerhard H. Findenegg, and Regine von Klitzing. Water contact angle on polyelectrolyte-coated surfaces: Effects of film swelling and droplet evaporation. *Soft Materials*, 5(2-3):61–73, 2007. [8](#)
- [22] Tadashi Kajiya, Adrian Daerr, Tetsuharu Narita, Laurent Royon, François Lequeux, and Laurent Limat. Dynamics of the contact line in wetting and diffusing processes of water droplets on hydrogel (PAMPS–PAAM) substrates. *Soft Matter*, 7(24):11425–11432, November 2011. [8](#), [115](#)
- [23] Pranesh Muralidhar, Elmar Bonaccorso, Günter K Auernhammer, and Hans-Jürgen Butt. Fast dynamic wetting of polymer surfaces by miscible and immiscible liquids. *Colloid and polymer science*, 289(14):1609–1615, 2011. [9](#)
- [24] P. G. de Gennes and Françoise Brochart. Kinetics of polymer dissolution. *Physico Chemical Hydrodynamics*, 4:313–322, 1983. [13](#)
- [25] Vivek V Ranade and Ramesh A Mashelkar. Convective diffusion from a dissolving polymeric particle. *AIChE Journal*, 41(3):666–676, March 1995. [13](#), [25](#)

REFERENCES

- [26] Alan Parker, Florence Vigouroux, and Wayne F Reed. Dissolution kinetics of polymer powders. *AIChE Journal*, 46(7):1290–1299, July 2000. [13](#)
- [27] Beth A. Miller-Chou and Jack L. Koenig. A review of polymer dissolution. *Progress in Polymer Science*, 28(8):1223–1270, August 2003. [13](#), [14](#)
- [28] Qi Wang, Peter R. Ellis, and Simon B. Ross-Murphy. Dissolution kinetics of water-soluble polymers: The guar gum paradigm. *Carbohydrate Polymers*, 74(3):519–526, November 2008. [13](#)
- [29] N L Thomas and A H Windle. A theory of case II diffusion. *Polymer*, 23(4):529–542, 1982. [13](#)
- [30] Qian T. and Taylor P.L. From the thomas-windle model to a phenomenological description of case-II diffusion in polymers. *Polymer*, 41(19):7159–7163, 2000. [13](#)
- [31] I. Hopkinson, R.A.L. Jones, S. Black, D.M. Lane, and P.J. McDonald. Fickian and case II diffusion of water into amylose: A stray field NMR study. *Carbohydrate Polymers*, 34(1–2):39–47, December 1997. [13](#)
- [32] V. G Levich. *Physicochemical hydrodynamics*. Prentice Hall, Englewood Cliffs, N.J., 1962. [13](#), [108](#), [109](#)
- [33] Veniamin Grigorevich Levich. *Physicochemical hydrodynamics: V. G. Levich Festschrift*. Advance Publications, 1977. [13](#), [108](#), [109](#)
- [34] L. Forný, A. Marabi, and S. Palzer. Wetting, disintegration and dissolution of agglomerated water soluble powders. *Powder Technology*, 206(1–2):72–78, January 2011. [14](#)
- [35] Edward W. Washburn. The dynamics of capillary flow. *Physical Review*, 17(3):273–283, March 1921. [14](#)
- [36] B.V. Zhmud, F. Tiberg, and K. Hallstenson. Dynamics of capillary rise. *Journal of Colloid and Interface Science*, 228(2):263–269, August 2000. [14](#)
- [37] José Bico and David Quéré. *Mécanismes d'imprégnation : Surfaces texturées, Bigouttes, Poreux*. PhD thesis, 2000. [14](#)
- [38] Asthana. Dissolutive capillary penetration with expanding pores and transient contact angles. *Journal of Colloid and Interface Science*, 231(2):398–400, 2000. [14](#)
- [39] C. Van den Berg. Description of water activity of foods for engineering purposes by means of the GAB model of sorption. *Engineering and food*, 1:311–321, 1984. [20](#)
- [40] T.P. Labuza, A. Kaanane, and J.Y. Chen. Effect of temperature on the moisture sorption isotherms and water activity shift of two dehydrated foods. *Journal of Food Science*, 50(2):385–392, 2006. [20](#)
- [41] Richard J Lloyd, X. Dong Chen, and Jim B Hargreaves. Glass transition and caking of spray-dried lactose. *International Journal of Food Science & Technology*, 31(4):305–311, August 1996. [20](#)
- [42] Yrjö Roos. Melting and glass transitions of low molecular weight carbohydrates. *Carbohydrate Research*, 238:39–48, January 1993. [20](#)
- [43] F Doumenc, H Bodiguel, and B Guerrier. Physical aging of glassy PMMA/toluene films: influence of drying/swelling history. *The European Physical Journal. E, Soft Matter*, 27(1):3–11, September 2008. PMID: 19230224. [21](#)
- [44] Paul J. Flory. *Principles of Polymer Chemistry*. Cornell University Press, 1953. [21](#)
- [45] E. O. Stejskal and J. E. Tanner. Spin diffusion measurements: Spin echoes in the presence of a time-dependent field gradient. *The Journal of Chemical Physics*, 42(1):288, 1965. [22](#)
- [46] C.S. Johnson. *Diffusion measurements by magnetic field gradient methods*. In *Encyclopedia of Nuclear Magnetic Resonance*. Wiley edition, 1996. [22](#)
- [47] R. Bachus and R. Kimmich. Molecular weight and temperature dependence of self-diffusion coefficients in polyethylene and polystyrene melts investigated using a modified n.m.r. field-gradient technique. *Polymer*, 24(8):964–970, August 1983. [22](#)
- [48] R Kimmich. *NMR : tomography, diffusometry, relaxometry*. Springer, Berlin; New York, 1997. [22](#)
- [49] Maxime Van Landeghem, Bruno Bresson, Bernhard Blümich, and Jean-Baptiste d’Espinoze de Lacaille. Micrometer scale resolution of materials by stray-field magnetic resonance imaging. *Journal of Magnetic Resonance*, 211(1):60–66, July 2011. [22](#)
- [50] D. E Woessner. Effects of diffusion in nuclear magnetic resonance spin-echo experiments. *The Journal of Chemical Physics*, 34(6):2057–2061, June 1961. [22](#)
- [51] S. Yamamoto, W.J. Coumans, and T.J.H. Vlucht. Determining concentration dependent diffusivity in food materials. Brighton, 1997. [23](#)
- [52] Masao Doi and S. F. Edwards. *The Theory of Polymer Dynamics*. Oxford University Press, November 1988. [23](#)
- [53] Michael Rubinstein and Ralph H. Colby. *Polymer Physics*. Oxford University Press, August 2003. [23](#)
- [54] Pierre-Gilles de Gennes, Françoise Brochard, and David Quéré. *Gouttes, bulles, perles et ondes*. Belin, March 2002. [32](#)
- [55] Hughes Bodiguel. *Propriétés de films polymères ultraminces*. PhD thesis, UPMC, Paris, 2006. [38](#)

- [56] Murat Guvendiren, Shu Yang, and Jason A. Burdick. Swelling induced surface patterns in hydrogels with gradient crosslinking density. *Advanced Functional Materials*, 19(19):3038–3045, 2009. [105](#)
- [57] Jiangshui Huang, Megan Juskiewicz, Wim H De Jeu, Enrique Cerda, Todd Emrick, Narayanan Menon, and Thomas P Russell. Capillary wrinkling of floating thin polymer films. *Science*, 317(5838):650–653, March 2007. [105](#)
- [58] Hugues Vandeparre, Miguel Piñeirua, Fabian Brau, Benoit Roman, José Bico, Cyprien Gay, Wenzhong Bao, Chun Ning Lau, Pedro M. Reis, and Pascal Damman. Wrinkling hierarchy in constrained thin sheets from suspended graphene to curtains. *Physical Review Letters*, 106(22):224301, June 2011. [106](#)
- [59] Elizabeth R. Jerison, Ye Xu, Larry A. Wilen, and Eric R. Dufresne. Deformation of an elastic substrate by a three phase contact line. *Physical Review Letters*, 106(18):186103, May 2011. [115](#)

Declaration

I hereby declare that this Ph.D. thesis entitled "Wetting of soluble polymers" was carried out without the prohibited assistance of third parties and without making use of aids other than those specified. I further declare that the thesis or any part thereof has not formed the basis for the award of any Degree, Diploma, Fellowship or other similar title.

The thesis work was conducted from November 2009 to November 2012 under the supervision of François Lequeux at ESPCI in Paris in order to obtain the Ph.D. degree of the Pierre & Marie Curie University.

PARIS,
Julien Dupas

Contacts

**Julien Dupas**

PPMD Laboratory - E003
ESPCI
10 rue Vauquelin, 75231 Paris Cedex 05
julien.dupas@espci.org
julien.dupas1985@gmail.com
01 40 79 58 48

Laurence Talini

PPMD Laboratory - H205
ESPCI
10 rue Vauquelin, 75231 Paris Cedex 05
laurence.talini@espci.fr
01 40 79 46 79

François Lequeux

Directeur scientifique
ESPCI
10 rue Vauquelin, 75231 Paris Cedex 05
françois.lequeux@espci.fr
01 40 79 45 16

Emilie Verneuil

PPMD Laboratory
ESPCI
10 rue Vauquelin, 75231 Paris Cedex 05
emilie.verneuil@espci.fr

**Laurent Forny**

Department Food Science & Technology
Nestlé Research Center
PO. Box 44, CH-1000 Lausanne 26, Switzerland
laurent.forny@rdls.nestle.com

Marco Ramaioli

Department Food Science & Technology
Nestlé Research Center
PO. Box 44, CH-1000 Lausanne 26, Switzerland
marco.ramaioli@rdls.nestle.com

Résumé : Le mouillage d'un substrat soluble est une situation couramment rencontrée dans la vie de tous les jours les jours. Par exemple, les motivations pratiques de cette étude concernent la préparation de boissons à partir de poudres déshydratées, constituées de substances solubles dans l'eau telles que les glucides. Les modèles hydrodynamiques décrivant le mouillage sur un substrat non soluble ne peuvent pas expliquer les observations expérimentales dans le cas d'un liquide s'étalant sur un substrat soluble. Tay *et al.*(1) ont émis l'hypothèse que la fraction d'eau ϕ à la ligne de contact contrôle la valeur de l'angle de contact θ et ils ont montré l'importance du processus d'évaporation/condensation du solvant lors du mouillage. Dans cette étude, nous montrons que d'autres transferts de matière doivent être considérés pour améliorer la compréhension du processus de mouillage d'une couche soluble; ainsi la diffusion dans le polymère de l'eau condensée, ou directement depuis la goutte sont des processus qui contribuent à hydrater le substrat et modifier l'angle de contact de la goutte. Nous avons utilisé l'approche suivante pour réaliser cette étude: (i) pour prendre en compte la diffusion dans le substrat, nous avons réalisé des simulations en éléments finis qui permettent de valider nos arguments théoriques, (ii) des expériences d'étalement de goutte sur des couches minces de maltodextrine ont été réalisées afin d'étudier le mouillage et l'hydratation en avant de la ligne de contact. Ce travail nous permet de mettre en avant l'influence de la diffusion dans la couche qui complexifie les profils d'hydratation en avant de la ligne de contact, avec notamment l'apparition d'une région de diffusion où de l'évaporation est observée. Un diagramme de mouillage épaisseur-vitesse ($e - U$) avec différents régimes est établi. Nous validons ces régimes expérimentalement et plus particulièrement un régime où l'angle de contact est une fonction du produit eU . Par ailleurs, nous montrons l'influence de la transition vitreuse du polymère sur l'angle de contact et l'hydratation. Enfin, une étude préliminaire est réalisée pour comprendre l'influence de la dissolution du polymère lors du mouillage.

Mots Clés : mouillage, évaporation, condensation, diffusion, dissolution, couches minces, transition vitreuse, maltodextrine.

Abstract: The wetting of a soluble substrate is a situation commonly encountered in day-to-day life. For instance, the practical motivation of this study concerns the preparation of beverages using dehydrated powders, consisting of water-soluble substances such as carbohydrates. Hydrodynamical theories describing wetting onto insoluble substrates cannot account for experimental observations in the case of a liquid spreading onto a soluble substrate. Tay *et al.*(1) made the hypothesis that the water content ϕ at the contact line controls the contact angle value θ and they showed the importance of the evaporation/condensation of the solvent during wetting. In this study, we demonstrate that other mass transfers have to be considered to improve the understanding on wetting dynamics on soluble surfaces; thus diffusion within the polymer of the condensed water or directly from the droplet are processes that contribute to the hydration of the substrate and the modification of the contact angle of the drop. Therefore, we use the following approach to carry out this study: (i) finite elements simulations are performed in order to take into account diffusion effects in the layer and validate our theoretical arguments, (ii) spreading experiments of water onto maltodextrin thin layers are performed in order to study the wetting and the hydration ahead the contact line. This work allows us to highlight the influence of the diffusion in the polymer that makes the hydration profiles ahead the contact line more complex with a diffusion region where evaporation occurs. A wetting diagram thickness-velocity ($e - U$) with different regimes is established. Those regimes are validated with the experimental data. In particular, we evidence a regime where the contact angle θ is a function of the quantity eU . Furthermore, we evidence the effect of glass transition in the polymer on the contact angle and the hydration of the substrate. Finally, a preliminary study is performed to understand the influence of another transfer at stake in the wetting process: the dissolution of the polymer in the solvent.

Key words: wetting, evaporation, condensation, diffusion, dissolution, thin layers, glass transition, carbohydrates.